Title

Machine Learning-Assisted Simulation and Design for Functional Nanomaterials

Author

Zheng, Bowen

Publication Date

2023

Peer reviewed|Thesis/dissertation

Machine Learning-Assisted Simulation and Design for Functional Nanomaterials

By

Bowen Zheng

A dissertation submitted in partial satisfaction of the

requirements for the degree of

Doctor of Philosophy

in

Engineering - Mechanical Engineering

in the

Graduate Division

of the

University of California, Berkeley

Committee in charge:

Professor Grace X. Gu, Chair
Professor Zeyu Zheng
Professor Panayiotis Papadopoulos

Fall 2023

Machine Learning-Assisted Simulation and Design for Functional Nanomaterials

Abstract

Machine Learning-Assisted Simulation and Design for Functional Nanomaterials

by

Bowen Zheng

Doctor of Philosophy in Engineering - Mechanical Engineering

University of California, Berkeley

Professor Grace X. Gu, Chair

Often deemed as a "wonder material", graphene has exhibited remarkable promises in a broad range of research fields thanks to its exceptional electronic, thermal, and mechanical properties. However, issues such as the inevitable existence of defects and the complex microstructures of graphene-based materials stand as a bottleneck in realizing its full potential in real-life applications. With the fast growth of big data, machine learning has been widely applied in many fields such as finance, biology, and healthcare. The advent of machine learning approaches also offers solutions to learning patterns from complex data in material design and discovery, reducing the need for expensive, time-consuming, and tedious laboratory experiments or numerical simulations. In the present thesis, machine learning-assisted simulation and design approaches for functional nanomaterials are demonstrated, with a focus on the graphene family. Molecular dynamics simulations are conducted to numerically investigate the mechanical behavior of graphene-based materials such as graphene, graphene oxide and graphene aerogel, and various machine learning techniques including kernel ridge regression, Gaussian process metamodels, and deep reinforcement learning are used in the predictive and generative modeling of these materials. Finally, the concept and the promise of machine learning interatomic potentials in achieving efficient and accurate simulations for metal-organic framework materials are presented. The research constituting the present thesis may shed light on some new possibilities of simulating and designing functional nanomaterials, which may further improve the performances of applications such as stretchable electronics, supercapacitor devices, carbon sequestration technologies, among others.

Contents

Contents **i**

List of Figures **ii**

List of Tables **xiv**

1 Introduction **1**
1.1 Graphene and graphene-related materials 1
1.2 Machine learning for nanomaterial simulation, prediction and design 2

2 Graphene defect engineering **4**
2.1 Tuning graphene mechanical anisotropy 4
2.2 Graphene defect mitigation 24
2.3 Stress field properties of defective graphene 36

3 Machine learning for graphene-based materials **52**
3.1 Graphene defect detection 52
3.2 Scalable graphene defect prediction 65
3.3 Chemical composition identification for graphene oxide 77
3.4 Graphene oxide design using deep reinforcement learning 92

4 Simulation and machine learning for graphene aerogel **108**
4.1 Uncertainty quantification and prediction for mechanical properties 108
4.2 Structral integrity of graphene aerogels 119

5 Simulation acceleration via machine learning force fields **137**
5.1 Machine learning force fields for metal-organic frameworks 139

6 Summary and future directions **153**

Bibliography **154**

List of Figures

2.1 Model setup and simulation results of pristine graphene. (a) Schematic of pristine graphene and illustration of tensile loading directions. (b) Morphology of monolayer graphene after running for equilibrium at 300 K. (c) Stress-strain curves and fracture modes of pristine graphene upon zigzag and armchair loadings. . . 6

2.2 Simulation results of graphene design with single centered line defect. Deformation and fracture modes of graphene sheets with (a) a zigzag and (b) an armchair defect. Stress-strain curves of graphene sheets with (c) zigzag and (d) armchair defect. The failure stresses and strains of the pristine monolayer graphene under two loading conditions are marked in the curve figures for comparison. 8

2.3 Parametric study of graphene with single centered line defect with respect to defect length. Influence of defect length on (a) the failure stress and (b) failure strain of graphene with zigzag defect. Influence of defect length on (c) the failure stress and (d) failure strain of graphene with armchair defect. Zero defect length corresponds to pristine graphene. (e) Evolution of data points with increasing defect length on ratio graph. Data point corresponding to pristine graphene is illustrated with a star symbol. 10

2.4 Simulation results of graphene design with single centered oblique line defect. Deformation and fracture modes of graphene sheets with (a) $\theta = 30^\circ$ and (b) $\theta = 60^\circ$ defect. Stress-strain curves of graphene sheets with (c) $\theta = 30^\circ$ and (d) $\theta = 60^\circ$ defect. The failure stresses and strains of the pristine graphene sheet under two loading conditions are marked in the curve figures for comparison. . . 12

2.5 Parametric study of graphene with a centered oblique line defect with respect to a variable tilting angle θ. The influence of tilting angle θ on (a) failure stress and (b) failure strain of defected graphene. Defect angles of $\theta = 0^\circ$ and $\theta = 90^\circ$ correspond to line defect in zigzag and armchair direction, respectively. 13

2.6 Evolutionary paths or distribution of data points on the ratio graph. (a) Evolutionary path of data points of graphene with centered oblique line defect when the tilting angle θ increases. (b) Distribution of data points of graphene with offset line defect with various offset distances e_{D}. (c) Evolutionary path of data points of graphene with multiple parallel line defects with increasing defect number N_{D}. 13

2.7 Simulation results of graphene design with offset line defect. Deformation and fracture modes of graphene sheets with (a) zigzag and (b) armchair defect. Stress-strain curves of graphene sheets with (c) zigzag and (d) armchair defect. The failure stresses and strains of the non-offset defected graphene sheet under two loading conditions are marked in the curve figures for comparison. 15
2.8 Parametric study of graphene with offset line defect with respect to offset distance e_{D}. The influence of offset distance on (a) the failure stress and (b) failure strain of graphene with zigzag defect. The influence of offset distance on (c) the failure stress and (d) failure strain of graphene with armchair defect. (e) Illustration of defect elimination and bond forming of graphene sheet with armchair defect with $e_{\mathrm{D}}/L_{\mathrm{A}} = 0.4$ upon armchair loading. 16
2.9 Simulation results of graphene with uniform parallel line defects. Deformation and fracture modes of graphene sheets with (a) zigzag and (b) armchair defect. Stress-strain curves of graphene sheets with (c) zigzag and (d) armchair defect. The lengths of zigzag and armchair defect are $0.5L_{\mathrm{Z}}$ and $0.5L_{\mathrm{A}}$, respectively. The failure stresses and strains of the centered line defect with the same length are marked in the curve figures for comparison. 17
2.10 Parametric study of graphene with uniform parallel line defects with respect to defect number N_{D}. The influence of defect number on (a) the failure stress and (b) strain of graphene with zigzag defects. The influence of defect number on (c) the failure stress and (d) strain of graphene with armchair defects. 18
2.11 Complex defect pattern designs. (a) Network-like graphene kirigami, (b) graphene kirigami with parallel zigzag interior and exterior cuts, and (c) graphene kirigami with parallel armchair interior and exterior cuts. 19
2.12 Simulation results of the network-like graphene kirigami. (a) Deformation and fracture modes and (b) stress-strain curves of the exemplar network-like graphene kirigami. 20
2.13 Distribution or evolutionary paths of data points of complex patterned defect designs on 2D ratio graph. (a) Distribution of data points of a variety of designs of network-like graphene kirigami. (b) Evolution of data points of graphene kirigami with parallel interior and exterior cuts. The attainable region of network-like graphene kirigami design is marked on the graph to draw comparison. 21
2.14 Fracture modes and stress-strain curves of graphene kirigami with zigzag parallel interior and exterior cuts with parameters $(L_1, L_2) = (0.6L_{\mathrm{Z}}, 0.35L_{\mathrm{Z}})$. Fracture modes of graphene kirigami upon (a) zigzag and (b) armchair loadings, where spots of fracture are highlighted with blue circles. (c) Stress-strain curve of graphene kirigami upon zigzag loading with the failure stress and strain of pristine graphene sheet upon zigzag loading as a comparison. (d) Stress-strain curve of graphene kirigami upon armchair loading with the failure strains of pristine graphene sheet upon zigzag and armchair loadings for comparison. 22

2.15 2D map representations of parametric study of graphene kirigami with interior and exterior cuts with respect to parameter pair (L_1, L_2). The influence of L_1 and L_2 on failure stress and strain of graphene kirigami with zigzag parallel defects upon (a, b) zigzag and (c, d) armchair loading. The influence of L_1 and L_2 on failure stress and strain of graphene kirigami with zigzag parallel defects upon (e, f) zigzag and (g, h) armchair loading. 23
2.16 Schematic of pristine and defective graphene sheets used for MD simulation. (a) Square pristine graphene sheet and illustration of tensile loading directions. Arrows with 'Z' and 'A' represent tensile loading in the zigzag and armchair directions, respectively. (b) Square graphene sheets with an elliptical defect of various sizes and shapes. 26
2.17 Demonstration of degradation recovery by enlarging the preexisting defect to an elliptical shape. (a) Calculated stress–strain curves, and (b) unloaded and failure morphologies of a pristine graphene sheet, graphene sheet with a circular defect, and graphene sheet with an elliptical defect for degradation recovery. 27
2.18 Illustration of proposed recovery mechanism and its validation. (a) Morphologies of surrounding areas of circular and elliptical defects right before fracture. Red arcs show the defect rims before the loading. (b) Change in curvature at any point on the rim of the circular and the elliptical defect, where the arrows point to the maximum changes in curvature in the two cases. (c) Stress–strain curves of graphene sheets with the elliptical defect and the rectangular defect of the same dimensions in the zigzag and armchair directions. (d) Mode of fracture initiation of graphene sheets with the rectangular defect. 29
2.19 Stress distributions during the failure process of pristine graphene sheets and graphene sheets with circular and elliptical defects. To illustrate the stress concentration more clearly, stress that is over 80% of the maximum stress $\sigma_{\max}$ of the individual case is colored red. 30
2.20 The influence of 1D lengthening of a circular defect on the mechanical properties of graphene sheet. (a) Failure stress and (b) failure strain of graphene sheet with a defect of increasingly lengthened dimension parallel to the loading and unchanged dimension in the perpendicular direction. The failure stress and strain of a pristine graphene sheet are added on the figures for comparison, as are marked with dashed-horizontal lines and the letter 'P'. (c) Evolutionary path of data points on the 2D anisotropy graph as the axis of the elliptical defect in the examined direction is lengthened, while the axis perpendicular to the examined direction is fixed. 31

2.21 The influence of size and shape of an elliptical defect on the mechanical properties of graphene sheet. Failure stress maps of graphene sheet with elliptical defects of various sizes and shapes in the (a) zigzag and (b) armchair directions. Failure strain maps of a graphene sheet with elliptical defects of various sizes and shapes in the (c) zigzag and (d) armchair directions. Recovering effect and the weakening effect of the defect dimension perpendicular to the examined direction are illustrated with green and blue arrows pointing to the direction of greater intensity. White lines represent circular defects. The influence of circular defects on (e) failure stress and (f) failure strain of graphene sheet. The failure stresses and strains of pristine graphene sheet are added on the figures for comparison, as are marked with dashed-horizontal lines and the letter 'P'. 33
2.22 Evaluation of recovery potential with respect to variable size of a circular defect. Failure stress in the (a) zigzag and (b) armchair directions. Failure strain in the (c) zigzag and (d) armchair directions. 34
2.23 Graphene sheets containing one-atom vacancy and its corresponding line defect. Geometries of graphene with (a) the one-atom vacancy and (b) the line defect. (c) Stress–strain relations of above two defective graphene sheets. 35
2.24 Stress–strain relations of graphene with a circular defect (diameter = $0.15L$) and graphene with a square defect (side length = $0.15L$) in the (a) zigzag and (b) armchair directions. 36
2.25 Stress fields, stress–strain curves, and distributions of displacement magnitude of pristine and defective graphene sheets. (a–c) Stress fields, (d) stress–strain curves, and distributions of (e–g) out-of-plane and (h–j) in-plane displacement magnitude of stretched pristine graphene, defective graphene with a line defect, and defective graphene with a circular defect, respectively. Distributions are plotted based on the morphologies right before the initiation of failure. 38
2.26 Ultimate strengths of graphene sheets centered a rectangular defect with varying geometric parameter pair $(L_\parallel, L_\perp)$. (a) Illustration of the geometric parameter pair $(L_\parallel, L_\perp)$. (b) Ultimate strength σ_{u} as a function of $(L_\parallel, L_\perp)$, normalized by $\sigma_{\mathrm{u},max} = 107.1\mathrm{GPa}$ at $(L_\parallel, L_\perp) = (0.8L, 0.1L)$. Black lines represent defect geometries sharing the same area. The white line represents square-shaped defects. The arrow indicates the major degradation direction. 41
2.27 Simulation results of defective graphene sheets with rectangular defects of various $L_\parallel/L_\perp$ but a fixed area. (a) Stress fields and distributions of out-of-plane and in-plane displacement magnitude and (b) stress–strain curves of the defective graphene sheets with $(0.1L, 0.8L)$, $(0.2L, 0.4L)$, $(0.4L, 0.2L)$, $(0.8L, 0.1L)$, rectangular defects, and a line defect parallel to the stretch with a length of $0.5L$. 42
2.28 Influence of defect shape on the mechanical properties of graphene sheets. (a–c) Initial shapes, (d–f) stress fields, distributions of (g–i) out-of-plane and (j–l) in-plane displacement magnitude, and (m) stress–strain curves of square-shaped, circular, and diamond-shaped defects. 43

2.29 Simulation results of graphene sheets with a centered diamond-shaped defect. Stress distributions of graphene sheets with diamond-shaped defects parametrized by (a) $|x| + 3|y| = 0.4L$ and (b) $3|x| + |y| = 0.4L$. (c) Stress–strain curves of above two defective graphene sheets. 45
2.30 Comparisons between predicted dichotomizing points and simulation results of graphene sheets with a (a) circular defect, (b) elliptical defect, (c) quadratic polynomial-shaped defect, and (d) sine-shaped defect. 46
2.31 Stress fields of graphene sheets with two defects. Graphene sheets with two (a) rectangular and (b) circular defects aligned on the center line parallel to the stretch. (c) Graphene sheet with two identical rectangular defects but not aligned on the center line parallel to the stretch. (d) Graphene sheet with two identical rectangular defects with no overlap transverse to the stretch. 47
2.32 Stress-strain curves of defective graphene sheets with multiple defects in Fig. 2.31. 48
2.33 Simulation results of graphene sheets with N circular defects aligned in the stretching direction. Stress distributions for (a) $N = 1$, (b) $N = 2$, and (c) $N = 3$. (d) Stress–strain curves for $N = 1$–3. 49
2.34 σ_{u}-ε_{f} plots summarizing mechanical properties of all the defects studied. Graphene sheets with (a) a single defect and (b) multiple defects. The gray area in (b) represents the distribution of data points in (a). 50
2.35 Influences of $L_{\parallel}$ and $L_{\perp}$ on the ultimate strength σ_{u} of the defective graphene sheet. σ_{u} as a function of (a) $L_{\parallel}$ and (b) $L_{\perp}$. Data points of elliptical and line defects are from refs [218] and [220]. 51

3.1 Descriptions of graphene sheets with vacancies and the procedure of data preparation. (a) Schematic of the defected graphene sheet and vacancy indexing, where a graphene sheet containing vacancies (6,6), (27,8), and (36,17) is used as an example. (b) Route of data preparation. (c) 2D energy distribution of graphene sheet with a vacancy (18,11), fixed atoms on the edges are not included in the contour plot. (d) 1D energy vector compressed from the 2D energy distribution and its correlation with the original graphene lattice. 54
3.2 2D energy distributions of (a) a pristine graphene sheet and (b) a graphene sheet with a vacancy (5, 16). 56
3.3 Portions of energy vector corresponding to (a) the first row and (b) the last row of atoms. The graphene sheet here contains a single vacancy at (1,10), which lies on the first row of atoms. 56
3.4 Results of the atom-based ML prediction for a single-atom vacancy. (a) An example of energy vector from the test data. (b) Predicted label vector. (c) 2D presentation of the predicted label vector. (d) Validation and testing accuracies as a function of regularization parameter λ. (e) Predicted label vector under a relatively strong regularization $\lambda = 10^{-3}$. 58

3.5 Domain discretization of a graphene sheet. (a) Schematic of an N_{R}-by-N_{R} uniform domain discretization. (b) 2D energy distributions by 18-by-18 discretization converted from the atom-based energy vector in Fig. 3.4(a). (c) 1D energy vector compressed from 18-by-18 discretization in (b). (d) 2D energy distribution of 10-by-10 discretization converted from the atom-based energy vector in Fig. 3.4(a). (e) 1D energy vector compressed from 10-by-10 energy discretization in (d). . . 59
3.6 ML predictions of a single-atom vacancy with domain discretization. (a–c) Predicted label vectors on an 18-by-18 discretization with kernel degrees 1, 2, and 3, respectively. The margin h is illustrated by the gray areas. (d) 2D presentation of the predicted label vector of kernel degree 2. (e) Validation and f testing accuracies with kernel degrees $p \in \{1, 2, 3\}$, as a function of N_{R} 60
3.7 Effect of regularization on predicting a single-atom vacancy by the domain-based method. (a) Validation and (b) testing accuracies as a function of N_{R} and λ. . . 61
3.8 ML predictions of multiple vacancies with domain discretization. (a) An example of energy vectors from the test data. (b) Predicted label vector by a quadratic kernel from the energy vector in (a). (c) True label vector. (d–f) 2D presentations of (a–c), respectively. 62
3.9 Parametric study and optimal performances of predicting multiple vacancies. (a–c) Testing accuracies of kernel degree $p \in \{1, 2, 3\}$, as a function of N_{R} and threshold τ. (d–f) Validation accuracies of kernel degree $p \in \{1, 2, 3\}$, as a function of N_{R} and threshold τ. (g) Validation and (h) testing accuracies as a function of N_{R} with optimal choices of τ^*. 63
3.10 Effect of regularization on predicting multiple vacancies by the domain-based method. (a) Validation and (b) testing accuracies as a function of N_{R} and λ, with $\tau = 0.4$. 64
3.11 Schematics of defect-containing graphene sheets. Smaller graphene sheets with (a) one defect and (b) multiple defects for training. Larger graphene sheets with (c) one defect and (d) multiple defects for testing. "A" and "Z" denote the armchair and zigzag directions, respectively. (e) An example of vibration amplitude distributions in a defect-containing graphene sheet. Distributions at three different time instances are plotted: before vibration, 15 ps, and 30 ps after the initialization of the NVT ensemble. t denotes the time passed in the NVT ensemble where the vibrational responses are recorded. 66
3.12 Data preparation procedure for ML. Boxes in red are properties of each individual atoms. (a) Illustration of query point and grid construction. (b) Displacement time series $z(t)$ and (c) the corresponding frequency response $z(f)$ of a vibrating atom in the graphene sheet. 68
3.13 ML results of validation sets for one-defect scenarios. (a) Schematic of discretized graphene domain for one-defect graphene sheets. The entire vibrating graphene domain is discretized by an M-by-M mesh (in this case, $M = 10$, $a = 4.37$ Å). Defect-containing grid is highlighted in light blue. (b) Validation accuracies (TA, TPR, TNR) as a function of the grid size a for 9-grid and 25-grid approaches. . 70

3.14 Validation accuracies with and without query point locations. (a) 9-grid and (b) 25-grid approaches. 70
3.15 Test accuracies for one-defect scenarios. (a) TA, (b) TPR, and (c) TNR as a function of the grid size a based on three test sets. (d) Average accuracies over all three test sets as a function of a. 71
3.16 Validation accuracies of multiple-defect graphene sheets. 72
3.17 Validation and test accuracies of Type 1 near-edge/-corner defects. The length of feature vectors is 9. (a) Illustration of Type 1 near-edge/-corner defects. (b) Validation and (c) test accuracies. 73
3.18 Validation and test accuracies of Type 2 near-edge/-corner defects. The length of feature vectors is 12. (a) Illustration of Type 2 near-edge/-corner defects. (b) Validation and (c) test accuracies. 73
3.19 Validation and test accuracies of Type 3 near-edge/-corner defects. The length of feature vectors is 16. (a) Illustration of Type 3 near-edge/-corner defects. (b) Validation and (c) test accuracies. 73
3.20 Validation and test accuracies of Type 4 near-edge/-corner defects. The length of feature vectors is 15. (a) Illustration of Type 4 near-edge/-corner defects. (b) Validation and (c) test accuracies. 74
3.21 Validation and test accuracies of Type 5 near-edge/-corner defects. The length of feature vectors is 20. (a) Illustration of Type 5 near-edge/-corner defects. (b) Validation and (c) test accuracies. 74
3.22 Test accuracies for multiple-defect scenarios. (a) TA, (b) TPR, and (c) TNR as a function of the grid size a based on three test sets. (d) Average accuracies over all three test sets as a function of a. 75
3.23 Accuracies when a weighted cost function is used (weight ratios $w_0/w_1 = 0.5, 1, 2$). Average (a) TA, (b) TPR, and (c) TNR of three test sets as a function of grid size a for one-defect graphene sheets. Average (d) TA, (e) TPR, and (f) TNR of three test sets as a function of grid size a for multiple-defect graphene sheets. . . 76
3.24 An example of graphene sheet that contains a larger defect (circled). 77
3.25 Schematic of GO sheets and mechanical responses upon tensile loading. (a) Schematic of the GO sheet with a side length of L. "a" and "z" refer to the armchair and zigzag directions of the GO basal plane. (b) Shape of the GO sheet upon full relaxation at a temperature of 300 K. (c) Comparison between the stress–strain curves of the present MD simulation and the result in ref. (26) The inset shows the GO structure used in this simulation case. (d) Stress–strain curves of GO sheets of various sizes with fixed parameters $\varphi_{\mathrm{O}} \simeq 0.253$ and $\varphi_{\mathrm{f}} \simeq 0.561$. . 81
3.26 Thermal effect on the mechanical properties of GO sheets. (a) Stress-strain curves of GO sheet under various temperatures. (f) GO structure immediately after relaxation at $T = 1000$ K. 82
3.27 Mechanical responses of four GO sheets with $\varphi_{\mathrm{O}} \simeq 0.253$ and $\varphi_{\mathrm{f}} \simeq 0.561$ and random spatial distributions of functional groups. (a–d) Structures of four exemplar GOs. (e) Stress–strain curves and (f) system potential energy evolutions. 83

3.28 Distributions of all 1,670 sample points on (a) the $N_{\text{-O-}}$-$N_{\text{-OH}}$ plane and (b) the φ_{O}-φ_{f} plane. the maximum $N_{\text{-OH}} = 336$ is achieved when $N_{\text{-O-}} = 0$ and all 336 non-edge atoms are functionalized by hydroxyl groups, resulting in $N_{\text{-OH}} = 336$. The estimation of maximum $N_{\text{-O-}}$ is more complex, because the order of assigning epoxides on pairs affect the removal due to violating physics. When all 226 potential sites are pre-selected with multiple arrangements, the maximum $N_{\text{-O-}}$ is close to 100. It is noteworthy that both of the extreme cases above are extremely rare in real GOs. The purpose is to cover all possibilities. 84
3.29 Extracted features as a function of φ_{O} and φ_{f}. (a) σ_{u}, (b) ϵ_{u}, and (c) U_{V} as a function of φ_{O} and φ_{f}. Data are from the training and the validation sets. . . . 85
3.30 Flow-chart presentation of the ML procedure. 86
3.31 Hyperparameter tuning results of gradient boosting. R^2_{avg} as a function of (a) M and (b) α on validation data. 87
3.32 MSE_{avg} of φ_{O} and φ_{f} on the validation data as a function of N_{training}. Results of (a) φ_{O} and (b) φ_{f}. Hyperparameters of gradient boosting in this case are $\alpha* = 0.11$ and $M* = 70$ 87
3.33 R^2_{avg} of φ_{O} and φ_{f} on the validation data as a function of N_{training}. Hyperparameters of gradient boosting in this case are $\alpha* = 0.11$ and $M* = 70$ 88
3.34 Evaluation of ML prediction accuracies of φ_{O} and φ_{f} on the test data. Scatter plots of (a) d_{O} against φ_{O} and (b) d_{f} against φ_{f}. Histograms of (c) $|d_{\text{O}}|$ and (d) $|d_{\text{f}}|$. The data point with a d_{f} of ~ -0.7 is not represented in (d). 89
3.35 Hyperparameter tuning results of KRR. R^2_{avg} as a function of (a) λ and (b) p on validation data. 90
3.36 R^2_{avg} P of φ_{O} and φ_{f} on the validation data as a function of N_{training} where the feature is only U_{V}. Results of (a) φ_{O} and (b) φ_{f}. Hyperparameters of gradient boosting in this case are $\alpha* = 0.11$ and $M* = 70$. 91
3.37 GO schematics and mechanical responses. (a) Schematic of GBP, where red atoms (66 in total) are hosts for functional groups while gray atoms are functional group-free atoms on which the tensile loading is exerted. Arrows show the loading direction. (b) Illustrations of hydroxyl and epoxide groups, where green and blue atoms are oxygen and hydrogen atoms, respectively. (c) Fracture of a low-toughness GO under tension. (d) Fracture of a high-toughness GO under tension. (e) Stress-strain curves of GOs in (c) and (d). 95
3.38 Deep RL state transition and trajectory. (a) Illustration of deep RL policy and state transition. (b) An example full trajectory. 98
3.39 Deep RL performances on various experiments. (a) Easy, (b) Medium, (c) Hard, and (d) Extra Hard experiments. 102
3.40 Toughness distributions for random and RL-designed GOs. (a-c) Easy, low oxidation experiment. (d-f) Easy, high oxidation experiment. (g-i) Medium, low oxidation experiment. (j-l) Medium, high oxidation experiment. (m-o) Hard, low oxidation experiment. (p-r) Hard, high oxidation experiment. (s-u) Extra Hard, low oxidation experiment. (v-x) Extra Hard, high oxidation experiment. 103

3.41 Rupturing comparison between a random GO and an RL-designed GO. Examples are from the Hard, high-oxidation experiment. 104
3.42 Functional group count distributions for high-toughness GOs. Functional group count distributions for GOs (a) 1.5 and (b) 2 standard deviations above the mean for the Easy difficulty. Functional group count distributions for GOs (c) 1.5 and (d) 2 standard deviations above the mean for the Medium difficulty. Functional group count distributions for GOs (e) 1.5 and (f) 2 standard deviations above the mean for the Hard difficulty. Functional group count distributions for GOs (g) 1.5 and (h) 2 standard deviations above the mean for the Extra Hard difficulty. 105

4.1 Construction of GAs in the MD simulation. (a) Initial stage of the material system. (b) Probability distribution of the graphene flake side length L. (c) Targeted temperature and pressure under NPT and NVT ensembles within one annealing cycle. (d) Number of C–C bonds per atom $N_{\mathrm{C-C}}$ and system volume V as functions of the annealing cycle number. (e) An example of material system configurations immediately after 8 annealing cycles. (f) Final configuration of a GA after spherical inclusions are removed. 111
4.2 Temperature and pressure evolution during 8 annealing cycles. 112
4.3 Stress–strain curve and deformation/fracture modes of one example GA. (a) Stress–strain curve of the GA under a uniaxial tensile load. σ_{xx} and ε_{xx} denote the stress and the strain in the loading direction. GA molecular configurations at critical points on the stress–strain curve are provided. The density of the GA in this example is 0.924 g·cm^{-3}. (b) Illustrations of local deformation and fracture modes of the GA. 113
4.4 Stress-strain curve of one GA subject to cyclic loading with 3 cycles. The density of the GA in this example is 0.920 g·cm^{-3}. 114
4.5 GA density as a function of the effective radius of inclusions. 115
4.6 Scatter plots of the Young's modulus and the ultimate stress against the density of all 270 GAs. Plots of (a) the Young's modulus and (b) the ultimate tensile stress. 115
4.7 Scatter plots of the GA density, Young's modulus, and ultimate tensile stress against the effective radius of the inclusions. Plots of (a) the density, (b) the Young's modulus, and (c) the ultimate tensile stress. 116
4.8 GPR prediction results of GA properties. Observations, GPR predictions and 95% confidence intervals of (a) the density, (b) the Young's modulus, and (c) the ultimate tensile stress. 118
4.9 Construction of GA structures in the MD simulation. (a) Initial material system where $N_{\mathrm{flake}} = 500$ and $N_{\mathrm{inc}} = 1000$. (b) Dimensions of the graphene flake and the spherical inclusion. (c) Pressure and temperature profiles during one annealing cycle. (d) $\log(L_{\mathrm{box}})$ as a function of N_{cycle}, where L_{box} denotes the side length of the cubic simulation box. (e) Condensed material system after 10 annealing cycles. (f) Final GA structure after the removal of inclusions. 121

4.10 Stress-strain curves where $N_{\text{flake}} = 200$, $N_{\text{inc}} = 500$, $\sigma = 5.0$ Å, $N_{\text{cycles}} = 10$, and $T_{\text{A}} = 2000$ K. Stress-strain curves under (a) tension and (b) compression. 122
4.11 Stress-strain curves without the relaxation process after annealing cycles where $N_{\text{flake}} = 200$, $N_{\text{inc}} = 500$, $\sigma = 5.0$ Å, $N_{\text{cycles}} = 10$, and $T_{\text{A}} = 2000$ K. Stress-strain curves under (a) tension and (b) compression. 122
4.12 Mechanical properties of GA as a function of σ, proportional to the effective radius of inclusions. (a) Illustration of the effect of σ. (b) Density ρ, (c) tensile strength σ_{u}, (d) tensile failure strain ε_{u}, (e) tensile and (f) compressive moduli E_{t} and E_{c} of GA as a function of σ. 123
4.13 Mechanical properties of GA as a function of the LJ parameter ϵ. (a) Density ρ, (b) tensile strength σ_{u}, (c) tensile failure strain ε_{u}, (d) tensile and (e) compressive moduli E_{t} and E_{c} of GA as a function of ϵ. 124
4.14 Mechanical properties of GA as a function of the inclusion-to-flake ratio R. (a) Illustration of the effect of R. (b) Density ρ, (c) tensile strength σ_{u}, (d) tensile failure strain ε_{u}, (e) tensile and (f) compressive moduli E_{t} and E_{c} of GA as a function of R. 125
4.15 Disconnected GA structure. The structure when (a) unloaded and (b) under tension. (c) Stress-strain relation of the GA under tension. 126
4.16 GA structure where $N_{\text{flake}} = 200$, $R = 5.0$, $\sigma = 15.0$ Å, and $T_{\text{A}} = 2000$ K under various numbers of annealing cycles. Initial structure and the structure under tension of GAs prepared with (a) 10, (b) 20, and (c) 50 annealing cycles. $N_{\text{bond/atom}}$ for (a-c) are 1.384, 1.386, 1.389, respectively. 127
4.17 Mechanical properties of GA as a function of N_{flake}. (a) Illustration of the effect of N_{flake}. (b) Density ρ, (c) tensile strength σ_{u}, (d) tensile failure strain ε_{u}, (e) tensile and (f) compressive moduli E_{t} and E_{c} of GA as a function of N_{flake}. . . . 128
4.18 Mechanical properties of GA as a function of density ρ for all well-formed GAs. (a) Tensile strength σ_{u}, (b) tensile failure strain ε_{u}, (c) tensile and (d) compressive moduli E_{t} and E_{c} of GA as a function of ρ. 129
4.19 GA connectivity property in response to changes in various simulation parameters. $N_{\text{bond/atom}}$ versus N_{cycle} plots (a) under various σ with $N_{\text{flake}} = 200$ and $R = 1.0$, (b) under various inclusion-to-flake ratios R with $N_{\text{flake}} = 200$ and $\sigma = 5.0$ Å, (c) under various R with $N_{\text{flake}} = 200$ and $\sigma = 15.0$ Å, and (d) under various annealing temperature T_{A} with $N_{\text{flake}} = 200$, $R = 1.0$, and $\sigma = 5.0$ Å. . . 130
4.20 GA structure where $N_{\text{flake}} = 200$, $R = 1.0$, $\sigma = 13.0$ Å, and $T_{\text{A}} = 2000$ K. The structure when (a) unloaded and (b) subject to tension. 130
4.21 GA structure where $N_{\text{flake}} = 200$, $R = 5.5$, $\sigma = 5.0$ Å, and $T_{\text{A}} = 2000$ K. The structure when (a) unloaded and (b) subject to tension. 131
4.22 GA structure formed with annealing temperature $T_{\text{A}} = 4000$ K where bond breakings and thermally unstable behavior are observed. Problematic geometries are circled. 131

4.23 Mechanical properties of GA under different probability distributions of the graphene flake side length L. (a) Probability densities of the log-normal distribution, and half-normal distributions with $\sigma_{\mathrm{hn}} = 3.0$ Å and 8.0 Å. (b) Density ρ, (c) tensile strength σ_{u}, (d) tensile failure strain ε_{u}, (e) tensile and (f) compressive moduli E_{t} and E_{c} of GA as a function of σ under three L distributions. 132
4.24 GA connectivity property under different distributions of graphene flake side length L. $N_{\mathrm{bond/atom}}$ versus N_{cycle} plots with (a) $\sigma = 5.0$ Å and (b) $\sigma = 11.0$ Å. . 133
4.25 GA connectivity property under different distributions of graphene flake side length L. $N_{\mathrm{bond/atom}}$ versus N_{cycle} plots with (a) $\sigma = 3.0$ Å, (b) $\sigma = 7.0$ Å, (c) $\sigma = 9.0$ Å, and (d) $\sigma = 13.0$ Å 134
4.26 Experimental data of mechanical properties of GA as a function of density ρ. (a) Tensile strength σ_{u}, (b) tensile failure strain ε_{u}, (c) tensile and (d) compressive moduli E_{t} and E_{c} of GA as a function of ρ. 135
4.27 Images of GA showing catastrophic failure during tensile test. Compression tests were performed on dynamic mechanical analysis (DMA, TA Instrument Q800). A preload of 10 mN was applied on the GA samples to assure full contact. The samples were compressed to 80% strain with a loading rate of 10% strain/min. Tension tests were performed on universal testing machines (Instron) with a loading rate of 10% strain/min. 136

5.1 Atomistic simulations of CO_2 in Mg-MOF-74. (a) Illustration of one CO_2 molecule chemically adsorbed at an open metal site in Mg-MOF-74. (b) Comparisons of existing QC and classical atomistic simulations. (c) Scheme of the QMLFF-based simulation approach. 138
5.2 Training and verification of QMLFF with the trajectory from the QC MD simulation of Mg-MOF-74 with one CO_2 at 600 K that guarantees proper sampling for CO_2 both on and off the Mg sites. (a) Energy and (b) forces as a function of the training step. Time series of (c) Mg–OCO_2 bond length and (d) tilting angle Mg–OCO_2–CCO_2 from the QMLFF-based MD simulation (blue) and from the DFT-based MD simulation (green) at 300 K. The starting time for results from the DFT based MD simulation is shifted from 0 ns to 1.02 ns for clarity. The red horizontal lines represent the mean values from DFT calculations (at 0 K), and the shaded areas indicated one standard deviation from the mean. 142
5.3 Adsorption energies of CO_2 when it moves from the channel center ($r = 0$ Å) to a Mg-site ($r \sim 5.4$ Å). The reference energy is chosen when CO_2 is at the center of a MOF channel. 144
5.4 ML potential training and verification with DFT trajectories of Mg-MOF-74 and one CO_2 at 300 K as the training data. RMSEs of (a) energy and (b) forces as a function of the training step. Time series of (c) Mg-O_{CO_2} bond length and (d) the tilting angle Mg-O_{CO_2}-C_{CO_2}. 145
5.5 Probability-of-density distributions of CO_2 inside one Mg-MOF-74 channel. Probability density distributions in (a) the x-y plane and (b) the θ-z plane. 145

5.6 Free energy landscape of CO_2 inside one Mg-MOF-74 channel. (a) Free energy landscape on the x–y plane. The position of the Mg-MOF-74 framework is also plotted for reference. (b) Free energy landscape on the θ-z plane. (c) 1D free energy sliced along $y = 0$ Å from (a). 1D free energy sliced along (d) $z = 2.8$ Å and (e) $\theta = 301°$ from (b). All plots use the same color bar scale. 146
5.7 Free energy landscape generated from the 30-ns MD simulation at 600 K using the classical force fields (UFF+DDEC). The NVT ensemble is used and Mg-MOF-74 is kept rigid during the simulation. The binding free energy of CO_2 from the channel center to a Mg-site is -0.14 eV, which is about two times smaller (i.e. weaker binding) than the one obtained from the QMLFF-based MD simulation. No chemisorption is observed in the classical-force-field-based MD simulation. . 148
5.8 1D free energy plot passing benzene rings obtained from the QMLFF-based MD simulation. 1D free energy plots sliced (a) along $x = 0$ Å on the x-y plane free energy landscape (Fig. 5.6(a)), and (b) along $\theta = 270°$ on the θ-z plane free energy landscape (Fig. 5.6(b)). 148
5.9 Diffusion phenomenon of one CO_2 molecule inside the Mg-MOF-74 channel. (a) z coordinate and (b) θ coordinate of the CO_2 molecule as functions of time. (c) $\langle \Delta z^2 \rangle$ and $\langle \Delta \theta^2 \rangle$ as functions of Δt. 149
5.10 Diffusion of CO_2 inside Mg-MOF-74 channel from the 10-ns MD simulation with classical force fields (UFF+DDEC). (a) Diffusion along the z direction; (b) Diffusion along the θ direction; (c) $\langle \Delta z^2 \rangle$ and (d) $\langle \Delta \theta^2 \rangle$ as functions of Δt. 151

List of Tables

2.1 Equation and derived dichotomizing points of high/low stress regions of circular, elliptical, quadratic polynomial-shaped and sine-shaped defects, where the applied strain ε is included. 45

3.1 Neural network input and output dimensions for all experiment difficulties. For Hard and Extra Hard output, the first number refers to the hydroxyl network and the second number refers to the epoxide network. 96
3.2 Neural network parameters for all experiments. 96
3.3 Experiment difficulty descriptions. 98
3.4 Summary of the number of hydroxyl groups n_{h}, the number of epoxide groups n_{e}, and the number of carbon atoms that are hosts for functional groups n for all experiments. 99
3.5 Summary of statistics of random GOs in all experiments (unit: GPa). 99

5.1 Hyperparameters for ML potential training. 142
5.2 Cost of computation in this study 144

Acknowledgments

First and foremost, I thank my PhD advisor Prof. Grace Gu, who is one of the most important people in my life. I thank her for giving me the opportunity to be one of her earlier PhD students. I see her as a role model who works tirelessly without letting the world know, who handles every matter as professionally as it gets, who is kind, understanding, and fair. It is easy to say that I have experienced the most growth throughout my life with her being my advisor.

I thank my parents, who were living in China during my entire PhD. Their financial and emotional support made sure that I did not have much to worry about but my PhD studies. It also made me very happy when I shared good news with them on our weekly video calls

I thank my partner, Lillian, who is the kindest and the most considerate person I know. She makes me happy and grow into a better person. Going home to her is what I look forward to the most after a long day's work.

I thank my good friends Dr. Sangryun Lee, Sara Shonkwiler, Dr. Jimin Gu, Grace Hu, Ailin Chen, and many others. They play a very important role during my PhD and I have had a lot of fun with them. I have taken many pictures with my friends and they always bring back good memories.

I also express my gratitude to the following professors, collaborators and coworkers: Prof. Zeyu Zheng (UC Berkeley), Prof. Panayiotis Papadopoulos (UC Berkeley), Dr. Binquan Luan (IBM), Prof. Debbie Senesky (Stanford), Dr. Zhou Li (Stanford), Dr. Zhizhou Zhang, Kahraman Demir, Zeqing Jin, Ailin Chen, Dr. Jeong-Ho Lee, Daniel Lim, Dr. Jiyoung Jung, Zilan Zhang, Shao-Yi Yu, Maya Horii, Elizabeth Pegg, Ekaterina Antimirova.

Chapter 1

Introduction

1.1 Graphene and graphene-related materials

Graphene, a 2D material consisting of hexagonally packed carbon atoms, has exhibited remarkable capabilities in a broad range of state-of-the-art research fields thanks to its exceptional electronic [12, 185, 98], thermal [9, 8], and mechanical [90, 207] properties since its discovery [123]. Despite being one-atom thick, the monolayer graphene possesses an exceptional combination of mechanical properties, including an ultrahigh Young's modulus of $\sim$1 TPa and an extreme tensile strength of 130 GPa [90]. These mechanical properties make graphene not only ideal for the fabrication of ultra-strong fibers [190, 191] and membranes [37, 86], but also an elite candidate for emerging technologies such as stretchable electronics [84, 76], micro-/nano-electromechanical systems (M-/N-EMS) [109, 16, 144], supercapacitor devices [230, 233, 176], among others. In addition, these properties of graphene can be tuned by means of chemical doping [178, 155] and functionalization [33], making graphene a favorable material choice for a variety of research purposes.

Graphene oxide (GO), one of the best-known graphene derivatives, also opens up avenues for a broad spectrum of novel, tunable properties [234, 26] and is widely used in state-of-the-art applications such as biomedical devices [36, 59, 80], flexible electronics [78, 94], and functional nanocomposites [73, 194]. GO is composed of a graphene basal plane and oxygen-containing functional groups such as epoxide (-O-), hydroxyl (-OH), carbonyl (C=O), and carboxyl (-COOH) groups. The absolute and relative concentrations of these functional groups can be viewed as the fingerprint of GO, determining multiple important physical properties and therefore the potential usage of the nanomaterial. The control of oxygen content, epoxide-to-hydroxyl group ratio, and spatial distribution of functional groups has enabled rational material design and optimization [184, 101].

Graphene aerogels (GAs), 3D porous assemblies of 2D graphene sheets, inherit many properties of graphene and manifest a desirable combination of low density and high strength [61, 50]. Notably, GAs with a density lower than that of air have been fabricated by assembling commercial carbon nanotubes and chemically converted graphene sheets [160], which

may substitute for helium to infill unpowered flight balloons. In addition to being ultra-lightweight, GAs also possess other excellent material properties such as high specific surface area (due to high porosity) [158, 102, 203], high conductivity [186, 212], and good thermal stability [95]. As a result, GAs have quickly drawn research attention since their first fabrication, and have become an enticing candidate for various cutting-edge applications such as supercapacitors [200, 99, 195], gas sensing [102, 100], energy storage [193, 189], oil sorption [72], among others.

Despite the attractive properties of these graphene-based materials, there have been pressing challenges and room for improvement associated with them. First, defects usually exist in these materials, which can seriously compromise the performances of graphene-based nano-devices. Second, microstructures of these materials can be highly variable, which can result in significant property randomness. Third, the complex structure creates a large design space, which may lead to high potential in performance enhancement via optimization. As a result, the analysis and design of graphene-based materials is of high research interest and is valuable to the advancement of various nanotechnologies.

1.2 Machine learning for nanomaterial simulation, prediction and design

As one of the most important and exciting branches of artificial intelligence (AI), machine learning (ML) refers to making classifications, predictions or decisions using data and algorithms [77]. In recent years, with the fast growth of big data, ML has been widely applied in many fields such as finance [177, 1], biology [39, 82], and healthcare [119, 147]. The advent of ML approaches also offers solutions to learning patterns from complex data in material design and discovery problems [19, 21, 231, 225], reducing the need for expensive, time-consuming, and tedious laboratory experiments or numerical simulations.

Much to our interest, ML has witness great success in the research and development of nanotechnologies and nanomaterials [32, 10, 79], where the applications largely fall in the following categories: prediction, design, and acceleration. For prediction tasks, ML techniques have been used to detect structural defects and predict various material properties such as electronic properties, thermal conductivities and biological toxicity. Maksov et al. developed a deep-learning framework to locate the lattice defects in layered WS_2 using scanning transmission electron microscopy (STEM) data [107]. Wu et al. used various ML algorithms to predict the adsorption, separation, and mechanical stability of defective zirconium metal–organic frameworks (MOFs) [188]. Fernandez et al. used ML algorithms to predic the electronic properties of graphene nanoflakes such as the Fermi level and the band gap [52]. Koohi-Moghadam et al. used a multichannel convolutional neural network (CNN) model in the prediction of disease-associated mutation of metal-binding sites in proteins [88]. Fujii et al. used linear regression and hierarchical clustering to predict grain boundary thermal conductivities from local atomic environments [55].

For design tasks, ML techniques have been used to inverse-design high-performance nanomaterials and nano-devices. Ma et al. used bidirectional neural networks to automatically design and optimize 3D chiral metamaterials at predesignated wavelengths [105]. Copp et al. developed a closed-loop data-driven design strategy for DNA-stabilized silver clusters with specific fluorescence colors [38]. Zeng et al. designed catalytic water-cleaning nanomotors where ML is used to identified key features for the catalyst performance [202]. Li et al. used multi-target random forest regressors to inverse-design nanoparticles [93]. Vallone et al. used an inverse CNN to design multilayered nanoparticles with favorable absorption and scattering properties [168].

For acceleration tasks, ML techniques have been used to accelerate materials discovery and simulation. Lu et al. used a target-driven ML method to accelerate the discovery of stable lead-free hybrid organic-inorganic perovskites [103]. Zhang et al. accelerated the discovery of high-performing MOFs for methane-storage and carbon-capture applications using Monte Carlo tree search and recurrent neural networks [211]. Lu et al. achieved rapid discovery of stable ferroelectric photovoltaic perovskites via a multistep screening scheme combining high-throughput calculations and ML feature engineering [104]. Additionally, ML interatomic potentials, which learn to predict the energy and forces of an assembly of atoms for accurate quantum-based simulation data, have emerged as a tool to accelerate atomic-scale computer simulations. Successes of ML interatomic potentials have facilitated numerous simulation-based research, including the prediction of thermal and phonon properties of graphene [146], the modeling of the bond breaking process of silicon [11], the simulation of nanoscale amorphous carbon structures [43], among others.

In the following chapters, I will present my PhD research on the ML-assisted simulation and design for functional nanomaterials, with a focus on graphene-based materials. Chapter 2 will cover the topic of graphene defect engineering, including research on tuning graphene mechanical anisotropy, graphene defect mitigation, and stress field properties of defective graphene. Chapter 3 will demonstrate some ML applications for graphene-based materials, including research on graphene defect detection, chemical composition identification for graphene oxide, and graphene oxide design using deep reinforcement learning. Chapter 4 will present simulation and ML for graphene aerogels, including research on uncertainty quantification and prediction for mechanical properties of graphene aerogels, and structral integrity of graphene aerogels. Chapter 5 will discuss the possibility of simulation acceleration via ML approaches, featured by quantum-informed ML force fields for MOFs. Finally, Chapter 6 will provide conclusions and future research directions.

Chapter 2

Graphene defect engineering

2.1 Tuning graphene mechanical anisotropy

Exceptional mechanical properties of graphene have been extensively studied and benefited various applications. However, the fine-tuning of the degree of graphene mechanical anisotropy has been rarely discussed. The mechanical anisotropy means that the mechanical properties in one direction differ intrinsically from those in another direction [121]. For graphene, Ni et al. observed the anisotropic mechanical properties using molecular dynamics (MD) simulation and studied fracture modes and stiffness property in different directions [121]. Fan et al. studied anisotropic mechanical properties of monolayer graphene using density functional theory (DFT) method and related the intrinsic anisotropy to the sp^2 hybridization of the hexagonal lattice [49]. Pereira et al. studied the anisotropic thermal and mechanical properties of phagraphene, a newly theoretically proposed defective graphene structure consisting of pentagonal, heptagonal and hexagonal rings [133]. Although much research has been conducted on the anisotropy of graphene, a systematic fine-tuning paradigm for graphene mechanical anisotropy remains unexplored. Hence, a systematic investigation on graphene mechanical anisotropy can provide insight into designing graphene with tunable properties, which can potentially circumvent property tradeoffs such as between strength and ductility. Also, from the perspective of engineering applications, the tunability of graphene anisotropy has the potential to improve the mechanical integrity of biological composites and flexible electronics by directing crack propagation and energy dissipation to more ductile materials [67].

Graphene kirigami [14], a defect engineering strategy of graphene inspired by the art of paper cutting, has shown great potential in tuning the mechanical [14, 150] and thermal [180] properties of graphene. While one research direction in tuning properties of graphene involves adding a second material to make a nanocomposite [126, 25, 22], graphene kirigami research can offer property tunability with just cuts. Similar design concept such as graphene nanomesh [7, 81, 232] has also shown to be successful. Because of the high design freedom [140] of defect engineering, it is possible to design particular defect pattern to realize

the specific requirement of anisotropic property, or to even produce an isotropic graphene.

Here, the potential of fine-tuning the mechanical anisotropy of monolayer graphene is explored via defect design, from designs consisting of basic elements to more complex patterned graphene kirigami. For basic defect designs, the influences of defect length, obliquity, offset from the center, and number of parallel defects are discussed. For more complex defect designs, network-like graphene kirigami and graphene kirigami with parallel interior and exterior cuts are investigated. MD simulations are conducted to study the mechanical properties of these proposed defected graphene designs. A novel stress-ratio-versus-strain-ratio graph is proposed to visualize and rationalize the tuning of mechanical anisotropy of defected graphene sheets. Through our defect design, all the four quadrants of the 2D ratio graph are covered, indicating a high capability and versatility of fine-tuning the mechanical properties of graphene in both directions. More complex designs such as designs involving curved defects as well as other 2D materials will be covered in future work.

System description and molecular modeling

To explore the potential of fine-tuning anisotropic properties using defect engineering, square-shaped monolayer graphene is studied to compare fairly the mechanical properties in the zigzag and armchair directions. A schematic of simulated graphene and loading conditions is shown in Fig. 2.1(a), where the graphene edge lengths in zigzag and armchair directions are $L_{\mathrm{Z}} = 110.3$ Å and $L_{\mathrm{A}} = 112.0$ Å. The length of the covalent C–C bond in the initial configuration is 1.421 Å and after equilibrium the average bond length is 1.399 Å. Tensile loading is applied uniformly on one side of the graphene with the opposite side fixed.

To investigate the mechanical properties of monolayer graphene with designed defects, MD simulations are performed using the open-source code LAMMPS [166]. The interactions of carbon atoms are modeled by the Adaptive Intermolecular Reactive Empirical Bond Order (AIREBO) potential, which is used to model the bond breaking and reforming involved in the fracture process of graphene [214, 138]. The AIREBO potential consists of a REBO term to model short-ranged interaction, and a Lennard-Jones (LJ) term to model long-ranged interaction, expressed by

$$E = E^{\mathrm{REBO}} + E^{\mathrm{LJ}} + E^{\mathrm{tors}} \tag{2.1}$$

where E is the total system energy; E^{REBO}, E^{LJ}, and E^{tors} are energy components corresponding to the REBO (short-ranged), LJ (long-ranged), and torsional potentials [157]. The REBO term consists of two cutoff distances in the switching function that controls the breaking of C-C bonds, which by default are 1.7 Å and 2.0 Å [157]. Here, the smaller cutoff distance is modified to 1.92 Å to better capture the stress-strain relation of graphene benchmarked by DFT calculations, which has been used and validated by many previous studies [183, 62, 172, 210]. The cutoff distance of the LJ term is set as 6.8 Å [150, 137]. The integration time step is set as 1 fs. Periodic boundary conditions are applied to two in-plane dimensions and a fixed boundary condition is used in the perpendicular out-of-plane dimension. The in-plane dimensions of the simulation box (~ 175 Å$\times \sim 175$ Å) are larger

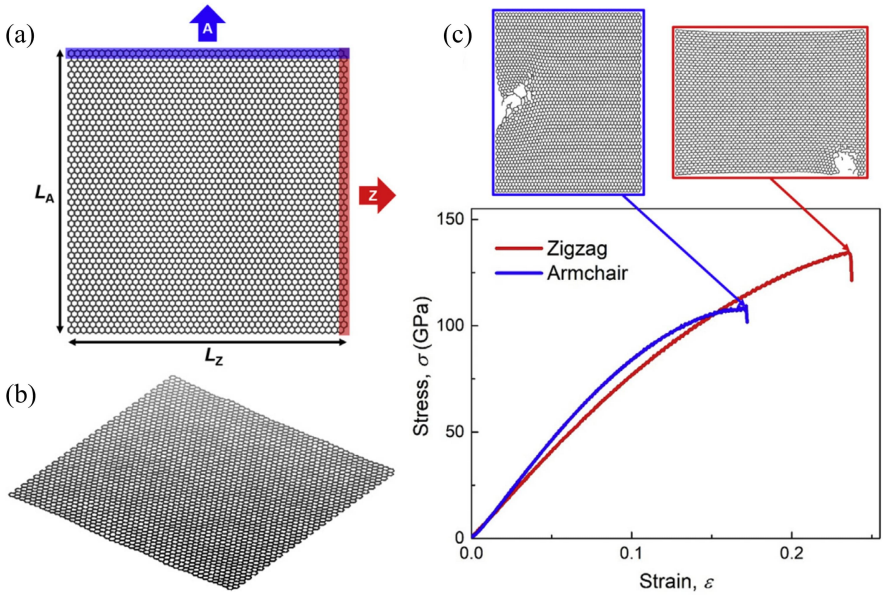

Figure 2.1: Model setup and simulation results of pristine graphene. (a) Schematic of pristine graphene and illustration of tensile loading directions. (b) Morphology of monolayer graphene after running for equilibrium at 300 K. (c) Stress-strain curves and fracture modes of pristine graphene upon zigzag and armchair loadings.

than the dimensions of graphene sheets ($\sim$ 110 Å$\times$ $\sim$ 110 Å). After the generation of an ensemble of random velocity at 300 K, the system is running for equilibrium at 300 K in the isothermal-isobaric (NPT) ensemble with the Nose-Hoover thermostat [70] for 50 ps. The 3D shape of the graphene sheet after running for equilibrium is shown in Fig. 2.1(b), where the maximum out-of-plane fluctuation of the rippling is $\sim$ 2 Å. The loading scenario is simulated in the canonical (NVT) ensemble at 300 K. Tensile loading is exerted based on the deformation-control method by assigning displacement at a constant speed to a 3 Å wide atom stripe at one end, while fixing a 3 Å-wide atom stripe at the other end in all three dimensions. Strain rate applied in the MD simulation is 10^9 s^{-1}.

The method to calculate the stress of a loaded graphene sheet is described as follows. The stress tensor S_{ij}^{α} for atom α is firstly calculated by the following equation:

$$S_{ij}^{\alpha} = \frac{1}{2} m^{\alpha} v_i^{\alpha} v_j^{\alpha} + \sum_{\beta=1}^{n} r_{\alpha\beta}^{j} f_{\alpha\beta}^{i} \tag{2.2}$$

where i and j take on x, y, or z to generate the six components of the symmetric tensor; m^{α} and v^{α} are the mass and velocity of atom α; $r_{\alpha\beta}$ and $f_{\alpha\beta}$ are the distance and force between atoms α and β. After the calculation of stress tensor on each individual atom, the equivalent

stress σ of a graphene sheet is calculated based on von Mises stress

$$\sigma = \sqrt{\frac{1}{2}[(\sigma_{xx} - \sigma_{yy})^2 + (\sigma_{yy} - \sigma_{zz})^2 + (\sigma_{zz} - \sigma_{xx})^2 + 6(\sigma_{xy}^2 + \sigma_{yz}^2 + \sigma_{zx}^2)]} \tag{2.3}$$

where

$$\sigma_{ij} = \frac{1}{V_0} \sum_{\gamma=1}^{n} S_{ij}^{\gamma}$$

where $V_0 = L^2 t_e$ is the initial volume, and $t_e = 3.35$ Å is the equivalent thickness of monolayer graphene [196]. Fig. 2.1 shows the calculated stress-strain curves of pristine graphene under the two loading directions. The obtained curve shapes and failure stresses/strains in zigzag and armchair directions are in good agreement with previous studies [183, 35, 131], which validates the simulation setup. It is shown that both failure stress and strain in the zigzag direction (referred to as zigzag/armchair failure stress/strain below) are higher than those in the armchair direction, while Young's modulus is slightly lower within a small strain, revealing the intrinsic anisotropic mechanical property of pristine monolayer graphene. The fracture modes in Fig. 2.1(c) show that in both directions, fracture initiates on the unloaded edge. As widely acknowledged, the mechanical behavior of materials can be altered by introducing certain types of defects. Hence, it is rational to consider the possibility to fine-tune the anisotropy of graphene through rational design of defects. For example, can we use defect design to create an isotropic graphene sheet? Can we intensify the anisotropy of graphene? Can we design graphene that is stronger in one direction but more stretchable in the other?

Basic defect designs

To start with, the influence of basic defect elements on the mechanical properties and the potential of tuning anisotropy are investigated. In this section, the influences of defect length, obliquity, offset from the center, and number of parallel defects are separately discussed. Defect width is twice the C-C bond length and is a constant.

Centered line defect with variable length

Single centered line defect in the zigzag or the armchair direction (referred to as zigzag or armchair defect below) is studied first. To illustrate how introducing a single centered line defect affects the mechanical properties of the graphene sheet, MD simulations are conducted to study graphene with single centered line defect with a length of half the graphene edge length, i.e., $L_D = 0.5L_Z$ for zigzag defect or $L_D = 0.5L_A$ for armchair defect, of which the results are presented in Fig. 2.2. Figs. 2.2(a) and (b) demonstrate the deformation and fracture modes of defected graphene by showing the shapes of unloaded, deformed, and fractured graphene sheets. For the graphene sheet with zigzag defect shown in Fig. 2.2(a), upon zigzag loading, the line defect is lengthened and the fracture initiates from along the

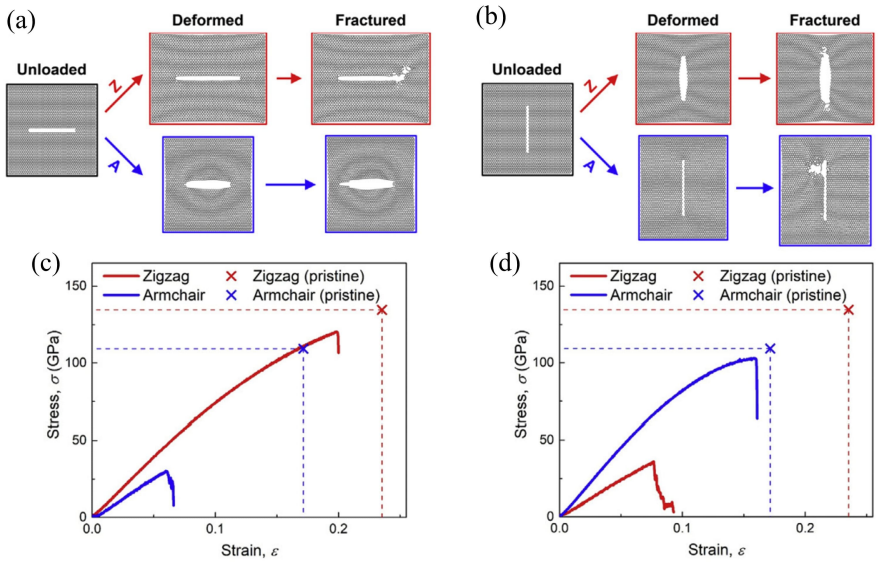

Figure 2.2: Simulation results of graphene design with single centered line defect. Deformation and fracture modes of graphene sheets with (a) a zigzag and (b) an armchair defect. Stress-strain curves of graphene sheets with (c) zigzag and (d) armchair defect. The failure stresses and strains of the pristine monolayer graphene under two loading conditions are marked in the curve figures for comparison.

defect, different from the defect-free scenario where the fracture initiates on a graphene edge. Upon the armchair loading, the line defect expands and the fracture initiates at the defect tip. A graphene sheet with an armchair defect exhibits similar deformation and fracture modes to those with a zigzag defect, as illustrated in Fig. 2.2(b). If the loading direction is perpendicular to the line defect, the defect expands and fracture initiates at the tip where it is the easiest to rupture, and ultimately leading to an early failure. Figs. 2.2(c) and (d) present the calculated stress-strain curves of defected graphene with the failure stress and strain of the pristine counterpart for comparison. When the loading and the defect are parallel, a minor decrease of mechanical behavior is shown compared to pristine graphene, while the loading and the defect are perpendicular, both failure stress and strain decrease significantly. It is notable that for graphene with an armchair defect, the armchair direction becomes the stronger and more stretchable direction, flipping the anisotropy of graphene.

After studying examples of the centered line defect, a parametric study is carried out to examine the influence of defect length, and the results are summarized in Fig. 2.3. Figs. 2.3(a) and (b) show the failure stress and strain of graphene with a zigzag defect of various lengths. Results show that upon the zigzag loading, both failure stress and strain exhibit minor, unpatterned change with an increasing defect length, suggesting that the zigzag defect has an insignificant effect on the zigzag mechanical properties. Upon the armchair loading,

however, failure stress decreases monotonously as the defect length increases. Failure strain also shows a decreasing tendency, yet the rate of decrease slows down and the failure strain remains relatively unchanged for defect lengths above $0.3L_{\mathrm{Z}}$. Figs. 2.3(c) and (d) present the result of graphene with armchair defect. Upon the zigzag loading (perpendicular to the line defect), the failure stress and strain decrease in a similar fashion to graphene with zigzag defect subject to armchair loading. Upon the armchair loading (parallel to the line defect), the defect length has a relatively insignificant effect, similar to the scenario of zigzag defect upon zigzag loading. It can be concluded that the defect length weakens the mechanical properties of graphene sheet only when the line defect is perpendicular to the loading, and that the effect intensifies as defect length increases. Mechanical property is fairly unchanged when the line defect and the loading are parallel. A dual relationship between the zigzag and the armchair directions is observed. Specifically, the scenario of zigzag defect upon armchair loading produces similar results as the scenario of armchair defect upon zigzag loading; the scenario of zigzag defect upon zigzag loading produces similar results as the scenario of armchair defect upon armchair loading.

To quantify the anisotropic property and to rationalize the defect design, the ratios between the zigzag and the armchair failure stresses $\sigma_{\mathrm{F,Z}}/\sigma_{\mathrm{F,A}}$, between the zigzag and the armchair failure strains $\epsilon_{\mathrm{F,Z}}/\epsilon_{\mathrm{F,A}}$, are calculated. The calculated results are then mapped onto a $\ln(\epsilon_{\mathrm{F,Z}}/\epsilon_{\mathrm{F,A}})$-$\ln(\sigma_{\mathrm{F,Z}}/\sigma_{\mathrm{F,A}})$ graph (referred to as ratio graph below). The ratio graph, by definition, can be divided into the following four quadrants: Quadrant 1 ($\ln(\sigma_{\mathrm{F,Z}}/\sigma_{\mathrm{F,A}}) > 0$ and $\ln(\epsilon_{\mathrm{F,Z}}/\epsilon_{\mathrm{F,A}}) > 0$), where the failure stress and strain are both higher in the zigzag direction than the armchair direction; Quadrant 2 ($\ln(\sigma_{\mathrm{F,Z}}/\sigma_{\mathrm{F,A}}) < 0$ and $\ln(\epsilon_{\mathrm{F,Z}}/\epsilon_{\mathrm{F,A}}) > 0$), where the failure stress is higher in the armchair direction, and the failure strain is higher in the zigzag direction; Quadrant 3 ($\ln(\sigma_{\mathrm{F,Z}}/\sigma_{\mathrm{F,A}}) < 0$ and $\ln(\epsilon_{\mathrm{F,Z}}/\epsilon_{\mathrm{F,A}}) < 0$), where the failure stress and strain are both higher in the armchair direction than zigzag direction; Quadrant 4 ($\ln(\sigma_{\mathrm{F,Z}}/\sigma_{\mathrm{F,A}}) > 0$ and $\ln(\epsilon_{\mathrm{F,Z}}/\epsilon_{\mathrm{F,A}}) < 0$), where the failure stress is higher in the zigzag direction, and the failure strain is higher in the armchair direction. A defect-containing graphene sheet is defined as "single-isotropic" if one of the values of $\ln(\sigma_{\mathrm{F,Z}}/\sigma_{\mathrm{F,A}})$ and $\ln(\epsilon_{\mathrm{F,Z}}/\epsilon_{\mathrm{F,A}})$ equals zero (data point landing on one of the axes of ratio graph), and is defined to be "double-isotropic" if both values equal zero (data point landing on the origin of ratio graph). The purpose of the 2D ratio graph is to visualize the anisotropy of defect designs. By presenting the trajectories or distributions on the ratio graph when one or more parameters are changed, the technique schematizes how changing these parameters influences the anisotropic property of graphene. Fig. 2.3(e) shows the evolution on the ratio graph given an increasing defect length, reaching the following conclusions:

- Pristine graphene lies in Quadrant 1 on the ratio graph.
- As the length of zigzag defect increases, the data point is driven away from the origin within Quadrant 1, implicating an intensified anisotropy with respect to both failure stress and strain.

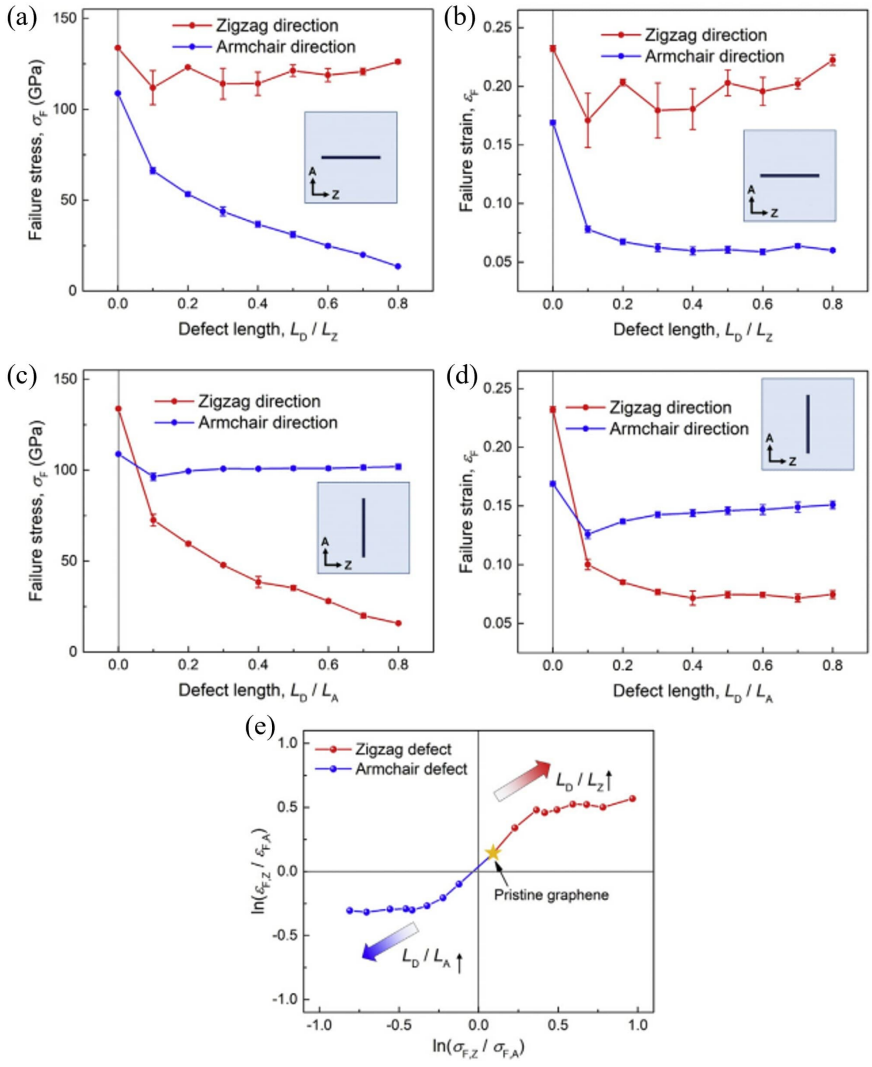

Figure 2.3: Parametric study of graphene with single centered line defect with respect to defect length. Influence of defect length on (a) the failure stress and (b) failure strain of graphene with zigzag defect. Influence of defect length on (c) the failure stress and (d) failure strain of graphene with armchair defect. Zero defect length corresponds to pristine graphene. (e) Evolution of data points with increasing defect length on ratio graph. Data point corresponding to pristine graphene is illustrated with a star symbol.

- As the length of armchair defect increases, the data point is driven towards Quadrant 3, implicating a reduced anisotropy with respect to both failure stress and strain at first, followed by the regain of anisotropy where armchair direction is the stronger direction in both failure stress and strain.

- When driven toward Quadrant 3, the data point passes the surrounding region of the origin, suggesting a potential strategy to design a nearly "double-isotropic" graphene.

Centered line defect with variable tilting angle

In this section, graphene with a centered oblique line defect is studied, with a defect tilting angle θ defined as the angle between the line defect and the zigzag direction. Simulation results of graphene with a centered oblique line defect with a tilting angle of $\theta = 30°$ and $60°$ are presented in Fig. 2.4, where the defect length here is $L_{\mathrm{D}} = 0.5L_{\mathrm{Z}}$. Figs. 2.4(a) and (b) show the deformation and fracture modes. For graphene sheet with $\theta = 30°$ in Fig. 2.4(a), upon zigzag loading, the line defect is both lengthened and widened, while upon armchair loading, the widening of the line defect dominates. In both scenarios, fracture initiates from the defect and close to the defect tip. Graphene sheet with a $\theta = 60°$ defect in Fig. 2.4(b) exhibits similar deformation and fracture modes as the one with a $\theta = 30°$ defect but in a dual relation: Graphene with a $\theta = 60°$ defect upon zigzag (armchair) loading has similar deformation and fracture mode as graphene with a $\theta = 30°$ defect upon armchair (zigzag) loading. It is observed that the deformation and fracture modes lie in between the scenarios where the loading and the defect are parallel and perpendicular, exhibiting both widening and lengthening phenomena. Figs. 2.4(c) and (d) present the calculated stress-strain curves. Fig. 2.4(c) shows the stress-strain curves of graphene with $\theta = 30°$ defect under two loading conditions with the failure stress and strain of the pristine counterpart as a comparison. It is shown that the mechanical properties in both directions are weakened, exhibiting decrease in both failure stress and strain, and zigzag is still the stronger direction. Fig. 2.4(d) shows the stress-strain curves of graphene with $\theta = 60°$ defect. Similar to the scenario of $\theta = 30°$, both failure stress and strain are lowered by the introduction of an oblique line defect. However, a larger decrease happens to the zigzag direction and the armchair direction becomes mechanically stronger, thus flipping the anisotropy. It can be therefore concluded that an oblique line defect lowers the failure stresses and strains of graphene in both directions and the effect is equivalent to projecting the oblique line defect onto zigzag and armchair directions and acting as two orthogonal components.

A systematic parametric study of the defect tilting angle θ is carried out and summarized below. Figs. 2.5(a) and (b) show the influence on failure stress and strain, respectively. As the tilting angle increases (line defect rotates from along the zigzag direction to along the armchair direction), both failure stress and strain decrease upon zigzag loading and increase upon armchair loading. Within the small tilting angle range, for example, from $\theta = 0°$ to $30°$, the rate of decrease upon the zigzag loading is much faster than the rate of strengthening upon the armchair loading, while within the large tilting angle range, for example, from

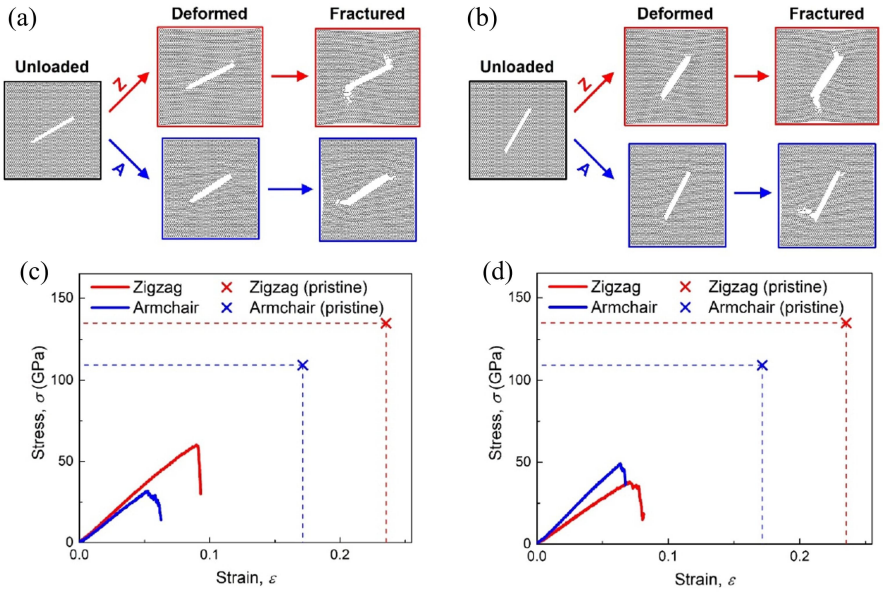

Figure 2.4: Simulation results of graphene design with single centered oblique line defect. Deformation and fracture modes of graphene sheets with (a) $\theta = 30°$ and (b) $\theta = 60°$ defect. Stress-strain curves of graphene sheets with (c) $\theta = 30°$ and (d) $\theta = 60°$ defect. The failure stresses and strains of the pristine graphene sheet under two loading conditions are marked in the curve figures for comparison.

$\theta = 60°$ to $90°$, the rate of decrease upon zigzag loading becomes much slower than the rate of strengthening upon armchair loading. Above observations can be explained by the fact that the projection of line defect on the perpendicular direction of the loading $L_D \sin\theta$ increases fastest when θ is small and the increasing rate decreases as θ grows. In the meantime, the projection of line defect on the orthogonal direction lengths at an increasing rate. These relations again incorporate a strong duality between the two chiralities.

Fig. 2.6(a) shows the evolution of data points on the ratio graph given an increasing defect tilting angle θ. As θ increases, the result is driven from Quadrant 1 towards Quadrant 3, indicating a reduced anisotropy at first, followed by regaining anisotropy where the armchair direction is stronger in both failure stress and strain. The evolution of data points on the ratio graph demonstrates a similar path as the scenario of centered line defect with a variable length. This evolutionary pattern can be explained by the fact that the higher failure stress and strain are always in the same direction and the stronger direction is switchable. It is also noticeable that the evolutionary path on the ratio graph passes the surrounding region of the origin, implying that the defect design featured by oblique line defect is possible to produce a double-isotropic graphene sheet.

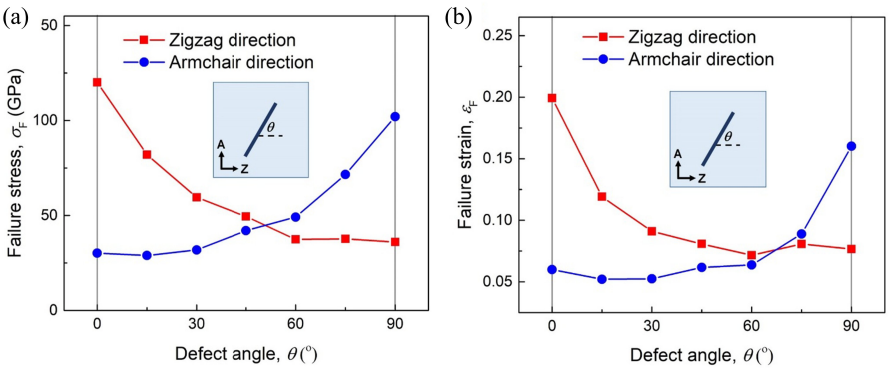

Figure 2.5: Parametric study of graphene with a centered oblique line defect with respect to a variable tilting angle θ. The influence of tilting angle θ on (a) failure stress and (b) failure strain of defected graphene. Defect angles of $\theta = 0°$ and $\theta = 90°$ correspond to line defect in zigzag and armchair direction, respectively.

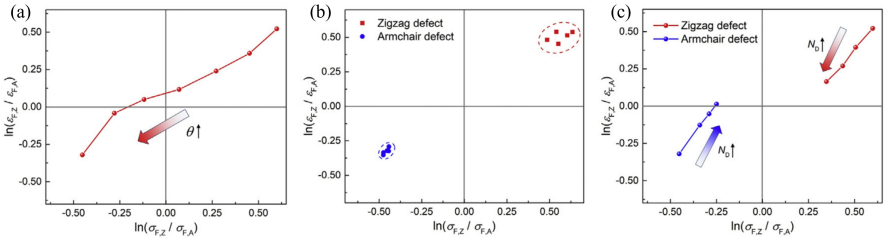

Figure 2.6: Evolutionary paths or distribution of data points on the ratio graph. (a) Evolutionary path of data points of graphene with centered oblique line defect when the tilting angle θ increases. (b) Distribution of data points of graphene with offset line defect with various offset distances e_D. (c) Evolutionary path of data points of graphene with multiple parallel line defects with increasing defect number N_D.

Line defect with an offset from the center

A single line defect in the zigzag or the armchair direction with an offset from the center is studied below. It is important to understand how an offset defect affects the mechanical properties, because for complex patterned designs involving multiple defects, most defects are offset from the center of the graphene sheet. For the discussion in this section, the offset is introduced in the armchair direction for the zigzag defect, and is in the zigzag direction for the armchair defect.

Simulation results of graphene with single offset line defect are presented in Fig. 2.7. As examples, graphene designs featured by a zigzag offset $e_{\mathrm{D}} = 0.2L_{\mathrm{A}}$ and an armchair offset $e_{\mathrm{D}} = 0.2L_{\mathrm{Z}}$ are studied. The defect length is $L_{\mathrm{D}} = 0.5L_{\mathrm{Z}}$ for zigzag defect and $L_{\mathrm{D}} = 0.5L_{\mathrm{A}}$ for armchair defect. Figs. 2.7(a) and (b) show the deformation and fracture modes. When the loading and the defect are parallel, the line defect is lengthened and the fracture initiates from along the line defect. When the loading and the defect are perpendicular, the line defect widens and the fracture initiates at the defect tip. The deformation and fracture modes of the two defect graph are connected in a dual manner. Figs. 2.7(c) and (d) present the calculated stress-strain curves. Fig. 2.7(c) shows the stress-strain curves of graphene with offset zigzag defect under two loading conditions with the failure stress and strain of the non-offset counterpart for comparison. In both the zigzag and the armchair directions, mechanical properties of graphene sheets with an offset defect show a minor decrease compared to the non-offset counterparts. Fig. 2.7(d) shows the stress-strain curves of graphene with an offset zigzag defect. Again, no substantial change in stress-strain relation is observed. From the observation of the two simulation results, the offsetting of line defect in fact has an insignificant effect on the mechanical properties and fracture modes of defect-containing graphene sheets.

A parametric study of the offset distance e_{D} is conducted and summarized as below. Figs. 2.8(a) and (b) show how the failure stress and strain of graphene with a zigzag defect evolve under various offset distances. Compared to the non-offset design ($e_{\mathrm{D}} = 0$), changes of the mechanical property with respect to failure stress and strain are insignificant. Similar to the trends in Figs. 2.3 and 2.6(b), as the e_{D} increases, the mechanical properties in the zigzag direction has more fluctuations compared to armchair direction. The offset armchair defect show similar trends as the zigzag counterpart, as presented in Figs. 2.8(c) and (d).

Results of the parametric study are converted to a representation on the ratio graph as Fig. 2.6(b). No clear evolutionary path is detected as the offset distance increases, and scenarios of zigzag and armchair defect with various offset distances are clustered within a relatively small region in Quadrant 1 and Quadrant 3. Therefore, introducing an offset to a single line defect may not effectively change the anisotropic property of the graphene sheet and its influence on mechanical properties is rather minor.

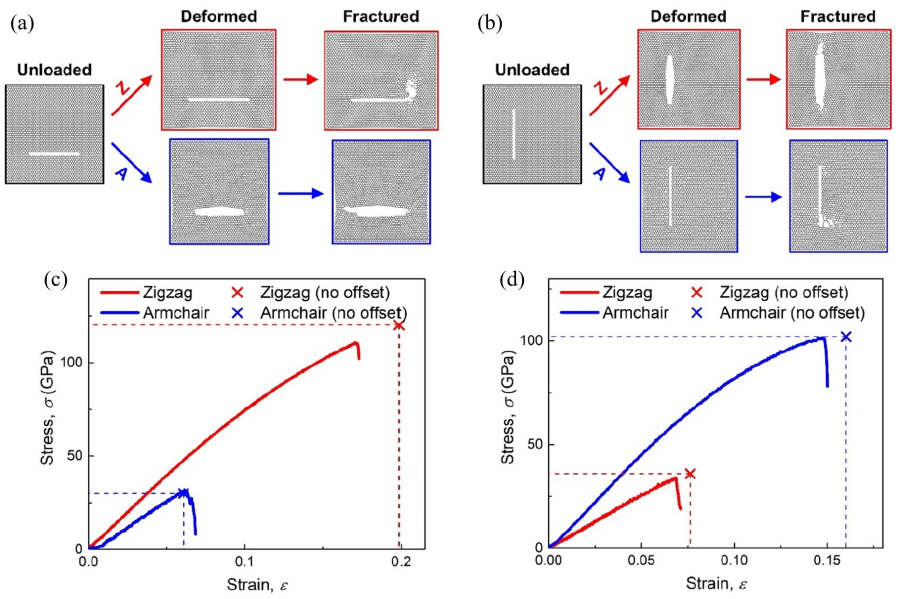

Figure 2.7: Simulation results of graphene design with offset line defect. Deformation and fracture modes of graphene sheets with (a) zigzag and (b) armchair defect. Stress-strain curves of graphene sheets with (c) zigzag and (d) armchair defect. The failure stresses and strains of the non-offset defected graphene sheet under two loading conditions are marked in the curve figures for comparison.

Parallel uniform line defects

Patterned defect designs usually involve multiple defects. Amongst the most straightforward multiple-defect designs are parallel line defects. The following simplifications are adopted: 1) Parallel defects are only in the zigzag or the armchair direction. 2) All defects have the same and a fixed length. 3) Graphene sheets are uniformly divided by parallel defects. Above simplifications make the number of defects the only design variable. To study how parallel defects affect the mechanical properties of graphene, MD simulations of graphene with parallel line defects with a defect number $N_{\mathrm{D}} = 3$ are performed, presented in Fig. 2.9, where the defect length is fixed as $0.5L_{\mathrm{Z}}$ for zigzag defect and $0.5L_{\mathrm{A}}$ for armchair defect. Figs. 2.9(a) and (b) demonstrate the deformation and fracture modes. For loading parallel to the defects, fracture initiates randomly from along one of the defects, while for loading perpendicular to the defects, the defects widen almost uniformly and fracture also takes place at one of the defect tips in a random fashion. These deformation and fracture modes consist with previous designs with single defect. Figs. 2.9(c) and (d) present the calculated stress-strain curves. Fig. 2.9(c) shows the stress-strain curves of graphene with parallel zigzag defects with the failure stress and strain of the centered line defect with the same length (equivalent to parallel zigzag defects with $N_{\mathrm{D}} = 1$) as a comparison. Results show that

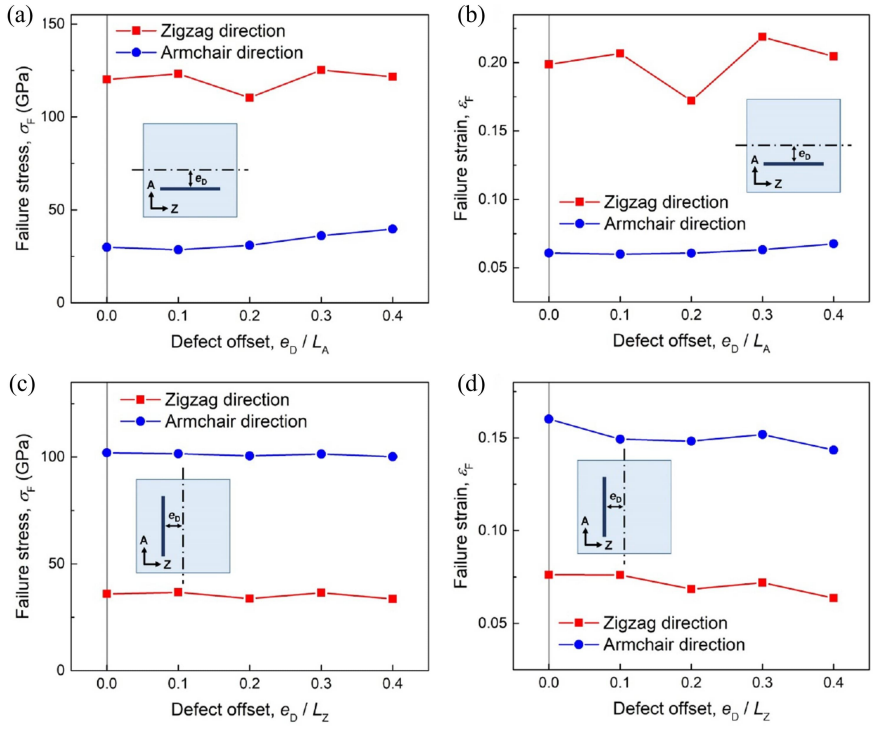

Figure 2.8: Parametric study of graphene with offset line defect with respect to offset distance e_D. The influence of offset distance on (a) the failure stress and (b) failure strain of graphene with zigzag defect. The influence of offset distance on (c) the failure stress and (d) failure strain of graphene with armchair defect. (e) Illustration of defect elimination and bond forming of graphene sheet with armchair defect with $e_D/L_A = 0.4$ upon armchair loading.

although the zigzag failure stress and strain are reduced compared to the scenario of single defect, the armchair failure strain is improved, which overall lowers the level of anisotropy. Fig. 2.9(d) shows the stress-strain curves of graphene with parallel armchair defects and also compares the results with the $N_D = 1$ case. It is noteworthy that upon zigzag loading the graphene design has a lower failure stress but almost an identical failure strain compared to upon armchair loading, showing the possibility of entering Quadrant 2 on the ratio graph. Upon loading perpendicular to the defects, the enhancement of failure strain results from the deformation mode of the simultaneous widening of all three line defects. Upon loading parallel to the defects, the slightly lowered failure stress and strain may be explained by the increasing number of defect involved in the deformation process, which may lead to a higher probability of fracture at a given large strain. In addition, although the line defects are parallel to the loading direction, the total defect width multiplies with the increase of defect number, of which the effect is equivalent to a line defect perpendicular to the loading with an increasing length.

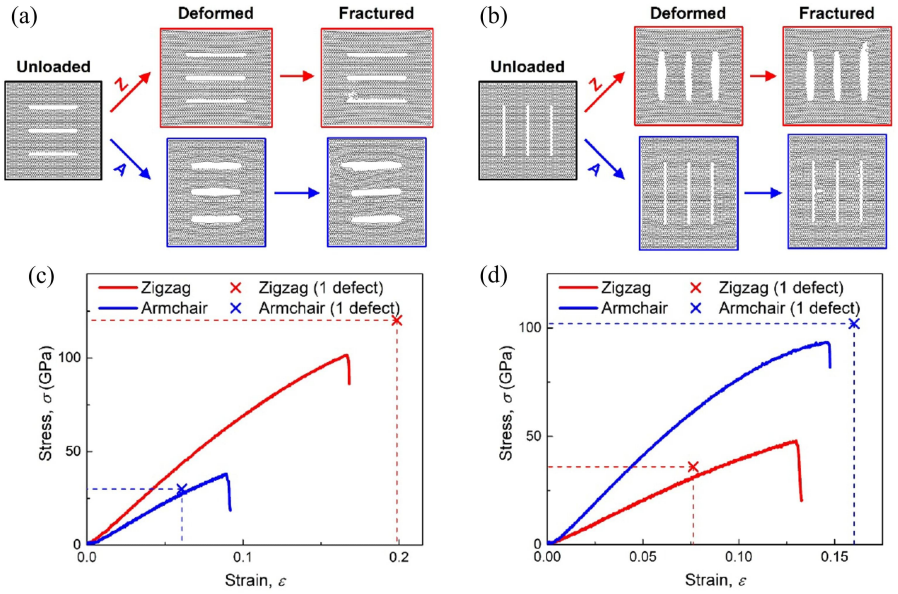

Figure 2.9: Simulation results of graphene with uniform parallel line defects. Deformation and fracture modes of graphene sheets with (a) zigzag and (b) armchair defect. Stress-strain curves of graphene sheets with (c) zigzag and (d) armchair defect. The lengths of zigzag and armchair defect are $0.5L_{\mathrm{Z}}$ and $0.5L_{\mathrm{A}}$, respectively. The failure stresses and strains of the centered line defect with the same length are marked in the curve figures for comparison.

A systematic parametric study of defect number N_{D} is conducted and summarized as below. Mechanical properties of graphene with parallel uniform zigzag defects of various defect numbers are presented in Figs. 2.10(a) and (b). As the defect number increase, the failure stress and strain in zigzag direction decrease slightly. As of the armchair direction, the failure stress and strain are enhanced, especially the failure strain. The increase of defect number can allocate the loading strain within these defects, resulting in a reduced widening on a single line defect. Therefore, the failure strain of the whole graphene sheet is increased. Although the Young's modulus of the graphene sheet can slightly decrease with an increasing number of perpendicular line defects, the softening effect can be compensated by the increase of failure strain, which explains the increase of overall failure stress. The influence of defect number on mechanical properties of graphene with parallel armchair defects presented in Figs. 2.10(c) and (d). Similarly, the failure stress and strain in the armchair direction decrease slightly, while the failure stress and strain in the zigzag direction increase. It is noteworthy that the armchair failure strain overtakes zigzag failure strain after $N_{\mathrm{D}} = 3$, indicating qualitative change of anisotropy and a resultant cross of quadrants on the ratio graph.

The parametric results are then mapped onto the ratio graph to provide insights to the

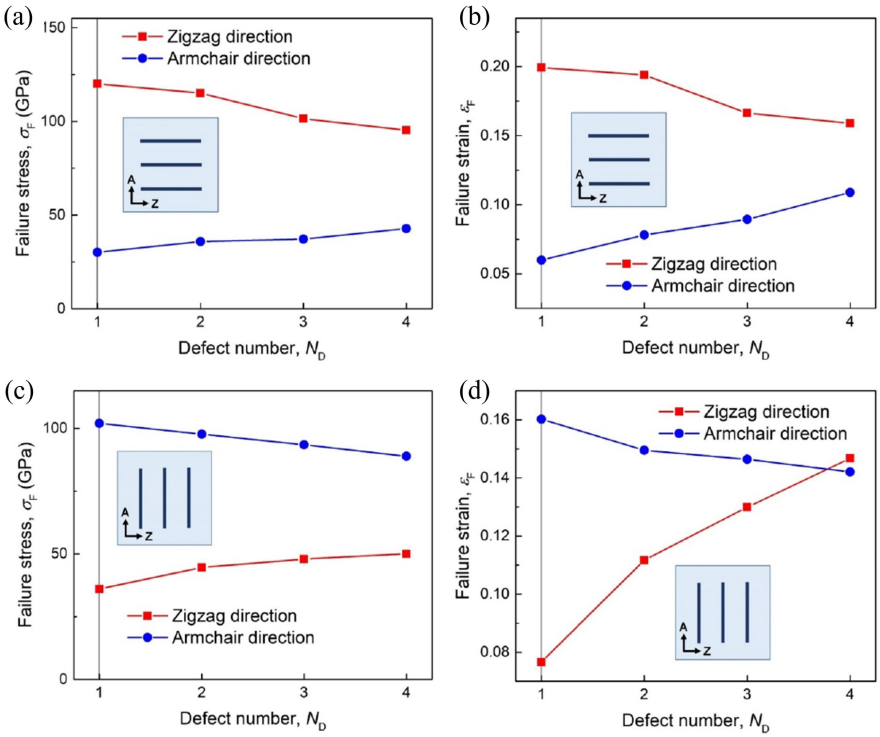

Figure 2.10: Parametric study of graphene with uniform parallel line defects with respect to defect number N_D. The influence of defect number on (a) the failure stress and (b) strain of graphene with zigzag defects. The influence of defect number on (c) the failure stress and (d) strain of graphene with armchair defects.

anisotropy-oriented defect design, as illustrated in Fig. 2.6(c). It is shown that as the defect number increases, the parallel zigzag defect design is driven from Quadrant 1 down towards Quadrant 4 but does not end up entering, while the parallel armchair defect design immigrates from Quadrant 3 to Quadrant 2. It is therefore concluded that the design of parallel uniform line defects advances the tuning capability of graphene anisotropy by exploiting a new region on the ratio graph which is inaccessible for designs using single line defects.

Complex patterned defect design

Although the above defect designs with basic elements have exhibited the capability to fine-tune the mechanical anisotropy of the graphene sheet, a few limitations exist. Firstly, designs with a single defect has yet to be able to produce data points in Quadrant 4 or deep into Quadrant 2, Secondly, the fine-tuning of anisotropy using a single defect is sacrificial, where either the failure stress or the failure strain are weakened compared to pristine

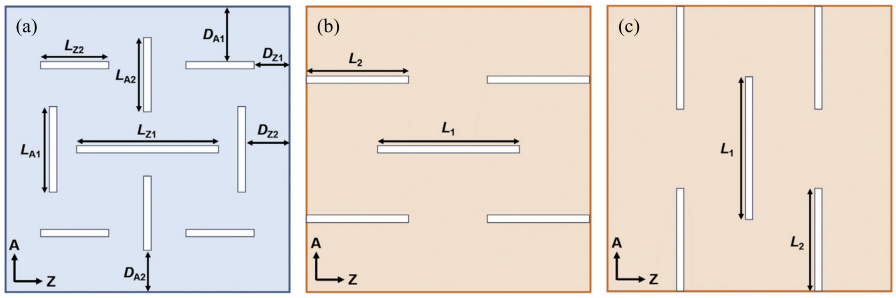

Figure 2.11: Complex defect pattern designs. (a) Network-like graphene kirigami, (b) graphene kirigami with parallel zigzag interior and exterior cuts, and (c) graphene kirigami with parallel armchair interior and exterior cuts.

graphene sheet, and no improvement in mechanical property can be obtained. In the following, two specific complex patterned defect designs are proposed: network-like graphene kirigami and graphene kirigami with parallel interior and exterior cuts, which may lead to new unexplored anisotropic properties and help overcome the limitations of designs with basic defects. Fig. 2.11 shows the geometric parameters of these designs. The design of network-like graphene kirigami is schematized in Fig. 2.11(a), where the set of parameters addresses the lengths of various cuts as well as the positions relative to the graphene edge. The purpose of the network-like graphene kirigami is to achieve the entry into Quadrant 4 which is not yet accessible for designs discussed above. Landing in Quadrant 4 requires a higher zigzag failure stress together with a higher armchair failure strain. The zigzag-oriented central cut is designed to maintain the zigzag strength and improve the armchair stretchability. The designs of graphene kirigami with parallel interior and exterior cuts are illustrated in Figs. 2.11(b) and (c), corresponding to designs consisting of zigzag and armchair defects, respectively. The purpose of this design is to produce graphene more stretchable than the pristine graphene using interior and exterior cuts [137]. Specifically, parallel zigzag defects are designed to improve the stretchability in the armchair direction, and parallel armchair defects are designed to improve the stretchability in the zigzag direction. To reduce the design space, graphene sheet is tri-sectioned by line defects by default, leading to only two independent parameters being in the system, i.e. the length of the central interior defect L_1 and the length of the exterior defect L_2. To experimentally realize the complex designs proposed in this study, patterned graphene sheets can be fabricated by a variety of methods such as etching techniques using thermally activated metallic nanoparticles [20, 41], atomic force microscopy anodic oxidation [111], and scanning tunneling microscopy lithography [164], which can produce ultrafine patterns on monolayer and multilayer graphene.

As an example, simulation results of the design of network-like graphene kirigami with

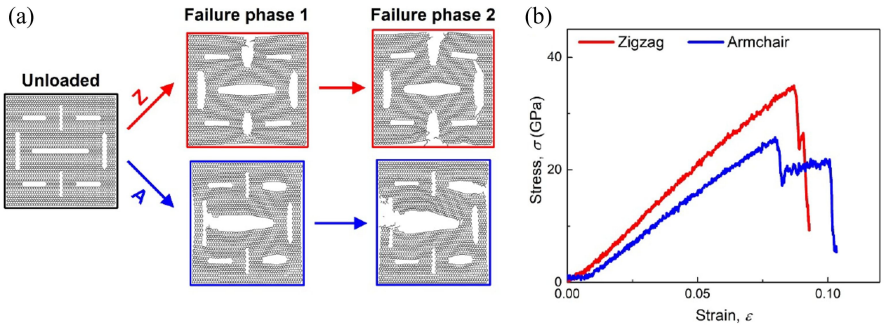

Figure 2.12: Simulation results of the network-like graphene kirigami. (a) Deformation and fracture modes and (b) stress-strain curves of the exemplar network-like graphene kirigami.

the following geometric parameters

$$(L_{Z1}, L_{Z2}, L_{A1}, L_{Z2}, D_{Z1}, D_{Z2}, D_{A1}, D_{A2}) \\ = (0.5L_Z, 0.2L_Z, 0.3L_A, 0.2L_A, 0.15L_Z, 0.1L_Z, 0.2L_A, 0.1L_A)$$

are presented in Fig. 2.12. The complex defect design gives rise to a multi-phase failure pattern characterized by a local failure prior to the global failure, as demonstrated in Fig. 2.12(a). Upon zigzag loading, fracture occurs first at the tip of one of the armchair defects closest to the unloaded edge, followed by fractures at the tips of many other armchair defects. Upon armchair loading, a localized failure firstly initiates between the leftmost armchair cut and the central cut, and then more fractures occur between multiple defects and their closest unloaded edges. Fig. 2.12(b) presents the stress-strain curves. Different from previous defect designs, the network-like graphene kirigami achieved a higher zigzag failure stress together with a higher armchair failure strain, finally entering Quadrant 4. Due to the high complexity of the design, the design space becomes too vast to be practical to study the influences of all design parameters and their interplay exhaustively. Fig. 2.13(a) shows the distribution on the ratio graph of a couple of designs of network-like graphene kirigami. It is observed that a majority of data points successfully land in Quadrant 4 and some data points are also distributed in Quadrant 1.

Although the design of network-like graphene kirigami has entered Quadrant 4, the data points are relatively close to the origin, indicating a weak mechanical anisotropy. Additionally, entering Quadrant 4 by lowering zigzag failure strain, making it sacrificial. The design of graphene kirigami with parallel interior and exterior cuts may be more promising to drive deeper into Quadrant 4 by achieving stretchability superior to the pristine monolayer graphene.

To illustrate, simulation results of graphene kirigami with zigzag parallel interior and exterior cuts with the parameter pair $(L_1, L_2) = (0.6L_Z, 0.35L_Z)$ are presented in Fig. 2.14.

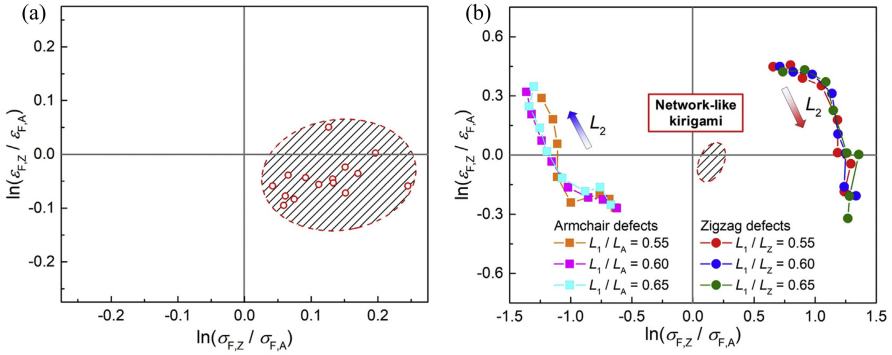

Figure 2.13: Distribution or evolutionary paths of data points of complex patterned defect designs on 2D ratio graph. (a) Distribution of data points of a variety of designs of network-like graphene kirigami. (b) Evolution of data points of graphene kirigami with parallel interior and exterior cuts. The attainable region of network-like graphene kirigami design is marked on the graph to draw comparison.

Figs. 2.14(a) and (b) show the fracture modes. Upon zigzag loading, fracture occurs in between of one of the exterior cuts and the interior cut. Upon armchair loading, the deformation mode exhibits significant 3D features and the fracture takes place at several spots Figs. 2.14(c) and (d) present the calculated stress-strain curves. Fig. 2.14(c) shows that upon zigzag loading, stress-strain curve shape resembles the pristine counterpart and failure stress and strain are lowered by $\sim 30\%$. Fig. 2.14(d) shows the stress-strain curves upon armchair loading together with the zigzag and armchair failure strain $\varepsilon_{\mathrm{FZ,P}}$ and $\varepsilon_{\mathrm{FA,P}}$ of pristine graphene sheet as a comparison. As can be observed, the armchair failure strain of the graphene kirigami design is higher than that of pristine counterpart in both directions, indicating a non-sacrificial nature of the present design. It is also noticed that the stress-strain curve is less smooth than those previously seen, which can be accounted for by the low stress level, making the random noise more visible.

A systematic parametric study with respect to the parameter pair (L_1, L_2) is provided as below. Because the number of design variables is reduced down to 2, the influence of L_1 and L_2 can be presented in 2D graphs, as shown in Fig. 2.15. Simulation results of $8 \times 8 \times 2 = 128$ instances of graphene kirigami with parallel interior and exterior cuts are conducted, where L_1/L_{Z} (or L_1/L_{A}) $\in [0.30, 0.35, ..., 0.65]$ and L_2/L_{Z} (or L_2/L_{A}) $\in [0.05, 0.10, ..., 0.40]$. Figs. 2.15(a) and (b) present the influence of L_1 and L_2 on failure stress and strain of graphene kirigami with zigzag parallel defects upon zigzag loading, showing that the two parameters in fact play a relatively insignificant role. Figs. 2.15(c) and (d) show the results subject to armchair loading. It can be observed that the failure stress increases with decreasing lengths of both interior and exterior cuts, while the failure strain increases with increasing lengths of both interior and exterior cuts. The arrows on the figures point to the increasing direction

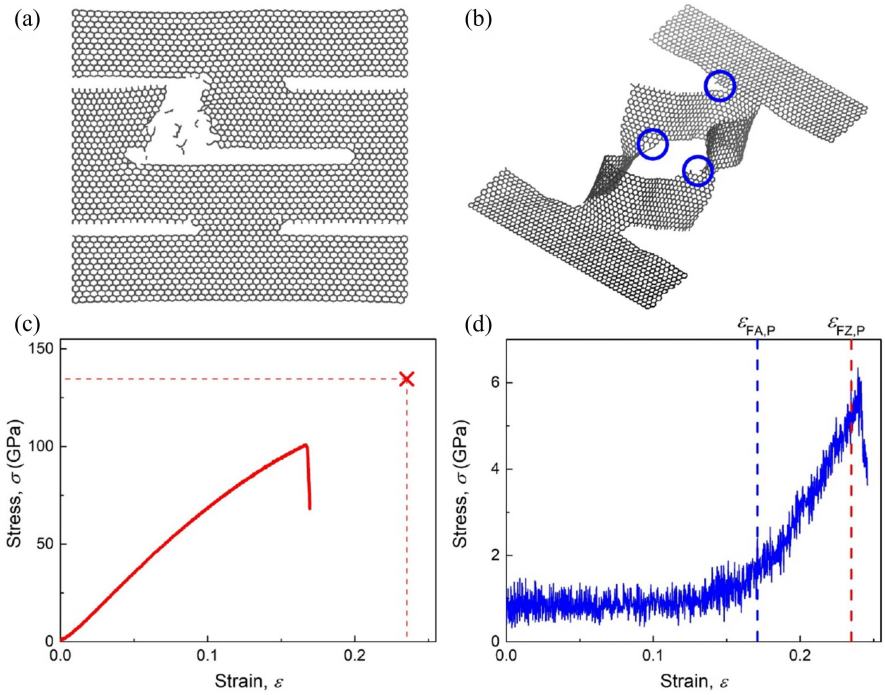

Figure 2.14: Fracture modes and stress-strain curves of graphene kirigami with zigzag parallel interior and exterior cuts with parameters $(L_1, L_2) = (0.6L_Z, 0.35L_Z)$. Fracture modes of graphene kirigami upon (a) zigzag and (b) armchair loadings, where spots of fracture are highlighted with blue circles. (c) Stress-strain curve of graphene kirigami upon zigzag loading with the failure stress and strain of pristine graphene sheet upon zigzag loading as a comparison. (d) Stress-strain curve of graphene kirigami upon armchair loading with the failure strains of pristine graphene sheet upon zigzag and armchair loadings for comparison.

of a mechanical property. According to Fig. 2.15(d), certain combinations of L_1 and L_2 produce higher failure strain than pristine graphene, making designs with these parameters non-sacrificial. Figs. 2.15(e) and (f) present the influence of L_1 and L_2 on graphene kirigami with armchair parallel defects upon zigzag loading. Similar to the scenario of zigzag defect upon armchair loading, the failure stress increases with decreasing lengths of both interior and exterior cuts, while the failure strain increases with increasing lengths of both interior and exterior cuts. According to Fig. 2.15(f), combinations of high L_1 and L_2 can produce higher failure strain than pristine graphene, making the design strategy non-sacrificial. Figs. 2.15(g) and (h) present the influence on failure stress and strain upon armchair loading, showing that L_1 and L_2 in fact play a relatively insignificant role, similar to the scenario of zigzag defects upon zigzag loading. Again, the design shows a strong duality relation. Combinations of high L_1 and L_2 can produce higher failure strain than pristine graphene, making the design

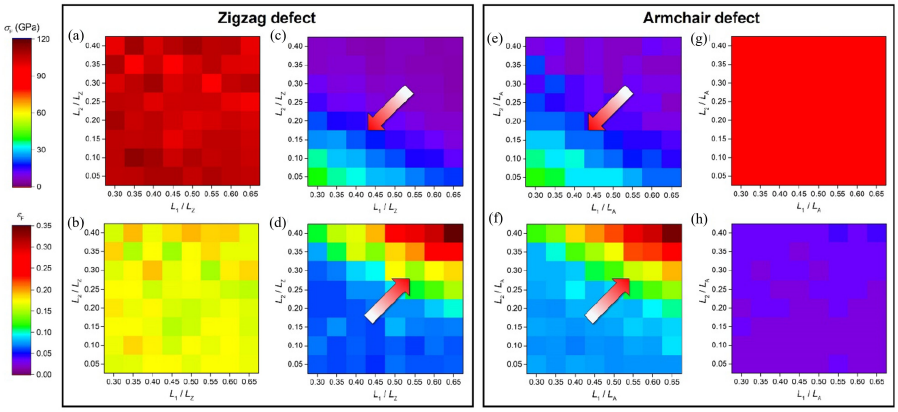

Figure 2.15: 2D map representations of parametric study of graphene kirigami with interior and exterior cuts with respect to parameter pair (L_1, L_2). The influence of L_1 and L_2 on failure stress and strain of graphene kirigami with zigzag parallel defects upon (a, b) zigzag and (c, d) armchair loading. The influence of L_1 and L_2 on failure stress and strain of graphene kirigami with zigzag parallel defects upon (e, f) zigzag and (g, h) armchair loading.

strategy non-sacrificial.

Given the 2D parametric study results, how graphene kirigami with parallel interior and exterior cuts can lead to new anisotropy properties can be discussed. According to Figs. 2.15(c-f), the most drastic failure strain change happens where the central interior cut is relatively long, data points corresponding to L_1/L_{Z} and $L_1/L_{\mathrm{A}} \in [0.55, 0.60, 0.65]$ are therefore selected to provide more prominent evolutionary paths on the ratio graph. L_2/L_{Z} and L_2/L_{A} still use the full results of parametric study, increasing from 0.05 to 0.40, to illustrate the longest path as has been studied. The evolution of the current graphene kirigami design on ratio graph is summarized in Fig. 2.13(b), compared with the data point region obtained by the network-like graphene kirigami design. Results show that for design of the zigzag interior and exterior defects, data points migrate down from Quadrant 1 to Quadrant 4 as the length of exterior defects increases, while for the armchair counterparts, data points move up from Quadrant 3 deep into Quadrant 2. In addition, compared to the network-like design, the design with parallel interior and exterior defects not only can dive much deeper into Quadrant 2 and Quadrant 4 but also has a significantly larger attainable region across the 2D plane.

Concluding remarks

In this section, a defect engineering strategy is adopted to tune the anisotropic property of monolayer graphene. Mechanical properties of various defect designs, from simple single-line defect designs to more complex designs with multiple defects, are systematically stud-

ied using MD simulation. For designs consisting of basic defect elements, the influences of defect length, obliquity, and offset from the center, number of parallel defects are separately discussed. For more complex defect designs, network-like graphene kirigami and graphene kirigami with parallel interior and exterior cuts are investigated. A novel ratio graph is proposed to visualize and rationalize the tuning of mechanical anisotropy of defected graphene sheet, which has ultimately helped answer the questions like how to make an isotropic graphene sheet, how to intensify the anisotropy of graphene, and design a defected graphene which is stronger in one direction and more stretchable in the other. Through our defect designs, all the four quadrants of the 2D ratio graph are covered, indicating a high capability and versatility of fine-tuning the mechanical properties of graphene in both directions. This research investigates the tunability of graphene mechanical anisotropy via defect design, which may shed light on the new possibility of fine-tuning mechanical properties of other 2D materials [220].

2.2 Graphene defect mitigation

Although previous section has shown that carefully and creatively engineering defects can lead to unconventional properties, naturally existing defects such as point defects, dislocations and grain boundaries generally have a negative effect on the mechanical properties of graphene. During the graphene production processes such as mechanical exfoliation [63, 197] and chemical vapor deposition (CVD) [29, 112], it is common that various structural defects can be introduced, and the mobility of defects profoundly enriches the roles that these defects can play. Defect behavior in graphene has received great attention [182]. The realization of the full potential of graphene often requires a defect-free or a defect-scarce state, because defects can compromise the theoretically predicted properties, resulting in the deteriorated operating efficiency of graphene-based applications. Much theoretical and numerical research has explored the influence of defects on the mechanical properties of graphene, showing that strength and stiffness losses are generally proportional to the defect size and concentration, and are also affected by temperature and chirality [175, 68, 4, 48]. Zandiatashbar et al studied the effect of various types of defects on the strength and stiffness of graphene, showing that although the mechanical properties of graphene can exhibit a significant drop in the presence of vacancies, strength and stiffness show little degradation when graphene bears sp^3-type defects [201]. However, these types of defects are intrinsically different from each other and therefore have a fundamentally different impact on the mechanical properties of graphene. Is it possible to recover from defect-induced mechanical degradation by counter-intuitively enlarging the defect (instead of miniaturizing the defect) without changing the defect type? A positive answer to this question has at least two promises. For one, degradation recovery by enlarging the defect reduces the number of atoms while improving the performance, which tremendously enhances the efficiency as a result. For another, enlarging the defect does not involve switching the type of defect and removes material instead of adding to the material, which makes it possible to modify the defective graphene as it is

rather than making graphene from scratch again.

In this section, the possibility of recovering from defect-induced mechanical degradation by enlarging the defect is explored via MD simulations. A centered circular defect is used as the initial defect. Enlargement modifications are made onto the preexisting circular defect aiming to achieve degradation recovery. Mechanical properties of interest include failure stress, failure strain, and mode of fracture initiation. These properties of initial defective graphene sheets and various modified graphene sheets are calculated and compared against a pristine graphene sheet to evaluate the recovery effect. Deformation characteristics of effective recovery are examined to shed light on the counterintuitive recovery mechanism. The influence of elliptical defects on the mechanical properties of graphene sheets is systematically studied, which has not been adequately discussed in the literature thus far. Finally, the degradation recovery potential with respect to various defect sizes is discussed to obtain an estimation of expected recovery given the information of preexisting defects.

System description and molecular modeling

The graphene sheet in this section has a side length of $L \sim 110$ Å and consists of 4966 atoms when defect-free. A schematic of the pristine graphene sheet is provided in Fig. 2.16(a) with tensile loading directions illustrated. It has been shown that when the diagonal length of graphene sheet is over 5 nm, the size effect of the model size can be largely neglected [215]. Based on a deformation-control manner, in-plane tensile loading is applied by assigning displacement at a constant speed to a 3 Å wide stripe at one end (shaded area in Fig. 2.16(a)), while a 3 Å wide stripe at the other end is held immobile in all three dimensions. A strain rate of 10^9 s^{-1} is used in all loading scenarios [215]. The defects studied in this section are circular and elliptical porous defects representing vacancy clusters of various sizes and shapes. To simplify the problem, defects are located at the center of the graphene sheet. Graphene sheets with a centered elliptical defect of various sizes and shapes are shown in Fig. 2.16(b), parametrized by the length of semi-axis in the zigzag direction a and the length of the semi-axis in armchair direction b. As a special case, the elliptical defect degenerates to a circular defect when $a = b = R$, where R is the defect radius.

MD simulations are conducted using LAMMPS and the AIREBO potential. The integration time step is set as 1 fs. Periodic boundary conditions are used in two in-plane dimensions and a fixed boundary condition is applied to the perpendicular out-of-plane dimension. An ensemble of random velocity corresponding to the temperature $T = 300$ K is firstly generated throughout the system. Then an equilibrium is realized by running a simulation in the NPT ensemble with a Nose–Hoover thermostat [70] at the same temperature for 50 ps, where the maximum out-of-plane fluctuation is ~ 2 Å. The loading scenario is simulated in the NVT ensemble at $T = 300$ K. The stress is calculated by Eq. 2.2.

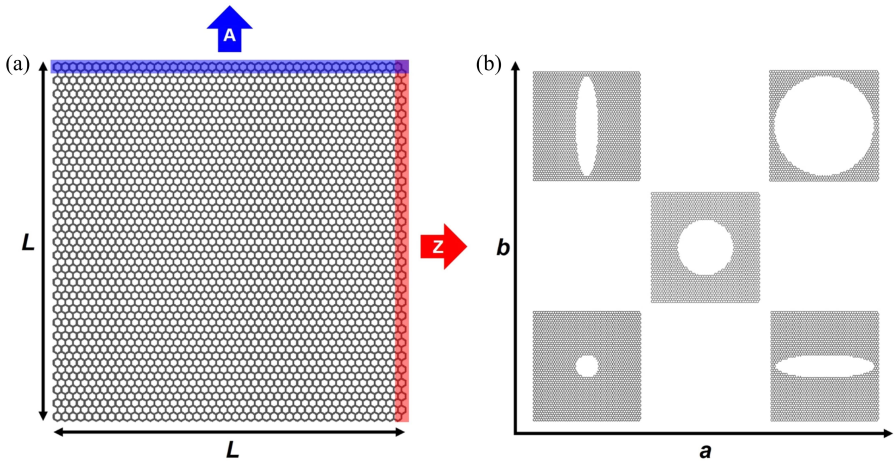

Figure 2.16: Schematic of pristine and defective graphene sheets used for MD simulation. (a) Square pristine graphene sheet and illustration of tensile loading directions. Arrows with 'Z' and 'A' represent tensile loading in the zigzag and armchair directions, respectively. (b) Square graphene sheets with an elliptical defect of various sizes and shapes.

Results and discussion

Firstly, MD simulations are conducted to investigate the mechanical properties of the following graphene sheets in the zigzag direction as a set of examples: (a) pristine graphene sheet as a benchmark, (b) graphene sheet with a circular defect with a radius $R = 0.1L$ as a defective graphene sheet, and (c) graphene sheet with an elliptical defect with a parameter pair $(a, b) = (0.45L, 0.1L)$ representing an enlarged circular defect in the zigzag direction only with the purpose of degradation recovery. The vacancy concentration of the representative defective graphene with a circular defect is $\sim 3\%$, which closely resembles graphene in an experimental setting [179], as well as other simulation studies [68, 204]. Here, the mechanical properties of interest are failure stress, failure strain, and mode of fracture initiation. The calculated stress–strain curves of the above three graphene sheets subject to loading in the zigzag direction are presented in Fig. 2.17(a). Comparing a graphene sheet with a circular defect with a pristine graphene sheet, failure stress and failure strain are lowered, suggesting mechanical degradation. However, a graphene sheet with an elliptical defect, despite bearing a larger defect compared to the circular defect, possesses a much higher failure stress and failure strain, suggesting a profound recovery effect. The mechanical properties of the above three graphene sheets are summarized below. Failure stress can be recovered from $56.4\%\sigma_{\mathrm{P}}$ to $73.6\%\sigma_{\mathrm{P}}$, and failure strain can be recovered from $47.9\%\varepsilon_{\mathrm{P}}$ to $79.3\%\varepsilon_{\mathrm{P}}$, where $\sigma_{\mathrm{P}} = 134.6$ GPa and $\varepsilon_{\mathrm{P}} = 0.235$ are the failure stress and failure strain of a pristine graphene sheet, respectively. The modes of fracture initiation of the three graphene sheets are provided in Fig. 2.17(b). For a pristine graphene sheet, fracture initiates at the edge close to

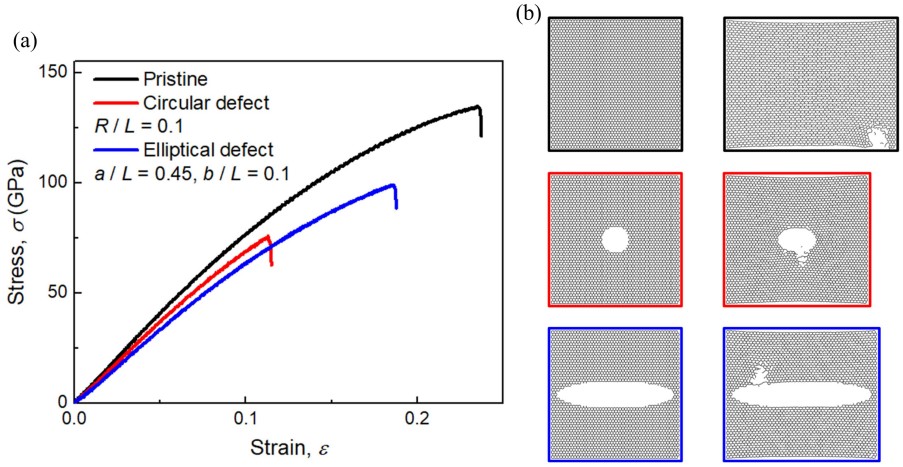

Figure 2.17: Demonstration of degradation recovery by enlarging the preexisting defect to an elliptical shape. (a) Calculated stress–strain curves, and (b) unloaded and failure morphologies of a pristine graphene sheet, graphene sheet with a circular defect, and graphene sheet with an elliptical defect for degradation recovery.

the loaded region; for a graphene sheet with circular defects, fracture occurs in the middle part of the arc; for graphene with elliptical defects, fracture initiates from along the arc close to the vertex of the defect where the most dramatic change in curvature happens during the deformation process. These differences in failure mode may provide valuable insights into the mechanism of degradation recovery.

To cast light on the mechanism of the degradation recovery via counterintuitive defect enlargement, the maximum deformation before the fracture is examined. To this end, shapes of the surrounding areas of circular with a radius $R = 0.1L$ and elliptical defects with $(a, b) = (0.45L, 0.1L)$ right before failure are shown in Fig. 2.18(a) to present the maximum deformation with the red arcs representing the defect rims in unloaded conditions. As can be observed, graphene with a circular defect, though having a lower failure strain, shows a much more drastic deformation at the defect rim compared to graphene with an elliptical defect before the onset of fracture, which can be characterized by a change in curvature on the defect rim. It is hypothesized that enlarging the circular defect to an elliptical shape reduces the change in curvature when the graphene sheet is loaded to a certain amount of strain, which leads to a mediated deformation process and a postponed onset of fracture, and ultimately results in enhanced failure strain. In addition, the failure initiates from the point on the defect rim having the maximum change in curvature. To test the hypothesis quantitatively, the curvature at any given stretching strain is formulated as follows. The lengths of both semi-axes of the elliptical defect are subject to change as the graphene sheet is stretched, which can be expressed as $a(\varepsilon) = a_0(1+\varepsilon)$ and $b(\varepsilon) = b_0(1-\nu\varepsilon)$. Here, a_0 and b_0

are the prescribed lengths of the semi-axes of the elliptical defect in the zigzag and armchair directions in the unloaded graphene. ν is defined as the ratio of the amount of shrinkage of the elliptical defect transversely to the loading to the amount of lengthening in the loading direction, similar to the concept of Poisson's ratio. ν is assumed to be independent of strain ε and ranges from 0 to 1. The curvature κ at a certain point on the defect rim $(a\cos t, b\sin t)$ at any moment during the loading process can be expressed as

$$\begin{aligned}\kappa(\varepsilon,t) &= a(\varepsilon)b(\varepsilon)(a^2\sin^2 t + b^2\cos^2 t)^{-\frac{3}{2}} \\ &= a_0b_0(1+\varepsilon)(1-\nu\varepsilon)(a_0^2(1+\varepsilon)^2\sin^2 t + b_0^2(1-\nu\varepsilon)^2\cos^2 t)^{-\frac{3}{2}} \quad (2.4)\end{aligned}$$

The curvature on defect rim in the unloaded state κ_0 can be expressed as

$$\kappa_0(t) = a_0b_0(a_0^2\sin^2 t + b_0^2\cos^2 t)^{-\frac{3}{2}} \quad (2.5)$$

Note that the tear-like deformation that results in the failure around the defect in fact corresponds to a decrease in curvature. Therefore, the sign of the change in curvature is inversed

$$\begin{aligned}\Delta\kappa(\varepsilon,t) = -[\kappa(\varepsilon,t) - \kappa_0(t)] &= a_0b_0[(a_0^2\sin^2 t + b_0^2\cos^2 t)^{-\frac{3}{2}} \\ &- (1+\varepsilon)(1-\nu\varepsilon)(a_0^2(1+\varepsilon)^2\sin^2 t + b_0^2(1-\nu\varepsilon)^2\cos^2 t)^{-\frac{3}{2}}] \quad (2.6)\end{aligned}$$

The approximation $1-\nu\varepsilon \simeq 1$ is used. Now Eq. 2.6 becomes

$$\Delta\kappa(\varepsilon,t) \simeq a_0b_0[(a_0^2\sin^2 t + b_0^2\cos^2 t)^{-\frac{3}{2}} - (1+\varepsilon)(a_0^2(1+\varepsilon)^2\sin^2 t + b_0^2\cos^2 t)^{-\frac{3}{2}}] \quad (2.7)$$

Because of the symmetric defect geometry, only the range $0 \le t \le \pi/2$ is considered. For the circular and elliptical defects in Fig. 2.18(a), results based on Eq. 2.7 can not only demonstrate the reduction of the maximum change in curvature by the defect enlargement, but also predict the location of the onset of failure in both cases. Plugging in Eq. 2.7 $a_0 = b_0 = 0.1L$ for the circular defect and $a_0 = 0.45L$, $b_0 = 0.1L$ for the elliptical defect and set the stretching strain $\varepsilon = 0.1$, the change in curvature at any point on the rim of the defect can be obtained, as is shown in Fig. 2.18(b). For the circular defect, the maximum change in curvature occurs at the vertex on the semi-axis transverse to the loading ($t = \pi/2$), while for the elliptical defect, the location of the maximum change in curvature moves toward the vertex perpendicular to the loading ($t = 0.17 \times \pi/2$). These predicted locations are in good agreement with the initiation of failure presented in Fig. 2.17(b). Additionally, the maximum change in curvature is substantially lowered by expanding the circular defect to an elliptical shape. The curves shown in Fig. 2.18(b) also capture the portion of the defect rim that exhibits tear-like deformation ($\Delta\kappa > 0$), the portion that exhibits contraction-like deformation ($\Delta\kappa < 0$), and the point on the rim not subject to any change in curvature ($\Delta\kappa = 0$).

To further validate the proposed degradation recovery mechanism based on the change in curvature, a graphene sheet with a rectangular defect of the same dimensions in the zigzag

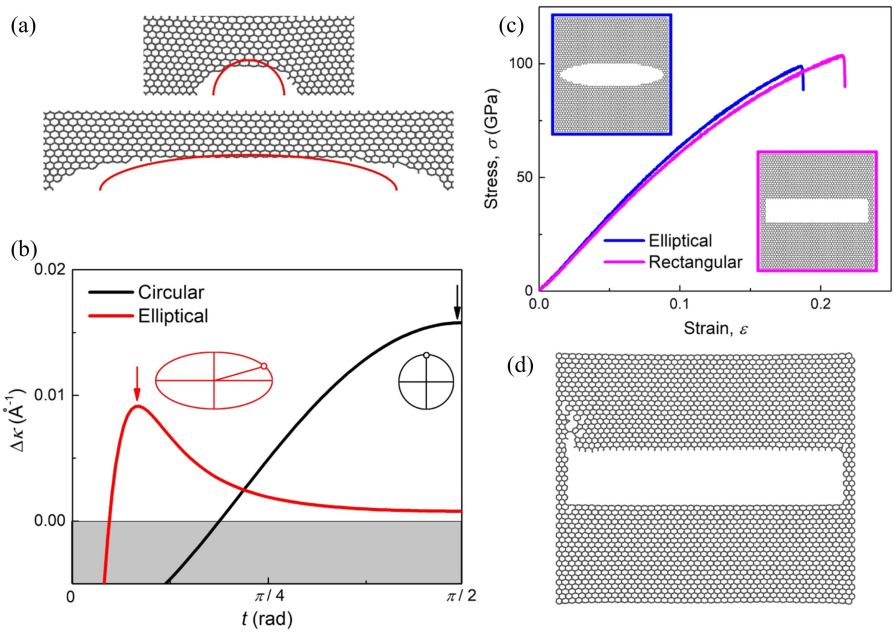

Figure 2.18: Illustration of proposed recovery mechanism and its validation. (a) Morphologies of surrounding areas of circular and elliptical defects right before fracture. Red arcs show the defect rims before the loading. (b) Change in curvature at any point on the rim of the circular and the elliptical defect, where the arrows point to the maximum changes in curvature in the two cases. (c) Stress–strain curves of graphene sheets with the elliptical defect and the rectangular defect of the same dimensions in the zigzag and armchair directions. (d) Mode of fracture initiation of graphene sheets with the rectangular defect.

and armchair directions as the elliptical defect is simulated. A rectangular defect produces an even smaller change in curvature compared to an elliptical defect and should therefore have higher failure strain. Fig. 2.18(c) presents the stress–stress curves of graphene sheets with an elliptical and rectangular defect, which confirms the hypothesis by showing that the graphene sheet with a rectangular defect has a higher failure stress and strain. It is also noteworthy in Fig. 2.18(d) that for a graphene sheet with a rectangular defect, fracture initiates at one of the vertices where the curvature changes more significantly than at any other point along the defect, which again supports the proposed mechanism. This observation also adequately explains the fracture initiation mode of a pristine graphene sheet: fracture initiates at the edge close to the loaded region where the curvature changes fastest. To further solidify the proposed theory related to the change in curvature, stress distributions during the failure process of pristine graphene sheet, graphene sheets with circular and elliptical defects are supplemented, as is shown in Fig. 2.19. To illustrate the stress concentration more clearly, stress that is over 80% of the maximum stress $\sigma_{\max}$ of the individual case is colored red.

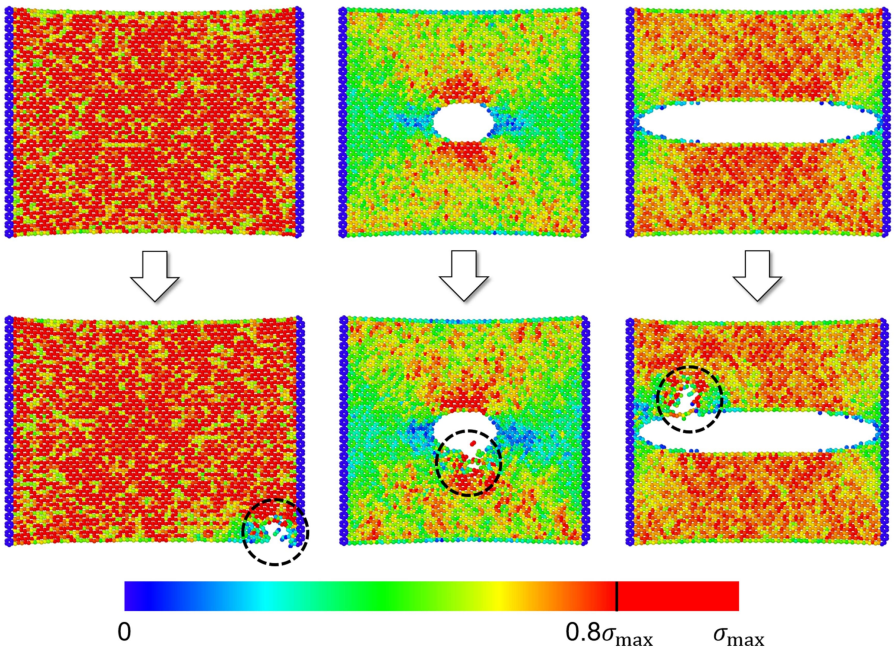

Figure 2.19: Stress distributions during the failure process of pristine graphene sheets and graphene sheets with circular and elliptical defects. To illustrate the stress concentration more clearly, stress that is over 80% of the maximum stress σ_{max} of the individual case is colored red.

As can be seen, for graphene with a circular defect, stress over $0.8\sigma_{max}$ is distributed in a more localized fashion compared to graphene with an elliptical defect. This phenomenon indicates that the latter utilizes a graphene sheet in a more efficient way where atoms are better involved in the deformation during the loading process, thus having a higher failure stress and strain. Furthermore, it is notable that fracture initiates in the area with high stress which is also associated with the maximum change in curvature on the defect rim. Hence, this observation is consistent with and solidifies the proposed mechanism.

Following the demonstration and reasoning of the degradation recovery capability by forming an enlarged elliptical defect, the influences of how long the defect is lengthened in the examined direction and the possible difference between the examined directions are discussed. In the discussion below, defects are lengthened in either the zigzag or armchair direction starting from a centered circular defect with a radius $R = 0.1L$. Figs. 2.20(a) and (b) show the failure stress when the defect is lengthened in the examined direction with the perpendicular dimension fixed. As can be seen, both failure stress and failure strain are enhanced as the length of the elliptical defect in the examined direction increases, and no fundamental difference is shown between the zigzag and the armchair directions. The stable growth can be associated with the proposed recovery mechanism, where the change

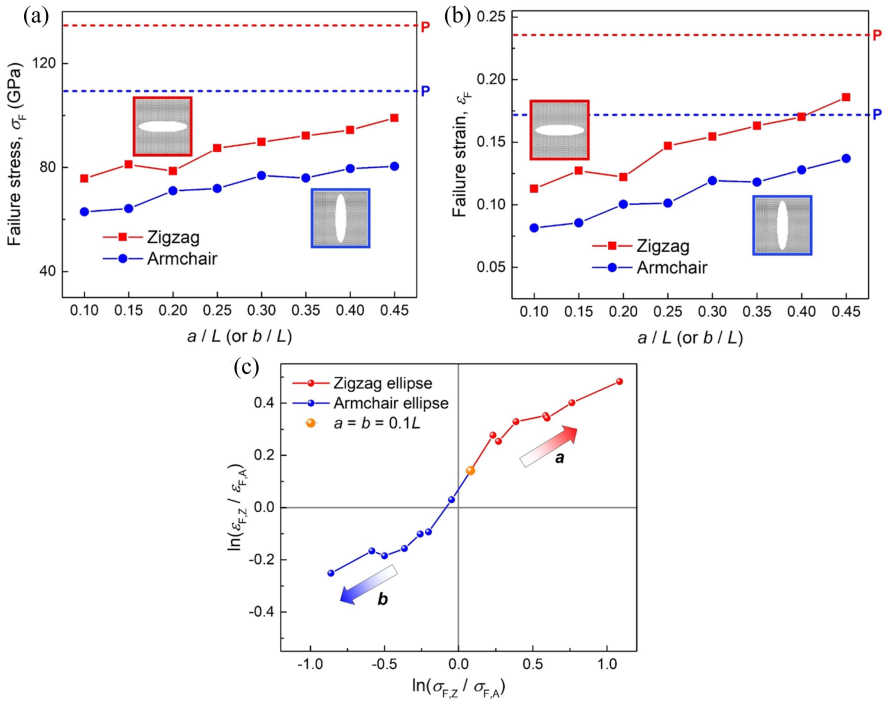

Figure 2.20: The influence of 1D lengthening of a circular defect on the mechanical properties of graphene sheet. (a) Failure stress and (b) failure strain of graphene sheet with a defect of increasingly lengthened dimension parallel to the loading and unchanged dimension in the perpendicular direction. The failure stress and strain of a pristine graphene sheet are added on the figures for comparison, as are marked with dashed-horizontal lines and the letter 'P'. (c) Evolutionary path of data points on the 2D anisotropy graph as the axis of the elliptical defect in the examined direction is lengthened, while the axis perpendicular to the examined direction is fixed.

in curvature is gradually reduced as the dimension of the defect in the examined direction increases. Because graphene is an intrinsically anisotropic material, it is interesting to look at the influence of 1D lengthening on the mechanical anisotropy of a graphene sheet by examining mechanical properties in the zigzag and armchair directions at the same time. A 2D anisotropy graph is proposed to quantify the anisotropic property of the graphene sheet with respect to both failure stress and failure strain. The evolutionary paths in Fig. 2.20(c) show that the mechanical anisotropy of graphene sheets can be concretely intensified going from a circular to an elliptical defect in both the zigzag and the armchair directions.

Having studied the effect of 1D lengthening of a circular defect to an elliptical defect, the influence of size and shape of elliptical defect on the mechanical properties of graphene sheet are systematically discussed with 2D variable parameter pair (a, b). Simulation results

of $8 \times 8 \times 2 = 128$ instances of graphene sheets with elliptical defect in the zigzag and armchair directions are conducted, where $a/L, b/L \in [0.10, 0.15, ..., 0.45]$. Figs. 2.21(a) and (b) show the influence of size and shape on failure stress in the zigzag and armchair directions, and Figs. 2.21(c) and (d) show the influence on failure strain. The recovering effect and the weakening effect of the defect dimension perpendicular to the examined direction are illustrated with green and blue arrows pointing to the direction of greater intensity. White lines represent circular defects where $a = b$, of which the failure stress and strain as a function of defect radius R are presented in Figs. 2.21(e) and (f). Observations and corresponding conclusions based on these figures are provided as below.

- In the zigzag direction, the maximum failure stress and strain are achieved when the zigzag dimension a is large and the armchair dimension b is small, while in the armchair direction, failure stress and strain reach their maximum in concord when the armchair dimension b is large and the zigzag dimension a is small. Therefore, for a graphene sheet with ellipse-shaped vacancy defect cluster, the defective graphene sheet obtains its best mechanical properties when the elliptical defect has a long axis in the examined direction while having a short axis perpendicular to the examined direction. This result goes against the intuition that a smaller defect produces higher strength and ductility.

- Although an elliptical defect with a long axis in the examined direction and a short axis in the perpendicular direction strengthens the examined direction best, this configuration weakens the unexamined direction and intensifies the mechanical anisotropy most, corresponding to the discussion in Fig. 2.20(c).

- According to the parametric results of a circular defect in Figs. 2.21(e) and (f), as the radius of the circular defect increases, failure stresses in both directions decrease monotonously, while failure strains change insignificantly. In addition, no recovering effect is observed with the defect being enlarged. Hence, it can be concluded that the recovery effect of elliptical defects is contributed by the geometric asymmetry of defect clusters. Furthermore, this result strengthens the theory of change in curvature because enlarging the circular defect does not change the curvature therefore no early or postponed fracture initiation is caused. This suggests a new design strategy of decoupling failure stress and failure strain.

Having systematically studied the influence of size and shape of an elliptical defect as well as the degenerated scenario of a circular defect, the potential of recovery from defect-induced mechanical degradation by circular defects of various sizes is discussed. The failure strains of pristine graphene in the zigzag and armchair directions are used as a benchmark to normalize the failure strains of circular and elliptical defects. An evaluation of the recovery potential of failure stress and strain with a variable radius of circular defects is provided in Fig. 2.22, where in the examined direction the axis is lengthened to $2 \times 0.45L$. It is observed that the recovery potential decreases as the circular defect becomes larger and that the recovery effect is in general closed when the diameter reaches $0.4L$. This is because the maximum

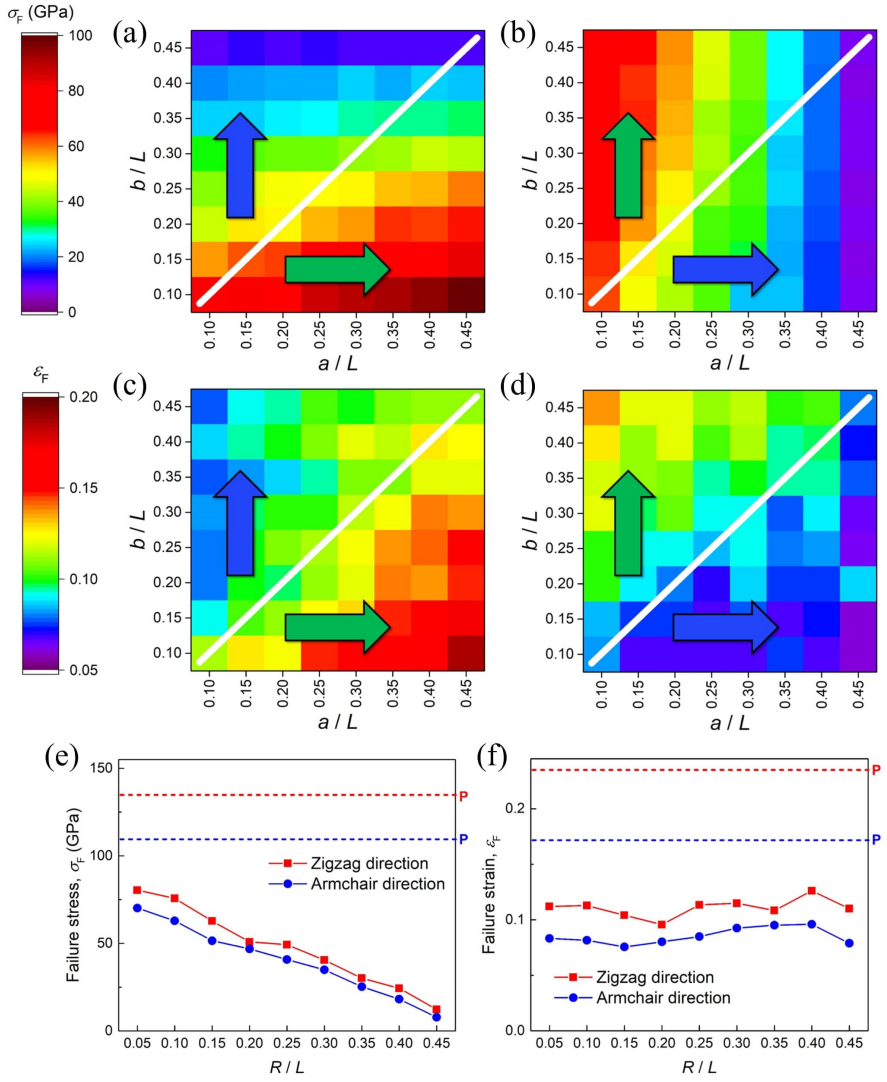

Figure 2.21: The influence of size and shape of an elliptical defect on the mechanical properties of graphene sheet. Failure stress maps of graphene sheet with elliptical defects of various sizes and shapes in the (a) zigzag and (b) armchair directions. Failure strain maps of a graphene sheet with elliptical defects of various sizes and shapes in the (c) zigzag and (d) armchair directions. Recovering effect and the weakening effect of the defect dimension perpendicular to the examined direction are illustrated with green and blue arrows pointing to the direction of greater intensity. White lines represent circular defects. The influence of circular defects on (e) failure stress and (f) failure strain of graphene sheet. The failure stresses and strains of pristine graphene sheet are added on the figures for comparison, as are marked with dashed-horizontal lines and the letter 'P'.

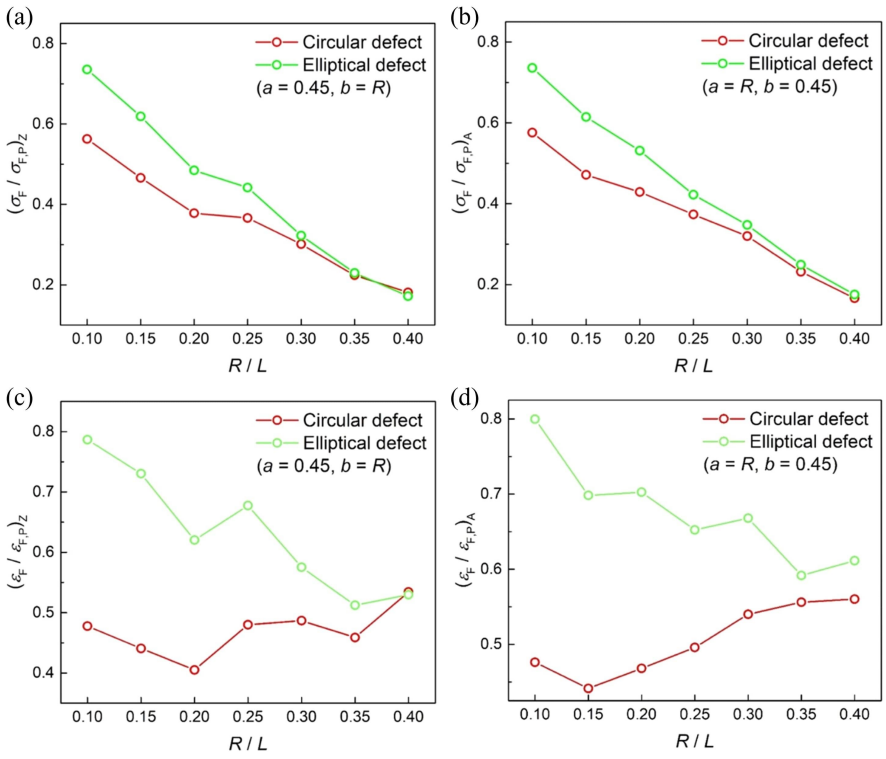

Figure 2.22: Evaluation of recovery potential with respect to variable size of a circular defect. Failure stress in the (a) zigzag and (b) armchair directions. Failure strain in the (c) zigzag and (d) armchair directions.

geometric asymmetry of the defect is reduced by the size of the defect. Comparing the results in Fig. 2.22, failure strain has a higher recovery capability than failure stress and the effect on the zigzag and armchair directions are similar. To investigate the opening of a recovery effect, the smallest vacancy in graphene is created by removing one atom at the center and also create a line defect with a length of $0.5L$ extended from the one-atom vacancy. Fig. 2.23 shows that the 1D enlargement of the one-atom vacancy exhibits a recovery effect, suggesting that there appears to be no threshold for opening a recovery effect.

To address the issue of strengthening one direction at the expense of weakening the other, the prescribed circular defect is expanded to a square shape to pursue enhanced mechanical performance in both the zigzag and armchair directions. The diameter of the circular defect and the side length of the square defect are both chosen as $0.15L$. Stress–strain relations of the above defective graphene in two directions are presented in Fig. 2.24. As is shown, by expanding the circular defect to the smallest square defect, the mechanical properties in both directions can be enhanced.

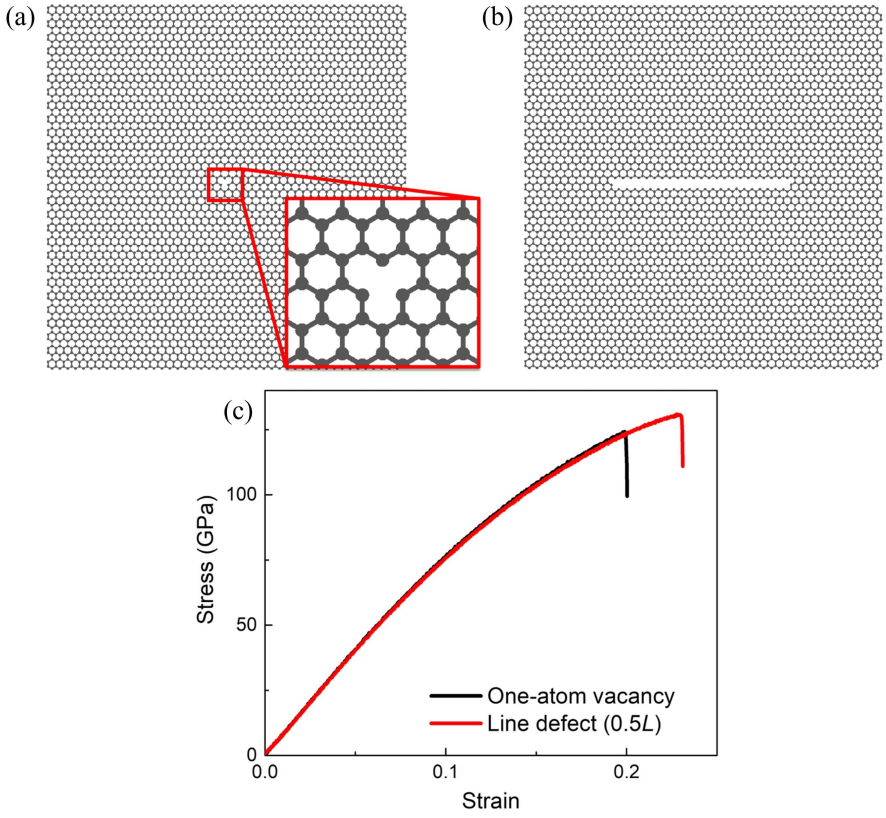

Figure 2.23: Graphene sheets containing one-atom vacancy and its corresponding line defect. Geometries of graphene with (a) the one-atom vacancy and (b) the line defect. (c) Stress–strain relations of above two defective graphene sheets.

Concluding remarks

In this section, the possibility of recovering from defect-induced mechanical degradation by enlarging the defect is explored via MD simulation. It is shown that the enlargement of the preexisting defect to an elliptical shape has a counterintuitive potential to recover from the mechanical degradation that the very defect has caused. The significance of this finding has two main implications. Firstly, degradation recovery by enlarging the defect reduces the atoms of the system while improving the performances, which tremendously enhances the efficiency. Secondly, enlarging the defect does not involve switching the type of defect and removes material instead of adding, thus increasing the feasibility of modifying and enhancing the defective graphene as it is. The mechanism of degradation recovery lies in a reduced change in curvature during deformation, which is further solidified by theoretical quantification and stress-field analysis. This theory can also predict and pinpoint the location of the initiation of the fracture—where the curvature changes most significantly during the

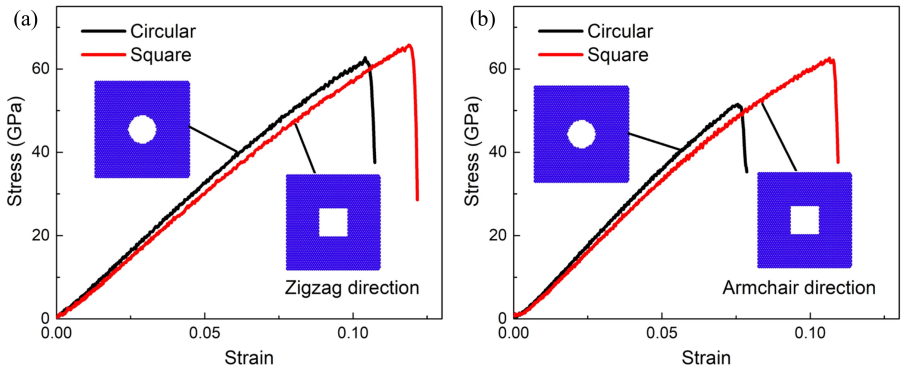

Figure 2.24: Stress–strain relations of graphene with a circular defect (diameter = $0.15L$) and graphene with a square defect (side length = $0.15L$) in the (a) zigzag and (b) armchair directions.

deformation. In addition, the influence of an elliptical defect on the mechanical properties of a graphene sheet is systematically studied. Finally, the degradation recovery potential of defects of various sizes is examined, showing that the initial defect that can create the highest degree of geometric asymmetry has the best potential for degradation recovery. This research, which investigates the recovery from defect-induced mechanical degradation and the influence of elliptical defect on the in-plane mechanical properties of a graphene sheet, sheds light on the new possibility of fine-tuning mechanical properties via defect engineering [218].

2.3 Stress field properties of defective graphene

As defects play a pivotal role in the mechanical properties of graphene, much research has been underway to understand their specific effects. However, the determination of mechanical properties of defective graphene such as strength and ductility remains challenging, due to the indeterminacy of local stress distributions, potentially released out-of-plane behavior, and multi-defect interactions that are involved when subject to external loads. In this section, stress field characteristics of defective graphene sheets subject to the unidirectional in-plane stretch are studied via MD simulation. Stress fields of various defective graphene sheets are calculated to draw the connection between defect properties and stress distribution, and ultimately to predict collective mechanical properties such as strength and ductility. The altered out-of-plane and in-plane behavior of defective graphene sheets are also inspected and related to stress distribution characteristics. To detail the influence of defect on the stress field, the role of defects is decoupled by separately studying the effects of size and shape. With the knowledge of the fundamental relation between defect properties and stress distribution, the stress field characteristics of graphene sheets with multiple defects are discussed. An application of stress field optimization via rational defect design is presented.

Results

In this section, square-shaped graphene sheets with a side length of $L \sim 110$ Å are simulated, consisting of 4966 atoms when defect-free. The unidirectional in-plane stretch is applied in the zigzag direction based on a deformation-control manner by assigning displacement at a constant speed to a 3 Å wide stripe at one end, while a 3 Å wide stripe at the other end is held immobile in all three dimensions. Here, only loading in the zigzag direction is studied, because our results in the previous sections have pointed to no qualitative difference between the mechanical properties of zigzag and armchair directions. The applied strain rate is constant at 10^9 s^{-1} in all simulations. To demonstrate how defects impact the mechanical properties, stress fields of graphene sheets are computed which not only can shed light on detailed mechanical responses in an atomic resolution but also can be used to derive collective mechanical properties of the entire graphene sheet.

To begin with, mechanical responses of two defective graphene sheets are studied and compared against pristine graphene. They are (1) a graphene sheet with a centered line defect with a length of $0.5L$ transverse to the stretch and (2) a graphene sheet with a centered circular defect with a diameter of $0.2L$. Stress fields are calculated based on von Mises stress σ_V using Eq. 2.3. Stress fields right before the fracture of a pristine graphene and the two defective graphene sheets above are visualized in Figs. 2.25(a–c). For the pristine graphene in Fig. 2.25(a), stress is uniformly distributed over the whole graphene sheet. Almost every point on the graphene sheet is able to reach a high stress level before failure, suggesting a highly efficient usage of the graphene sheet as a mechanical member where almost all atoms and bonds are leveraged and contribute to the collective mechanical properties. For the defective graphene sheet with a line defect transverse to the stretch, a non-uniform stress field is produced, as shown in Fig. 2.25(b). Upon the stretch the line defect widens and two defect tips localize high stress. In the meantime, along the line defect very low stress is hosted and the low-stress regions propagate in the stretching direction far to the edges of the graphene sheet. It is envisioned that these low-stress regions have little contribution to the collective mechanical properties because the atoms and bonds within are unstressed. In addition, a fracture initiates as soon as the stress of one part of the graphene sheet reaches the bond-breaking stress, which develops and causes a catastrophic failure. Because the bond-breaking stress in a defective graphene sheet is no higher than the pristine counterpart, the ultimate stress and strain should be significantly lower than those of the pristine graphene. Next, a graphene sheet with a circular defect is examined to see how the stress field varies with different defect properties, of which the resultant stress field is shown in Fig. 2.25(c). Although an uneven stress distribution is also observed, high stress is hosted over a larger area in comparison to the case of a line defect, while regions with a low stress level are significantly smaller, altogether indicating a more uniform stress field. Unlike the case of the line defect where low-stress regions develop in a spread-out manner and propagate to the graphene edges, here low-stress regions grow inwardly and diminish before propagating to the graphene edges. The above stress field properties indicate a better usage of atoms and bonds in comparison to the graphene sheet with a line defect, and thus, the

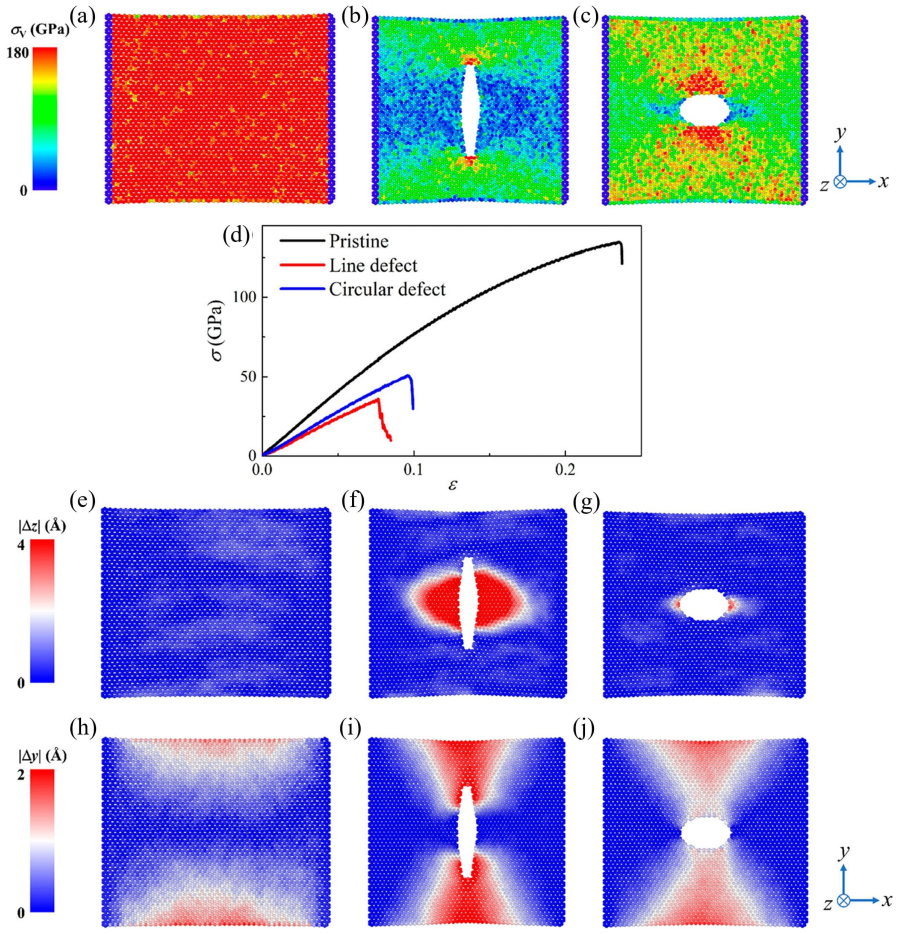

Figure 2.25: Stress fields, stress–strain curves, and distributions of displacement magnitude of pristine and defective graphene sheets. (a–c) Stress fields, (d) stress–strain curves, and distributions of (e–g) out-of-plane and (h–j) in-plane displacement magnitude of stretched pristine graphene, defective graphene with a line defect, and defective graphene with a circular defect, respectively. Distributions are plotted based on the morphologies right before the initiation of failure.

collective mechanical properties should be superior, but still, much lower than the pristine graphene.

To validate the above reasoning on the relation between stress field characteristics and collective mechanical properties, stress–strain curves of the above three graphene sheets are plotted in Fig. 2.25(d). The calculation methods of the collective stress σ from MD simulations are the same as in the previous sections. As shown, the ultimate stress and strain of the pristine graphene are significantly higher than the two defective graphene sheets, while

those of the graphene sheet with a circular defect are higher than one with a line defect. The results of the collective stress–strain relation plus stress fields of the demonstrative examples lead to the following two preliminary conclusions: (1) Various defects can pose different influences on the stress field. (2) The more uniformly stress is distributed upon the stretch, the higher the ultimate stress and strain can reach.

In addition to the ability of defects to alter stress fields, it is interesting to examine whether defects can induce certain displacement patterns and, if so, how these patterns and the stress field are related. Previous studies on graphene kirigami have shown outstanding out-of-plane behavior [14, 150, 137]. However, it remains not well understood how their out-of-plane patterns are related to the stress distribution. Also, the in-plane displacement has not been sufficiently discussed, which may potentially lead to a non-traditional Poisson effect. This section focuses on the potential out-of-plane and in-plane behaviors of defective graphene sheets and their relations to the stress field when subject to a unidirectional in-plane stretch.

The displacement in graphene is quantified as follows. For the graphene configurations in this work, the zigzag and armchair directions lie along x and y directions, respectively. Thus, the in-plane stretch is applied in the x direction in the x–y plane. The position vector of an atom at time t is denoted as $(x(t), y(t), z(t))$. The out-of-plane and in-plane displacement magnitude are expressed as $|\Delta z| = |z(t) - z(0)|$ and $|\Delta y| = |y(t) - y(0)|$. The displacement in the stretching direction $|\Delta x|$ mostly develops with the loading and is therefore not discussed here. The distributions of out-of-plane and in-plane displacement magnitude before fracture of the above three graphene sheets are provided in Figs. 2.25(e–g) and (h–j). For the pristine graphene in Figs. 2.25(e) and (h), the out-of-plane displacement is negligible over the whole domain while a moderate amount of in-plane displacement is exhibited along two free graphene edges, suggesting that the pristine graphene subject to an in-plane stretch can be characterized by totally in-plane lengthening and lateral contraction and is not featured by out-of-plane behavior. For the graphene with a line defect in Figs. 2.25(f) and (i), however, substantial out-of-plane displacement is induced along the defect. Regions with out-of-plane displacement develop inwardly and diminish before reaching the edges of the graphene sheet. Propagation outwardly or parallel to the stretch can violate the zero out-of-plane displacement boundary conditions. In addition, the in-plane displacement is intensified and localized, which develops from the defect and propagates up to the free edges of the graphene sheet. The propagation of regions with in-plane displacement starts from relevant segments of the defect rim and ends at unconstrained edges, exhibiting a spread-out pattern. Viewing segments of the defect rim as the sources of regions with out-of-plane and in-plane displacement, these segments complement each other. For the graphene sheet with a circular defect, although out-of-plane and in-plane displacement are also developed in a similar pattern as the line defect, it is less profound in comparison, as is shown in Figs. 2.25(g) and (j). Only the vicinities of two ends of the circular defect allow for out-of-plane displacement, and the in-plane displacement exhibit a lower magnitude. From the results of defective graphene sheets, it can be concluded that the existence of defects not only creates an out-of-plane degree of freedom which is absent in the pristine graphene, but also

intensifies and localizes in-place displacement. Additionally, the displacement features are co-determined by the defect geometry and boundary conditions. Comparing the above distributions of stress and displacement in pristine and defective graphene sheets, the relation between stress field characteristics and out-of-plane and in-plane behavior can be formulated as follows. Out-of-plane displacement can be induced only if the region has low stress. This is because high in-plane stress from stretching will eliminate any out-of-plane tendency due to the equilibrium requirement. High in-plane stress deforms the graphene and gives rise to in-plane displacement. Regions featured by out-of-plane and in-plane displacement are complementary in a way that regions with high stress and low stress are. Hence, it can be concluded that patterned out-of-plane and in-plane displacement is the consequence of defect-induced nonuniform stress field.

The illustrations above have demonstrated the ability of defects to alter the stress distribution and to induce displacement patterns. To cast light on the core factor governing the phenomenon, the effect of defect geometry is studied. The defect geometry can be elucidated by separately discussing the effects of pure size and shape. First, the effect of pure size is investigated. To this end, rectangular defects of various sizes are studied, aiming to minimize the effect of different defect shapes. The total lengths of the projection of defect on the direction parallel and perpendicular to the stretching direction are denoted as $L_\parallel$ and $L_\perp$, respectively. For a rectangular defect with sides parallel and perpendicular to the stretch, two side lengths are exactly $L_\parallel$ and $L_\perp$, as illustrated in Fig. 2.26(a). The effect of defect size $(L_\parallel, L_\perp)$ on the ultimate strength σ_u can be obtained by MD simulations and visualized on an $L_\parallel$-$L_\perp$ map, as shown in Fig. 2.26(b). The major direction of mechanical degradation is in the positive direction of the $L_\perp$-axis (noted by the arrow), while $L_\parallel$ has a relatively minor influence on the ultimate strength when $L_\perp \gtrsim 0.3L$. It is noteworthy that when $L_\perp < 0.3L$, ultimate stress is enhanced with larger $L_\parallel$, which may be counterintuitive considering the defective graphene sheet is strengthened by enlarging the defect. This is because lengthening the defect along the loading direction elevates the evenness of stress distribution, ultimately leading to improved mechanical properties. However, this phenomenon is in effect only when the length transverse to the loading is small, as deliberated in the previous section.

On each black line in Fig. 2.26(b) where defects share the same area, smaller $L_\perp$ indicates superior mechanical properties. The strengthening effect under small $L_\perp$ even adds to the dominance of the $L_\perp$ effect. To illustrate, the distributions of stress, out-of-plane and in-plane displacement magnitude, and stress–strain curves of four rectangular defects sharing the same area, i.e., $(0.1L, 0.8L)$, $(0.2L, 0.4L)$, $(0.4L, 0.2L)$, and $(0.8L, 0.1L)$, are provided in Fig. 2.27. For graphene sheets with these rectangular defects, high stress and low stress develop from edges parallel and perpendicular to the stretch, respectively. The covered area of high-/low-stress regions is in general proportional to the length of the corresponding edges. As $L_\parallel$ increases, the stress distribution becomes increasingly even. For example, when the size of the rectangular defect transits from $(0.8L, 0.1L)$ to $(0.1L, 0.8L)$, low-stress regions diminish and the high-stress regions expand. It is also notable that high- and low-stress regions are dichotomized at the vertices of the rectangle. When the rectangular defect is reduced down to a line defect parallel to the stretch, stress distributed uniformly over almost the whole

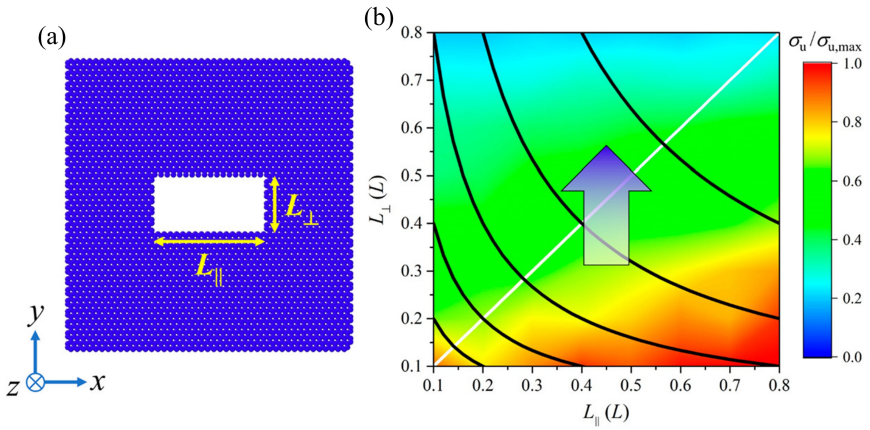

Figure 2.26: Ultimate strengths of graphene sheets centered a rectangular defect with varying geometric parameter pair $(L_\parallel, L_\perp)$. (a) Illustration of the geometric parameter pair $(L_\parallel, L_\perp)$. (b) Ultimate strength σ_u as a function of $(L_\parallel, L_\perp)$, normalized by $\sigma_{\mathrm{u},max} = 107.1\mathrm{GPa}$ at $(L_\parallel, L_\perp) = (0.8L, 0.1L)$. Black lines represent defect geometries sharing the same area. The white line represents square-shaped defects. The arrow indicates the major degradation direction.

graphene sheet except at the immediate vicinities of the two defect tips. A similar tendency applies for the distribution displacement magnitude: as the ratio $L_\parallel/L_\perp$ increases, regions exhibiting out-of-plane displacement shrink while regions exhibiting in-plane displacement expand in area but are reduced in intensity; when the rectangle degenerates to a line, both displacement features resemble those of a pristine graphene. Stress–strain curves of above defective graphene sheets with a rectangular defect as well as one with the line defect are calculated to show how these defects impact the collective mechanical properties, as presented in Fig. 2.27(b). It can be easily observed that the more uniformly distributed the stress is over the graphene sheet, the more superior the mechanical properties are in terms of ultimate stress and strain. It is noteworthy that the ultimate strength and strain of the graphene with the line defect are 89% and 85% of the pristine graphene, suggesting a rather low mechanical degradation. The white line in Fig. 2.26(b) represents square-shaped defects, indicating that the larger the defect, the weaker the mechanical strength. which can be also interpreted by the governance of the $L_\perp$ effect.

Comparing the above defective graphene sheets with a rectangular defect in Fig. 2.27 to one with a circular defect in Figs. 2.25(c) and (g), it can be seen that although they both produce high- and low-stress regions and induce the out-of-plane/in-plane behavior, the difference can be seen on how the defect shapes these influenced regions. For example, the high-stress regions of graphene with a rectangular defect are well distributed along the defect edges and the low-stress regions are formed in a spread-out fashion. A circular de-

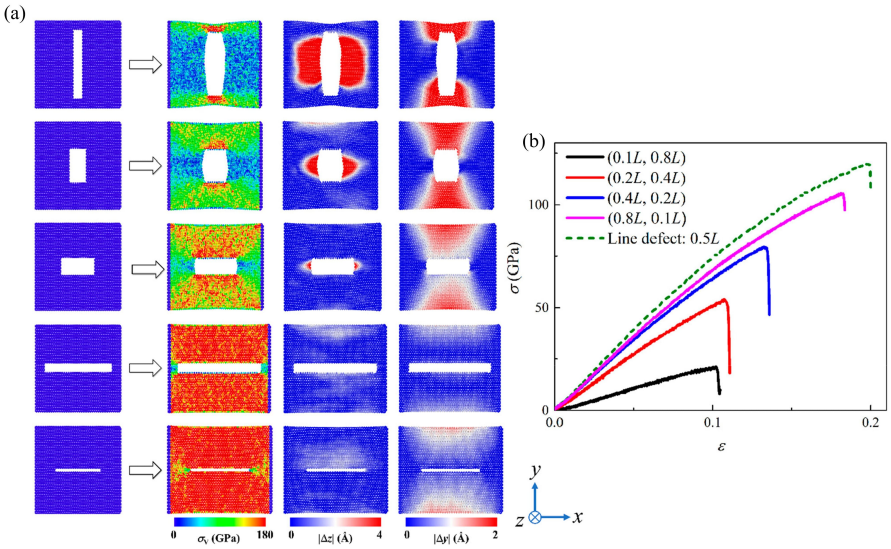

Figure 2.27: Simulation results of defective graphene sheets with rectangular defects of various $L_{\parallel}/L_{\perp}$ but a fixed area. (a) Stress fields and distributions of out-of-plane and in-plane displacement magnitude and (b) stress–strain curves of the defective graphene sheets with $(0.1L, 0.8L)$, $(0.2L, 0.4L)$, $(0.4L, 0.2L)$, $(0.8L, 0.1L)$, rectangular defects, and a line defect parallel to the stretch with a length of $0.5L$.

fect produces high-stress regions emitting from a part of the defect rim while having more localized low-stress regions. In addition, the displacement behavior is more profound when a rectangular defect is present other than a circular defect. These differences subsequently give rise to different collective mechanical properties of the defective graphene sheets. To shed light on the source of these differences, it is crucial to investigate not only the defect size but also the defect shape.

Having discussed the influence of $(L_{\parallel}, L_{\perp})$ on the mechanical properties of defective graphene sheets, the possible impact caused by different defect shapes is investigated where the parameter pair $(L_{\parallel}, L_{\perp})$ is fixed. To this end, a square-shaped defect, a circular defect, and a diamond-shaped defect with $L_{\parallel} = L_{\perp} = 0.3L$ are inspected. The original shapes, stress fields, distributions of out-of-plane and in-plane displacement magnitude, and stress–strain curves are shown in Figs. 2.28(a–c), (d–f), (g–i), (j–l), and (m), respectively. Stress fields of the above defective graphene sheets reveal a significant shape-related difference. Among these defects, the square-shaped defect produces the most even stress field where high stress is uniformly distributed long two edges parallel to the stretch, while the diamond-shaped defect is featured by an outstanding stress concentration at the upper and lower vertices. The effect of the circular defect lies in between the square-shaped defect and the diamond-shaped defect. Stress–strain curves of these three defective graphene sheets in Fig. 2.28(m)

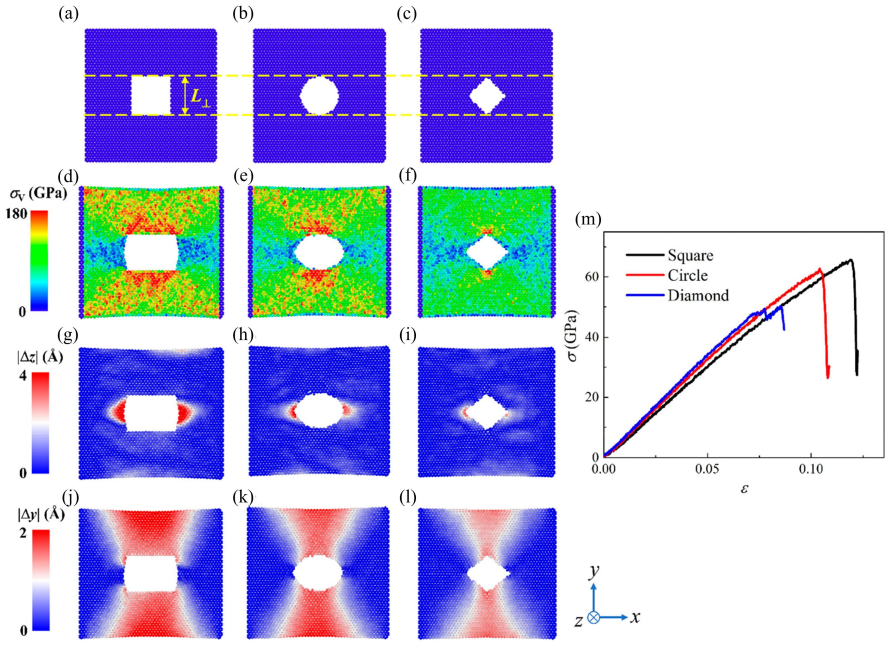

Figure 2.28: Influence of defect shape on the mechanical properties of graphene sheets. (a–c) Initial shapes, (d–f) stress fields, distributions of (g–i) out-of-plane and (j–l) in-plane displacement magnitude, and (m) stress–strain curves of square-shaped, circular, and diamond-shaped defects.

show that the graphene sheet with a square defect possesses the best mechanical properties while the graphene sheet with the diamond defect is the weakest. Therefore, similarly, the square defect has the most profound out-of-plane and in-plane behavior while the diamond defect does the least, as shown in Figs. 2.28(g–l). Interestingly, although the square-shaped defect requires the removal of the most number of atoms, it yields the highest failure stress and strain. This implies that the defect shape is a new factor to consider and opens up possibilities of defect design. From Figs. 2.28, the following can be observed: (1) High stress is concentrated at the farthest reach of the defect geometry transverse to the stretching direction, by which high-stress regions can be straightforwardly determined by inspection. (2) Dichotomizing points on the defect rim of out-of-plane-intense and in-plane-intense regions also dichotomize the low-stress and above-moderate stress regions, of which the locations are a function of the defect curve.

An analytical framework is developed as follows to predict the dichotomizing points of a general plane curve $\gamma(s) = (x(s), y(s))$. Slopes of the tangent and the normal lines at a point $(x(s_0), y(s_0))$ are $k(s_0) = dy/dx|_{s=s_0}$ and $n(s_0) = -dx/dy|_{s=s_0}$. Projecting the external loading onto the two directions, The tangential force $F_{\mathrm{t}}(S_0)$ and the normal force $F_{\mathrm{n}}(S_0)$ are obtained. It is assumed that the tangential force increases stress by the in-plane stretching

while the normal force does not contribute to stress at the examined point on the defect rim (because there is no atom inside the defect to balance the normal component). These two effects counteract each other. The dominance of the tangential force over the normal force gives rise to a high stress level, while the dominance of the normal force features a low stress. If the tangential force and the normal force are equal at certain points on the defect rim, these points dichotomize the high and low stress regions. This happens where the angle between the tangential and external tensile loading is $\pi/4$. Specifically, in this study where the stretch is along the x-axis, the requirement is simplified to the following: high stress: $|k| < 1$; low stress: $|k| > 1$; critical slope: $|k_{\mathrm{cr}}| = 1$. In fact, calculating the slope of a tangent line task for a given plane curve $\gamma(s) = (x(s), y(s))$ is a relatively simple task. The effectiveness of the above methods is tested by some examples.

(1) Rectangular defects. The defect rim of a rectangular defect has slopes of either $k = 0$ (edges parallel to the loading) or $k = \infty$ (edges perpendicular to the loading). Upon stretching, edges originally parallel to the loading remain parallel, emanating high stress regions. Edges perpendicular to the stretch widen by a small amount, where it is rational to assume that no point on the edges has a slope with an absolute value smaller than 1, hence initiating low stress regions. Dichotomizing points lie right on the four vertices. The above reasoning is confirmed by various results in Fig. 2.27.

(2) Diamond-shaped defects. Edges of diamond-shaped defects possess slopes of an identical absolute value $|k_{\mathrm{d}}|$. It is envisioned that if $|k_{\mathrm{d}}| < 1$, all edges contribute to high stress while low stress only appears at the vicinity of vertices on the x-axis. If $|k_{\mathrm{d}}| > 1$, all edges contribute to low stress while high stress only appears at the vicinity of vertices on the y-axis (regions of stress concentration). The above hypothesis is tested by simulating two graphene sheets with diamond-shaped defects $|x| + 3|y| = 0.4L$ and $3|x| + |y| = 0.4L$, respectively. Edges of the former diamond have a slope of $|k_{\mathrm{d}}| = \pm 1/3$, while those for the latter have a slope of $|k_{\mathrm{d}}| = \pm 3$. Simulation results are shown in Fig. 2.29, which confirm our hypothesis.

(3) Defects with a curved rim. Defects with a curved rim distinguish themselves from previously discussed rectangular and diamond-shaped defects in that the curvature of the rim is continuous in the tangential direction. Therefore, the dichotomizing points are to be determined by solving $k(s) = dy/dx = \pm 1$. Circular, elliptical, quadratic polynomial-shaped, and sine-shaped defects are utilized to test our method, of which the curve equations and derived dichotomizing points are summarized in Table 2.1. The predictions are tested by an example of each of the four classes. They are (a) $[x/(1+\epsilon)]^2 + y^2 = (0.15L)^2$, (b) $[x/(1+\epsilon)]^2/(0.2L)^2 + y^2/(0.1L)^2 = 1$, (c) $y = (4.8/L)\{(0.25L)^2 - [x/(1+\epsilon)]^2\}$, and (d) $y = 0.2L\cos\{(2\pi/L)[x/(1+\epsilon)]\}$, where ϵ is chosen as the strain immediate to the onset of fracture (0.101, 0.129, 0.0951, and 0.0932, respectively, for the four cases above). Predicted results are compared against the stress fields from MD simulations, as shown in Fig. 2.30, where predicted dichotomizing points are marked by red arrows. A good agreement between predictions and simulation results is reached, showing the validity of the method to address defects of all shapes.

Having qualitatively and quantitatively studied the influence of a single defect, scenarios where multiple defects are present can be readily discussed. The above results of a single

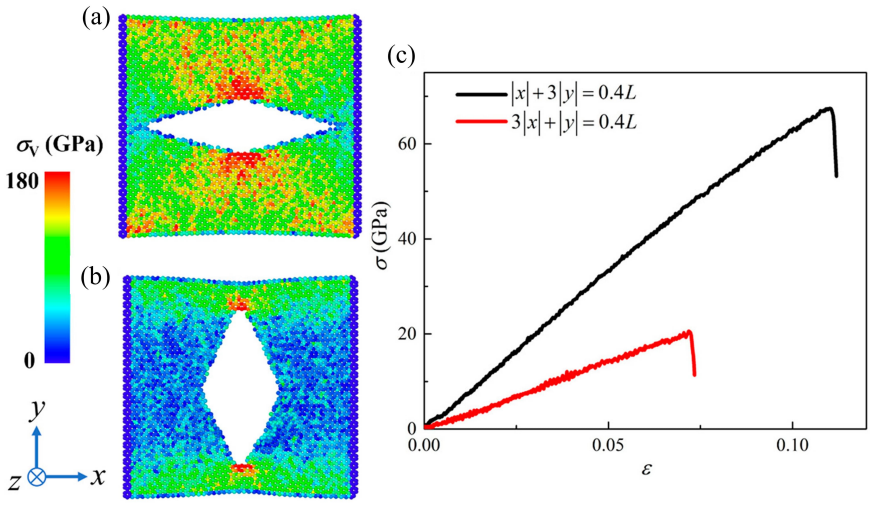

Figure 2.29: Simulation results of graphene sheets with a centered diamond-shaped defect. Stress distributions of graphene sheets with diamond-shaped defects parametrized by (a) $|x| + 3|y| = 0.4L$ and (b) $3|x| + |y| = 0.4L$. (c) Stress–strain curves of above two defective graphene sheets.

Table 2.1: Equation and derived dichotomizing points of high/low stress regions of circular, elliptical, quadratic polynomial-shaped and sine-shaped defects, where the applied strain ε is included.

Curve type	**Equation**	**Dichotomizing points**
Circle	$[x/(1+\epsilon)]^2 + y^2 = R^2$	$(\pm\frac{1}{(1+\varepsilon)\sqrt{1+(1+\varepsilon)^2}}R, \pm\sqrt{1-\frac{1}{1+(1+\varepsilon)^2}}R)$
Ellipse	$[x/(1+\epsilon)]^2/a^2 + y^2/b^2 = 1$	$(\pm\frac{a^2(1+\varepsilon)^2}{\sqrt{a^2(1+\varepsilon)^2+b^2}}, \pm b\sqrt{1-\frac{1}{1+[\frac{b}{a(1+\varepsilon)}]^2}})$
Quadratic polynomial	$y = b\{a^2 - [x/(1+\epsilon)]^2\}$	$(\pm\frac{(1+\varepsilon)^2}{2b}, \pm b[a^2 - \frac{(1+\varepsilon)^2}{4b^2}])$
Sine	$y = b\cos\{\frac{\pi}{2a}[x/(1+\epsilon)]\}$	$(\pm\frac{2a(1+\varepsilon)}{\pi}\sin^{-1}[\frac{2a(1+\varepsilon)}{\pi b}], \pm b\sqrt{1-\frac{4a^2(1+\varepsilon)^2}{\pi^2 b^2}})$

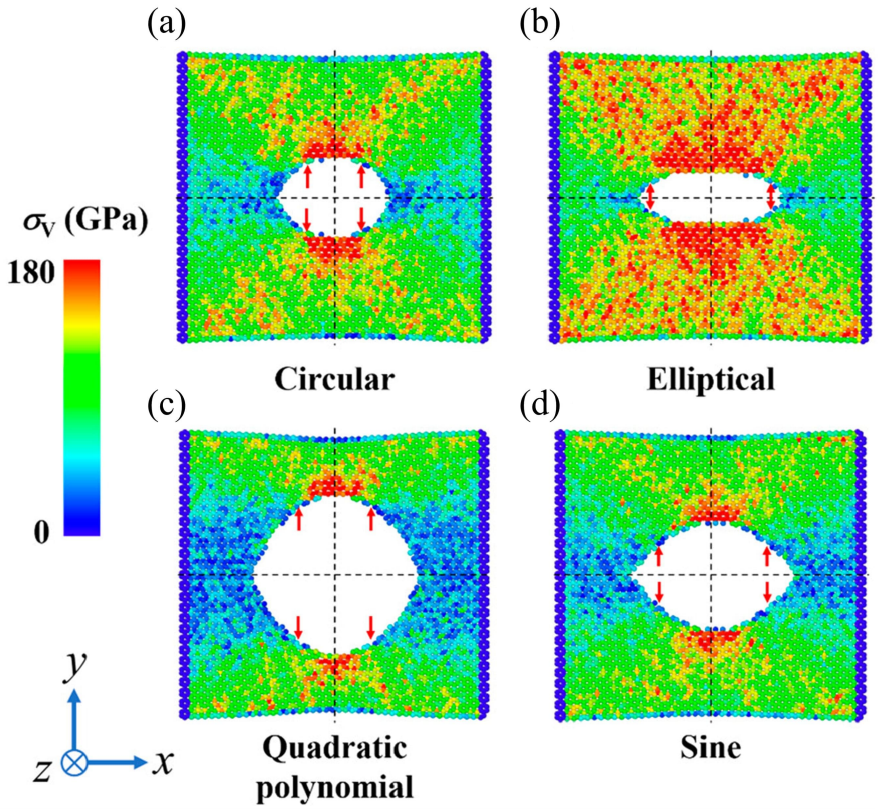

Figure 2.30: Comparisons between predicted dichotomizing points and simulation results of graphene sheets with a (a) circular defect, (b) elliptical defect, (c) quadratic polynomial-shaped defect, and (d) sine-shaped defect.

defect show that high-stress regions are located at the farthest ends of the defect transverse to the stretch. When multiple defects are present, this conclusion still holds by applying the strategy of defect grouping. When defects have overlaps transverse to the stretch, they can be viewed as a group and the farthest ends of the defect group localize high-stress regions. In Fig. 2.31(a), stress fields of graphene sheets with two rectangular defects with overlaps transverse to the stretch are illustrated, one with rectangular defects of different sizes ($(0.1L, 0.4L)$ and $(0.1L, 0.6L)$) and the other with two identical defects (both $(0.1L, 0.4L)$). The geometric centers of two defects are aligned on the center line parallel to the stretch and trisection of the graphene sheets. As can be seen, high-stress regions reside at the farthest ends of the defect group transverse to the stretch. For the graphene sheet with defects of different sizes, the ends of the smaller defect do not concentrate stress, while both ends of the larger defect do. For the graphene sheet with identical defects, both defects concentrate stress at their two ends; thus, in this case, high-stress regions are significantly larger, an indicator

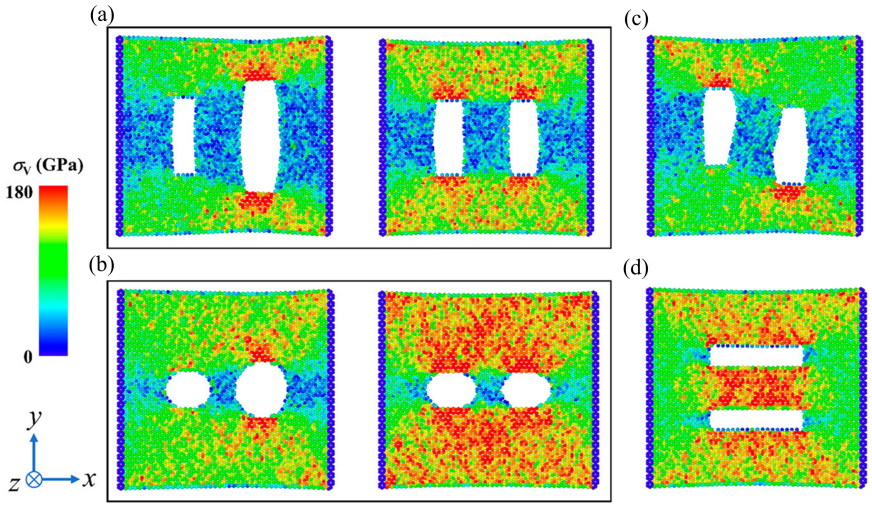

Figure 2.31: Stress fields of graphene sheets with two defects. Graphene sheets with two (a) rectangular and (b) circular defects aligned on the center line parallel to the stretch. (c) Graphene sheet with two identical rectangular defects but not aligned on the center line parallel to the stretch. (d) Graphene sheet with two identical rectangular defects with no overlap transverse to the stretch.

of a more uniform stress distribution. The same principle applies to circular defects, as is shown in Fig. 2.31(b), where the diameters are $0.2L$ and $0.3L$ for the graphene sheets with circular defects of different sizes and $0.2L$ for two identical defects. Also, by this principle, it is possible that only one end of a defect localizes high stress instead of both ends or no end. To showcase this, a graphene sheet with two identical defects (both $(0.1L, 0.4L)$) not aligned on the center line are simulated. Each defect has an offset of $0.05L$ from the centerline but in the opposite directions. The stress field in Fig. 2.31(c) shows that high-stress regions are located at the two farthest ends of the defect group, which in this case takes on one end from each of the two defects. When multiple defects have no overlaps transverse to the stretch and do not form a defect group, each defect affects the stress field independently. Fig. 2.31(d) presents the case of two identical rectangular defects (both $(0.1L, 0.4L)$) having no overlaps transverse to the stretch. As can be seen, both defects produce two high-stress and two low-stress regions. However, it is noteworthy that, due to the potential overlaps of high-stress regions by individual defects, some parts of the stress field can be double-strengthened, such as in between the two defects in Fig. 2.31(d). The stress–strain curves of defective graphene sheets are provided in Fig. 2.32.

From Fig. 2.31(b), it can be seen that a relatively small modification of defects can make a profound difference to the stress field, where the stress field is much more uniform when two identical defects are present. This inspires the optimization of the stress field by placing defects in the right locations. As a preliminary exploration, mechanical properties

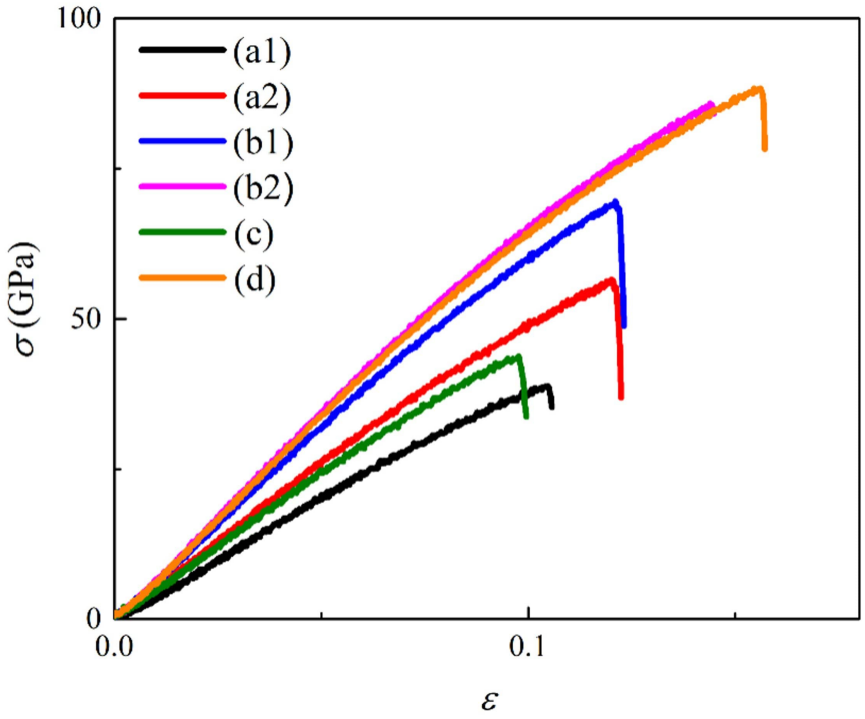

Figure 2.32: Stress-strain curves of defective graphene sheets with multiple defects in Fig. 2.31.

of graphene sheets with N identical circular defects aligned on the centerline parallel to the stretch are studied. The defect diameter is $0.2L$ and $N = 1, 2, 3$. Stress fields of graphene sheets with one, two, and three circular defects are shown in Figs. 2.33(a–c), respectively. It can be observed that, as the number of defects increases, the stress field becomes more and more uniform. Corresponding stress–strain curves of these graphene sheets are compared in Fig. 2.33(d). It is shown that the ultimate strength and strain can be stably enhanced with the increasing defect number even if more and more atoms are removed from the graphene sheet. It is worth mentioning that what dominates this strengthening effect is not a particular parameter such as defect size, shape, number, and alignment. Rather, it is how a more uniform stress field can be created by defect design. Adding identical defects parallel to the stretch is one way but not the only way to create a more uniform stress field. Also, this application has illustrated the potential of enhancing the mechanical properties of graphene by optimizing defects. This result is found to be consistent with classical mechanics. For a plate with a row of collinear holes, it is shown by boundary element methods that the maximum circumferential stress along the central hole decreases with an increasing number of holes [174]. This indicates a reduced stress concentration around stress raisers and an

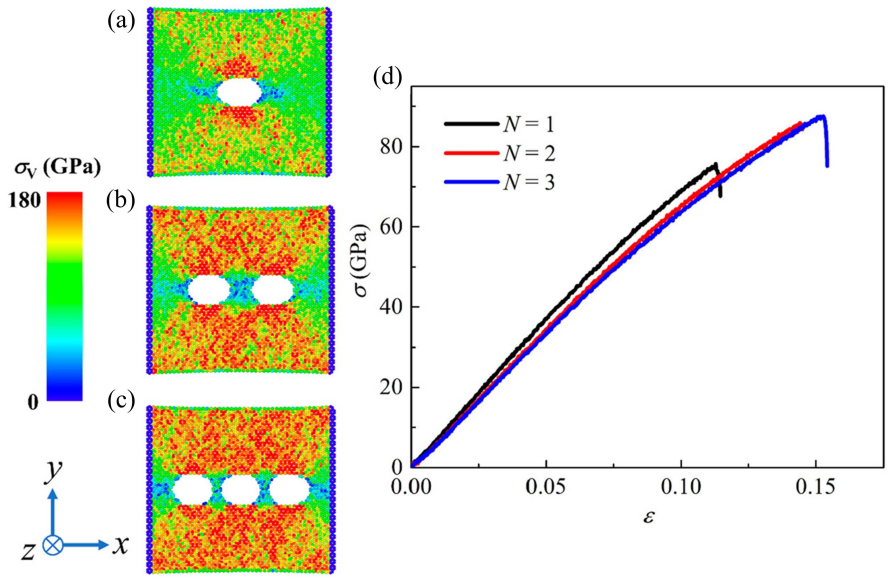

Figure 2.33: Simulation results of graphene sheets with N circular defects aligned in the stretching direction. Stress distributions for (a) $N = 1$, (b) $N = 2$, and (c) $N = 3$. (d) Stress–strain curves for $N = 1$–3.

enhanced collective mechanical property, which is observed in our results. In addition, the results of classical mechanics also show that as the number of holes increases, the decrease of the maximum stress slows down and the stress approaches an asymptotic solution [71]. The same tendency is shown in our simulation with an increasing number of collinear circular defects. Several important conclusions are the same across a broad range materials, scales, and numerical methods. Hence, it is envisioned that this enhancing effect can be extended to other 2D materials.

Discussion

Having studied a broad variety of defects as well as their combinations featured by a wide spectrum of mechanical properties, up to this point, it is necessary to summarize all the results and interesting to check if these different defect configurations share any underlying common ground. The mechanical properties of all defective graphene sheets in the present study are summarized in σ_u-ε_f plots in Fig. 2.34, where ε_f denotes the failure strain. Fig. 2.34(a) presents the results of graphene sheets with a single defect. Results of mechanical enhancement by increasing defect number in Fig. 2.33 are also included to illustrate the evolution path starting from a single circular defect to multiple identical collinear defects. The data point of the pristine graphene is also provided in Fig. 2.34(a) for reference, as is marked with the star symbol. As can be seen, despite the difference in defect geometry,

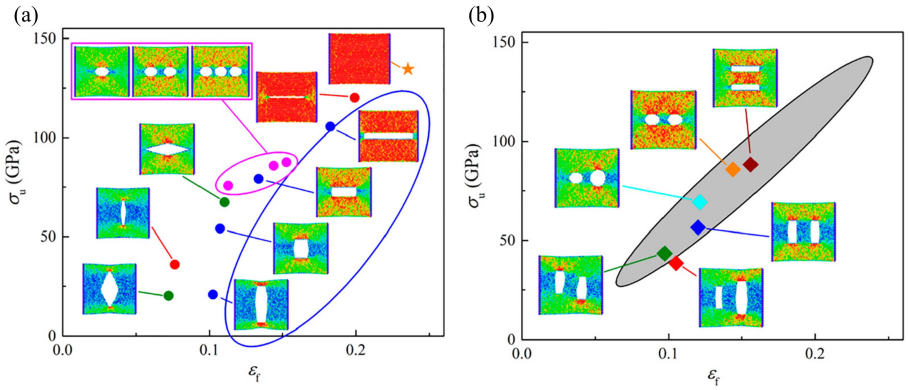

Figure 2.34: σ_u-ε_f plots summarizing mechanical properties of all the defects studied. Graphene sheets with (a) a single defect and (b) multiple defects. The gray area in (b) represents the distribution of data points in (a).

all results lie within a narrow-banded region, with no exception of the pristine graphene sheet. This suggests that the variation of defect geometry, though resulting in drastically different mechanical properties, in general preserves the proportionality of ultimate strength and failure strain. Graphene sheets with multiple defects are summarized in Fig. 2.34(b). The gray region represents the banded region in Fig. 2.34(a) which embodies the proportionality. As can be seen, results of various configurations of multiple defects still lie within the banded region, suggesting that the proportionality is one of the underlying common grounds of various defective graphene sheets (including the pristine graphene sheet).

Another way of a summary is to plot mechanical properties such as ultimate strength against parameters, which can help shed light on the relative significance of system parameters by examining the relevancy and distribution pattern. Here, σ_u as a function of $L_\parallel$ and $L_\perp$for all defect shapes and configurations in the present paper as well as in our previous work [218, 220] is investigated, as summarized in Fig. 2.35. In Fig. 2.35(a), no outstanding correlation between $L_\parallel$ and σ_u is exhibited and Pearson's correlation coefficient r is 0.213, indicating that $L_\parallel$ may not be a governing factor of mechanical properties of defective graphene sheets. Contrarily, the banded distribution in Fig. 2.35(b) shows a strong correlation between $L_\perp$ and σ_u, with an r value of -0.933. Therefore, $L_\perp$ is a much more dominant parameter than $L_\parallel$. In addition, Fig. 2.35(b) is able to give a strong indication on the relative significance of size effect and shape effect, where the latter can be reflected by the width of the banded distribution under a certain $L_\perp$ value. It is noteworthy that, at a given $L_\perp$, rectangular defects possess higher σ_u than elliptical defects.

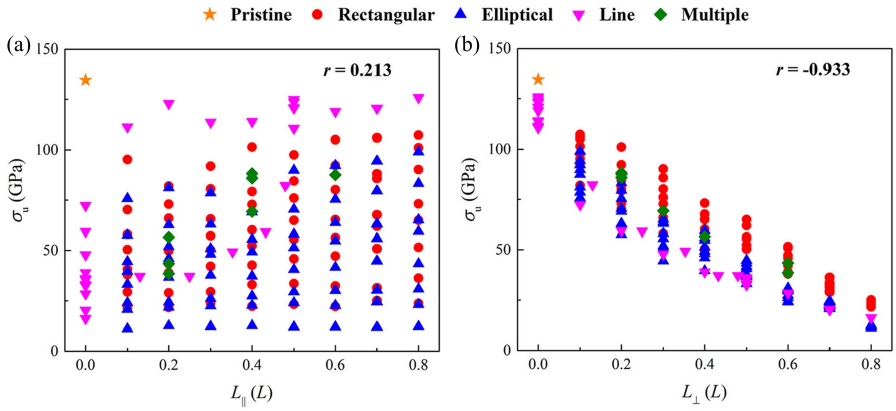

Figure 2.35: Influences of $L_{\parallel}$ and $L_{\perp}$ on the ultimate strength σ_{u} of the defective graphene sheet. σ_{u} as a function of (a) $L_{\parallel}$ and (b) $L_{\perp}$. Data points of elliptical and line defects are from refs [218] and [220].

Conclusion remarks

In this section, stress field characteristics of defective graphene sheet subject to unidirectional in-plane stretch are studied via MD simulation. It is shown that stress distribution is strongly dependent on defect properties, which ultimately impacts collective mechanical properties such as strength and ductility. The out-of-plane degree of freedom can be released by the introduction of defects and the relationship between stress distribution and displacement patterns are revealed. The effect of defect geometry can be decoupled by studying defect size and shape, where the former determines the area shielded from increasing stress and consequently produces low-stress regions, while the latter determines local stress concentration and governs stress distribution along the defect rim. An analytical approach is developed to pinpoint the dichotomizing points on the defect rim, which shows good agreement with the results of MD simulations. The strategy of defect grouping is proposed to analyze the stress field when multiple defects are present in the graphene sheet. Knowing the relation between defect properties and stress distribution characteristics, the optimization of mechanical properties can be achieved by rational defect design. In addition, it is shown that even though the mechanical properties of defective graphene sheets vary with different defect geometry, the proportionality of ultimate strength and failure strain is in general preserved. Finally, the relative significance of the system parameters is discussed. This paper has systematically discussed the influence of defects on the stress distribution in graphene sheets, which opens up the tuning approach of the mechanical properties of graphene as well as other 2D materials via defect engineering. A major contribution of the present work is the incorporation of variable defect presentations into the feature of the stress field only, which enables us to evaluate the collective properties and pinpoint regions prone to fracture of defective graphene a priori [219].

Chapter 3

Machine learning for graphene-based materials

3.1 Graphene defect detection

During the growth and processing of graphene the existence of defects is almost inevitable, which can compromise the expected performances of graphene-based nanodevices. Much research has been underway to understand the effect of defects on specific graphene properties [182, 220, 5, 209, 218, 219, 110, 42]. Given the defect information such as size, location, and density, the properties of a defected graphene can be evaluated. Nevertheless, obtaining detailed defect information at atomic resolution is a difficult task. Ideally, defects such as vacancies can be discovered by examining the atomic structure of a graphene sheet. Despite some experimental successes using high-resolution transmission electron microscopy (TEM) [74, 60, 134], it remains technically challenging and involves complex sample preparation procedures to obtain an image of graphene at an atomic resolution. As a result, a method to reliably detect unknown graphene defects without using atomic-resolution probes is appealing.

Compared to elliptical holes and cracks which can be shed light on using traditional fracture mechanics, randomly distributed atomic vacancies have a much more implicit but not necessarily less profound impact on the mechanical properties of graphene. Emerging ML approaches offer solutions for learning patterns from complex data and have been extensively applied in material design and discovery problems [18, 24, 148, 23, 142, 192, 213, 115]. The power of ML-based approaches can be fully utilized with a rational selection of features. In this problem, because the defect location is a local feature (instead of a global feature), data need to be constructed with observations possessing local information. Collective properties such as strength or strain to failure may not be suitable here, because defects at different locations can produce the same result, making these defect locations indistinguishable [220]. One of the simplest observations with local features is the thermal vibration at room temperature with all edges of the graphene sheet clamped, which does not require

specific actuations or precise environment controls. Previous research has investigated the effect of defects on the vibrational properties of graphene via various technical approaches such as MD simulation [114, 161, 162], continuum elasticity theory [161, 120, 163], and Monte Carlo-based finite element method [34]. The local amplitudes of thermal vibrations can be affected when surrounded by defects, because the absence of atoms changes the local boundary conditions of mini-oscillators. Experimentally, to obtain a vibration topography that has a lower resolution than atomic resolution is less taxing than obtaining an image of atomic structures. Low-amplitude mechanical vibrations of graphene can be readily imaged using a scanning force microscope [58]or an interferometry [16].

In this section, an ML strategy is proposed to detect unknown defects in single-layer graphene sheets to overcome the complicated relationship between thermal vibration topographies and defect locations. Trained by tens of thousands of thermal vibration topographies calculated by MD simulations, the ML model is used to predict defect locations. From predicting a single-atom vacancy to predicting an unknown number of vacancies with an arbitrary distribution, a kernel ridge regression (KRR) model addresses problem by progressively building up the model complexity while maintaining the computational cost. Finally, an optimal model with the best prediction capability can be obtained by an extensive hyperparameter tuning.

Methods

Molecular modeling

The thermal vibrations of single-layer graphene sheets are computed by MD simulations using LAMMPS and the AIREBO potential. Periodic boundary conditions are applied to two in-plane dimensions, and a fixed boundary condition is used in the orthogonal out-of-plane dimension. The box size is $D_x \times D_y \times D_z = 70$ Å $\times 70$ Å $\times 25$ Å, where D_x, D_y, D_z are the lengths of the box in x, y, z directions, respectively. The integration time step is 1 fs. An ensemble of random velocity at $T = 300$ K is generated throughout the graphene sheet. Graphene sheets are firstly relaxed in the NVT ensemble at $T = 300$ K for 10 ps. Then, the simulation is run in the NPT ensemble at the same temperature for 30 ps for graphene sheets to vibrate. The sampling frequency of atom displacement is 20 THz. The size of vacancy-containing graphene sheets is $L_{\mathrm{Z}} = 52.1$ Å by $L_{\mathrm{A}} = 44.8$ Å, where L_{Z} and L_{A} denote the zigzag and the armchair dimensions, respectively. The graphene sheet consists of 966 atoms when defect-free. To enforce the boundary conditions, a 3-atom-wide stripe on each edge is set fixed by eliminating all degrees of freedom of the associated atoms, while the rest of the graphene sheet, composed of 38 rows and 19 columns of atoms, is free to vibrate. This boundary control resembles the experimental setup in Ref. [58], where the graphene sheet is clamped and suspended to vibrate with no substrate involved. Simulation temperature is chosen as the room temperature $T = 300$ K, which requires the least temperature control in a potential experimental setup and can produce a sufficient vibration intensity. A location in the graphene sheet is indexed as (i, j), where i and j represent the ith row and the jth

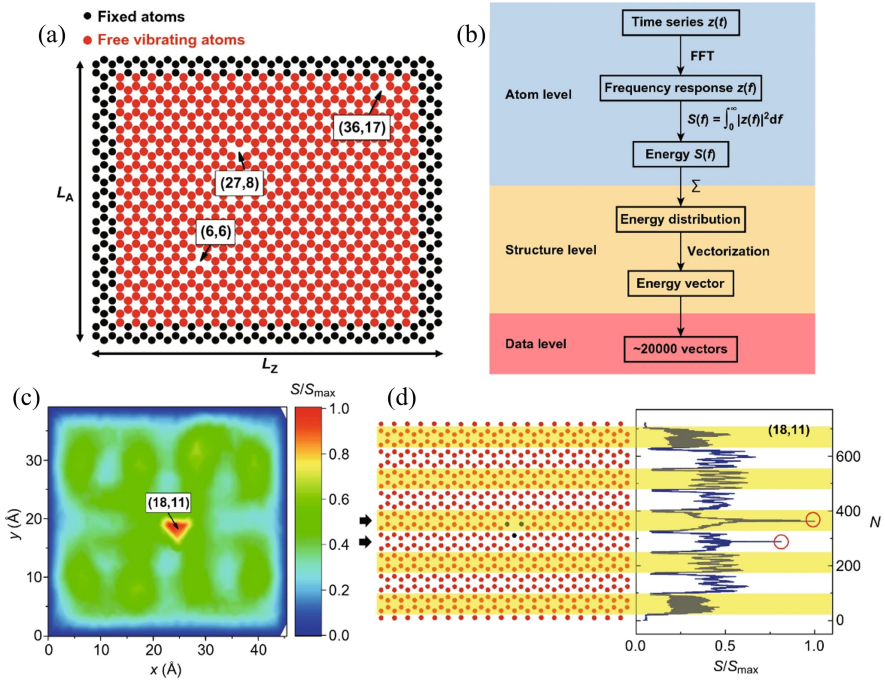

Figure 3.1: Descriptions of graphene sheets with vacancies and the procedure of data preparation. (a) Schematic of the defected graphene sheet and vacancy indexing, where a graphene sheet containing vacancies (6,6), (27,8), and (36,17) is used as an example. (b) Route of data preparation. (c) 2D energy distribution of graphene sheet with a vacancy (18,11), fixed atoms on the edges are not included in the contour plot. (d) 1D energy vector compressed from the 2D energy distribution and its correlation with the original graphene lattice.

column, respectively. A vacancy can be referred to by the index of the location where an atom is missing. The size and the boundary conditions of graphene sheets, and the strategy of location indexing are illustrated in Fig. 3.1(a). The easily satisfied loading conditions make both numerical and experimental approaches promising. For a pristine graphene sheet of this size and subject to the same boundary conditions, the amplitude of vibration is ~ 0.3 Å, which agrees well with quantitative results in Ref. [57].

Data preparation for machine learning

Training and testing data for ML implementations are prepared and organized into the following three levels: atom level, structure level, and data level. On the atom level, the time series of the out-of-plane displacement $z(t)$ of each atom is firstly computed. Then, a fast Fourier transformation is performed on $z(t)$ to obtain the frequency response $z(f)$. Next, the vibrational energy is calculated by $S(f) = \int_0^\infty |z(f)|^2 df$, as a scalar to featurize

each atom. Onto the structure level, an energy distribution throughout the graphene sheet is obtained by associating the energies of all atoms with their coordinates. Next, the 2D energy distribution is compressed to a 1D energy vector for the ML implementation. The energy vectors are based on atom indices, and the coordination information is suppressed. Finally, onto the data level, a total of near 20,000 energy vectors are prepared as the ML data and are assembled into a design matrix. The above procedure of data preparation is shown in the flowchart in Fig. 3.1(b).

Among all presentations, the 2D energy distribution offers the best visualization. An example is provided in Fig. 3.1(c), where the graphene sheet hosts a single-atom vacancy $(18, 11)$. As can be seen, the energy distribution is highly dependent on the location of vacancy: the vibrational energy tends to localize at defected regions. However, it is noteworthy that around the vacancy is not the global energy maximum, but a local maximum. The existence of vacancies creates additional local energy maxima off the energy distribution of pristine graphene, as shown in the examples in Fig. 3.2. An energy vector compressed from the previous 2D energy distribution is illustrated in Fig. 3.1(d), where the atom is indexed as $N = 19(i - 1) + j$. The energy vector reveals that one single-atom vacancy can produce not one but multiple characteristic spikes, which is not the most obvious in the 2D energy distribution. In addition, energy vectors, though less intuitive compared to energy distributions, offer another perspective and can be correlated with the original graphene structure. Considering each hexagonal ring of atoms as a unit, the graphene sheet can be divided into 9 rows of rings (RoRs) (the first and the last rows of atoms excluded). Each RoR is represented by a hump on the energy vector. Atoms surrounding the vacancy give rise to spikes on the humps that these atoms are associated with. For example, rows that are marked by two arrows in Fig. 3.1(d) are affected by the vacancy $(18, 11)$, hosting characteristic spikes. Atoms next to the fixed boundary exhibit low vibrational energy, as is the case for the first and the last row of atoms. Nevertheless, a vacancy in these atoms can still stimulate spikes, of which an example is provided in Fig. 3.3. This enables the ML approach to also predict vacancies next to the clamped edges.

Results

Atom-based prediction for single-atom vacancy

The prediction of a single-atom vacancy, as the simplest case for the vacancy prediction, is studied first. The construction of energy vectors (featurized sample points) and label vectors is based on atom indices. The length of the energy vector is $722 - 1 = 721$ because of the one missing atom. All entries indexed after the missing atom need to be shifted accordingly. For example, if the 100th location corresponds to a vacancy, the energies of 101st to 722nd atoms are 100th to 721st entries of the energy vector. Label vectors are one-hot encoded, the length being the total number of possible atom locations. For example, if the mth location is a vacancy while others are occupied by atoms, the mth entry is 1 while other entries are 0's. Despite that one-hot labels often work well with classification models, in

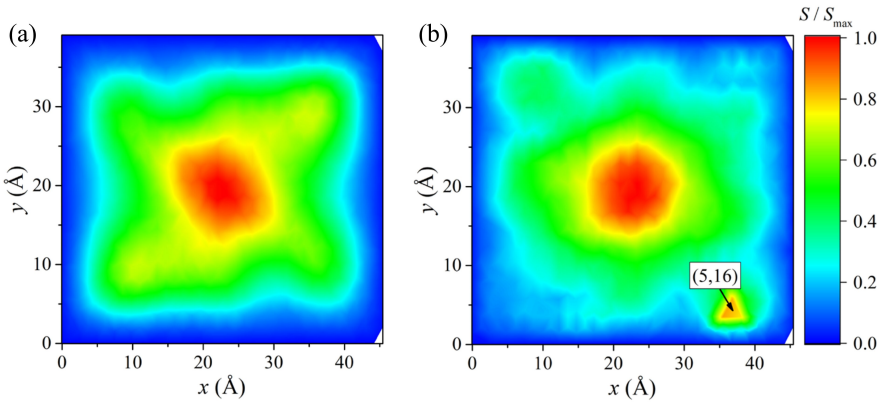

Figure 3.2: 2D energy distributions of (a) a pristine graphene sheet and (b) a graphene sheet with a vacancy (5, 16).

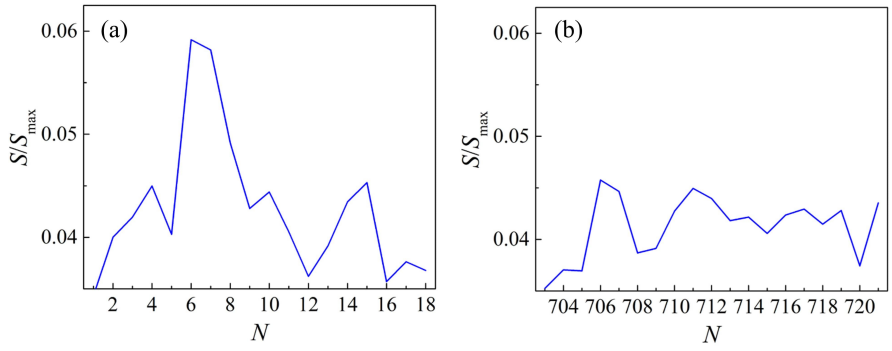

Figure 3.3: Portions of energy vector corresponding to (a) the first row and (b) the last row of atoms. The graphene sheet here contains a single vacancy at (1,10), which lies on the first row of atoms.

this study they become infeasible due to the excessively many classes. For the scenario of a single-atom vacancy, the number of classes totals 722 (38 rows $\times$ 19 columns). For up to 10 vacancies, the number of classes grows to $\sum_{r=1}^{10} C_r^{722} \simeq 1.01 \times 10^{22}$, which goes far beyond realistic. Hence, a regressor is used to map energy vectors to one-hot labels. KRR model is selected to predict locations of vacancies, which enables us to progressively build up the model complexity without adding to the computational cost (the kernel trick). Hyperparameters include polynomial kernel degree p and regularization parameter λ. Algorithmic details of KRR are provided in Alg. 1.

Algorithm 1 Kernel ridge regression

1: Normalize each energy vector $\mathbf{x}$ with its $\mathcal{L}_2$ norm, $\mathbf{x} \leftarrow \mathbf{x}/\|\mathbf{x}\|_2$.
2: Center each energy vector $\mathbf{x}$ with the mean of all energy vectors $\boldsymbol{\mu} = \frac{1}{n}\sum_{i=1}^{n} \mathbf{x}_i$, $\mathbf{x} \leftarrow \mathbf{x} - \boldsymbol{\mu}$.
3: Objective function $J(W) = \|XW - Y\|^2 + \lambda\|W\|^2$, where $X = [\mathbf{x}_1 \cdots \mathbf{x}_n]^T$ is the design matrix; W is the weight matrix; $Y = [\mathbf{y}_1 \cdots \mathbf{y}_n]^T$ is the label matrix.
4: Normal equations $(X^TX + \lambda I)W = X^TY$.
5: Write W as a linear transformation of sample points $W = X^TA$, where A is the dual weight matrix.
6: Objective function rewritten as $J(A) = \|XX^TA - Y\|^2 + \lambda\|X^TA\|^2$.
7: Normal equations rewritten as $(X^TX + \lambda I)A = Y$.
8: The polynomial kernel of degree p is $k(\mathbf{q}_1, \mathbf{q}_2) = (\mathbf{q}_1^T\mathbf{q}_2 + 1)^p$.
9: Construct kernel matrix K, $\forall i, j, K_{ij} \leftarrow k(\mathbf{x}_i, \mathbf{x}_j)$.
10: Solve $(K + \lambda I)A = Y$ for A
11: Predict labels for the design matrix of test data $Z = [\mathbf{z}_1 \cdots \mathbf{z}_{n'}]^T$ ($\mathbf{z}_{n'}$'s are normalized, centered testing energy vectors), $\hat{Y} = [\hat{\mathbf{y}}_1 \cdots \hat{\mathbf{y}}_{n'}]^T = h(Z) = K'A$, where $K'_{ij} = k(\mathbf{z}_i, \mathbf{z}_j)$

Because there are in total 722 possible locations that are candidates to host a single-atom vacancy, to achieve an effective training process, all these possible locations need to be visited. Therefore, a total of 722 different configurations need to be simulated to survey all scenarios of the single-atom vacancy. Structured as the energy vector in Fig. 3.1(d), results of 23 sets of 722 configurations ($722 \times 23 = 16606$ energy vectors in total) are prepared as data. The only difference between sets is the seed of random number generator of initial velocities, which ensures the data free from duplication or being a linear combination of any other data sets; 22 sets of data are used for training and validation, which, after random shuffling, are split into 80% for training and 20% for validation. An individual data set is set aside for testing. It is critical that the test data are not from shuffling and splitting from a large data set, but completely new, unseen data. A good performance on the test data can indicate promising extrapolation into future new sample points.

To illustrate, an energy vector from the test set, normalized by its maximum entry value $S_{\max}$, is shown in Fig. 3.4(a). The outstanding spike indicates that the vacancy potentially resides in its vicinity. The predicted label vector $\hat{\mathbf{y}}$ from the energy vector is shown in Fig. 3.4(b), where $v = \arg\min_{N\in\{1,2,\ldots,722\}} |\hat{y}_N - y_N|$ is to be returned as the predicted vacancy

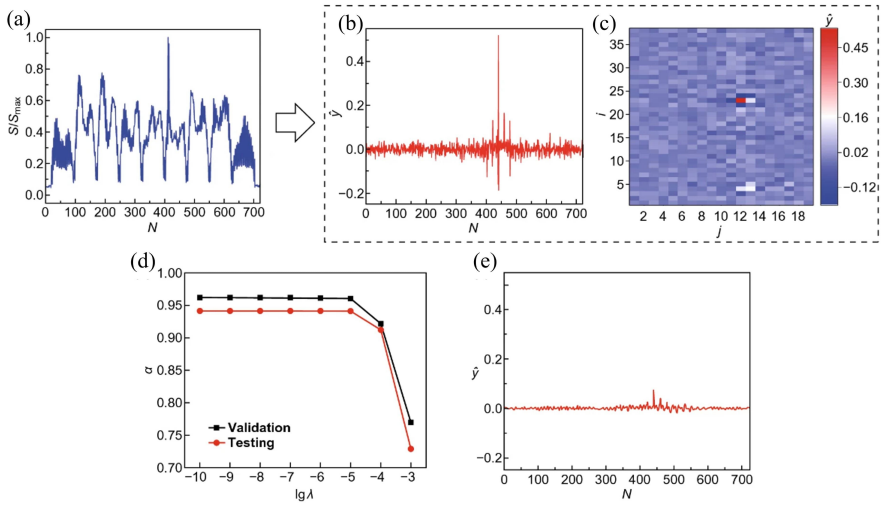

Figure 3.4: Results of the atom-based ML prediction for a single-atom vacancy. (a) An example of energy vector from the test data. (b) Predicted label vector. (c) 2D presentation of the predicted label vector. (d) Validation and testing accuracies as a function of regularization parameter λ. (e) Predicted label vector under a relatively strong regularization $\lambda = 10^{-3}$.

location. To retrieve a better intuition from the prediction, $\hat{\mathbf{y}}$ is converted to 2D, as is shown in Fig. 3.4(c) where the predicted vacancy location stands out. Prediction accuracies α on the validation and the test data, as a function of regularization parameter λ, are shown in Fig. 3.4(d). For $\lambda < 10^{-5}$, the validation accuracy is above 95% and the testing accuracy lies slightly below 95%, indicating a highly effective ML prediction. For a stronger regularization, for example, $\lambda = 10^{-3}$, the validation and the testing accuracies drop down to below 80% and 75%. Fig. 3.4(e) shows the predicted label vector when $\lambda = 10^{-3}$. Although the noise level gets suppressed by a strong regularization, $\hat{y}_v$ becomes less preeminent, which explains the lowered prediction accuracies. Because both the validation and testing accuracies converge as λ decreases, for this problem the ML model is not subject to high variance-related issues.

Domain-based prediction for multiple vacancies

The atom-based method, despite a high prediction accuracy on the test set, becomes infeasible to predict multiple vacancies of an unknown quantity or density. This is because the length of energy vectors $722 - n_{\mathrm{V}}$ is no longer a constant, where n_{V} is the number of vacancies. More importantly, the atom-based method still requires counting atoms, which is not viable without an atomic-resolution probe. To circumvent this issue, an approach based on domain discretization is proposed, aiming to predict subdomains that contain one or more vacancies instead of the locations of missing atoms. The domain of free vibrating

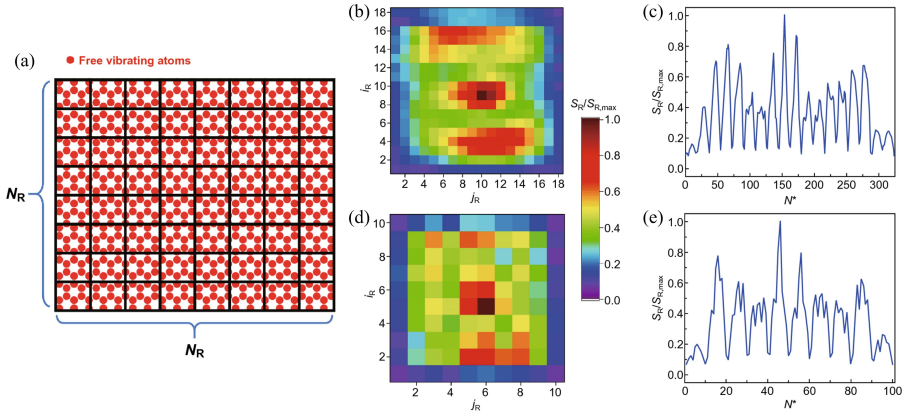

Figure 3.5: Domain discretization of a graphene sheet. (a) Schematic of an N_{R}-by-N_{R} uniform domain discretization. (b) 2D energy distributions by 18-by-18 discretization converted from the atom-based energy vector in Fig. 3.4(a). (c) 1D energy vector compressed from 18-by-18 discretization in (b). (d) 2D energy distribution of 10-by-10 discretization converted from the atom-based energy vector in Fig. 3.4(a). (e) 1D energy vector compressed from 10-by-10 energy discretization in (d).

atoms is discretized into N_{R}-by-N_{R} uniform subdomains, as shown in Fig. 3.5(a). Similar to the indexing strategy of the atom-based method, the index of a subdomain can be expressed as $N^* = (i_{\mathrm{R}} - 1)N_{\mathrm{R}} + j_{\mathrm{R}}$, where i_{R} and j_{R} are the row index and the column index of a particular subdomain. Furthermore, when the size of the subdomains is substantially small, an atomic-resolution prediction can be approached. Notably, the domain-based method is computationally cheaper compared to the atom indexing-based method. For instance, for a graphene sheet with 722 freely vibrating atoms, the atom-based method renders each sample point $722 - n_{\mathrm{V}}$ features. For domain-based method, the number of features is N_{R}^2 (for a 14-by-14 discretization, the number of features is $14^2 = 196$), thus achieving a dimensionality reduction by a multiple of $722/N_{\mathrm{R}}$. Label vectors are one-hot encoded based on subdomains instead of atom indices, length being N_{R}^2: if the sth and tth subdomains contain a vacancy, the sth and tth entries of the energy vector are 1's while the other entries are 0's. Unlike the atom-based method, no index shift is involved.

As a sanity check, the same data used for the atom-based method are discretized and used to test the domain-based method: a good performance on the single-atom vacancy scenario must be achieved in order to proceed into predicting unknown multiple vacancies. To illustrate, the atom-based energy vector in Fig. 3.4(a) is converted to a domain-based energy vector. Figs. 3.5(b) and (c) shows 2D and 1D presentations of the domain-based sample points with an 18-by-18 discretization, while Figs. 3.5(d) and (e) corresponds to a 10-by-10 discretization. Energy vectors of the domain-based method have less obvious characteristic spikes compared to the atom-based counterpart, making defected regions almost indiscernible

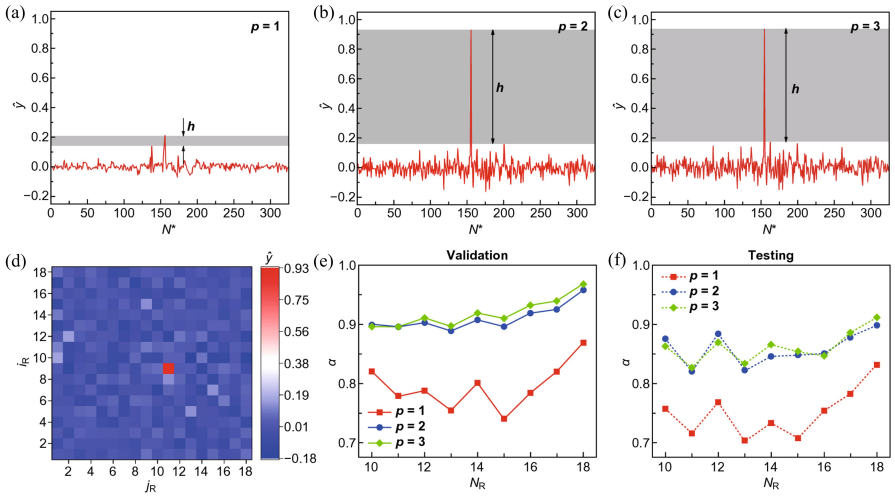

Figure 3.6: ML predictions of a single-atom vacancy with domain discretization. (a–c) Predicted label vectors on an 18-by-18 discretization with kernel degrees 1, 2, and 3, respectively. The margin h is illustrated by the gray areas. (d) 2D presentation of the predicted label vector of kernel degree 2. (e) Validation and f testing accuracies with kernel degrees $p \in \{1, 2, 3\}$, as a function of N_{R}

by an "eyeball" test and potentially adding to the difficulty of prediction.

To quantify the robustness of prediction, a margin is defined as $h = \min_{N^* \in V} |\hat{y}_{N^*}| - \max_{N^* \notin V} |\hat{y}_{N^*}|$, where V is the set of indices of vacancy-containing subdomains. A large margin indicates that the model is less likely to confuse defected subdomains with pristine ones. λ is kept small, set as 10^{-10}. Input with the energy vector in Fig. 3.5(c), the predicted label vector of model with a linear kernel is shown in Fig. 3.6(a). Although $v = \arg\min_{N^* \in \{1,2,\ldots,N_{\mathrm{R}}^2\}} |\hat{y}_{N^*} - y_{N^*}|$ can still correctly return the defected subdomain, the margin becomes particularly small and $|\hat{y}_v - y_v|$ becomes large, making predictions less reliable. To reduce the bias, polynomial kernels of higher degree are implemented. The predicted label vectors of quadratic and cubic kernels are shown in Figs. 3.6(b) and (c). The margin is profoundly enlarged and $|\hat{y}_v - y_v|$ is sufficiently small for both cases, indicating a reliable prediction and a reduced bias. Little difference is observed between the predicted label vectors of quadratic and cubic kernels, indicating that a quadratic kernel already suffices to address the domain-based problem. A 2D presentation of the predicted label vector is provided in Fig. 3.6(d), as the most intuitive visualization. Validation and testing accuracies with kernel degrees $p \in \{1, 2, 3\}$, as a function of N_{R}, are summarized in Figs. 3.6(e) and (f). As can be seen, quadratic and cubic kernels, which have achieved accuracies over 90% on validation and over 80% on testing, are superior to a linear kernel. In addition, accuracies increase with larger N_{R}, i.e., finer discretization, despite some fluctuations in the testing accuracies. The effects of λ on the validation and the testing accuracies are provided in Fig. 3.7.

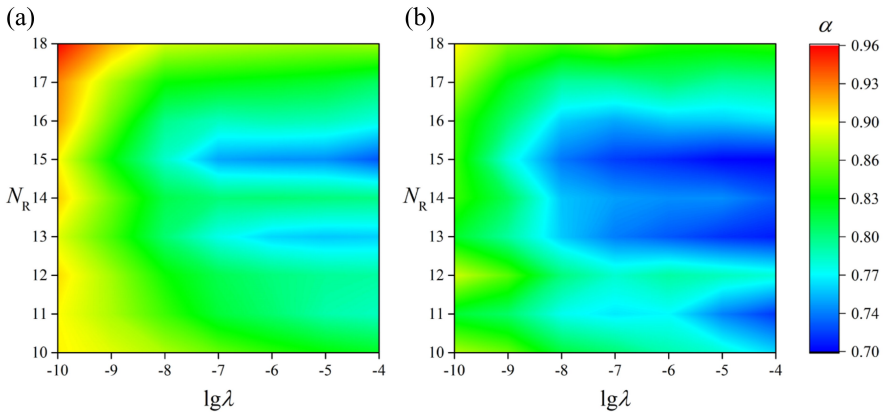

Figure 3.7: Effect of regularization on predicting a single-atom vacancy by the domain-based method. (a) Validation and (b) testing accuracies as a function of N_{R} and λ.

Having validated the domain-based method with predicting a single-atom vacancy, the model is used to predict locations of multiple vacancies with an arbitrary distribution. Data are prepared by the following way. The number of vacancies n_{v} is a random integer from 1 to 10. Specifically, $n_{\mathrm{v}} \sim \mathcal{U}(1, 10)$, where $\mathcal{U}(\cdot)$ denotes a uniform distribution. The index of each vacancy is a pair of random integers corresponding to all possible atom locations, i.e., $i_{\mathrm{R}} \sim \mathcal{U}(1, 38)$ and $j_{\mathrm{R}} \sim \mathcal{U}(1, 19)$. This vacancy generation algorithm naturally does not rule out the existence of vacancy clusters, which free us from the issue of distinguishing between vacancy clusters and individual single-atom vacancies if the prediction is successful. This property is especially advantageous when the defect information is unknown a priori in an experimental setting. A total of 19,438 domain-based energy vectors are prepared by MD simulation, of which 80%, 10%, and 10% are used as training, validation, and test data, respectively. Each graphene configuration has a different seed of random number generator for the vacancy setup. Each simulation case also has a different seed for initial velocities. Once again, training and validation data are shuffled together and split into two sets, while the test data are not involved in any shuffling and splitting to be used as new data. Because of the unknown number of vacancies, returning $\arg\min_{N^* \in \{1,2,\ldots,N_{\mathrm{R}}^2\}} |\hat{y}_{N^*} - y_{N^*}|$ or the indices of the k smallest $|\hat{y}_{N^*} - y_{N^*}|$ as the predicted subdomain indices is no longer feasible. To this end, a threshold parameter τ is introduced and the set of indices of predicted defected subdomains can be obtained as $V = \{v : \hat{y}_v > \tau\}$. λ is set as 10^{-10}. An example of energy vectors from the test data on an 18-by-18 discretization is shown in Fig. 3.8(a). Multiple spikes are exhibited, but there is no intuition which of these spikes imply subdomains that contain vacancies. The predicted label vector by a quadratic kernel and the true label vector are shown in Figs. 3.8(b) and (c), where a large margin is obtained. Given a threshold τ within the margin, the ML prediction returns 9 different subdomains that contain at least one vacancy, which are proved to be correct predictions by the true label vector in Fig. 3.8(c). 2D presentations of the

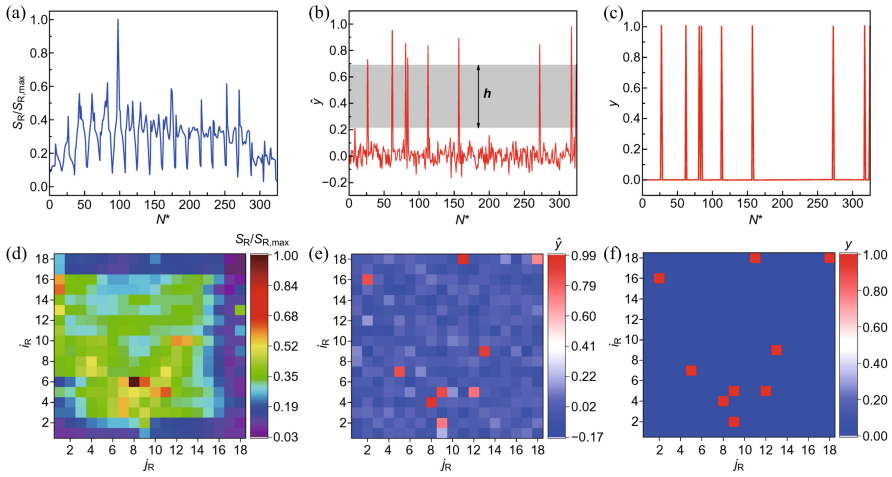

Figure 3.8: ML predictions of multiple vacancies with domain discretization. (a) An example of energy vectors from the test data. (b) Predicted label vector by a quadratic kernel from the energy vector in (a). (c) True label vector. (d–f) 2D presentations of (a–c), respectively.

input data point, prediction label, and true label are shown in Figs. 3.8(d–f), respectively, to offer a better intuition. For a sample point on the domain-based method, both 1D and 2D presentations have lost the ability to implicate locations of vacancies. However, the model can still discover the vacancies with high accuracy and reliability. Validation accuracies of kernel degree $p \in \{1, 2, 3\}$, as a function of N_{R} and threshold τ, are summarized in Figs. 3.9(a–c), respectively. A linear kernel becomes incapable to predict vacancy locations, of which the best accuracy is below 40% and is only attainable when subdomain size is sufficiently small (for example, $N_{\mathrm{R}} = 18$). However, for both quadratic and cubic kernels with an optimal τ^*, validation accuracies above 80% can be achieved for N_{R} values ranging from 10 to 18. As N_{R} increases, validation accuracy increases and τ^* can be chosen within a broader range centered at near 0.4. Testing accuracies of kernel degree $p \in \{1, 2, 3\}$, as a function of N_{R} and threshold τ, are shown in Figs. 3.9(d–f), respectively. Trends in general resemble validation accuracies, but with a lower magnitude overall. Finally, prediction accuracies on validation and testing with optimal threshold values τ^* are summarized in Figs. 3.9(g) and (h). As N_{R} increases, the validation accuracy approaches 100% and the testing accuracy approaches 90%, suggesting a potent performance of locating multiple unknown vacancies in graphene sheets. The effects of λ on the validation and the testing accuracies with $\tau = 0.4$ are provided in Fig. 3.10.

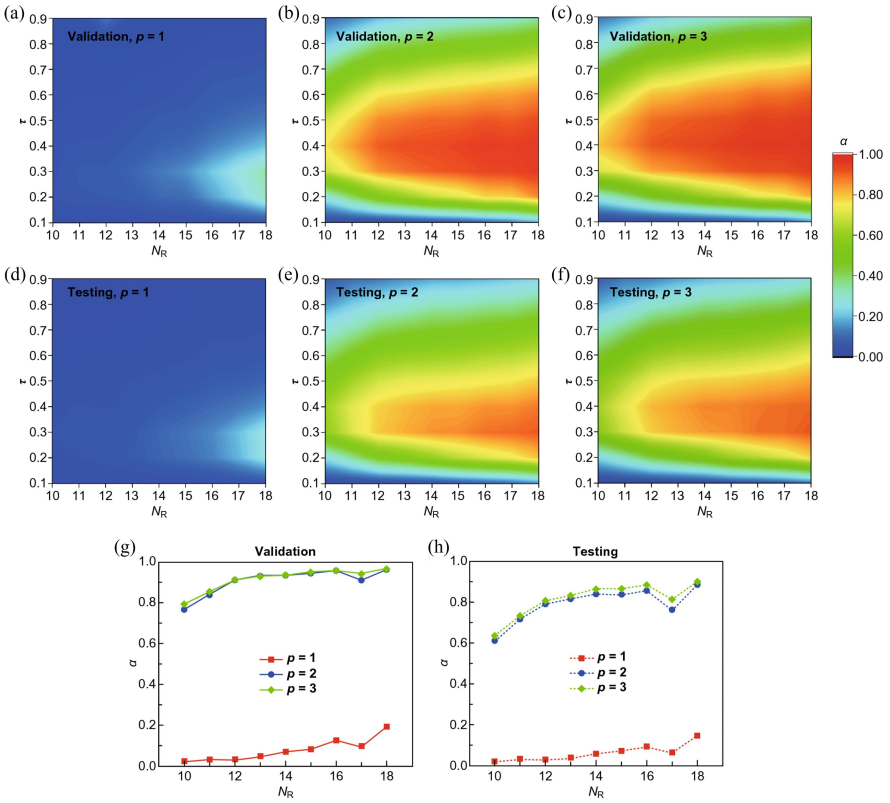

Figure 3.9: Parametric study and optimal performances of predicting multiple vacancies. (a–c) Testing accuracies of kernel degree $p \in \{1, 2, 3\}$, as a function of N_{R} and threshold τ. (d–f) Validation accuracies of kernel degree $p \in \{1, 2, 3\}$, as a function of N_{R} and threshold τ. (g) Validation and (h) testing accuracies as a function of N_{R} with optimal choices of τ^*.

Discussion

Both the atom-based and the domain-based methods can predict the locations of unknown vacancies with high accuracy. However, the latter is in general advantageous for multiple reasons. First, the domain-based method does not require an atomic-resolution probe, while the atom-based method does. Second, the domain-based method can predict an unknown number of vacancies, which makes it a more natural way to approach the problem. On the contrary, the atom-based method can only predict the vacancies of a known number, which poses an outstanding limit. Last but not least, the domain-based method enjoys cheaper computational cost and thus a faster training speed, due to the dimensionality reduction by discretization. Despite the fact that in order to achieve an over 90% prediction accuracy, the domain-based method requires at least a quadratic kernel while the atom-based method only needs a linear kernel, the kernel trick ensures that the computational costs of kernels

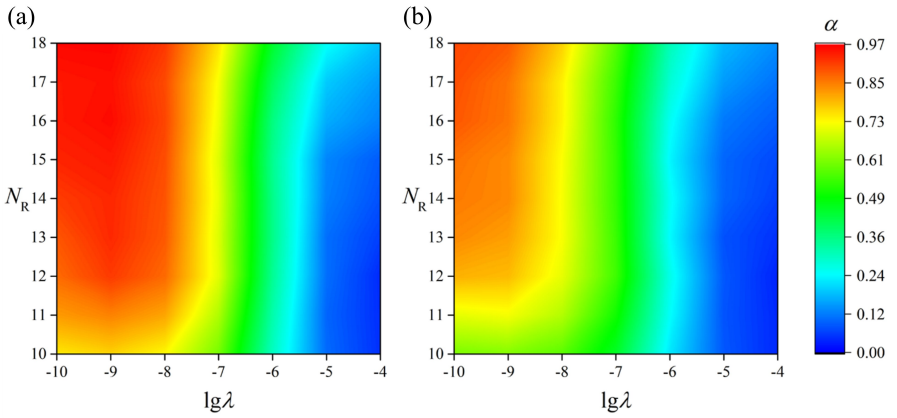

Figure 3.10: Effect of regularization on predicting multiple vacancies by the domain-based method. (a) Validation and (b) testing accuracies as a function of N_{R} and λ, with $\tau = 0.4$.

of different degrees are generally equal. These advantages make the domain-based method more practical than the atom-based method for applications of interest. In an experimental setting, graphene samples can be fabricated by mechanical exfoliation following Ref. [58], which are relatively free of contamination such as oxygen-containing functional groups. For graphene sheets contaminated by foreign functional groups, based on the presented method these functional groups can be treated as defects and can be potentially distinguished from atomic vacancies. Also, it is suggested that the contamination layer can be removed by a high temperature cleaning process in a H_2/Ar atmosphere, enabling measurements of the properties of contamination-free graphene sheets [40].

Concluding remarks

In this section, an ML approach to predict locations of unknown vacancies in graphene is presented. Thermal vibration properties at room temperature are used to featurize graphene sheets, which is shown to be effective to reveal the local vacancy information. Two prediction strategies are developed, an atom-based method which constructs data by atom indices, and a domain-based method which constructs data by domain discretization. Both strategies are based on the KRR algorithm, which allows us to progressively build up model complexity while maintaining the computational cost. While the atom-based method is capable of predicting a single-atom vacancy, the domain-based method can predict an unknown number of multiple vacancies with high accuracy. Both methods can achieve approximately a 90% prediction accuracy on reserved test data, indicating a good extrapolation into unseen new graphene configuration. A dimensionality reduction is also achieved by domain discretization. The proposed ML approach shows a prediction capability beyond analytical and numerical modeling and can be further enhanced by the improvement in quality and speed

of data generation. This strategy may also shed light on predicting defects of a broader variety, for instance, interstitials, dislocations, grain boundaries, among others [216].

3.2 Scalable graphene defect prediction

Previous section demonstrates the prediction of unknown graphene defects using ML. However, it requires the size of material systems used in training to be identical to the ones they predict. This limits its application in reality because an identical size of newly encountered materials is by no means guaranteed. It is thereby hoped that the effectiveness of ML models be transferable across size and shape to more broadly apply the techniques. In the context of graphene defect prediction, transferable ML will enable the prediction of differently sized or shaped graphene sheets trained by data of graphene sheets of a uniform size. In addition, due to the large size, directly simulating graphene used in actual applications can be rather computationally expensive, especially when a large amount of training data is demanded. Transferable ML will allow us to use smaller graphene as training data that are more computationally tractable. Hence, a transferable ML approach for defect prediction is very much desired.

In this section, a transferable learning strategy to detect unknown defects in larger graphene sheets using information obtained from a smaller graphene system is developed. Trained by tens of thousands of local vibrational energy distributions of smaller graphene sheets calculated by MD simulations, the ML model is used to predict whether certain locations on larger graphene sheets are in the vicinity of any defect. From predicting graphene sheets that contain only one defect to predicting an unknown number of defects with an arbitrary distribution, a logistic regression model is applied, of which the performance is quantified by three practical metrics: total accuracy, true positive rate, and true negative rate. Finally, by adjusting the weights associated with defects and non-defects in the cost function, this work aims to find a way of improving the prediction accuracy of defects while maintaining a relatively low false positive rate.

Methods

Molecular modeling

Geometries of defect-containing monolayer graphene sheets used in this study are shown in Fig. 3.11 (defects highlighted in blue). Two different sizes of graphene sheets are constructed: smaller ones for training and larger ones for testing. Figs. 3.11(a) and (b) illustrate small graphene sheets, sized L_x^0 by L_y^0, where $L_x^0 = 43.6$ Å, $L_y^0 = 39.2$ Å; Figs. 3.11(c) and (d) illustrate larger graphene sheets, sized L_x by L_y^0, where $L_x = 58.2$ Å, $L_y^0 = 51.8$ Å. "A" and "Z" denote the armchair and zigzag directions of graphene, respectively. On each edge of the graphene sheet, a width of three atoms is fixed (colored gray), while the rest of the graphene sheet could vibrate without enforced restriction (colored red). If defect-free,

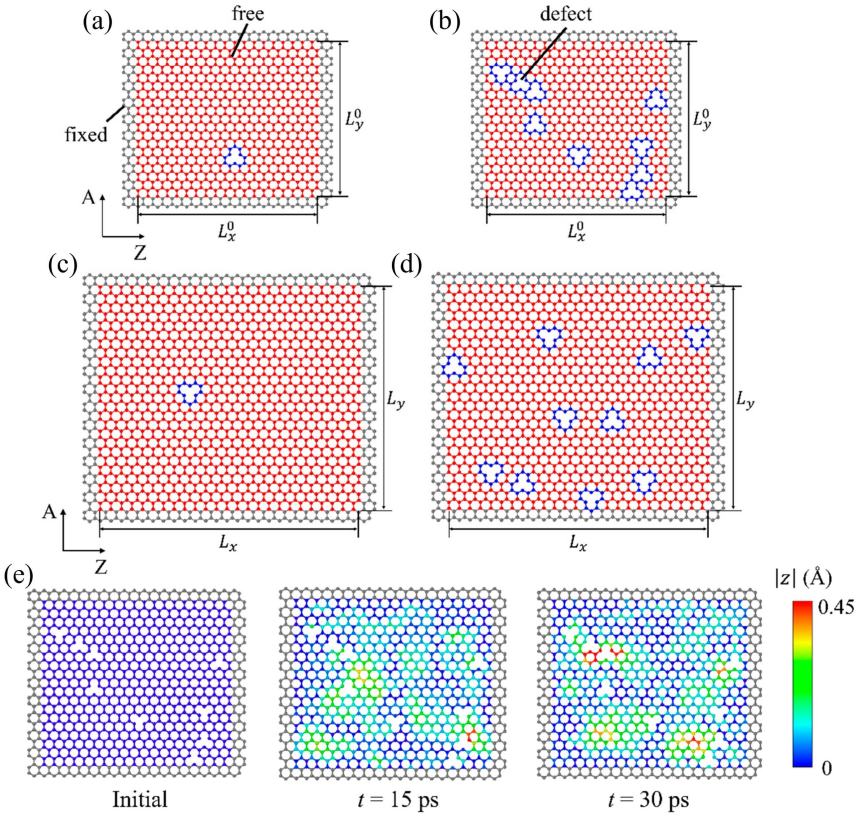

Figure 3.11: Schematics of defect-containing graphene sheets. Smaller graphene sheets with (a) one defect and (b) multiple defects for training. Larger graphene sheets with (c) one defect and (d) multiple defects for testing. "A" and "Z" denote the armchair and zigzag directions, respectively. (e) An example of vibration amplitude distributions in a defect-containing graphene sheet. Distributions at three different time instances are plotted: before vibration, 15 ps, and 30 ps after the initialization of the NVT ensemble. t denotes the time passed in the NVT ensemble where the vibrational responses are recorded.

the smaller graphene sheet contained 722 vibrating atoms, while the larger graphene sheet contained 1250 vibrating atoms. The out-of-plane displacement z of atoms is used to quantify vibration. In Figs. 3.11(a) and (c), the graphene sheets contained only one defect, of which the location is uniformly random throughout the vibrating graphene domain; in Figs. 3.11(b) and (d), the graphene sheets contained multiple defects where the number of defects followed a uniform distribution from 1 to 10, and the locations are also uniformly random throughout the vibrating graphene domain.

MD simulations are used to compute the vibration of graphene using LAMMPS and the AIREBO potential. A timestep of 1 fs is used. Periodic boundary condition is applied to the

two in-plane dimensions, while the height of the simulation box is fixed. For fixed atoms near the graphene edges, the atom displacement in all three directions is set to zero. Each atom in the vibrating region is initiated with a random velocity, and for each individual graphene sheet the seed of the random number generator is different. This practice ensures that even if two graphene sheets contained the same number of defects at the same locations (meaning the two graphene sheets are governed by the same physics) their mechanical responses are not numerically identical, thus preventing data duplication. Graphene sheets are firstly relaxed in the NPT ensemble at temperature $T = 300$ K and pressure $p = 0$ for 25 picoseconds to eliminate stress. Then, the graphene sheet is stretched biaxially to 1% strain in the NVT ensemble at $T = 300$ K, with a strain rate of 10^9 s^{-1}. The small tensile pre-strain is applied to imitate the experimental setup of graphene vibration in [16]. Finally, the pre-strained graphene sheet is set to vibrate in the NVT ensemble at $T = 300$ K for 30 picoseconds, during which the out-of-plane displacement of all vibrating atoms are extracted for subsequent data processing. The sampling frequency of atom trajectories is 20 THz. Using the graphene sheet in Fig. 3.11(b) as an example, the distributions of vibration amplitudes 15 ps and 30 ps after the initialization of the NVT ensemble are plotted in Fig. 3.11(e). The initial graphene configuration is also provided for comparison.

Machine learning

The data preparation procedure for ML is shown in the flowchart in Fig. 3.12. First, one or multiple query points are assigned on the graphene sheet. Grids are subsequently constructed surrounding the query point, as illustrated in Fig. 3.12(a). The query point resides at the center of the center grid. Each grid is sized a-by-b, where $a : b = L_x^0 : L_y^0$, making the length-to-height ratio of grids equal to the length-to-height ratio of the smaller graphene sheet. Because of the fixed ratio, a single variable a is sufficient to depict the grid size. In the present study, 9-grid (3 by 3) and 25-grid (5 by 5) approaches are considered. The accuracy comparison of the two approaches will be conducted. Next, the vibration of atoms in these grids is computed, detailed as follows: The time series of out-of-plane displacement $z(t)$ of each atom is computed by MD simulations, and an example is provided in Fig. 3.12(b). Then, a fast Fourier transformation is performed on $z(t)$ to deduce its frequency response $z(f)$, as shown in Fig. 3.12(c).

The next goal is to associate the vibration of each atom to a scalar. To this end, based on the frequency response, the energy is calculated as $S(f) = \int_0^\infty |z(f)|^2 df$. Afterwards, the total energy in each grid S_g is computed as $S_\mathrm{g} = \sum_{i=1}^{N_\mathrm{g}} S_i$, where i is the index of atom in the grid, and N_g is the total number of atoms in the grid. Finally, a feature vector is formed as $(S_\mathrm{g}^1 \cdots S_\mathrm{g}^N)$, where N is the number of grids ($N = 9$ or 25). Up to this point, each query point is associated with a feature vector that quantifies vibration properties in the grids. The label Y is determined by the existence of defects in the center grid: if there is one or more defects in the center grid, label $Y = 1$; otherwise $Y = 0$. It is a natural choice to apply a logistic regression model to predict binary classes using feature vectors. The loss function

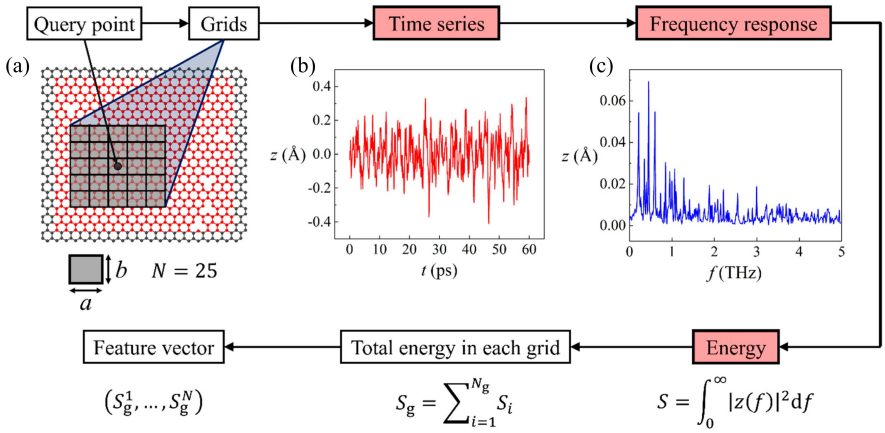

Figure 3.12: Data preparation procedure for ML. Boxes in red are properties of each individual atoms. (a) Illustration of query point and grid construction. (b) Displacement time series $z(t)$ and (c) the corresponding frequency response $z(f)$ of a vibrating atom in the graphene sheet.

of logistic regression can be expressed as:

$$L(\hat{Y}, Y) = -Y \ln \hat{Y} - (1 - Y) \ln 1 - \hat{Y} \tag{3.1}$$

where $\hat{Y}$ is the predicted label. The cost function can be expressed as:

$$J = \sum_{i=1}^{n} L(\hat{Y}_i, Y_i) \tag{3.2}$$

where i is the index of one data point, and n is the total number of data points. In this study, logistic regression is performed using the ML library Scikit-Learn [130].

Results

For the binary classification problem, prediction accuracy is quantified by the following three metrics: total accuracy (TA), true positive rate (TPR), and true negative rate (TNR), expressed below:

$$\mathrm{TA} = \mathrm{P}(\hat{Y} = 1|Y = 1)\mathrm{P}(Y = 1) + \mathrm{P}(\hat{Y} = 0|Y = 0)\mathrm{P}(Y = 0) \tag{3.3}$$

$$\mathrm{TPR} = \mathrm{P}(\hat{Y} = 1|Y = 1) \tag{3.4}$$

$$\mathrm{TNR} = \mathrm{P}(\hat{Y} = 0|Y = 0) \tag{3.5}$$

where $\hat{Y}$ is the predicted label; P() is the probability notation, and $\mathrm{P}(\cdot|\cdot)$ denotes the conditional probability.

Prediction for single defect

The prediction of single-defect graphene sheets is studied first. The preparation of training data based on the smaller graphene is detailed as follows: First, the entire vibrating graphene domain is discretized with an M-by-M mesh, as shown in Fig. 3.13(a). M is an integer parameter ranging from 7 to 17, giving values of a from 6.23 Å to 2.57 Å. This practice aims to thoroughly scan the graphene domain during training. The ratio $a : b = L_x^0 : L_y^0$ ensures that the numbers of grids in the two orthogonal directions (i.e., the armchair and the zigzag directions) are equal. To prepare unbiased training data for the binary classification model, the numbers of $Y = 1$ data and $Y = 0$ data are equal. Here, the defect-containing grid is purposefully selected as the center grid and the rest of the grids are constructed around it. Then, another grid is randomly selected as a center grid, which is bound to be defect-free. Hence, each graphene provides two sets of training data, and the numbers of $Y = 1$ data and $Y = 0$ data are equal. The total number of one-defect graphene sheets for training is 10,148. However, not all these graphene sheets are used to construct training data—graphene sheets that contained a near-edge/-corner defect are excluded due to different lengths of feature vectors. For the 9- (25-) grid approach, graphene sheets whose defect-containing center grids that are within one (two) grid(s) to graphene edges are excluded. A total of five types of near-edge/-corner defects are addressed separately. Data are randomly split into 9:1 for training and validation. Validation accuracies are based on the average of three different splits. Fig. 3.13(b) shows validation accuracies (TA, TPR, TNR) as a function of grid size a. The results of 9-grid and 25-grid approaches are also compared. It is shown that as a increases, all three accuracy metrics decrease. This suggests that smaller grids give rise to higher training accuracies. In addition, 9-grid and 25-grid approaches have similar trends and the 25-grid approach strikes higher accuracy in all three metrics. Hereafter, ML results will be based on only the 25-grid approach for simplicity. The method of specifying the query point location x/L_x^0 and y/L_y^0 in the feature vectors is also tested, where (x, y) are the coordinates of the query point. It is shown that adding these two features has little impact on the accuracies of either 9-grid and 25-grid approaches, as illustrated in Fig. 3.14.

The preparation of test data based on larger graphene sheets differed from the training data, as is outlined below. The number of larger graphene sheets for ML testing is 875. Each provided five randomly chosen query points that are at least two grids away from graphene edges. Because of the random selection, center grids that contained defects are outnumbered by defect-free center grids, different from the previous training data where the numbers of defective and defect-free center grids are equal. Test accuracies based on three distinct test sets are presented in Fig. 3.15. Figs. 3.13(a–c) show TA, TPR, and TNR as a function of the grid size a, respectively. It is shown that both TA and TNR decrease as a increases. TPR, on the other hand, increases as a increases, which differs from the trend of TPR in the validation result. This suggests that for TPR, the ML model is subject to a high-variance issue; this shows that it is more ideal to choose moderately larger grid sizes for this system. In all, TA, TPR, and TNR, the results of three test sets show good consistency. Fig. 3.15(d) shows the average accuracies of test results. TA and TNR appear to coincide. This is because in the

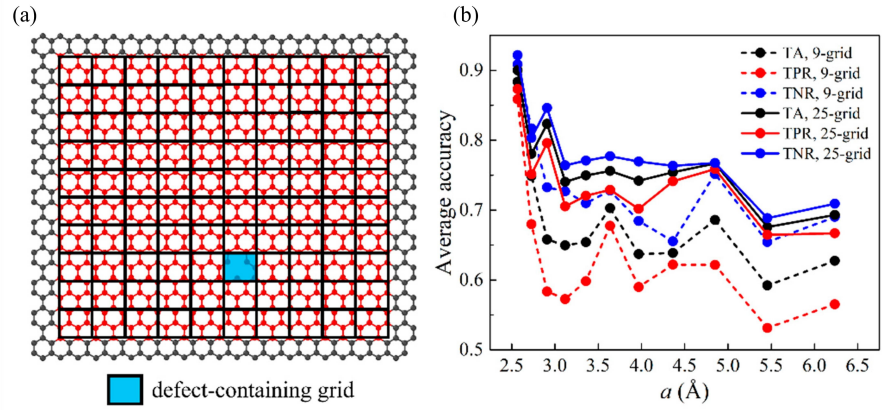

Figure 3.13: ML results of validation sets for one-defect scenarios. (a) Schematic of discretized graphene domain for one-defect graphene sheets. The entire vibrating graphene domain is discretized by an M-by-M mesh (in this case, $M = 10$, $a = 4.37$ Å). Defect-containing grid is highlighted in light blue. (b) Validation accuracies (TA, TPR, TNR) as a function of the grid size a for 9-grid and 25-grid approaches.

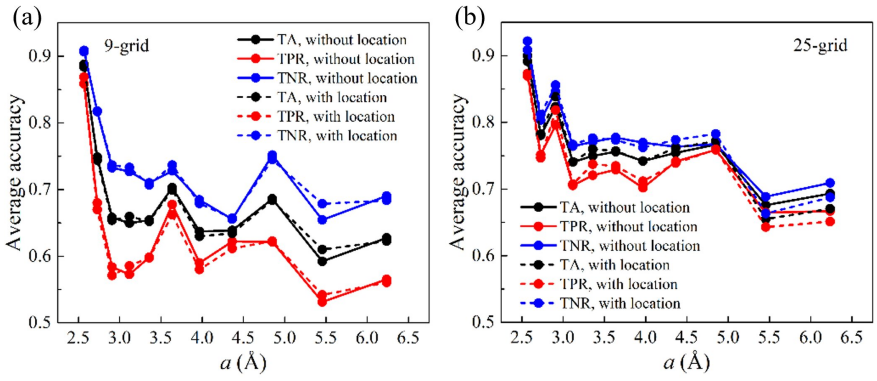

Figure 3.14: Validation accuracies with and without query point locations. (a) 9-grid and (b) 25-grid approaches.

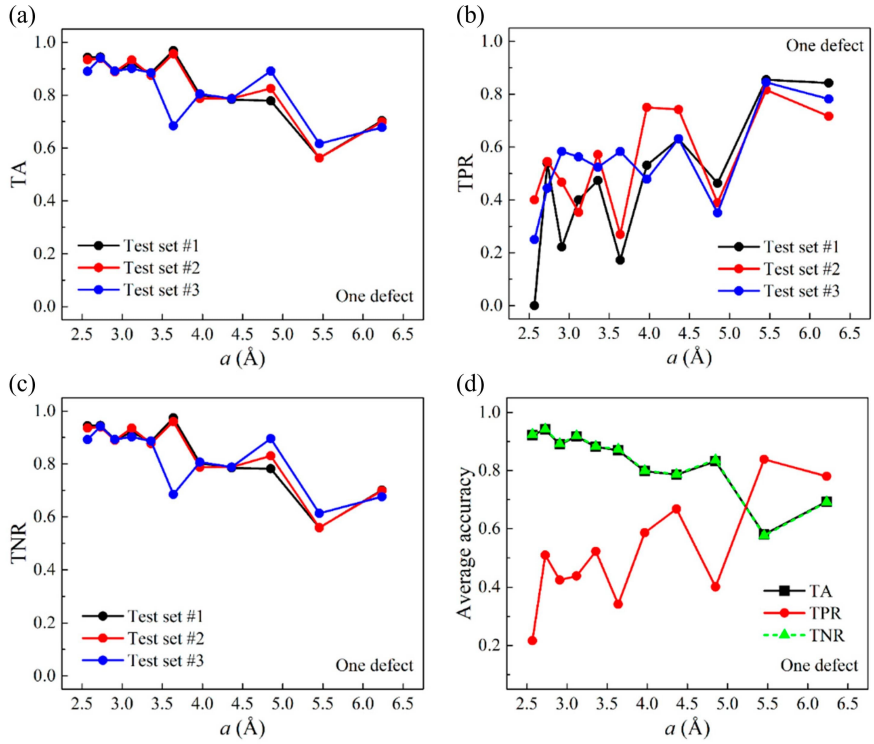

Figure 3.15: Test accuracies for one-defect scenarios. (a) TA, (b) TPR, and (c) TNR as a function of the grid size a based on three test sets. (d) Average accuracies over all three test sets as a function of a.

test data, label $Y = 0$ data take on more than 99% of the total data.

Prediction for multiple defects

With the successful implementation of predicting one-defect graphene sheets, more complex multiple-defect cases are studied. The total number of smaller multiple-defect graphene sheets for training is 10,108. Same as one-defect scenarios, the vibrating graphene domain is discretized by an M-by-M mesh. Defect-containing grids that are more than two grids away from any graphene edge are used as center grids. To equalize $Y = 1$ data and $Y = 0$ data, an equal number of defect-free grids are randomly selected as center grids. These data are randomly split into 9:1 for training and validation. Validation accuracies as a function of the grid size a are shown in Fig. 3.16.

The preparation of multiple-defect test data based on the larger graphene sheets is outlined below. A total of 621 larger graphene sheets are used and each provided five randomly chosen query points at least two grids away from graphene edges. The prediction of query points within two grids to graphene edges is shown in Figs. 3.17-3.21. Because of the random

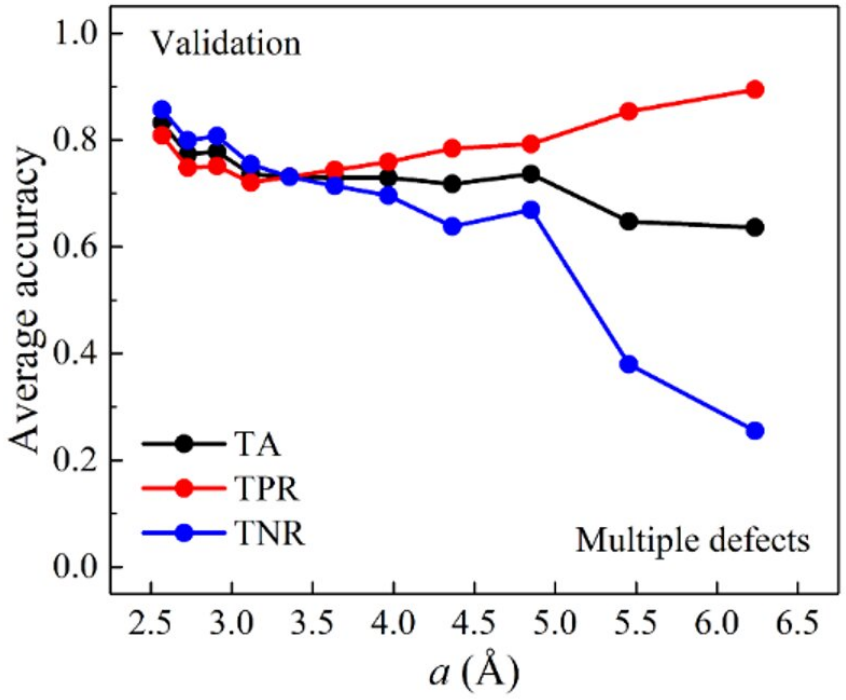

Figure 3.16: Validation accuracies of multiple-defect graphene sheets.

selection, grids that contain defects are outnumbered by defect-free grids. Figs. 3.22(a–c) show TA, TPR, and TNR as a function of the grid size a. It is shown that both TA and TNR decrease as a increases, and that TPR increases as a increases. Compared to one-defect scenarios, TPR is lower in general but is higher for small grid sizes, indicating less susceptibility to the high-variance-related issue. Fig. 3.22(d) presents the average accuracies of test results. TA and TNR appear to coincide. This is because in the test data, label $Y = 0$ data take on more than 98% of the total data. The above results of one-defect and multiple-defect scenarios indicate that, trained by local thermal vibration properties of uniformly sized small graphene sheets, the ML model is able to predict the existence of defects at all locations on unseen larger graphene sheets.

Weighted cost function

It is desired that the prediction accuracy of a defect in larger graphene sheets can be further improved, and that the fine-tuning of TPR and TNR is enabled as the prediction of defects or non-defects is emphasized as needed. A solution to this can be offered by a weighted

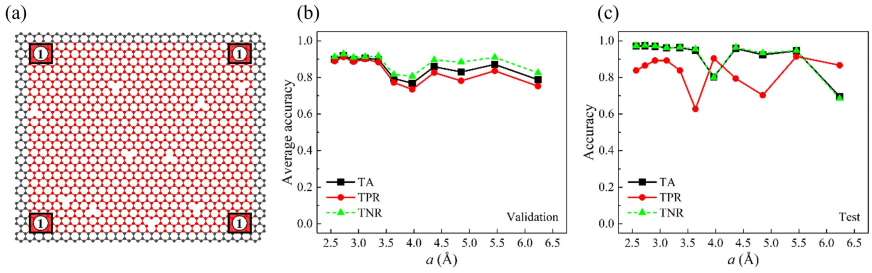

Figure 3.17: Validation and test accuracies of Type 1 near-edge/-corner defects. The length of feature vectors is 9. (a) Illustration of Type 1 near-edge/-corner defects. (b) Validation and (c) test accuracies.

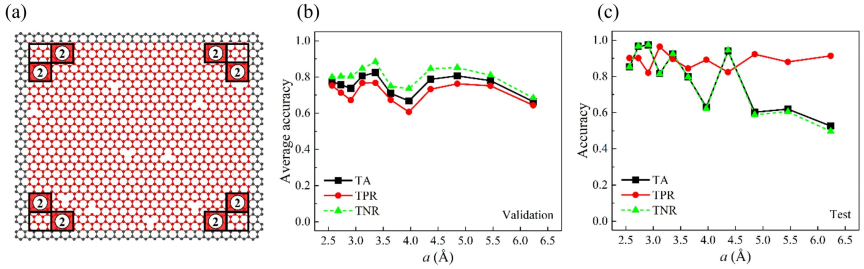

Figure 3.18: Validation and test accuracies of Type 2 near-edge/-corner defects. The length of feature vectors is 12. (a) Illustration of Type 2 near-edge/-corner defects. (b) Validation and (c) test accuracies.

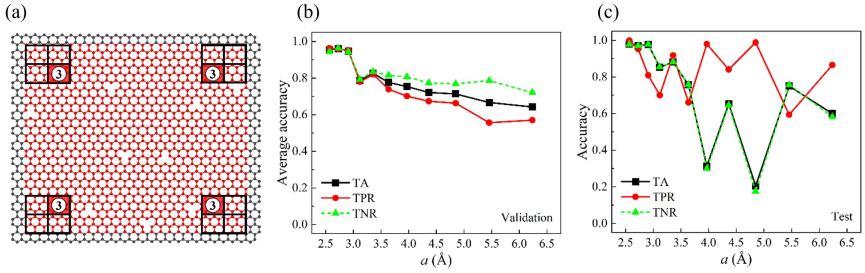

Figure 3.19: Validation and test accuracies of Type 3 near-edge/-corner defects. The length of feature vectors is 16. (a) Illustration of Type 3 near-edge/-corner defects. (b) Validation and (c) test accuracies.

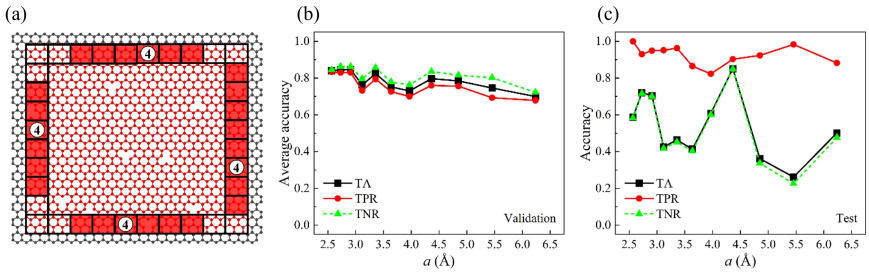

Figure 3.20: Validation and test accuracies of Type 4 near-edge/-corner defects. The length of feature vectors is 15. (a) Illustration of Type 4 near-edge/-corner defects. (b) Validation and (c) test accuracies.

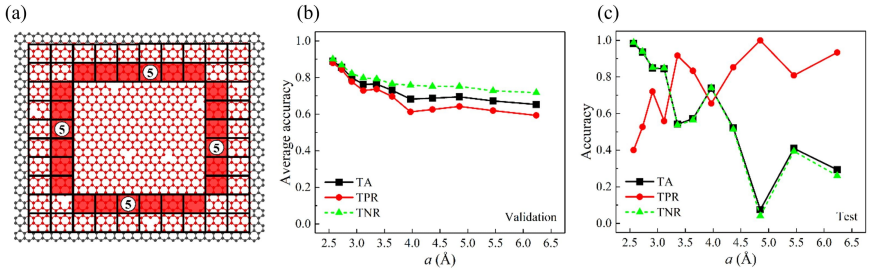

Figure 3.21: Validation and test accuracies of Type 5 near-edge/-corner defects. The length of feature vectors is 20. (a) Illustration of Type 5 near-edge/-corner defects. (b) Validation and (c) test accuracies.

version of the cost function, expressed as:

$$J = \sum_{i=1}^{n} w_i L(\hat{Y}_i, Y_i) \tag{3.6}$$

where

$$w_i = \begin{cases} w_0, & Y_i = 0 \\ w_1, & Y_i = 1 \end{cases}$$

By tuning the weights w_0 and w_1, the significance attached to the correct prediction of defects and non-defects is changed. Concretely, if $w_0/w_1 < 1$, accuracy of defects is emphasized; if $w_0/w_1 > 1$, accuracy of non-defects is emphasized; if $w_0/w_1 = 1$, defects and non-defects are equally emphasized, which is the default for all previous ML results. Here, the prediction accuracies using a weighted cost function with weight ratios $w_0/w_1 = 0.5, 1, 2$ are compared. Figs. 3.23(a–c) show the average test accuracies of one-defect cases. Figs. 3.23(d–f)show

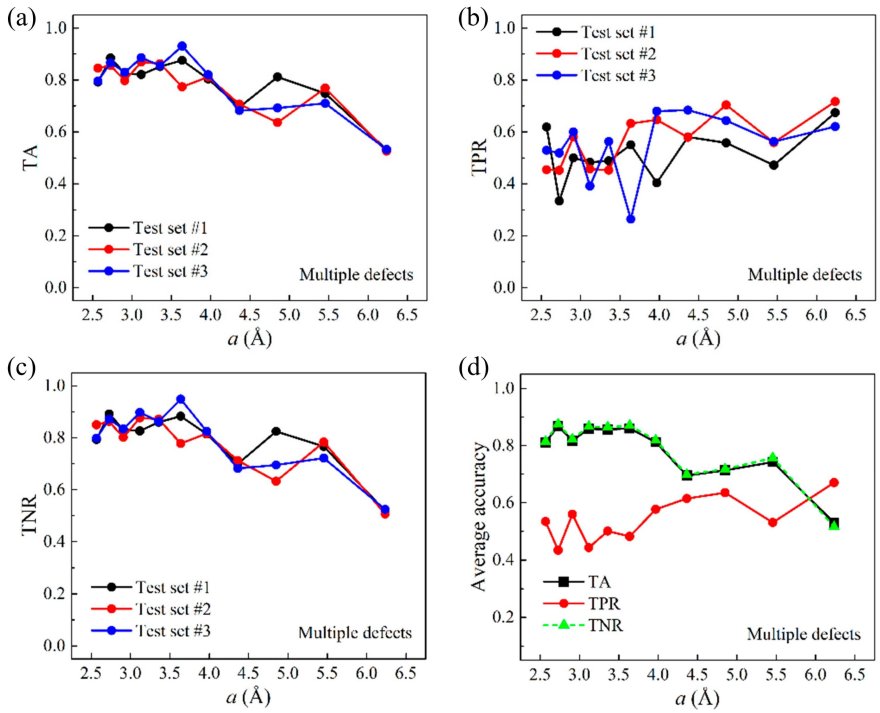

Figure 3.22: Test accuracies for multiple-defect scenarios. (a) TA, (b) TPR, and (c) TNR as a function of the grid size a based on three test sets. (d) Average accuracies over all three test sets as a function of a.

the average test accuracies of multiple-defect cases. In all cases, TPR increases as w_0/w_1 decreases, while TNR increases as w_0/w_1 increases. For all three metrics, there is a tradeoff between TPR and TNR, giving us the opportunity to emphasize one label over another. Notably, the weight ratio $w_0/w_1 = 2$ gives the highest TA. This is because in both one-defect and multiple-defect test sets, $Y = 0$ data outnumber $Y = 1$ data. By applying weighted cost function, the ability to improve the prediction accuracy of defects while maintaining a relatively low false positive rate is achieved.

Discussion

Due to the randomized atom removal process of defect creation, most defects assigned to graphene sheets are unreconstructed single vacancies. Even though unreconstructed single vacancies have been observed in experiments [91] and studied in other computational work as the main defect type [205, 227], graphene displays an incredibly rich restructuring capability which gives rise to reconstructed vacancy defects, for instance, through a Jahn–Teller distortion [145]. The proposed ML approach is believed to be applicable to all types of

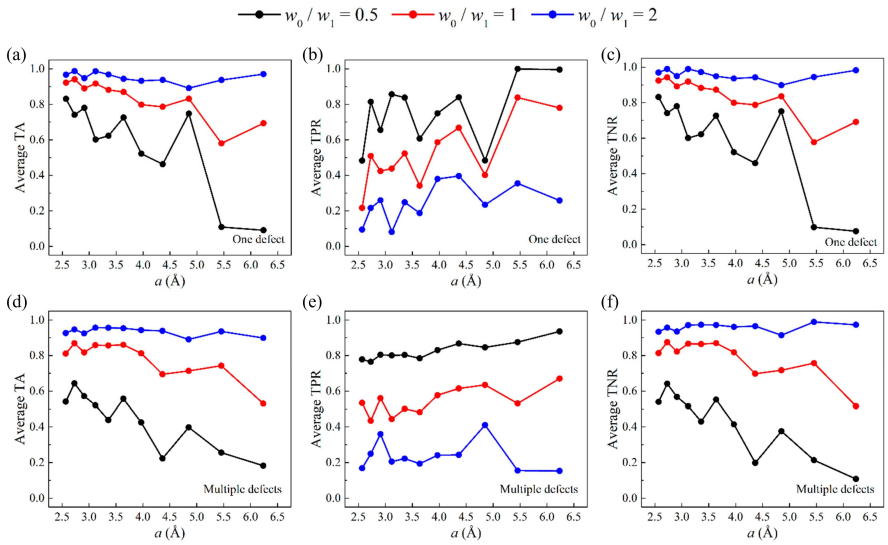

Figure 3.23: Accuracies when a weighted cost function is used (weight ratios $w_0/w_1 = 0.5, 1, 2$). Average (a) TA, (b) TPR, and (c) TNR of three test sets as a function of grid size a for one-defect graphene sheets. Average (d) TA, (e) TPR, and (f) TNR of three test sets as a function of grid size a for multiple-defect graphene sheets.

vacancies, because these vacancies give rise to structural anomalies that can cause changes to local vibration properties. Additionally, the existence of larger defects is not ruled out, which arise when removed atoms are next to each other (see Fig. 3.24 for an example).

Concluding remarks

In this section, A transferable learning strategy to detect unknown defects in larger graphene sheets using information obtained from only a smaller graphene system is presented. Trained by tens of thousands of local vibrational energy distributions in uniformly sized smaller graphene sheets from MD simulations, the logistic regression model can predict defects in unseen larger graphene sheets with satisfactory accuracies for both one-defect and multiple-defect graphene sheets, quantified by three practical metrics: TA, TPR, and TNR. Through adjusting the weights associated with defects and non-defects in the cost function, an improvement in the prediction accuracy of defects is achieved while maintaining a relatively low false positive rate. The present research sheds light on scalable graphene defect prediction and opens doors for accelerated data-driven defect detection of a broad range of two-dimensional materials [222].

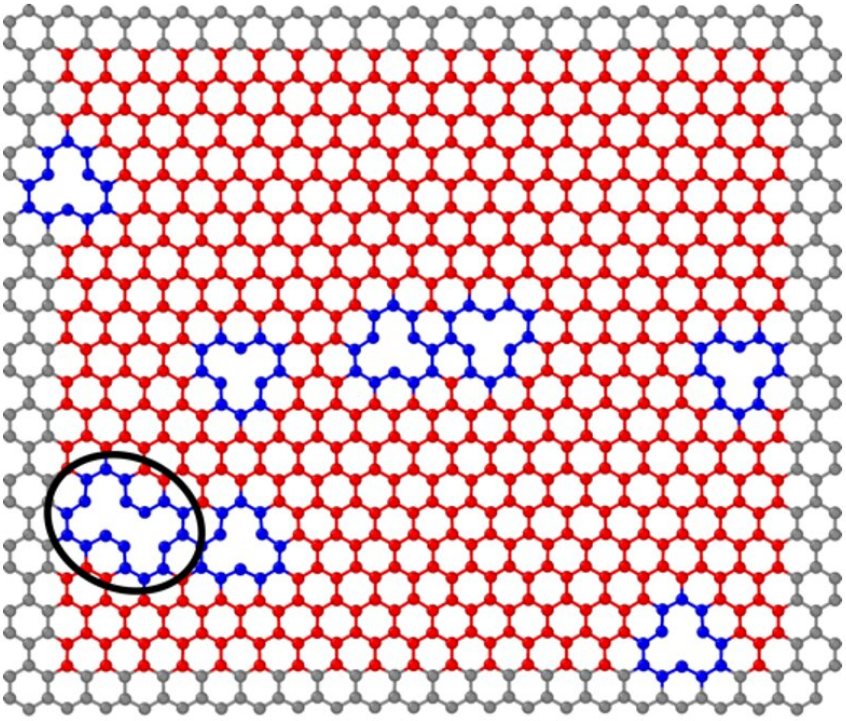

Figure 3.24: An example of graphene sheet that contains a larger defect (circled).

3.3 Chemical composition identification for graphene oxide

GOs have exhibited alluring potential for state-of-the-art applications such as biomedical devices and functional nanocomposites. Compared to pure graphene, the mechanical properties of GO are more challenging to model from a theoretical perspective, mainly because of the profound but implicit influences of the functional groups within. For example, hydroxyl groups cause GOs to behave in a brittle manner [165], while epoxide groups may potentially increase the ductility via a mechanochemical epoxide-to-ether functional group transformation [171, 181]. In addition, with the same amount of oxygen atoms, different epoxide-to-hydroxyl group ratios yield diverse ultimate strengths [154]. Last but not least, the spatial distribution of functional groups triggers specific mechanochemical reactions under certain loading conditions [181], which in turn affect the properties of the GO sheet. The correlation between collective properties of GO and the amount and types of functional groups, however, is not well understood.

ML is a potent method to uncover the hidden structure–property relations and to accelerate new material discovery, which has been applied to study nanomaterials of a broad

variety, including GO. Motevalli et al. used classification, regression, and causal inference to understand and predict the causes of defects in GO [117]. Motevalli et al. used multiple clustering ML models to determine representative structures of GO [118]. Amani et al. used regression models to estimate the temperature-dependent moduli of GO-reinforced nanocomposites [2]. However, the potential of ML has not been sufficiently used in predicting the degree and type of oxidation, which is one of the most defining and fundamental features of GO. The investigation of functionalization can shed light on how GOs can be optimally used in multiple research and technological fields such as flexible electronics, nonlinear optics, gas storage, and lubrication. Some examples are as follows. First, the probe of oxygen coverage percentage can help determine if the GO of interest is a semiconductor or an insulator. Carbon atoms comprising of pure graphene are of sp^2 hybridization. Hydroxyl and epoxide groups are both responsible for the hybridization change from sp^2 to sp^3. A substantial oxygen coverage renders GO insulating, while a low oxygen coverage makes it a semiconductor [47]. Second, the degree and type of oxidation can be used to estimate band gaps, which contain information of optical modulation. The combination of sp^2 and sp^3 hybridization can break the symmetry and therefore result in band gaps [83]. Third, the knowledge of functional groups can be used to evaluate the applicability of GOs in gas storage. The reaction between hydroxyl groups and boronic acids can link GO layers together, forming a layered structure that provides room for gas storage [17]. Fourth, the degree and type of oxidation can shed light on the friction coefficient of GO-based lubricant additives. It is shown that GO containing a high percentage of epoxide groups exhibits a better lubrication ability than GOs with a high content of hydroxyl groups [65]. The above applications can be much better realized if one can access the functionalization properties of GO in quantitative details.

In this section, an ML-based strategy is developed to determine the functionalization properties of monolayer GO sheets, which are quantified by two nondimensional features: the oxygen-to-carbon atom ratio and the fraction of epoxide groups. Data are prepared based on the mechanical responses upon a uniaxial tensile load, computed by MD simulation with a reactive force field. A gradient boosting ML model, which is built up by forming an ensemble of weak prediction submodels in a stagewise fashion, is trained and used to predict the functionalization properties of unknown GO configurations. ML features are extracted from both stress–strain relations and potential energy-related metrics, which successfully circumvent the uncertainty from the spatial distribution of functional groups. Physical insights into failure mechanisms associated with different functional groups are provided to rationalize prediction errors. This study demonstrates the power of ML models in uncovering complex, hidden structure–property relations in GO, offering possibilities for material discovery of a broader range using data-driven approaches.

Results

Molecular modeling

GOs in the present study are configured by following four sequential steps: (1) construction of a graphene basal plane; (2) assignment of epoxide groups; (3) assignment of hydroxyl groups; and (4) decoration of carbonyl and carboxyl groups on graphene basal plane edges. For the graphene basal plane, square-shaped monolayer graphene sheets with a side length of $L = 3$ nm are constructed, consisting of 446 carbon atoms in total and 336 non-edge atoms. For the epoxide group assignment, each epoxide group resides on two neighboring nonedge carbon atoms and there are 226 such pairs in total in the graphene basal plane. Additionally, the sp^3 hybridization requires that one carbon atom cannot be associated to two epoxide groups. Herein, N_p pairs are randomly picked from all 226 possibilities and pairs that violate the sp^3 hybridization requirement are removed from selection. For the hydroxyl group assignment, hydroxyl groups are hosted by non-edge sp^2 atoms (not associated to any epoxide group). N_a non-edge carbon atoms that are not associated to epoxide groups are randomly picked to host hydroxyl groups. The numbers of epoxide and hydroxyl groups assigned to both sides are roughly equal. Lastly, the edges of the graphene basal plane are decorated with carbonyl and carboxyl groups, where the numbers of both functional groups obey a uniform distribution $\mathcal{U}(0, 20)$ and the locations are random.

To quantify the degree and type of oxidation independent of the absolute GO sheet size, the following two non-dimensional features are used to label GO sheets: (1) oxygen-to-carbon atom ratio φ_O, the ratio between total number of oxygen and carbon atoms $\varphi_\mathrm{O} = N_\mathrm{O}/N_\mathrm{C}$ where N_O and N_C are the total number of oxygen and carbon atoms and (2) fraction of epoxide group φ_f, the ratio of the number of epoxide groups to the total number of hydroxyl and epoxide groups $\varphi_\mathrm{f} = N_\text{-O-}/N_\text{-O-} + N_\text{-OH}$, where $N_\text{-O-}$ and $N_\text{-OH}$ are the total number of epoxide and hydroxyl functional groups. φ_O quantifies the intensity of oxidation, while φ_f quantifies the relative concentrations of two distinct functional groups. For example, $\varphi_\mathrm{f} \to 0$ and $\varphi_\mathrm{f} \to 1$ indicate hydroxyl-rich and epoxide-rich, respectively.

Mechanical responses of various GO sheets upon uniaxial tensile loads are computed by reactive MD simulations using LAMMPS. ReaxFF potential, a reactive force field, is utilized to model the interactions among carbon, hydrogen and oxygen atoms in GO [31]. ReaxFF potential enables the modeling of both non-bonded interactions such as van der Waals and Coulomb interactions, and bond breaking and formation. Specifically, potential parameters developed in Ref. [31] are used, which has been proved viable by various studies on the physical and chemical behavior of graphene systems [28, 170, 13, 198]. A 3D, full atomistic model is used. Periodic boundary conditions are applied in all three spatial dimensions. The size of the simulation box is $D_x \times D_y \times D_z = 70$ Å $\times$ 70 Å $\times$ 25 Å, where D_x, D_y, D_z are the lengths of the box in x, y, z directions, respectively. GO sheet is centered in the simulation box. The equations of motion are integrated with a timestep of 0.1 fs using the Verlet algorithm, which ensures the computational stability. The trajectories, velocities, forces, and energies of all atoms are recorded every 100 timesteps. To simulate tensile loads

at room temperature, an ensemble of random velocity corresponding to the temperature $T = 300$ K is firstly generated throughout all atoms. Then an equilibrium is realized by running a simulation in the NPT ensemble at the same temperature for 20,000 timesteps. The loading scenario is simulated in the NVT ensemble at $T = 300$ K. The unidirectional in-plane stretch is applied in the zigzag direction based on a deformation-control manner by assigning displacement at a constant speed to a 3 Å wide stripe at one end, while a 3 Å wide stripe at the other end is held immobile in all three dimensions. The strain rate of loading is 10^{11} s^{-1}.

The structure of GO in Fig. 3.25(a) immediately after full relaxation at 300 K is shown in Fig. 3.25(b), indicating that GO upon loading is not flat and shows a zigzag sheet-like structure. First, to validate the simulation setup, the stress–strain curve of a GO sheet with a side length of $L = 3$ nm is recorded and compared against a stress–strain curve in Ref. [181] with $L = 3$ nm. To draw a fair comparison with the reported results, following Ref. [181], the fraction of oxidized carbon atoms of all four GO sheets is set as 0.36 and the epoxide-to-hydroxyl functional group ratio is set as 4 : 1. Also, the same effective thickness $t_e = 0.75$ nm is used to calculate the normal stress component in the zigzag direction σ_z [181]. The comparison result is shown in Fig. 3.25(c), which exhibits a good agreement despite not knowing the exact locations of functional groups and the difference in size. The von Mises stress σ is used for all stress–strain curves in this section (Eq. 2.3). Next, the effect of GO size is investigated. MD simulations of GOs with side lengths of 3, 5, 7, and 10 nm, with fixed generic parameters $\varphi_O \simeq 0.253$ and $\varphi_f \simeq 0.561$ are performed, and the results are shown in Fig. 3.25(d). As can be seen, despite the difference in size and the uncertainty in functional group distribution, the results agree well in the general trend and the ultimate strength, indicating the reliability and reasonable dimensional scalability of the current simulation settings. Despite larger GO sheets ($L = 7$ nm and $L = 10$ nm) have smoother stress–strain curves, $L = 3$ nm enjoys the advantage of much reduced computational expenses, which makes this choice of GO size more realistic in the preparation of a large amount of data. This also poses greater challenges to ML implementation to overcome the fluctuation issue, which is common in an experimental setting. A successful prediction with $L = 3$ nm can indicate good performance with noisy data. In addition, $L = 3$ nm creates more variations of functional group distribution compared to $L = 2$ nm in the reported results [181], which facilitates the generation of more diverse GO configurations that benefit the training and extrapolation ability of the ML model. The temperature effect toward the mechanical responses and the stability of GO is also investigated. Stress–strain curves of GO with parameters $\varphi_O \simeq 0.253$ and $\varphi_f \simeq 0.561$ under various temperatures (100, 200, 300, 400, and 1000 K) are recorded and are shown in Fig. 3.26(a). The results show that as the temperature increases, GO is slightly softened and the mechanical properties are not subject to major changes. Fig. 3.26(b) shows the GO structure immediately after relaxation at $T = 1000$ K, which suggests that no thermal instability has occurred. To approximate a realistic setting, the rest of the MD simulations in this section are performed at 300 K.

It is critical that a specific combination of the oxygen-to-carbon atom ratio and the epoxide-to-hydroxyl group ratio is not sufficient to reflect a single GO configuration because

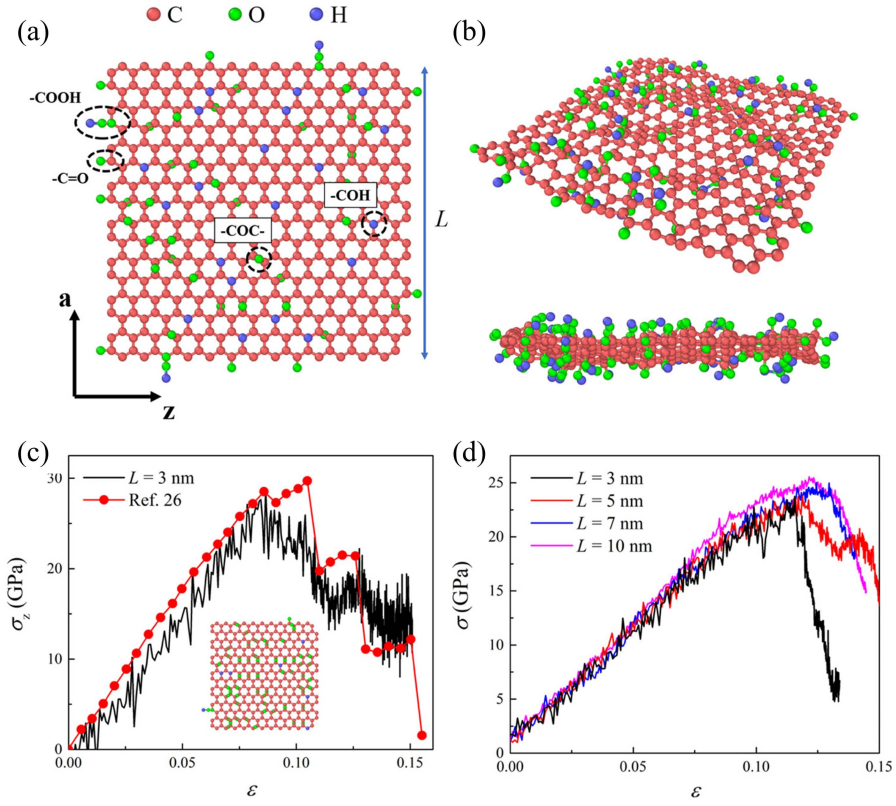

Figure 3.25: Schematic of GO sheets and mechanical responses upon tensile loading. (a) Schematic of the GO sheet with a side length of L. "a" and "z" refer to the armchair and zigzag directions of the GO basal plane. (b) Shape of the GO sheet upon full relaxation at a temperature of 300 K. (c) Comparison between the stress–strain curves of the present MD simulation and the result in ref. (26) The inset shows the GO structure used in this simulation case. (d) Stress–strain curves of GO sheets of various sizes with fixed parameters $\varphi_{\mathrm{O}} \simeq 0.253$ and $\varphi_{\mathrm{f}} \simeq 0.561$.

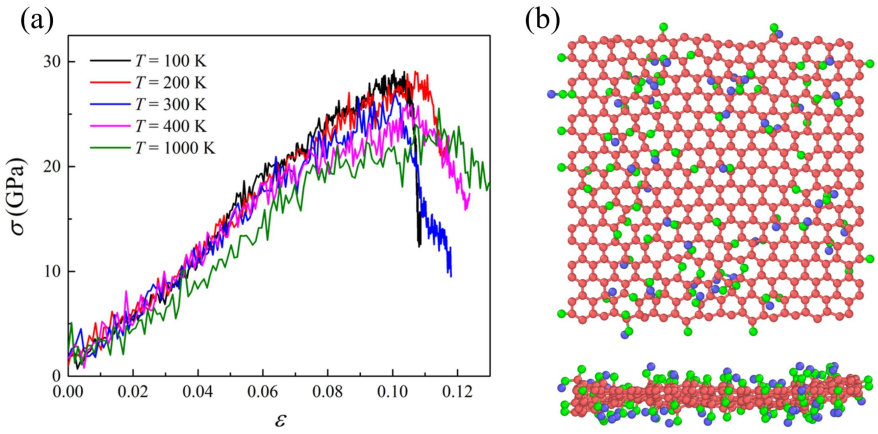

Figure 3.26: Thermal effect on the mechanical properties of GO sheets. (a) Stress-strain curves of GO sheet under various temperatures. (f) GO structure immediately after relaxation at $T = 1000$ K.

the parameter pair does not possess information of locations of functional groups. In fact, there exists an effectively infinite number of different functional group spatial distributions, whose effect is non-trivial. The effect of distribution can exist when investigating multiple randomly generated GO sheets with the same φ_{O} and φ_{f}. To this end, four GO sheets with $\varphi_{\mathrm{O}} \simeq 0.253$ and $\varphi_{\mathrm{f}} \simeq 0.561$ but randomly diverse functional group distributions are simulated, of which the structures after relaxation are shown in Figs. 3.27(a–d). The stress–strain curves of these GO sheets are shown in Fig. 3.27(e), which indicates that the functional group distribution has a profound effect on the mechanical properties of GO. Although the ultimate strengths are roughly on the same level, the ductility and curve shape differ dramatically. This finding implies that one unique combination of φ_{O} and φ_{f} does not yield one unique mechanical response. Therefore, to reliably predict φ_{O} and φ_{f} using mechanical responses of GO, more useful features need to be used besides the ones extracted from stress–strain relations.

To this end, the energy-related phenomena are visited. The system potential energy evolutions of the four GO sheets mentioned above are computed, as shown in Fig. 3.27(f). It is shown that there are substantial differences in these curves. GO sheets with the same φ_{O} and φ_{f} are characterized by distinct starting energy (energy at thermal vibration before subject to loading), maximum energy increase, and the general curve shape. It can be assumed that these differences in strain–strain relations and system potential energy evolutions stem from different functional group distributions. It is envisioned that by extracting features from both stress–strain curves and potential energy evolutions, a unique (or approximately unique) combination of φ_{O} and φ_{f} may be obtained, which makes ML-based prediction possible. If so, the issue of random functional group spatial distribution can be circumvented.

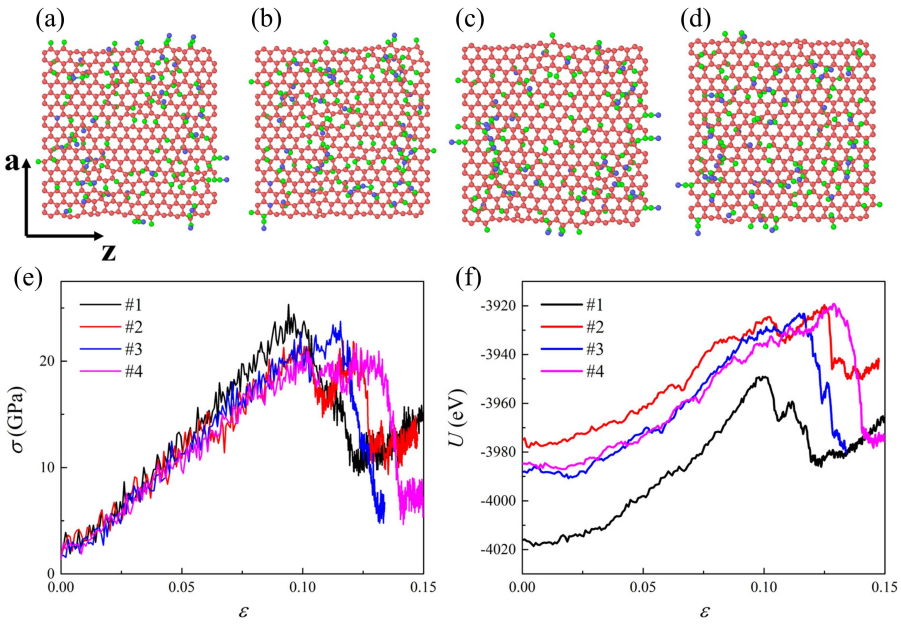

Figure 3.27: Mechanical responses of four GO sheets with $\varphi_{\mathrm{O}} \simeq 0.253$ and $\varphi_{\mathrm{f}} \simeq 0.561$ and random spatial distributions of functional groups. (a–d) Structures of four exemplar GOs. (e) Stress–strain curves and (f) system potential energy evolutions.

It is worth noting that energy-related quantities can be more challenging to measure in experiments compared to mechanical stress and strain. To this end, when extracting features from potential energy curves, the experimental viability needs to be taken into account.

Machine learning

Our ML model implementation using computational tensile test results can be broken down into the following three phases: (1) sample preparation, (2) feature extraction, and (3) model training and testing. For sample preparation, 1570 sample instances of mechanical responses of GO are computed for training and validation, while 100 sample instances are reserved for testing. The distributions of all 1670 sample points on the $N_{\text{-O-}}$-$N_{\text{-OH}}$ plane and the φ_{O}-φ_{f} plane are shown in Fig. 3.28. While φ_{f} naturally ranges from 0 to 1, $N_{\text{-O-}}$ ranges from 0.1 to 0.8. In an experimental setting, $N_{\text{-O-}}$ varies from 0.25 to 0.75 [83], which has been covered by the range of the sample space. Data for training and validation are randomly shuffled together and then separated into $N_{\text{training}} = 1470$ and $N_{\text{validation}} = 100$ before use, where N_{training} and $N_{\text{validation}}$ are the number of training and validation data. During training, the shuffle-and-split process is repeated 20 times where each time is based on a different random seed. The aim of this practice is to avoid good results by chance and to ensure better generalized results. Test data totaling $N_{\text{test}} = 100$ are not involved in

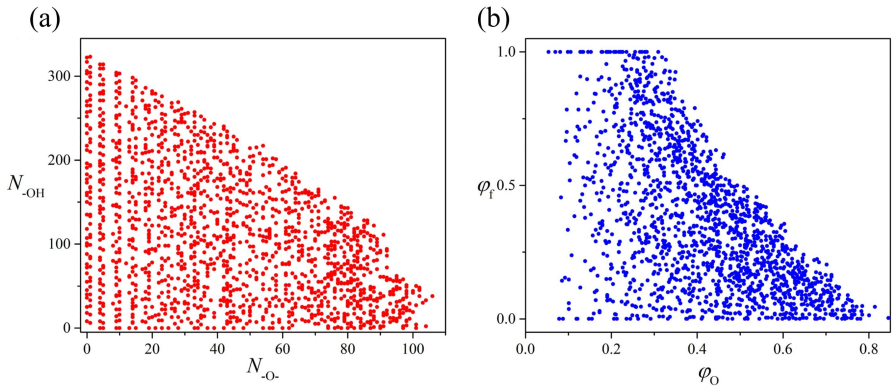

Figure 3.28: Distributions of all 1,670 sample points on (a) the $N_{\text{-O-}}$-$N_{\text{-OH}}$ plane and (b) the φ_{O}-φ_{f} plane. the maximum $N_{\text{-OH}} = 336$ is achieved when $N_{\text{-O-}} = 0$ and all 336 non-edge atoms are functionalized by hydroxyl groups, resulting in $N_{\text{-OH}} = 336$. The estimation of maximum $N_{\text{-O-}}$ is more complex, because the order of assigning epoxides on pairs affect the removal due to violating physics. When all 226 potential sites are pre-selected with multiple arrangements, the maximum $N_{\text{-O-}}$ is close to 100. It is noteworthy that both of the extreme cases above are extremely rare in real GOs. The purpose is to cover all possibilities.

the shuffling with training and validation data, implying that the test data represent future unseen configurations. A good test accuracy can indicate promising extrapolation ability of the ML model.

For feature extraction, the features to extract from both stress–strain relations and potential energy properties comprise of (1) ultimate strength σ_{u}, (2) strain at ultimate strength ϵ_{u}, and (3) total potential energy at room-temperature-free vibration U_{V} (the starting energy of potential energy evolution). In an experimental setting, vibrational energy distributions can be measured using a scanning force microscope [58] or by interferometry [16], after which the total potential energy can be computed. From a physical point of view, the above features can be related to the target properties, namely, the oxygen-to-carbon atom ratio and the relative concentrations of functional groups, in the following ways. First, ultimate strength σ_{u} is dependent on the sheer amount and types of bond interactions due to functionalization. For a pure graphene, the ultimate strength is dictated only by carbon–carbon (C-C) bonds formed by sp^2 carbon atoms. Oxidation not only adds new carbon–oxygen (C-O) covalent bond interactions but also disturbs the sp^2 carbon atom lattice by introducing sp^3 hybridization, thus affecting the ultimate strength. Second, strain at ultimate strength ϵ_{u} is impacted by both the amount of hydroxyl and epoxide groups, where the former tends to result in brittleness and the latter can trigger mechanochemical epoxide-to-ether functional group transformation to enhance ductility. The coexistence of two functional groups gives rise to uncertainty. Third, the total potential energy at room-temperature-free vibration U_{V} is highly related to molecular weight and therefore to oxygen percentage. The general trend

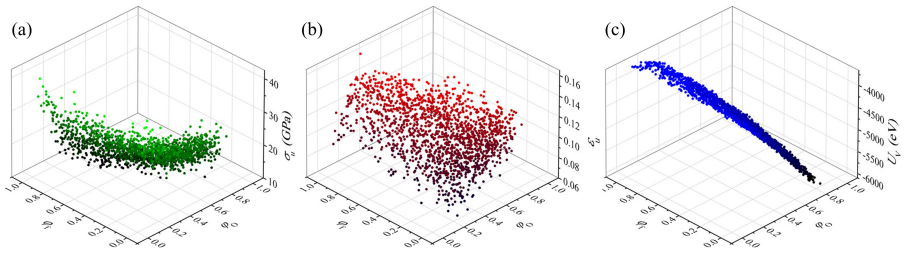

Figure 3.29: Extracted features as a function of φ_{O} and φ_{f}. (a) σ_{u}, (b) ϵ_{u}, and (c) U_{V} as a function of φ_{O} and φ_{f}. Data are from the training and the validation sets.

is that the higher the oxygen percentage, the higher the molecular weight, the lower the potential energy when GO is at rest. In addition, the relative concentrations of functional groups also play an implicit role in affecting the potential energy. σ_{u}, ϵ_{u}, and U_{V} as a function of φ_{O} and φ_{f} are shown in Fig. 3.29, suggesting that U_{V} is the strongest indicator of GO functionalization, followed by σ_{u} and ϵ_{u}.

The procedure of model training and testing is described as follows. For the ith sample instance, the sample vector can be formulated as $\mathbf{x}_i = [\sigma_{\mathrm{u,i}}, \varepsilon_{\mathrm{u,i}}, U_{\mathrm{V,i}}]^T \in \mathbb{R}^3$ and the label vector can be formulated as $\mathbf{y}_i = [\varphi_{\mathrm{O,i}}, \varphi_{\mathrm{f,i}}]^T \in \mathbb{R}^2$. A gradient boosting ML model, which is built by forming an ensemble of weak prediction sub-models in a stage-wise fashion, is used to map the above features to φ_{O} and φ_{f}. Tunable hyperparameters include learning rate (shrinkage factor) α and the number of boosting stage to perform M. Algorithmic details of the gradient boosting model are provided in Alg. 2. The framework of ML implementation is summarized in the flow chart shown in Fig. 3.30. The coefficient of determination R^2 as well as the mean squared error (MSE) are used as metrics to quantify the model predictions. Particularly for the training session, the means of R^2 and MSE over 20 random shuffle-and-splits, denoted as R^2_{avg} and $\mathrm{MSE}_{\mathrm{avg}}$, are used as metrics. The hyperparameter tuning results of φ_{O} and φ_{f} in the training session are shown in Fig. 3.31. The results provide an optimal hyperparameter combination $\alpha* = 0.11$ and $M* = 70$, scoring $R^2_{\mathrm{avg}} = 0.980$ and $\mathrm{MSE}_{\mathrm{avg}} = 0.000488$ for φ_{O} and $R^2_{\mathrm{avg}} = 0.906$ and $\mathrm{MSE}_{\mathrm{avg}} = 0.00661$ for φ_{f}. Convergence with respect to the size of the training data set is shown by plotting R^2_{avg} and $\mathrm{MSE}_{\mathrm{avg}}$ of φ_{O} and φ_{f} on the validation data as a function of the number of training data, as shown in Figs. 3.32 and 3.33.

After the training process, predictions are performed on the reserved test set using optimal hyperparameters $\alpha*$ and $M*$, which yields $R^2 = 0.978$ and $\mathrm{MSE} = 0.000499$ for φ_{O} and $R^2 = 0.870$ and $\mathrm{MSE} = 0.0103$ for φ_{f}, slightly inferior to the performance on the validation set. Prediction results of φ_{O} and φ_{f} are shown in Fig. 3.34. The differences between the predicted label and the true label (denoted as $d_{\mathrm{O}} = \varphi_{\mathrm{O}} - \hat{\varphi}_{\mathrm{O}}$ and $d_{\mathrm{f}} = \varphi_{\mathrm{f}} - \hat{\varphi}_{\mathrm{f}}$, where $\hat{\varphi}_{\mathrm{O}}$ and $\hat{\varphi}_{\mathrm{f}}$ are the predicted labels) of all 100 sample points in the test set are plotted against the true labels, as shown in Figs. 3.34(a) and (b). For φ_{O}, the difference between the predicted

Algorithm 2 Gradient boosting

1: Initialize the algorithm with a constant value $\boldsymbol{\rho}$. $\mathbf{F}_0 = \arg\min_{\boldsymbol{\rho}} \sum_{i=1}^{n} L(\mathbf{y}_i, \boldsymbol{\rho})$, where $\mathbf{F}_m$ is the ML model at mth boosting stage of a total of M stages; $\mathbf{y}_i$ is the label vector of ith sample point; L is a differentiable loss function of choice, for example, squared-error loss $L(\mathbf{y}, \mathbf{F}) = \|\mathbf{y} - \mathbf{F}\|_2^2/2$; $n = N_{\text{training}}$.
2: For $m = 1$ to M do:
3: Pseudo-residual $\mathbf{r}_{im} = -[\frac{\partial L(\mathbf{y}_i, \mathbf{F}(\mathbf{x}_i))}{\partial \mathbf{F}(\mathbf{x}_i)}]_{\mathbf{F}(\mathbf{x})=\mathbf{F}_{m-1}(\mathbf{x})}$ for $i = 1 \cdots n$.
4: Fit a regression tree $\mathbf{h}_m(\mathbf{x})$ to pseudo-residuals. Train $\mathbf{h}_m(\mathbf{x})$ using the set $(\mathbf{x}_i, \mathbf{r}_{im})$, $i = 1 \cdots n$.
5: $\boldsymbol{\rho}_m = \arg\min_{\boldsymbol{\rho}} \sum_{i=1}^{n} L(\mathbf{y}_i, \mathbf{F}_{m-1}(\mathbf{x}) + \boldsymbol{\rho} \circ \mathbf{h}_m(\mathbf{x}_i))$.
6: $\mathbf{F}_m(\mathbf{x}) = \mathbf{F}_{m-1}(\mathbf{x}) + \boldsymbol{\rho} \circ \mathbf{h}_m(\mathbf{x})$.
7: End For.
8: Output $\mathbf{F}_M(\mathbf{x})$ as the final trained model.
9: Predict labels of test data $\hat{\mathbf{y}}_i = \mathbf{F}_M(\mathbf{z}_i)$, $i = 1 \cdots n'$, where $n' = N_{\text{test}}$.

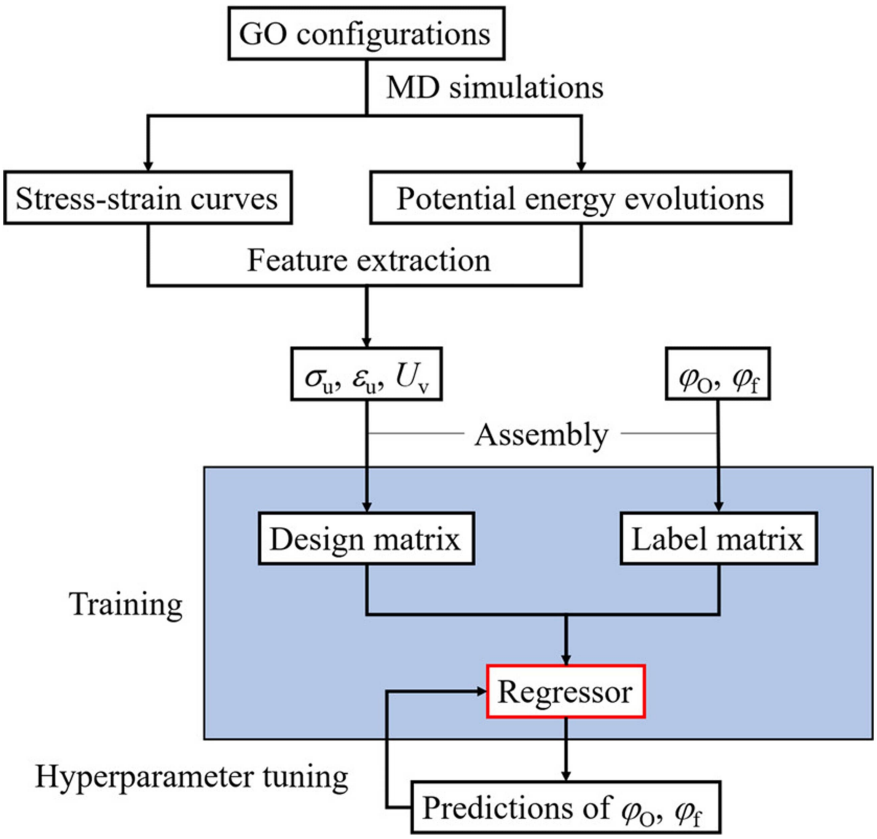

Figure 3.30: Flow-chart presentation of the ML procedure.

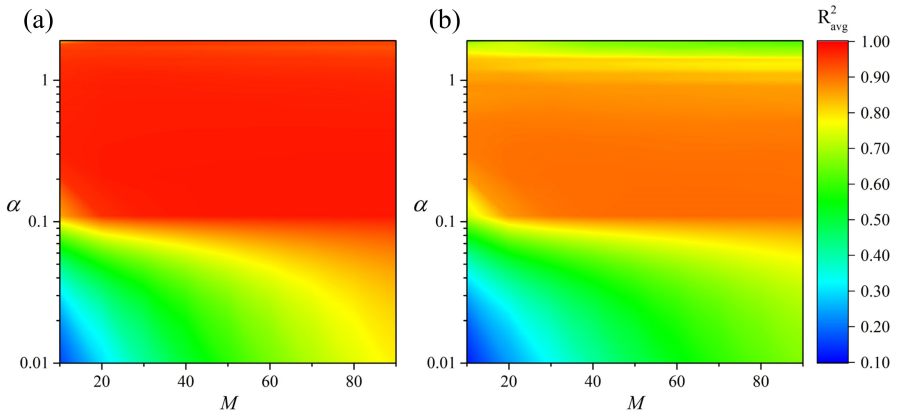

Figure 3.31: Hyperparameter tuning results of gradient boosting. R^2_{avg} as a function of (a) M and (b) α on validation data.

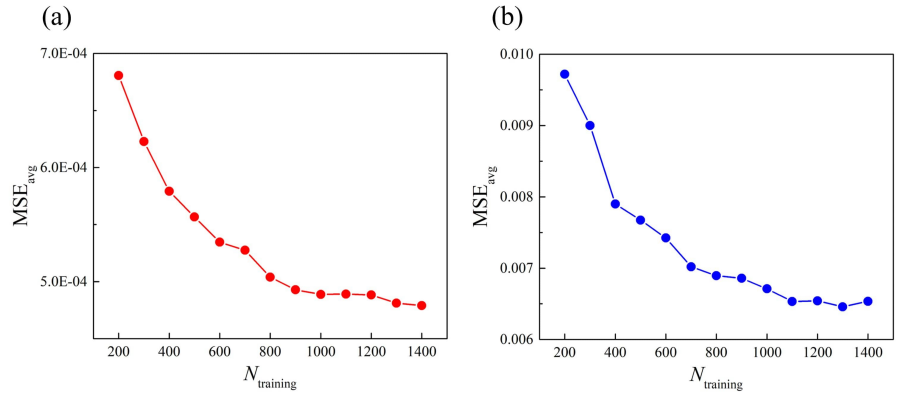

Figure 3.32: MSE_{avg} of φ_{O} and φ_{f} on the validation data as a function of N_{training}. Results of (a) φ_{O} and (b) φ_{f}. Hyperparameters of gradient boosting in this case are $\alpha* = 0.11$ and $M* = 70$

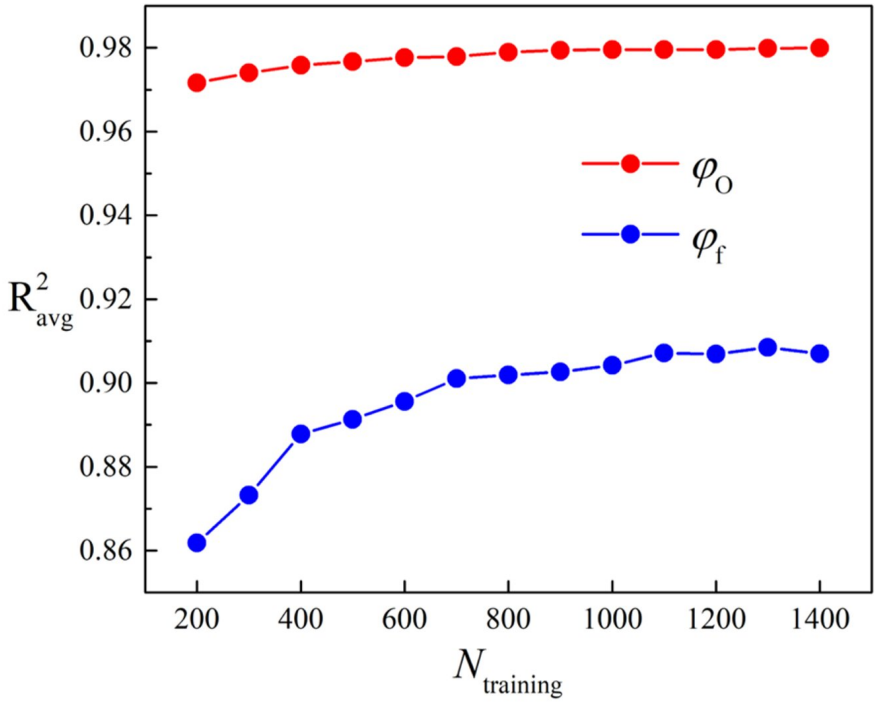

Figure 3.33: R^2_{avg} of φ_{O} and φ_{f} on the validation data as a function of N_{training}. Hyperparameters of gradient boosting in this case are $\alpha* = 0.11$ and $M* = 70$

label and the true label for most sample points ranges within ± 0.06, and for φ_{f}, the difference for most sample points ranges within ± 0.02 (excluding one sample point with a true label $\varphi_{\text{f}} = 1.0$. For both labels, no dependency of prediction error on the absolute value of true label is detected. Based on the results of Figs. 3.34(a) and (b), histograms of $|d_{\text{O}}|$ and d_{f} are constructed, as shown in Figs. 3.34(c) and (d). For φ_{O}, 63% of GO sheets achieved an error of $< 1\%$, while 99% of GO sheets achieved an error of $< 5\%$. For φ_{f}, 58% of GO sheets achieved an error of $< 5\%$, while 95% of GO sheets achieved an error of $< 20\%$.

Additionally, a KRR model (Alg. 1) is used to make predictions. Tunable hyperparameters include polynomial kernel degree p and regularization parameter λ. The hyperparameter tuning results of φ_{O} and φ_{f} in the training session are presented in Fig. 3.35. It is observed that for both φ_{O} and φ_{f}, R^2_{avg} and MSE_{avg} are rather insensitive to p and is a monotonic increasing function of λ. Therefore, an optimal hyperparameter choice is a small λ plus a moderate p, for example, $\lambda* = 10^{-7}$ and $p* = 3$, which scores $R^2_{\text{avg}} = 0.983$ and $\text{MSE}_{\text{avg}} = 0.000405$ for φ_{O}, and $R^2_{\text{avg}} = 0.829$ and $\text{MSE}_{\text{avg}} = 0.0103$ for φ_{f}. Using above hyperparameters $\lambda*$ and $p*$, KRR scores $R^2 = 0.978$ and $\text{MSE} = 0.000499$ for φ_{O}, and $R^2 = 0.870$ and $\text{MSE} = 0.0103$ for φ_{f} on the test set. While having achieved a comparable performance predicting φ_{O} with respect to gradient boosting, KRR does a worse job in

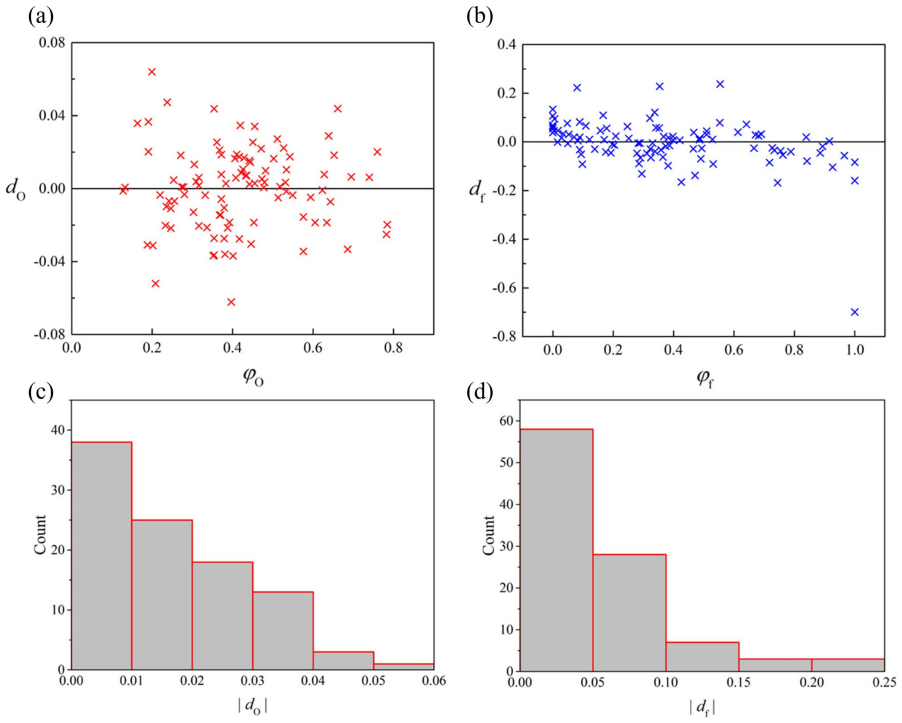

Figure 3.34: Evaluation of ML prediction accuracies of φ_O and φ_f on the test data. Scatter plots of (a) d_O against φ_O and (b) d_f against φ_f. Histograms of (c) $|d_O|$ and (d) $|d_f|$. The data point with a d_f of ~ -0.7 is not represented in (d).

predicting φ_f. Setting $\lambda = 0$ and $p = 1$, KRR degenerates to a multivariate least-squares regression, which scores $R^2 = 0.983$ and MSE $= 0.000380$ for φ_O, and $R^2 = 0.747$ and MSE $= 0.0202$ for φ_f on the test set. Despite a still competent prediction on φ_O, prediction on φ_f has deteriorated. This indicates that ML techniques have offered significant improvement over ordinary regression.

Discussion

One observation regarding the prediction of φ_O and φ_f is that the former can be more accurately predicted with models varying from gradient boosting to multivariate least squares regression, while the latter is far more demanding. In fact, using only U_V, the gradient boosting model can yield a R^2 of ~ 0.9, as shown in Fig. 3.36. A R^2 close to 1 can be achieved if all features are used for both gradient boosting and KRR models. The rationale is that φ_O is directly related to the molecular weight of GO, which poses a major effect on the potential energy especially when GO is at rest (when U_V is extracted). Assisted by features related to mechanical stress and strain, φ_O can be accurately pinned down. Meanwhile,

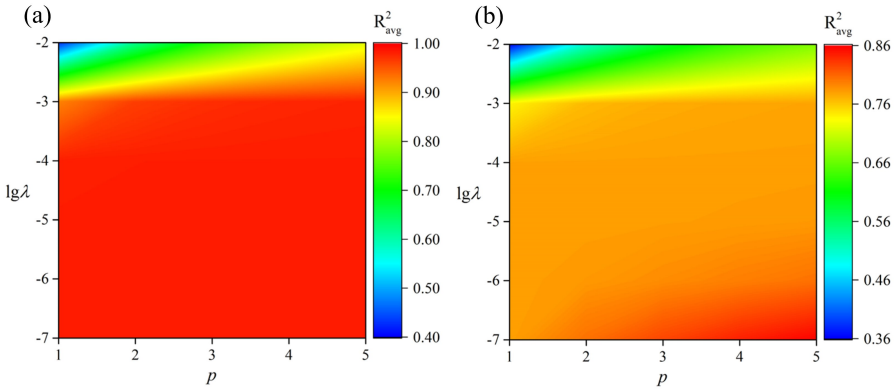

Figure 3.35: Hyperparameter tuning results of KRR. R^2_{avg} as a function of (a) λ and (b) p on validation data.

φ_{f} contains little molecular weight information. The composition of functional groups does not have a significant impact on the potential energy as molecular weight, reflected by the failure to predict φ_{f} with only U_{V}. Instead, φ_{f} dictates the types of bonding interaction, making the difference between hydroxyl and epoxide group properties to play a major role under different φ_{f} values. For example, the difference in failure mechanisms of hydroxyl and epoxide groups begins to take effect. Hydroxyl groups lead to a brittle failure mechanism where only C-C bonds are broken. Each hydroxyl group attaches to only one carbon atom on the basal plane, and the failure associated with a hydroxyl group happens only to one of the C-C bonds in its immediate vicinity. The C-O bonds in hydroxyl groups remain intact at all times. Conversely, epoxide groups can result in a progressive, ductile failure. Each epoxide group attaches to two bonded carbon atoms on the basal plane. If stress causes the bond between these two carbon atoms to break, the two initially bonded carbon atoms can still be connected by two C-O bonds, transforming the epoxide group to a new ether group. These two C-O bonds can continue to stretch and bear loads. After the stress reaches the C-O bond strength, one of the two C-O bonds will break and result in the failure of the local area. It is possible that the C-O bond strength is never reached. This happens when a catastrophic failure of the GO sheet has already taken place caused by crack propagation elsewhere. In addition, the mechanical properties of epoxide groups are sensitive to orientation. If the two bonded carbon atoms are aligned in the stretching direction, the epoxide group is more likely to fail; if the two bonded carbon atoms are perpendicular to the stretch, the epoxide group is less likely to fail. The above mechanisms together with random functional group spatial distributions increase the problem complexity drastically. One possibility to tackle the elevated complexity is to train neural networks with entire stress–strain curves as the input vectors, inspired by Ref. [92].

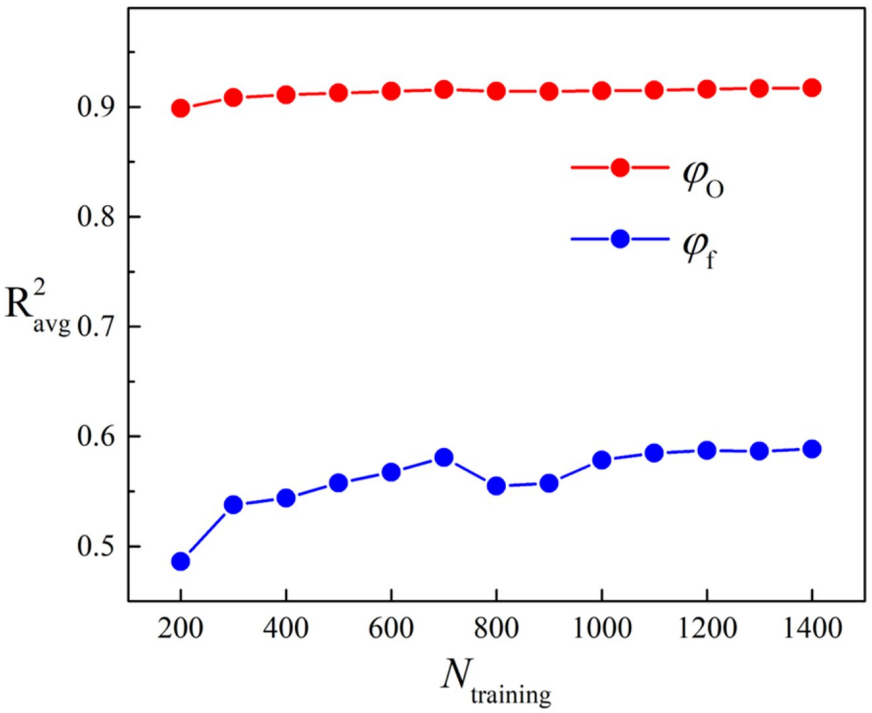

Figure 3.36: R^2_{avg} P of φ_O and φ_f on the validation data as a function of $N_{training}$ where the feature is only U_V. Results of (a) φ_O and (b) φ_f. Hyperparameters of gradient boosting in this case are $\alpha* = 0.11$ and $M* = 70$.

Concluding remarks

In this section, an ML strategy to determine the functional group contents of monolayer GO sheets is developed. By constructing a feature space with stress-based and energy-based mechanical responses computed by reactive MD simulations, the oxygen-to-carbon atom ratio and the relative concentrations of epoxide and hydroxyl groups in GO are predicted by gradient boosting. Despite the uncertainty brought by the random, uncontrolled functional group spatial distributions, the feature selection from both stress–strain relation and system potential energy enables the model to overcome this issue. The best prediction results of the reserved test data show that for the oxygen-to-carbon atom ratio, all test samples have achieved a prediction error of $< 5\%$, while for the fraction of epoxide groups, 95% of the test samples have achieved a prediction error of $< 20\%$. The difference in prediction accuracies between the oxygen coverage and the functional group composition is rationalized by GO molecular mechanisms. The proposed data-driven strategy may also shed light on the predictive modeling and identification of functionalized two-dimensional materials of a broad variety [217].

3.4 Graphene oxide design using deep reinforcement learning

The total amount and the relative ratio of functional groups dictate the chemical composition, which plays a central role in influencing the mechanical properties of GO. However, the mechanical property of a GO cannot be accurately inferred from only its chemical composition. Given one specific chemical composition, there can exhibit a range of GO mechanical properties, due to the variability in the functional group spatial distribution on the GBP. Research has shown that the functional group distribution can impact GO properties such as plasticity and ductility due to the mechanochemical interactions between functional groups [181]. One mechanical property of interest is toughness, defined as the amount of energy per unit volume that a material can absorb before rupturing. It quantifies the ability of a material to absorb energy and plastically deform without fracturing, thus requiring a balance of strength and ductility. GOs with high toughness are much desired, which can potentially enhance the performances of many GO-based applications such as nanocomposites, flexible electronics, among others.

Given a specific chemical composition such as the oxygen-to-carbon ratio and the relative concentrations of functional groups, the goal is to maximize the toughness of GO by altering only the functional group spatial distribution. The existing literature has not sufficiently addressed this problem, and presumes that the effect of functional group distribution is secondary. From the perspective of optimization, it is a challenging task and has the following difficulties. First, optimizing over functional group distribution is in essence a combinatorial optimization problem, which can be NP-hard and analytically intractable, especially when the problem dimension is large. Second, the problem involves complex functional group interactions that evolve over time. There is little intuition about where to place functional groups at the beginning such that the GO will benefit in the long run. Third, both GO simulations and experiments can be expensive. Hence, an effective, data-efficient optimization strategy is highly valued.

Reinforcement learning (RL), a mathematical formalism for learning-based decision making, describes an approach where an agent performs sequential actions based on interactions with an environment so as to yield the most cumulative rewards25. When integrated with deep neural networks and advanced computing, the capability of RL is greatly amplified: Deep neural networks can process high-dimensional input, while RL can choose complex actions. Deep RL applications are numerous. One of the most famous examples is the achievement of superhuman performance in the game Go, which is once considered an insurmountable task given the complexity of more than 10140 possible solutions. In the context of materials science, deep RL has been gaining ground in molecule discovery and microstructure design. Moreover, deep RL also has an advantage in solving difficult combinatorial optimization problems. For these problems, many traditional algorithms involve using hand-crafted heuristics that sequentially construct a solution. Nevertheless, the design of such heuristics can be a daunting task that requires domain expertise, and can often be suboptimal due

to the difficult combinatorial nature of the problems. Therefore, the idea to infer heuristics without human intervention is enticing. Deep RL has shown promise to learn efficient heurists to tackle these problems, and has been used to solve combinatorial optimization problems such as the Traveling Salesman Problem, the Maximum Cut Problem, and the Bin Packing Problem.

In this Section, a deep RL framework is developed to design mechanically tough GOs by optimizing over the functional group distribution. In the deep RL framework, the task of functional group assignment is formulated as a sequential (Markov) decision process, where the state is the current functional group distribution on the GBP and the action is to assign a new functional group. A policy-gradient RL model is employed to maximize GO toughness, which is calculated by reactive MD simulations. Experiments of four difficulties are designed to gradually challenge the deep RL model, and each difficulty consists of two experiments featuring two oxidation levels. The deep RL model should have the following characteristics: (1) stable generation of mechanically tough GO configurations; (2) good scalability in terms of functional group density and GBP size; (3) tractable computation given the large design space.

Results

Molecular modeling

In the present study, a majority of GOs are based on GBPs that comprise a total of 94 carbon atoms, where 28 functional group-free atoms near two opposite edges are clamped to enforce displacement, and 66 free-to-move atoms in the middle are active hosts for functional groups (referred to as the host atoms hereafter, and the number of these atoms are denoted by n_c), as shown in Fig. 3.37(a). Later in more complex experiments a larger GBP that is roughly twice the size will be used. In the GO model only hydroxyl and epoxide groups are considered, and less important carbonyl and carboxyl groups on GBP edges are omitted. Fig. 3.37(b) shows an example GO model and illustrates the molecular structures of hydroxyl and epoxide groups. Each hydroxyl group resides on only one carbon atom, while each epoxide group takes on two neighboring carbon atoms. This difference adds to the optimization difficulty when both functional groups are present on the GBP. In addition, these functional groups can be attached to either side of the GBP. For the loading condition, the GO sheet is subjected to uniaxial tensile loading with a constant loading speed in the zigzag direction of the GBP. The mechanical responses of GOs are computed by reactive MD simulations, which are favorable in modeling the failure of nanomaterials because they account for bond breaking and formation.

ReaxFF potential, a reactive force field, is used to model the interactions among carbon, hydrogen and oxygen atoms in GOs. ReaxFF potential models both non-bonded interactions such as van der Waals and Coulomb interactions, and bond breaking and formation. Specifically, potential parameters developed in Ref. [31] are used. Periodic boundary conditions are applied in all three spatial dimensions. The size of the simulation box is 58.5 Å

by 21.4 Å by 15.2 Å for Easy, Medium, and Hard experiments, and is 63.3 Å by 25.6 Å by 15.2 Å for Extra Hard experiments (to be detailed later). The equations of motion are integrated with a timestep of 0.1 fs using the Verlet algorithm, which ensures the computational stability. The trajectories, velocities, forces, and energies of all atoms are recorded every 10 timesteps. To simulate tensile loading at room temperature, an ensemble of random velocity corresponding to the temperature 300 K is firstly generated throughout all atoms. Then an equilibrium is realized by running a simulation in the NPT ensemble with a Nose–Hoover thermostat at the same temperature for 5000 timesteps. The loading scenario is simulated in the NVT ensemble at 300 K. The unidirectional in-plane tensile load is applied along the zigzag direction based on a deformation-control manner until failure. The loading speed is 1000 $\mathrm{m} \cdot \mathrm{s}^{-1}$. The components of stress tensor $[\sigma]$ are calculated by Eqs. 2.2 and 2.3. In this study, $t_\mathrm{e} = 7.76$ Å is used, the inter-layer spacing of GOs measured in experiments.

It is observed in simulations that given the same amount of hydroxyl and epoxide groups, different functional group distributions can result in substantially different stress-strain relations and failure behaviors. Examples are given in Figs. 3.37(c) and (d). GOs in Figs. 3.37(c) and (d) have the exact same amount of hydroxyl and epoxide groups, but Fig. 3.37(c) shows a brittle rupture while Fig. 3.37(d) shows a more ductile failure that involves considerable new bond formation and configuration change. Fig. 3.37(e) compares the stress-strain curves of the two GOs above. It is shown that GO in Fig. 3.37(d) is higher in both ultimate stress and failure strain, suggesting superior mechanical properties. The toughness of a material can be expressed as $u = \int_0^{\epsilon_\mathrm{f}} \sigma d\epsilon$, where u is toughness; ϵ is strain; ϵ_f is the strain upon failure; σ is stress. By the definition above, the toughness equals the area under the stress-strain curve. It is calculated that the toughness of GO in Fig. 3.37(d) is 2.1 times that of GO in Fig. 3.37(c). This amount of difference in toughness suggests that the functional group distribution potentially has a profound impact on mechanical properties, and that it is worthwhile to optimize GO mechanical properties over functional group distribution.

Deep reinforcement learning

The optimization problem to solve is given a fixed number of hydroxyl and epoxide groups, how to distribute these functional groups on the GBP so as to maximize the toughness of GO. Instead of treating the optimization problem as choosing the best functional group distribution in one shot, the functional group assigning problem is modeled as a sequential decision process which RL is used to solve. More specifically, each individual functional group is assigned to a location on the GBP at each of a sequence of discrete time steps $t = 0, 1, 2, ..., T$, where T equals the total number of functional groups. From here on, functional group distribution is referred to as functional group locations to emphasize the discreteness of the RL process and not to confuse it with probability distribution. At each t, the RL agent receives the representation of the environment's state $s_t \in \mathcal{S}$, where $\mathcal{S}$ is the state space that comprises all possible states. In this case, s_t is the current functional group locations at time step t, and $\mathcal{S}$ denotes the set of all possible functional group locations on the GBP. s_t is constructed as a one-hot encoded vector, of which the length equals the number of

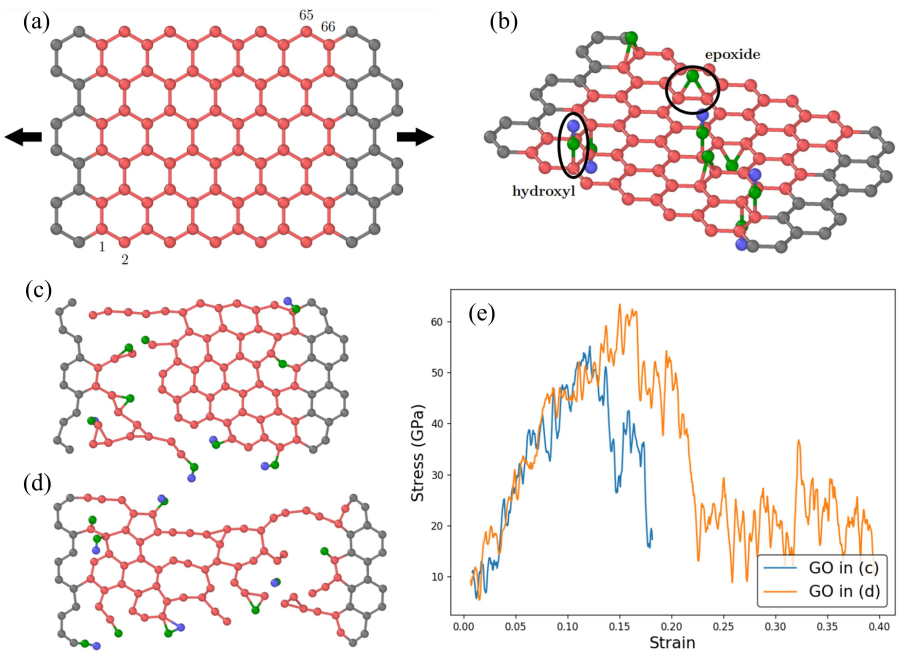

Figure 3.37: GO schematics and mechanical responses. (a) Schematic of GBP, where red atoms (66 in total) are hosts for functional groups while gray atoms are functional group-free atoms on which the tensile loading is exerted. Arrows show the loading direction. (b) Illustrations of hydroxyl and epoxide groups, where green and blue atoms are oxygen and hydrogen atoms, respectively. (c) Fracture of a low-toughness GO under tension. (d) Fracture of a high-toughness GO under tension. (e) Stress-strain curves of GOs in (c) and (d).

all possible spots for functional groups on the GBP. For example, if only hydroxyl groups are assigned to only one side of GBP that comprises 66 host atoms (one of the experiments to be introduced later), the length of s_t is 66 since there are 66 spots in total for hydroxyl groups. If both hydroxyl and epoxide groups are assigned, the length of s_t will increase to account for all possible spots for epoxide groups. If the ith spot has been assigned a functional group, the value of the ith entry of s_t, $s_t[i]$, is 1; otherwise, $s_t[i]$ is 0. The number of 1's in s_t equals the number of functional groups that have already been assigned at time step t.

After receiving a state s_t, the RL agent selects an action $a_t \in \mathcal{A}(s_t)$, where $\mathcal{A}(s_t)$ is the set of legal actions given state s_t. In this case, a_t is to assign a functional group to a functional group spot on the GBP, and $\mathcal{A}(s_t)$ is the set of all available functional group spots left given s_t. a_t is also a one-hot encoded vector, of which the length equals the number of possible spots for assigning a specific type of functional groups. In the RL framework, a_t is different from s_t in that a_t only accounts for one specific type of functional group (either hydroxyl or epoxide group) while s_t accounts for both types. If the action is to assign a functional

Table 3.1: Neural network input and output dimensions for all experiment difficulties. For Hard and Extra Hard output, the first number refers to the hydroxyl network and the second number refers to the epoxide network.

	Easy	Medium	Hard	Extra Hard
input (s_t)	66	132	308	570
output ($\pi(\cdot\|s_t)$)	66	132	132; 176	240; 330

Table 3.2: Neural network parameters for all experiments.

	Easy		Medium		Hard		Extra Hard	
	low	high	low	high	low	high	low	high
hidden layer number	2	2	2	2	2	2	2	2
hidden layer size	200	400	300	600	600	800	800	800
initial learning rate	1e-3	1e-3	1e-3	1e-3	1e-3	5e-4	1e-3	1e-3

group to ith spot among all possible spots, $a_t[i] = 1$. Because each action is restricted to the assignment of one functional group, there will only be one 1 entry in a_t. At each time step, the RL agent maps the current state to probability distribution over all actions. This mapping is called a policy, denoted as π_θ, where $\pi_\theta(a_t|s_t)$ is the probability that the selecting the action a_t if the state is s_t under the policy parameter θ, i.e., $\pi_\theta(a_t|s_t) = \mathbb{P}(a_t|s_t;\theta)$. Because of the complex nature of the functional group assignment task, in the present work neural networks are used to model the policy π_θ, where θ is the neural network parameters including weights and biases. Fully connected neural networks of various sizes and ReLU activations are used. At the last layer a fully connected layer is used followed by a softmax activation which outputs the probability distributions of actions, as a way to address the exploration-versus-exploitation dilemma. The input and output dimensions in different experiments are summarized in Table 3.1.

Next the probabilities of selecting invalid actions are set zero and the distribution is re-normalized such that the sum of the probabilities of all legal actions at each time step equals 1. An Adam optimizer is used. Learning rate shrinks by a factor of two every 500 iterations, but is set no smaller than 5e-5. The sizes and initial learning rates used in all experiments are summarized in Table 3.2. Weights and biases are initialized from $\mathcal{U}(-1/\sqrt{d_{in}}, 1/\sqrt{d_{in}})$, where $\mathcal{U}$ denotes a uniform distribution, and d_{in} denotes the dimensionality of the input for each layer.

In addition, a_t is strictly enforced by the hybridization condition of host atoms on the GBP, which requires that one host atom can be only associated with one functional group. Therefore, after each functional group assignment, one or more actions will become infeasible for the next time step, and the possibilities of selecting these actions will be set to zero. After

taking an action a_t at state s_t, the agent enters a new state s_{t+1}, and this process is called a state transition. In the context of the present research, after assigning a functional group to the current GO, a new GO is obtained. State transitioning function $f(s, a, \xi)$ defines the successor state after selecting action a in a state s and random input ξ. In the present research the state transitions are deterministic, $f(s, a, \xi) = f(s, a)$. The state transition process involving policy network and action is illustrated in Fig. 3.38(a). A trajectory is formulated as $\mathcal{T} = \{s_0, a_0, s_1, a_1, ..., s_{T-1}, a_{T-1}, s_T\}$, and GO configurations throughout a whole example trajectory are shown in Fig. 3.38(b). Notably, these states have the Markov property, where the future states depend only upon the current state, not on the past states, i.e., $\mathbb{P}(s_{t+1}|s_t, s_{t-1}, ..., s_1, s_0) = \mathbb{P}(s_{t+1}|s_t)$. The functional group positions on the GBP serves as a Markov state which summarizes the functional group assignment history that has led up to it. Upon entering a new state s_{t+1}, the RL agent also receives a numerical reward $r_{t+1} = r(s_t) \in \mathbb{R}$. The reward is crafted as:

$$r(s_t) = \begin{cases} 0 & t < T \\ \hat{u}(s_t) & t = T \end{cases} \tag{3.7}$$

where $\hat{u}(s_t)$ is standardized toughness given by

$$\hat{u}(s_t) = \frac{u(s_t) - \mu_u}{\sigma_u} \tag{3.8}$$

where μ_u and σ_u are the mean and the standard deviation of random GOs. The goal of RL is to maximize the expected return, where the return is a function of the reward sequence. However, based on the reward setting above, the agent will only receive a non-zero reward at the terminal step. This is inspired by the AlphaGo research where the agent only receives a non-zero reward when the game ends: $r = 1$ if the agent wins the game; $r = -1$ if the agent loses the game [152]. In this study, policy gradient algorithms are used to maximize the expected return, which directly optimizes a parametrized policy via gradient descent. Concretely, for a policy $\pi_\theta(a|s)$ parametrized by θ, the change of parameter after each episode (sampling a full trajectory $\mathcal{T}$) is given by

$$\Delta\theta = \frac{\partial}{\partial\theta}\left(\sum_{t=1}^{T} \log \pi_\theta(a_t|s_t)\right)\left(\sum_{t=1}^{T} r(s_t)\right) \tag{3.9}$$

The parameter update follows $\theta \leftarrow \theta + \alpha\Delta\theta$, where α is the current learning rate.

To conduct GO optimization using RL, experiment complexity increases progressively and four levels of difficulty are designed: Easy, Medium, Hard, and Extra Hard. For Easy experiments, only hydroxyl groups are assigned to only one side of the GBP. For Medium experiments, only hydroxyl groups are assigned to the GBP, but they can be assigned to both sides of the GBP. Medium experiments are more complex than Easy experiments in that the state space and the action space are doubled in size. For Hard experiments, both hydroxyl and epoxide groups are assigned to the GBP, and they can be assigned to both

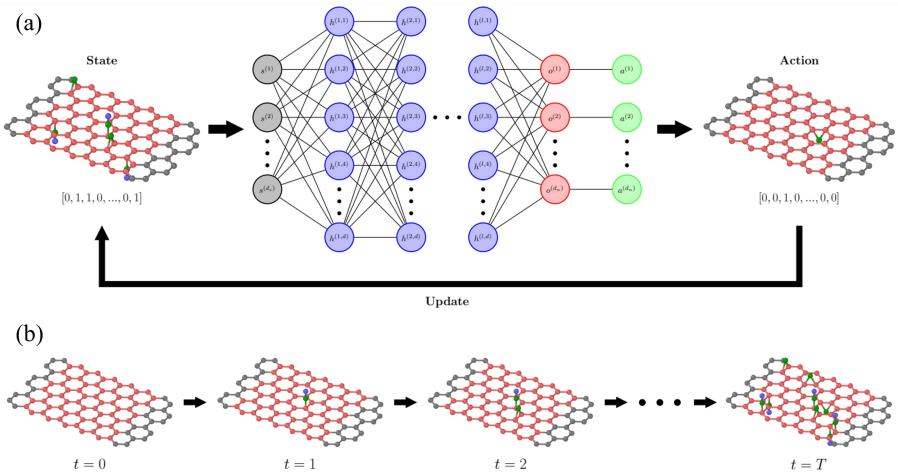

Figure 3.38: Deep RL state transition and trajectory. (a) Illustration of deep RL policy and state transition. (b) An example full trajectory.

Table 3.3: Experiment difficulty descriptions.

Difficulty	Description
Easy	Assigning only hydroxyl groups on only one side of the GBP
Medium	Assigning only hydroxyl groups on both sides of the GBP
Hard	Assigning hydroxyl and epoxide groups on both sides of the GBP
Extra Hard	Assigning hydroxyl and epoxide groups on both sides of a larger GBP

sides of the GBP. The settings of Hard experiments resemble GOs in reality and involve competition between hydroxyl and epoxide groups. Extra Hard experiments are similar to Hard experiments but a larger GBP is used, consisting of 120 functional group hosts compared with 66 in all previous experiments. The descriptions of all experiment difficulties are summarized in Table 3.3.

In addition, each difficulty consists of two oxidation levels: low and high, where the former has an oxygen-to-carbon ratio around 15% while the latter doubles that. The Extra Hard difficulty is used to test the scalability in terms of the GO size, while the different oxidation levels are for the scalability with respect to the functional group density. In summary, there are 8 different experiments in total that challenge the deep RL algorithms, and the result of each experiment is evaluated based on 4 different random seeds. The numbers of hydroxyl and epoxide groups, and host atoms are summarized in Table 3.4.

In all experiment, illegal actions can be simply stated as assigning a functional group to an already occupied carbon atom on the GBP. However, as the difficulty increases, the elimination of illegal actions becomes an increasingly delicate process. For Easy experiments,

Table 3.4: Summary of the number of hydroxyl groups n_{h}, the number of epoxide groups n_{e}, and the number of carbon atoms that are hosts for functional groups n for all experiments.

	Easy			Medium			Hard			Extra Hard		
	n_{h}	n_{e}	n_{c}	n_{h}	n_{e}	n_{c}	n_{h}	n_{e}	n_{c}	n_{h}	n_{e}	n_{c}
low oxidation	10	0	66	10	0	66	5	4	66	9	8	120
high oxidation	20	0	66	20	0	66	10	8	66	18	16	120

Table 3.5: Summary of statistics of random GOs in all experiments (unit: GPa).

	Easy		Medium		Hard		Extra Hard	
	μ_u	σ_u	μ_u	σ_u	μ_u	σ_u	μ_u	σ_u
low oxidation	7.814	1.299	7.668	1.259	7.120	1.326	8.108	1.340
high oxidation	7.694	1.368	7.245	1.355	6.236	1.249	7.115	1.310

because the lengths of one-hot encoded $\mathbf{s}_t$ and $\mathbf{a}_t$ are the same and equal to the number of the host atoms, n_{c}. Invalid actions can be eliminated by simply setting $\mathbf{a}_t[i] = 0$ where $\mathbf{s}_t[i] = 1$, $i \in [0, 1, ..., n_{\mathrm{c}} - 1]$. For Medium experiments, the lengths of $\mathbf{s}_t$ and $\mathbf{a}_t$ are both equal to $2n_{\mathrm{c}}$. If a host atom has been assigned a hydroxyl group regardless of which side of the GBP the hydroxyl group is on, assigning a hydroxyl group to this host atom from either side of the GBP is an invalid action. Therefore, the elimination of invalid actions can be done by setting $\mathbf{a}_t[i] = 0$ and $\mathbf{a}_t[i + n_{\mathrm{c}}] = 0$ where $\mathbf{s}_t[i] = 1$, $i \in [0, 1, ..., n_{\mathrm{c}} - 1]$, and setting $\mathbf{a}_t[i] = 0$ and $\mathbf{a}_t[i - n_{\mathrm{c}}] = 0$ where $\mathbf{s}_t[i] = 1$, $i \in [n_{\mathrm{c}}, n_{\mathrm{c}} + 1, ..., 2n_{\mathrm{c}} - 1]$. For Hard and Extra Hard experiments where both hydroxyl and epoxide groups are involved, the elimination of invalid action is more complex. The general approach is to keep track of the atom indices involved in previously assigned functional groups and determine invalid actions based on which functional group to assign next. To computed the reward formulated in Eq. 3.7, the mean μ and σ of random GO configurations need to be calculated. The statistics of 2000 random GOs in all experiments are summarized in Table 3.5.

The algorithm also varies with experiments. For Easy and Medium experiments, only one policy network π_θ is used to map the state to a probability distribution of all legal actions, i.e, assigning a hydroxyl group to an available spot. However, for Hard and Extra Hard experiments, two policy networks are needed to assign two types of functional groups. The networks for hydroxyl groups and epoxide groups are denoted by π_θ^h and π_ρ^e, where θ and ρ are respective network parameters. Next, the sequence of assigning hydroxyl and epoxide groups needs to be decided on. Because a non-zero reward is observed only at the terminal step, only the network that assigns the last functional group will get its parameters updated via backpropagation. Therefore, the assignment sequence cannot be a deterministic one since both networks need to be improved. To this end, a Bernoulli distribution

`Bernoulli`$(m_h/(m_h+m_e))$ is used to sample the index of network used at each step, where m_h and m_e are the numbers of hydroxyl and epoxide groups left to assign at the current time step. This approach randomizes the sequence of functional group assignment in each episode and give both networks an opportunity to update parameters. The pseudo-codes of these two policy gradient algorithms are summarized in Algs. 3 and 4. Fig. 3.39 shows the deep RL optimization results for all eight experiments. The numerical value of the return represents how many standard deviations the design is above the mean of random GOs with the same amount of functional groups (summarized in Table 3.5). It is shown in Figs. 3.39(a-c) that the final returns in the Easy, Medium and Hard experiments reach an average return around 3, suggesting that the RL generated GO functional group distributions have a higher toughness than roughly 99.87% of all GO configurations. In the Extra Hard experiments, the model achieves returns above 2, thus beating 97.73% of all GOs (Fig. 3.39(d)). In addition, all experiments reach a local maximum within only 5000 episodes (no more than 5000 MD simulations are run for each experiment), which is much smaller than the number of possible GO configurations. For the Easy difficulty, the low-oxidation and high-oxidation experiments have $C_{10}(66) = 2.1 \times 10^{11}$ and $C_{20}(66) = 4.1 \times 10^{16}$ possible functional group arrangements, and there are even much more arrangement possibilities for more difficult experiments. Last but not least, good performances in experiments of different oxidation levels and the Extra hard experiments suggests that out RL design approach is scalable in terms of the functional group density and the GO size. The distribution histograms of the RL design within first 2000 episodes (to compare with the distribution of 2000 random GOs) and full 5000 episodes are provided in Fig. 3.40.

Algorithm 3 Policy gradient for Easy and Medium experiments

Require: $n_{\mathrm{h}} > 0$, $n_{\mathrm{e}} = 0$ ▷ only hydroxyl groups

initialize π_θ
while `TRUE` **do**
  initialize zero $\mathbf{s}_0$ vector and empty list $\mathcal{L}$
  $T \leftarrow n_{\mathrm{h}}$
  for $t = 0, ..., T-1$ **do**
    obtain action distribution $\pi_\theta(\cdot|\mathbf{s}_t)$ ▷ feed $\mathbf{s}_t$ to policy network
    set invalid action probabilities to zero
    re-scale action distribution $\pi_\theta(\cdot|\mathbf{s}_t)$
    $\mathbf{a}_t \leftarrow \pi_\theta(\cdot|\mathbf{s}_t)$`.sample()` ▷ sample an action from action distribution
    append tuple $(\mathbf{a}_t, \pi_\theta(\cdot|\mathbf{s}_t))$ to $\mathcal{L}$
    $\mathbf{s}_{t+1} \leftarrow \mathbf{s}_t + \mathbf{a}_t$ ▷ update state with action
  end for
  collect terminal reward $r(\mathbf{s}_T)$ ▷ run MD simulation
  $\Delta\theta = \frac{\partial}{\partial\theta}\left(\sum_{t=0}^{T-1} \log \pi_\theta(\mathbf{a}_t|\mathbf{s}_t)\right) r(\mathbf{s}_T)$
  $\theta \leftarrow \theta - \alpha\Delta\theta$
end while

Algorithm 4 Policy gradient for Hard and Extra Hard experiments

Require: $n_{\mathrm{h}} > 0$, $n_{\mathrm{e}} > 0$ ▷ both hydroxyl and epoxide groups
initialize π_θ^{h} and π_ρ^{e}
while `TRUE` **do**
  initialize zero $\mathbf{s}_0$ vector and empty lists $\mathcal{L}_{\mathrm{h}}$ and $\mathcal{L}_{\mathrm{e}}$
  $m_{\mathrm{h}} \leftarrow n_{\mathrm{h}}$, $m_{\mathrm{e}} \leftarrow n_{\mathrm{e}}$
  $t \leftarrow 0$
  while $m_{\mathrm{h}} + m_{\mathrm{e}} > 0$ **do**
    $i_{\mathrm{net}} \leftarrow$ `Bernoulli`$(m_{\mathrm{h}}/(m_{\mathrm{h}} + m_{\mathrm{e}}))$`.sample()` ▷ choose a neural network
    if $i_{\mathrm{net}} == 1$ **then**
      $\pi \leftarrow \pi_\theta^{\mathrm{h}}$, $m_{\mathrm{h}} \leftarrow m_{\mathrm{h}} - 1$
    else
      $\pi \leftarrow \pi_\rho^{\mathrm{e}}$, $m_{\mathrm{e}} \leftarrow m_{\mathrm{e}} - 1$
    end if
    obtain action distribution $\pi(\cdot|\mathbf{s}_t)$ ▷ feed $\mathbf{s}_t$ to policy network
    set invalid action probabilities to zero
    re-scale action distribution $\pi(\cdot|\mathbf{s}_t)$
    $\mathbf{a}_t \leftarrow \pi_\theta(\cdot|\mathbf{s}_t)$`.sample()` ▷ sample an action from action distribution
    if $i_{\mathrm{net}} == 1$ **then**
      append tuple $(\mathbf{s}_t, \pi(\cdot|\mathbf{s}_t), t)$ to $\mathcal{L}_{\mathrm{h}}$
    else
      append tuple $(\mathbf{a}_t, \pi(\cdot|\mathbf{s}_t), t)$ to $\mathcal{L}_{\mathrm{e}}$
    end if
    $\mathbf{s}_{t+1} \leftarrow \mathbf{s}_t + \mathbf{a}_t$
    $t \leftarrow t + 1$
  end while
  $i_{\mathrm{final}} \leftarrow i_{\mathrm{net}}$ ▷ retrieve the network that assigned the final functional group
  collect terminal reward $r(\mathbf{s}_T)$ ▷ run MD simulation
  if $i_{\mathrm{final}} == 1$ **then**
    $\Delta\theta = \frac{\partial}{\partial\theta}\left(\sum_{t\in\mathcal{L}_{\mathrm{h}}} \log \pi_\theta^{\mathrm{h}}(\mathbf{a}_t|\mathbf{s}_t)\right) r(\mathbf{s}_T)$
    $\theta \leftarrow \theta - \alpha\Delta\theta$
  else
    $\Delta\rho = \frac{\partial}{\partial\rho}\left(\sum_{t\in\mathcal{L}_{\mathrm{e}}} \log \pi_\rho^{e}(\mathbf{a}_t|\mathbf{s}_t)\right) r(\mathbf{s}_T)$
    $\rho \leftarrow \rho - \alpha\Delta\rho$
  end if
end while

Discussion

Finally, to gain insights from the perspective of microstructure, the molecular structure and detailed failure behavior are compared between a random GO and an RL-designed GO. The

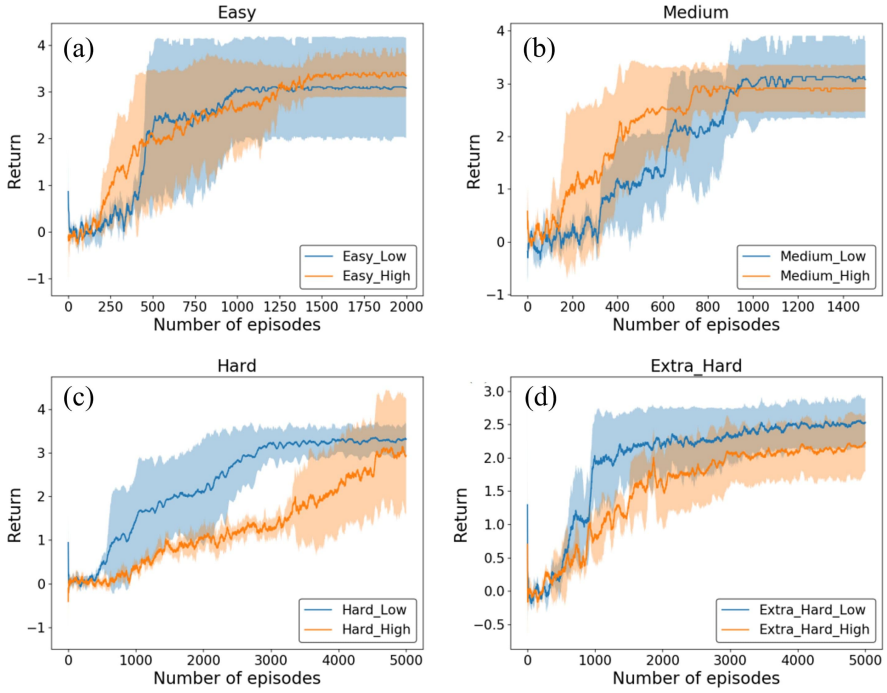

Figure 3.39: Deep RL performances on various experiments. (a) Easy, (b) Medium, (c) Hard, and (d) Extra Hard experiments.

two GO examples are drawn from the Hard, high-oxidation experiment, and the comparison between the two GOs under different strains is shown in Fig. 3.41. From the initial configurations, it is observed that the functional group distribution designed by RL tends to be more spread out than the random GO. Nevertheless, there is little intuition regarding how to design the specific functional group arrangement to achieve a high toughness. As the strain increases, the random GO fractures along a clearly defined path, while the fracture of RL designed GO initiates from multiple spots and forms a network-like structure that involves substantial new bond formation. This phenomenon suggests that the RL designed GO has more atoms contributing to energy absorption, which ultimately leads to a higher toughness (11.88 GPa versus 4.96 GPa for the random GO). To gain more physical insights as for what makes a GO tough, analysis is conducted to locate functional group sites that are more frequently occupied for high-toughness GOs. Concretely, the count of functional group appearances on every possible functional group site for high-toughness GOs for all levels of difficulty is calculated, and the results are shown in Fig. 3.42. It is shown that functional groups on high-toughness GOs seem to more likely distribute near the edges and not at the center. The observation can be interpreted as the following: functional groups generally have a negative effect on the GO toughness, and distributing them away from the center can help

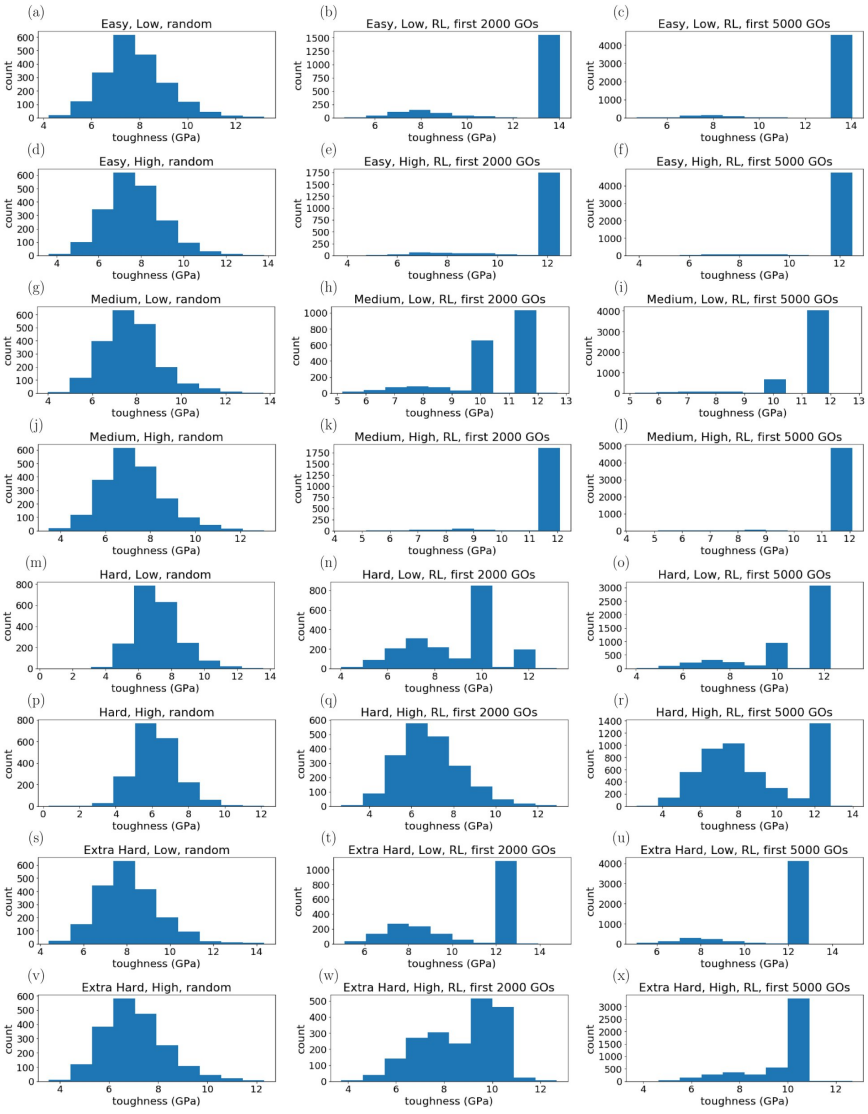

Figure 3.40: Toughness distributions for random and RL-designed GOs. (a-c) Easy, low oxidation experiment. (d-f) Easy, high oxidation experiment. (g-i) Medium, low oxidation experiment. (j-l) Medium, high oxidation experiment. (m-o) Hard, low oxidation experiment. (p-r) Hard, high oxidation experiment. (s-u) Extra Hard, low oxidation experiment. (v-x) Extra Hard, high oxidation experiment.

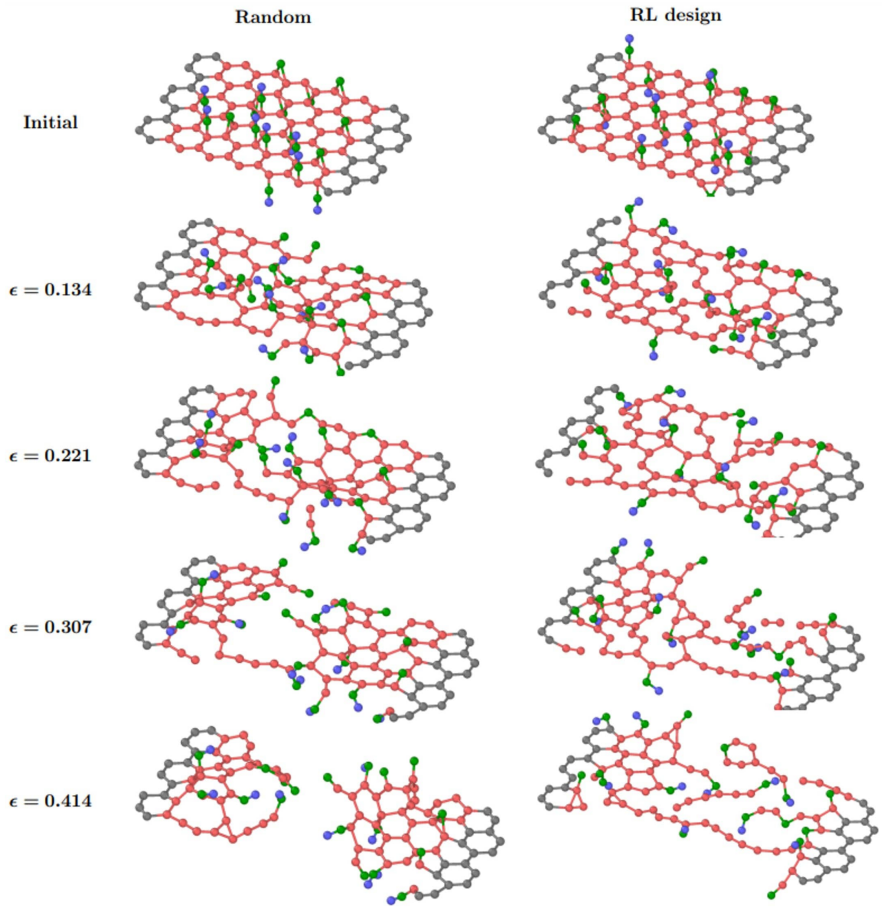

Figure 3.41: Rupturing comparison between a random GO and an RL-designed GO. Examples are from the Hard, high-oxidation experiment.

alleviate this effect. This is supported by the toughness results of random GO configurations, where high oxidation always has a lower mean toughness than low oxidation. However, it is shown that highly occupied functional group sites are not located only near the edges, and some sites inside the GBP also have a high occupancy. This may be explained by the involvement of other more complex mechanisms such as the interaction between functional groups, which emphasizes the necessity of using the RL-based design approach to solve this challenging problem.

The RL framework is on-policy, where the RL agent needs to sample a new trajectory for each episode. In this problem setting, an MD simulation will be called to run at the terminal step of each trajectory to generate the reward according to Eq. 3.7, and this is where the most computation is spent. Future work includes developing a surrogate model that takes the state as the input, and outputs the reward to alleviate the computation of MD

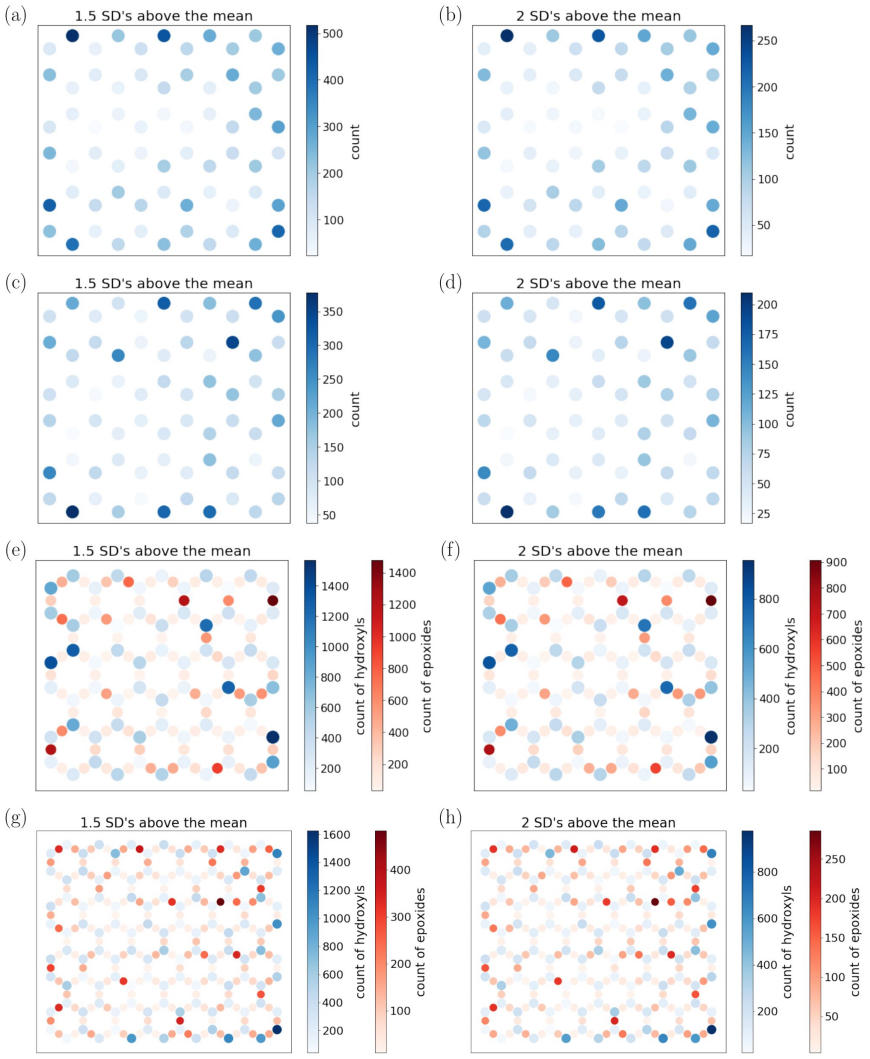

Figure 3.42: Functional group count distributions for high-toughness GOs. Functional group count distributions for GOs (a) 1.5 and (b) 2 standard deviations above the mean for the Easy difficulty. Functional group count distributions for GOs (c) 1.5 and (d) 2 standard deviations above the mean for the Medium difficulty. Functional group count distributions for GOs (e) 1.5 and (f) 2 standard deviations above the mean for the Hard difficulty. Functional group count distributions for GOs (g) 1.5 and (h) 2 standard deviations above the mean for the Extra Hard difficulty.

simulations during RL rollouts. Another issue arises from the present double policy network design. During each episode, only one network can get improved while the other network remains unchanged, which is not particularly a data-efficient algorithm design. In addition, when the numbers of two types of functional groups are imbalanced, the policy network of the minority functional group type may update very slowly. Future work includes designing a better policy network architecture to resolve or mitigate the two issues above.

For heterogeneous or disordered nanoscale systems, the arrangement of defects or functional groups has a major impact on the material properties when the system is small. However, as the system size increases, the effect of individual defect of functional group becomes smaller. It is expected that the potential of optimizing over functional group locations will become less significant. In the future work, the effect of functional group location on the mechanical properties of GOs as a function of the system size and its RL-based optimization capability will be investigated. Another limitation of the present study is that the thermodynamics of designed GOs is not taken into account, meaning the output GO configurations may not be thermally stable. Still, the present deep RL design approach can be of value in the following ways. First, the approach can be used as an effective layer of materials screening. For example, 100 deep RL designs can be generated and a thermodynamic criterion is applied to select both mechanically superior and thermally stable candidates. Second, the reward in the RL algorithm can be modified to favor thermally stable graphene oxides. Concretely, the binding energy per oxygen in the reward can be included

$$E_B = \frac{E_{\mathrm{GO}} - E_{\mathrm{g}} - n_{\mathrm{h}} E_{\mathrm{h}}}{n_{\mathrm{e}} + n_{\mathrm{h}}} \tag{3.10}$$

where E_{GO}, E_{g}, and E_{h} are the total energies of the GO structure, pure graphene, and hydroxyl groups, respectively. Third, the RL approach can be used to efficiently establish an upper bound for GO mechanical properties, given the chemical composition and the size.

Concluding remarks

In summary, a deep RL framework is developed to design GOs with high toughness by optimizing over the functional group distribution. The design task is formulated as a sequential decision process, where the state is the current functional group distribution on the GBP and the action is to assign a new functional group. A policy-gradient RL model is employed to maximize the toughness of GO, which is calculated by reactive MD simulations. Eight experiments with increasing difficulty are devised to gradually challenge the deep RL model. It is shown that in the first six experiments the model can stably generate functional group distributions that achieve a toughness three standard deviations above the mean of random GOs, suggesting that the RL generated GOs have a higher toughness than 98.87% of all GOs. In the final two most difficult experiments, the model achieves two standard deviations above the mean of random GOs, thus beating 97.73% of all GOs. In addition, the RL approach reaches an optimized functional group distribution within only 5,000 rollouts, while the easiest experiment has $C_{10}(66) = 2.1 \times 10^{11}$ possibilities. Finally, it is shown that the RL

design approach is scalable in terms of the functional group density and the GO size. The present research showcases the impact of functional group distribution on GO properties, and illustrates the effectiveness and data efficiency of deep RL in optimizing it [221].

Chapter 4

Simulation and machine learning for graphene aerogel

As a 3D extension of graphene, graphene aerogels (GAs) are well known for their exceptional combination of high strength, lightweightness, and high porosity. For the mechanical properties of GAs, both experimental and computational studies have been conducted. Experimentally, Zhu et al conducted compression tests and measured the compressive stress–strain curves of 3D periodic GA microlattices [229]. Cheng et al showed that a 75.0 mg GA cylinder with a bulk density of 56.2 mg·cm^{-3} could support at least 26000 times its own weight [30]. Zhang et al reported that GA–polydimethylsiloxane composites can sustain a compressive strain up to 80% and a tensile strain up to 90% [208]. Computationally, Qin et al conducted MD simulations to study the mechanics of porous 3D graphene assemblies, and showed that the mechanical properties decrease with density faster than those of polymer foams [139]. Patil et al systematically investigated the fracture behavior [129] and the shock wave response [128] using MD simulations, and showed that GAs can be a promising material for shock wave and energy absorption applications.

4.1 Uncertainty quantification and prediction for mechanical properties

Although recent studies on the mechanics of GAs have been fruitful, the observed high stochasticity of the mechanical properties of GAs remains unaddressed. For example, under a specific material density, GAs show a wide range of Young's modulus and tensile strength. This phenomenon is not particularly surprising, because the microstructures of GAs can be highly random and are difficult to control during the condensation process in both experiments and simulations. Nevertheless, previous studies either have not obtained enough data points under one density, or have largely grappled with this issue by averaging the test results. An understanding and quantitative modeling of the uncertainties in mechanical properties of GAs is crucial for the broader applications of GAs. In addition, MD simula-

tions of GAs can be expensive, mostly because of the time-consuming assembling procedure, which consists of a number of annealing cycles (meanwhile the mechanical testing portion is relatively fast). Therefore, an interpolation method to predict properties of GAs that have not been simulated is much desired.

In this section, Gaussian process metamodels are developed to not only predict important mechanical properties of GAs but also quantify their uncertainties. GAs are firstly assembled and condensed via annealing cycles in the MD simulation, and subsequently subject GAs to a quasi-static uniaxial tensile load to deduce mechanical properties such as the Young's modulus and the ultimate tensile strength. A total of 270 GAs with a range of densities are simulated. Different from previous literature where the mechanical properties of GAs are treated as a function of the density, the density, the Young's modulus and the ultimate tensile strength are considered as functions of the size of the inclusions, which dictates the GA microstructure and thus mechanical properties in a complex fashion. Using the properties of the simulated GAs as the training data, Gaussian process metamodels are developed which not only predict the properties of unseen GAs but also establish statistically valid confidence intervals centered around the predictions.

Molecular modeling

The starting point for GA fabrication in MD simulations comprises of 100 functional group-free square-shaped graphene flakes and 100 spherical inclusions, which mimic the effect of water clusters in freeze-casting porous graphene materials [189], as shown in Fig. 4.1(a). The side lengths of the graphene flakes L are sampled by a log-normal distribution to avoid negative values (illustrated in Fig. 4.1(b)), of which the probability density function is

$$p(L) = \frac{1}{L\sigma_L\sqrt{2\pi}} e^{(-(\log L-\mu)^2/2\sigma_L^2} \tag{4.1}$$

where

$$\sigma_L = \sqrt{\log\left(\frac{L_{\text{std}}}{\bar{L}^2}+1\right)}$$

and

$$\mu = \log\bar{L} - \frac{\sigma_L^2}{2}$$

are functions related to the mean value $\bar{L} = 12$ Å and the standard deviation $L_{\text{std}} = 4.8$ Å. The size of the spherical inclusions is constant, quantified by an effective radius R_{eff}. R_{eff} is given by $R_{\text{eff}} = 2^{1/6}\sigma$, where σ, the only simulation parameter that is variable in this study, encodes the equilibrium distance between two inclusions and between an inclusion and a carbon atom. It has been shown in the published results [139] that the density of GAs decreases as the spherical inclusions enlarge. The spatial distributions of both graphene flakes and inclusions are uniformly random over a cubic simulation box. The orientations of

graphene flakes are also random, dictated by the following 3D rotation tensor

$$R = R_z(\gamma)R_y(\beta)R_x(\alpha) = \begin{bmatrix} \cos\gamma & -\sin\gamma & 0 \\ \sin\gamma & \cos\gamma & 0 \\ 0 & 0 & 1 \end{bmatrix} \begin{bmatrix} \cos\beta & 0 & \sin\beta \\ 0 & 1 & 0 \\ -\sin\beta & 0 & \cos\beta \end{bmatrix} \begin{bmatrix} 1 & 0 & 0 \\ 0 & \cos\alpha & -\sin\alpha \\ 0 & \sin\alpha & \cos\alpha \end{bmatrix} \tag{4.2}$$

where γ, β, and α are independently and identically distributed from 0 to π. The initial density of the material system is 2 mg·cm^{-3}, and the initial volume of the simulation box is 6.80×10^7 Å^3. These graphene flakes are subsequently fused into a 3D GA structure. MD simulations are performed using LAMMPS and the Extreme Science and Engineering Discovery Environment (XSEDE) computing resources. The total system energy is given by:

$$E_{\text{total}} = E_{\text{C-C}} + E_{\text{C-inc}} + E_{\text{inc-inc}} \tag{4.3}$$

where $E_{\text{C-C}}$, $E_{\text{C-inc}}$, and $E_{\text{inc-inc}}$ denote the total energies of interactions between carbon atoms, between carbon atoms and inclusions, and between inclusions, respectively. $E_{\text{C-C}}$ is modeled by an AIREBO potential (Eq. 2.1). $E_{\text{C-inc}}$ and $E_{\text{inc-inc}}$ are modeled by the standard 12/6 LJ potential, expressed as:

$$E_{\text{C-inc}} = E_{\text{inc-inc}} = \sum_i \sum_{j>i} 4\epsilon[(\frac{\sigma}{r_{ij}})^{12} - (\frac{\sigma}{r_{ij}})^6]\Xi \tag{4.4}$$

where r_{ij} is the distance between particles i and j; ϵ is the depth of the potential well, which relates to the stiffness of the inclusion; σ is the distance at which the particle-particle potential energy is zero, where $R_{\text{eff}} = 2^{1/6}\sigma$ is the effective radius of the inclusion; Ξ is the cutoff function: $\Xi = 1$ for $r_{ij} < r_{\text{c}}$, and $\Xi = 1$ for $r_{ij} \geq r_{\text{c}}$, where r_{c} is the cutoff distance. In this work, $\epsilon = 0.625$eV [139]; σ ranges from 2 Å to 10 Å; $r_{\text{c}} = \sigma + 3$ Å. The mass of each spherical inclusion is set as 1 g/mol. A timestep of 1 fs is used. Periodic boundary conditions are applied to all three dimensions. All carbon atoms and inclusions are initiated with a random velocity corresponding to the temperature $T = 300$ K, and for each individual GA the seed of the random number generator is different. This guarantees that the formation trajectories of GAs are randomly different. The stress tensor is calculated by Eq. 2.2.

The condensation of the material system is realized by a number of designed annealing cycles. Each cycle consists of four stages: (a) in the NPT ensemble where the temperature is maintained at $T = 300$ K and the pressure P increases linearly from 1 atm to 1000 atm; (b) in the NVT ensemble where the temperature T increases linearly from 300 K to 2000 K; (c) in the NVT ensemble where the temperature is held at $T = 2000$ K; (d) in the NVT ensemble where the temperature T decreases linearly from 2000 K to 300 K. The duration of each stage is 25 ps. The setting of one entire annealing cycle is illustrated in Fig. 4.1(c), and the true recorded temperature and pressure in multiple cycles are shown in Fig. 4.2. All volume change takes place in the first stage where the system volume is uncontrolled, while in the subsequent three stages, the system volume remains constant. The system volume V as a function of experienced annealing cycle number is shown in Fig. 4.1(d). As the

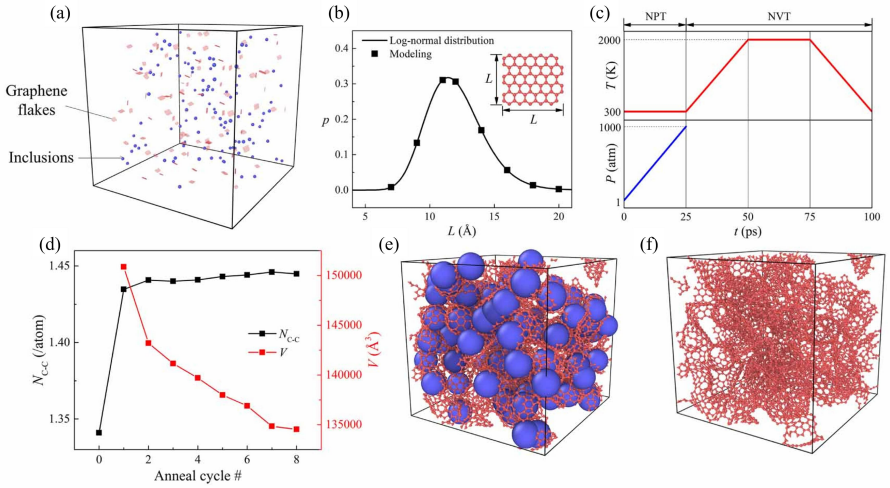

Figure 4.1: Construction of GAs in the MD simulation. (a) Initial stage of the material system. (b) Probability distribution of the graphene flake side length L. (c) Targeted temperature and pressure under NPT and NVT ensembles within one annealing cycle. (d) Number of C–C bonds per atom $N_{\mathrm{C-C}}$ and system volume V as functions of the annealing cycle number. (e) An example of material system configurations immediately after 8 annealing cycles. (f) Final configuration of a GA after spherical inclusions are removed.

annealing cycles go on, the system volume decreases, suggesting the material is condensed during the process. During annealing cycles, new C–C bonds are formed across initially disconnected graphene flakes. The number of C–C bonds per atom $N_{\mathrm{C-C}}$ is used to quantify the structural integrity of the GAs. After eight annealing cycles, $N_{\mathrm{C-C}}$ converges to 1.45, close to the value 1.5 for an infinitely large graphene sheet, as is shown in Fig. 4.1(d). This suggests that initially disconnected graphene flakes are now well integrated and will only improve marginally as more annealing cycles are simulated. Hence, and for the sake of efficiency, all GAs in this study are prepared with eight annealing cycles. An example of the closely packed GA structure and spherical inclusions after eight annealing cycles is shown in Fig. 4.1(e). Next, the inclusions are deleted from the system, and the 3D GA is relaxed in the NVT ensemble at $T = 300\,\mathrm{K}$ for another 25 ps to produce the final GA structure, as illustrated in Fig. 4.1(f). The final GA, with a density of g·cm^{-3}, is structurally stable.

For the mechanical testing, a uniaxial tensile load is applied to the prepared GAs in a quasi-static, incremental manner. At each step, the simulation box is deformed for a 1% uniaxial strain in x direction in the NPT ensemble with $T = 300\,\mathrm{K}$ and $P = 1$ atm applied to the two unloaded y and z directions. Each strain increment is followed by an energy minimization and equilibration in the NVT ensemble with $T = 300\,\mathrm{K}$. An example stress–strain curve, along with GA shapes corresponding to several critical points on the curve, are shown in Fig. 4.3. The stress–strain curve exhibits a clearly defined linear part,

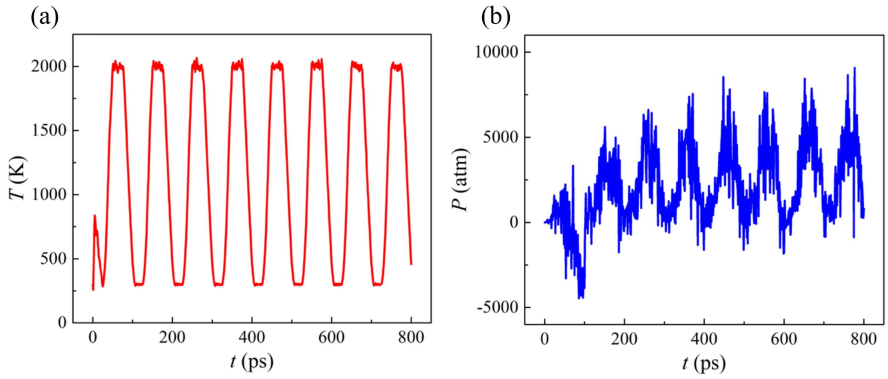

Figure 4.2: Temperature and pressure evolution during 8 annealing cycles.

followed by multiple peaks and a catastrophic failure. This suggests that the GA undergoes a progressive failure upon uniaxial tensile loading. The failure strain is close to 0.9, consistent with the result in Ref. [208], and is much enhanced compared to that of 2D graphene sheets (0.2–0.3). However, the Young's modulus (29.5 GPa) and the ultimate tensile stress (17.5 GPa) are much reduced compared to the defect-free graphene sheets (with a Young's modulus of 1000 GPa and an ultimate tensile strength of 130 GPa [90]). Different from anisotropic 2D graphene sheets, GAs are in principle isotropic due to the assembly of a large amount of randomly distributed graphene flakes. Therefore, the Young's modulus and the tensile strength in the loading direction are used to represent the Young's modulus and the tensile strength of the GA material. The stress–strain curve of one GA subject to cyclic loading is provided in Fig. 4.4, where the first cycle exhibits some elastic hysteresis while the subsequent cycles do not.

Results and discussion

To investigate the stochastic nature of GA mechanical properties, a total of 270 GAs are simulated. Nine values of $\sigma \in [2, 3, \ldots, 10]$ Å (equivalent to $R_{\text{eff}} \in 2^{1/6}\,[2, 3, \ldots, 10]$ Å) are used to generate GA structures, where each σ (or R_{eff}) value generates 30 random configurations. GA density ρ as a function of R_{eff} is illustrated in Fig. 4.5. It is shown that ρ decreases as R_{eff} increases, in good agreement with previously reported results [139]. To investigate the statistics of the bond breaking behavior of GAs, the fractions of broken bonds of the GA model where $R_{\text{eff}} = 2^{1/6} \times 5$ Å $= 4.45$ Å are computed based on 30 data points. The mean and the standard deviation of the fraction is 0.39% and 0.23%, suggesting that the catastrophic failure of GAs is related to a small number of broken bonds at critical locations. Fig. 4.6 shows scatter plots of the Young's modulus E and the ultimate tensile stress σ_{u} against ρ for all 270 GAs, where both E and σ_{u} increase as ρ increases. In addition, the variation E is relatively small for small ρ, but increases as ρ increases.

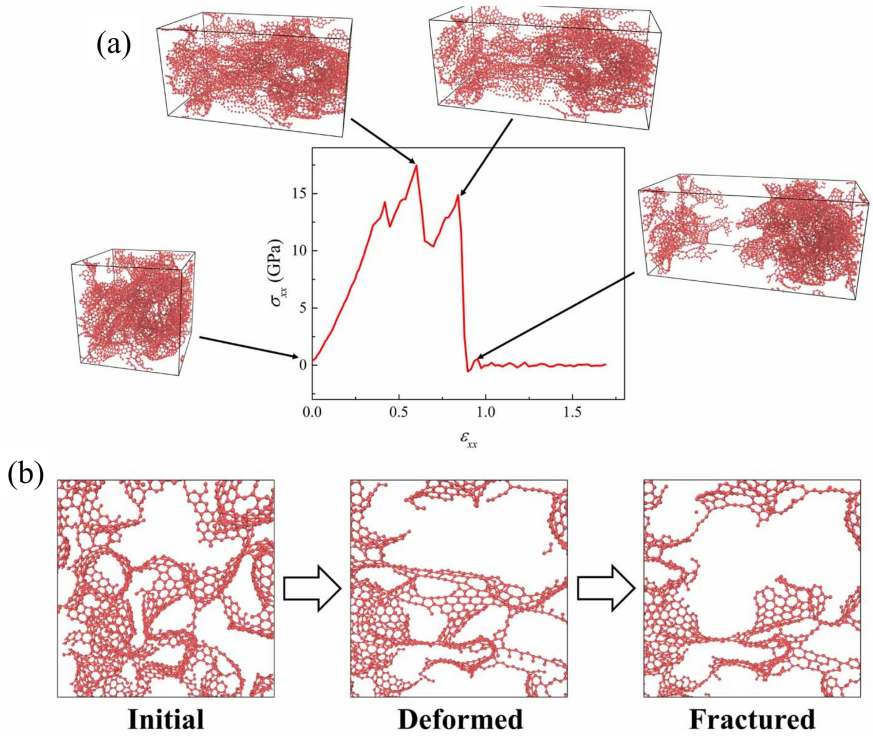

Figure 4.3: Stress–strain curve and deformation/fracture modes of one example GA. (a) Stress–strain curve of the GA under a uniaxial tensile load. σ_{xx} and ε_{xx} denote the stress and the strain in the loading direction. GA molecular configurations at critical points on the stress–strain curve are provided. The density of the GA in this example is 0.924 g·cm^{-3}. (b) Illustrations of local deformation and fracture modes of the GA.

However, the variation of σ_{u} is comparatively larger and independent of ρ. This shows that the randomness of the GA microstructure has different influencing mechanisms on the stiffness and the strength. One hypothesis is that the strength of GAs is more responsive to the progressive failure mode, which is rather unrelated to the density but highly dependent on the microstructure. The results are further clustered by R_{eff}, where the data points originating from different R_{eff} are colored differently. It is observed that between clusters there is significant overlapping in both horizontal and vertical directions, indicating that both density and mechanical properties are random given one R_{eff} value. Even though some data points on Fig. 4.6(b) have achieved roughly 25 times as strong as mild steel with a density 10% that of mild steel, this observed randomness poses substantial difficulty and uncertainty for engineers to effectively design and use GAs.

Previous works in literature treat mechanical properties of GAs, such as the Young's modulus and the ultimate tensile strength, as functions of the density [139, 129], just like in Fig. 4.6. However, in the present simulations the density is not a variable that can be

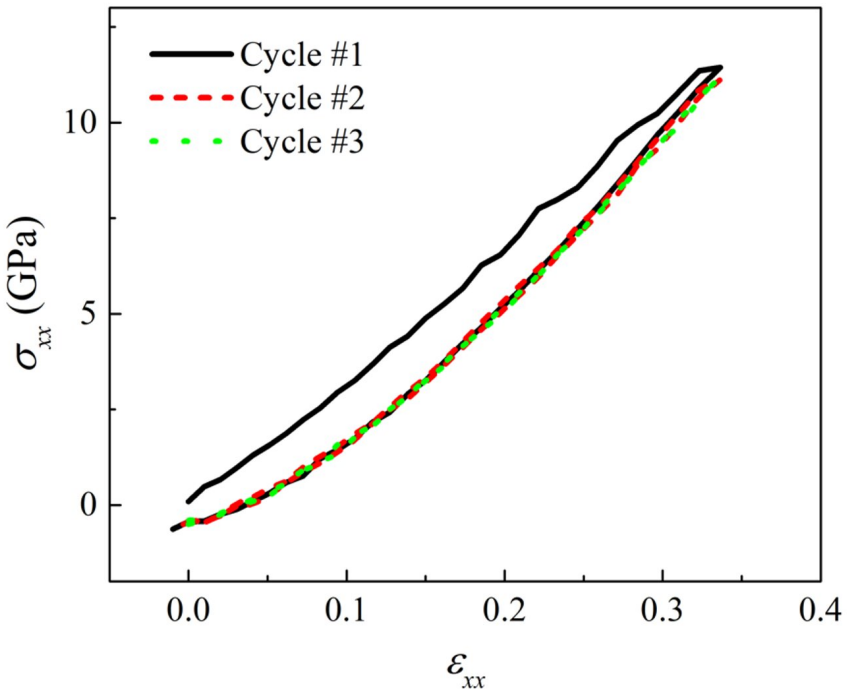

Figure 4.4: Stress-strain curve of one GA subject to cyclic loading with 3 cycles. The density of the GA in this example is 0.920 g·cm^{-3}.

controlled, and the mechanical properties can vary widely given one specific density value. Instead, the density ρ, Young's modulus E, and ultimate tensile strength σ_{u} are considered as functions of R_{eff}, the only parameter in this study that dictates the GA microstructure and, thus, mechanical properties. To this end, ρ, E, and σ_{u} are plotted against R_{eff}, as shown in Fig. 4.7. Now the results are transformed from nine heavily overlapped clusters to 1D distributions at nine different locations. This allows to fit the properties under each R_{eff} to a statistical distribution such as the Gaussian distribution, which establishes confidence intervals. More importantly, this presentation of the data offers an opportunity to interpolate and predict properties of unsurveyed R_{eff} given noise. This is particularly valuable in that the MD simulations of GA are rather computationally expensive and simulating GAs given more densely distributed R_{eff} are very time-consuming.

Here, a metamodel approach is proposed which employs a non-parametric regression method called Gaussian process regression (GPR), a probabilistic interpolation approach that integrates observed samples and prior distribution and covariances [3, 15]. In recent years, GPR has been widely applied in materials design and discovery problems [44, 122]. GPR predicts the value of a function at a target point by computing a weighted average of the known values of the function (the training data) in a statistically principled way. The weights

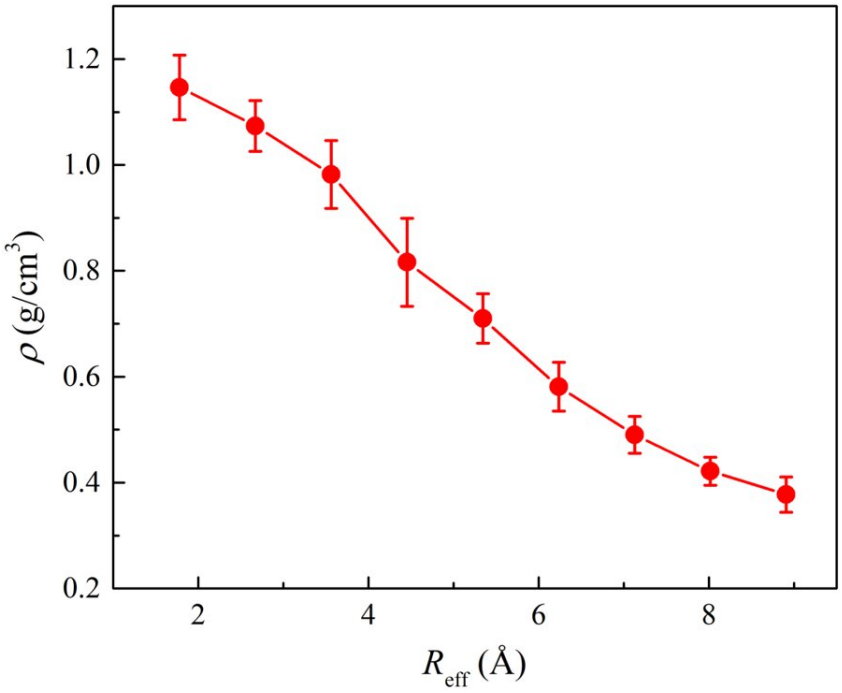

Figure 4.5: GA density as a function of the effective radius of inclusions.

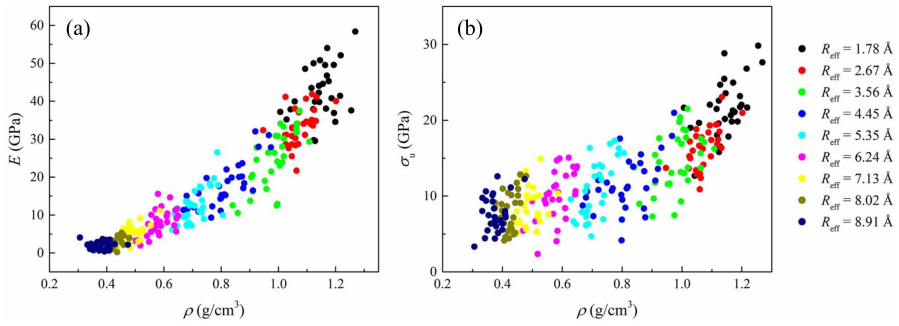

Figure 4.6: Scatter plots of the Young's modulus and the ultimate stress against the density of all 270 GAs. Plots of (a) the Young's modulus and (b) the ultimate tensile stress.

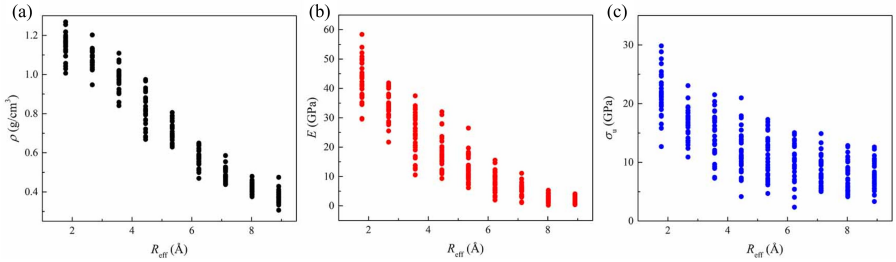

Figure 4.7: Scatter plots of the GA density, Young's modulus, and ultimate tensile stress against the effective radius of the inclusions. Plots of (a) the density, (b) the Young's modulus, and (c) the ultimate tensile stress.

are determined by a covariance function (or a kernel) that specifies the covariance between pairs of random variables. Concretely, given a training set $\mathcal{D} = \{(\mathbf{x}_i, y_i) \,|i = 1, \ldots, n\}$, where $\mathbf{x}_i$ denotes an input vector of a dimension D and y_i denotes a scalar output, a noise-free covariance function can be written as:

$$\mathrm{cov}(y_p, y_q) = \mathrm{cov}(f(\mathbf{x}_p, f(\mathbf{x}_q)) = k(\mathbf{x}_p, \mathbf{x}_q) \tag{4.5}$$

where $k(\cdot, \cdot)$ denotes a kernel function, or in matrix form:

$$\mathrm{cov}(\mathbf{y}) = K(X, X) \tag{4.6}$$

where $\mathbf{y}$ is an output vector; X is a $D \times n$ design matrix aggregated by n input vectors; K is an $n \times n$ kernel matrix. In this study, the linear combination of two radial-basis functions is used as the covariance function, given by:

$$k(\mathbf{x}_p, \mathbf{x}_q) = s_1^2 \exp -\frac{\|\mathbf{x}_p - \mathbf{x}_q\|^2}{2l_1^2} + s_2^2 \exp -\frac{\|\mathbf{x}_p - \mathbf{x}_q\|^2}{2l_2^2} \tag{4.7}$$

where s_1^2 and s_2^2 are scaling parameters known as the process variances; l_1^2 and l_2^2 are length-scale parameters; $\|\cdot\|$ denotes the L_2 norm. From the expression, the covariance between two data points depends only on their Euclidean distance and not on their absolute values. For noisy cases (as is fit to describe the simulation results in this study), the kernel matrix K is regularized by the "nugget", a positive value τ_i^2 $(i = 1, \ldots, n)$ added to the main diagonal of K. This corresponds to a probabilistic model with an additive white noise of variance τ_i^2 below

$$y_i = f(\mathbf{x}_i) + \varepsilon_i \tag{4.8}$$

where $\varepsilon_i \sim \mathcal{N}(0, \tau_i^2)$. Here, the shorthand representation of a probability distribution is used, where $\mathcal{N}(\mu, \sigma^2)$ denotes a normal distribution, $\mathcal{N}$, with mean, μ, and variance, σ^2. The covariance function now becomes

$$\mathrm{cov}(y_p, y_q) = k(\mathbf{x}_p, \mathbf{x}_q) + \tau_p^2 \delta_{pq} \tag{4.9}$$

where δ_{pq} is the Kronecker delta which equals 1 if $p = q$ and 0 otherwise, or in matrix form

$$\text{cov}(\mathbf{y}) = K(X, X) + \Lambda I \tag{4.10}$$

where $\Lambda = \text{diag}\,(\tau_1^2,\, \tau_2^2, \ldots,\, \tau_n^2)$ and I is the $n \times n$ identity matrix. The 'nugget' regularization improves the condition number of the covariance matrix by increasing the eigenvalues by τ_i^2. Additionally, it causes the GPR to smoothen the data and become non-interpolating. In this study, τ_i^2 takes on the variance of the training data under each R_{eff}. The parameters of the covariance function in Eq. 4.9 are optimized during fitting by maximizing the log marginal likelihood below

$$\log p(\mathbf{y}|X) = -\frac{1}{2}\mathbf{y}^T(K + \Lambda I)^{-1}\mathbf{y} - \frac{1}{2}\log|K + \Lambda I| - \frac{n}{2}\log 2\pi \tag{4.11}$$

To obtain predictions at an unseen point of interest $\mathbf{x}_*$, the predictive distribution can be calculated by weighting all possible predictions by their calculated posterior distribution as follows

$$p(f_*|\mathbf{x}_*, X, \mathbf{y}) = \int p(f_*|\mathbf{x}_*, \mathbf{w})p(\mathbf{w}|X, \mathbf{y})d\mathbf{w} \tag{4.12}$$

where f_* is the predicted function value at target $\mathbf{x}_*$, and $\mathbf{w}$ is the weight vector. For GPR, the joint distribution of the training data and the function values at the locations of interest under the prior can be written as

$$\begin{bmatrix}\mathbf{y} \\ \mathbf{f}_*\end{bmatrix} \sim \mathcal{N}\left(\mathbf{0}, \begin{bmatrix}K(X, X) + \Lambda I & K(X, X_*) \\ K(X_*, X) & K(X_*, X_*)\end{bmatrix}\right) \tag{4.13}$$

where $\mathbf{f}_*$ is the predicted function vector at target design matrix X_*. The key predictive equations for GPR is

$$\mathbf{f}_*|\mathbf{x}_*, X, \mathbf{y} \sim \mathcal{N}(\bar{\mathbf{f}}_*, \text{cov}(\mathbf{f}_*)) \tag{4.14}$$

where

$$\bar{\mathbf{f}}_* = \mathbb{E}[\mathbf{f}_*|\mathbf{x}_*, X, \mathbf{y}] = K(X_*, X)(K(X, X) + \Lambda I)^{-1}\mathbf{y} \tag{4.15}$$

is the mean of the predicted function vectors, which is considered as the GPR prediction, and

$$\text{cov}(\mathbf{f}_*) = K(X_*, X_*) - K(X_*, X)(K(X, X) + \Lambda I)^{-1}K(X, X_*) \tag{4.16}$$

is the predicted covariance matrix. The vector of the predicted variance $\boldsymbol{\sigma}_*^2$ can be obtained from the diagonal of cov $(\mathbf{f}_*)$

$$\boldsymbol{\sigma}_*^2 = \text{diag}(\text{cov}(\mathbf{f}_*)) \tag{4.17}$$

Finally, the 95% confidence interval can then be established as $\left[\bar{\mathbf{f}}_* - 1.96\boldsymbol{\sigma}_*,\, \bar{\mathbf{f}}_* + 1.96\boldsymbol{\sigma}_*\right]$. The GPR results of the present study are shown in Fig. 4.8, where the GPR predicted means are plotted in solid lines and 95% confidence intervals are illustrated in shaded areas. Red dots and error bars are results from Fig. 4.7 that are used as the training data. The significance of this result is that given an R_{eff} value, the most probable ρ, E, and σ_{u} of the

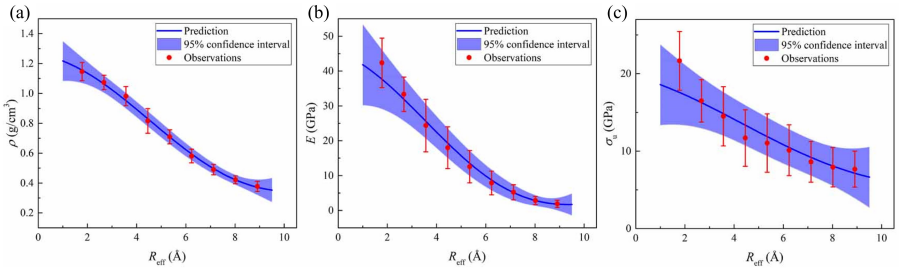

Figure 4.8: GPR prediction results of GA properties. Observations, GPR predictions and 95% confidence intervals of (a) the density, (b) the Young's modulus, and (c) the ultimate tensile stress.

unsimulated GA can be predicted. Inversely, given target ρ, E, and σ_{u}, the R_{eff} value that gives the best chance to achieve the goal can be known. It is observed in Fig. 4.8 that one can be more confident about ρ compared to E and σ_{u}. This is expected because R_{eff} intuitively has a more direct impact on the structural properties than on the mechanical properties. In addition, for all three properties, the 95% confidence intervals are tighter in the middle compared to both ends. This observation indicates that there are more uncertainties if the GPR approach is used to do extrapolations compared to interpolations. Notably, this is common in all metamodel approaches, because intrinsically there are more "informative" data points available to do interpolations compared to extrapolations. From a quantitative perspective, the kernel becomes small fast (in this study, exponentially) as the target is farther away from the known data points, as indicated by Eq. 4.7. One can change the kernel to take different forms in practice, and they all will present a decaying phenomenon as the target is farther away. The difference would be how fast the kernel decays. The recommendation is that, one can still use GPR to make predictions for extrapolations that are not too far away from the center of the data, but one should be aware of the level of uncertainties.

Concluding remarks

A bottom-up atomistic simulation model and a statistical metamodel are constructed to investigate the uncertain mechanical properties of GAs. Using MD simulations, GAs are firstly assembled from randomly distributed graphene flakes and spherical inclusions via annealing cycles, and are subsequently subject to a quasi-static uniaxial tensile load to deduce mechanical properties. Results show that given a specific density, the Young's modulus and the ultimate tensile strength of GAs can vary substantially. Different from most previous literature where the mechanical properties of GAs are treated as a function of the density, the density, the Young's modulus and the ultimate tensile strength are considered as functions of the size of the inclusions, which dictates the GA microstructure and thus mechanical

properties in a complex fashion. Using the properties of the simulated GAs as the training data, Gaussian process metamodels are built which not only predict the properties of unseen GAs but also establish statistically valid confidence intervals centered around the predictions. This metamodel approach is particularly beneficial when the data acquisition requires expensive experiments or computation, which is the case for the GA simulations. The present research quantifies the uncertain mechanical properties of GAs, which may shed light on the statistical analysis of novel nanomaterials of a broad variety [223].

4.2 Structral integrity of graphene aerogels

MD simulations have been favored by researchers due to their capability in shedding light on detailed mechanical responses of GAs that are beyond the experimental capabilities. However, there have been some shortcomings in previous MD simulation works. First, the properties of GAs have not been extensively studied in response to changes in simulation variables. Previous studies have only examined very few parameters (mainly the radius of inclusions), while many other parameters such as the inclusion-to-flake ratio, the total number of particles in the simulation, and the annealing properties can have a great impact on the GA properties. Second, the structural integrity of GAs in MD simulations has not been studied against changes in the variables. Number of bonds per atom has been used as a metric to quantify how well graphene flakes are connected inside a GA structure. However, it has not been investigated how this metric changes in response to changes of simulation parameters. Third, there has been a deviation of an order of magnitude between densities in MD simulations and experiments. GAs with a density below 10 $mg{\cdot}cm^{-3}$ have been fabricated in experiments, while the lowest density studied in MD simulations is around 100 $mg{\cdot}cm^{-3}$. Lastly, there has been rarely reported research that directly compares MD simulation results with experimental data.

In this section, above challenges will be address and the limitations of MD simulations in modeling GAs will be discussed. First, various mechanical properties as a function of a broad set of simulation parameters are studied. Second, the structural integrity of GAs is quantified and evaluated as simulation parameters change. Additionally, the reason why the density of GAs in MD simulations cannot reach the low values obtained experimentally is discussed. Finally, the findings are compared with experimental results to discuss both the capabilities and the limitations of the simulation technique.

Results and discussion

Molecular modeling

Similar to the previous section, a GA structure is formed by condensing an initially sparse and disconnected system into an integrated structure. The initial system for GA preparation is a cubic box, consisting of graphene flakes and spherical inclusions, as shown in Fig. 4.9(a).

The periodic boundary condition is applied in all three dimensions to approximate an infinitely large system. The numbers of graphene flakes and inclusions are denoted by N_{flake} and N_{inc}. The initial density is set as low as 1 mg·cm^{-3} to minimize the probability of overlapping atoms. Graphene flakes are square-shaped with a side length L, while the inclusions are modeled as spheres with an effective radius R_{eff}, as illustrated in Fig. 4.9(b). R_{eff} is mathematically defined as $R_{\text{eff}} = 2^{1/6}\sigma$, where σ is a parameter of the LJ potential that models the equilibrium spacing between two particles. Because R_{eff} and σ are proportional, here, "the effect of R_{eff}" and "the effect of σ" are used interchangeably. In section, the value of L within one simulation system follows various distributions, which has not been studied in previous work. the distribution of L is considered a variable and its effect on the mechanical and structural properties of GAs is studied. One distribution that L follows is the log-normal distribution, of which the probability density function is described in Eq. 4.1. $\bar{L} = 12$ Å and $L_{\text{std}} = 4.8$ Å are used. By default, L follows the log-normal distribution. L is also modeled with half normal distributions, of which the probability density function is

$$p(L) = \sqrt{\frac{2}{\pi}} \frac{1}{\sigma_{\text{hn}}} \exp\left[-\frac{1}{2}\left(\frac{L-\mu_{\text{hn}}}{\sigma_{\text{hn}}}\right)^2\right], \text{for } L \leq \mu_{\text{hn}} \tag{4.18}$$

where μ_{hn} and σ_{hn} are the location and the scale parameters. In this study, μ_{hn} is set as the largest L that is sampled by the log-normal distribution to favor larger graphene flakes. σ_{hn} is a variable that controls the "width" of the half bell curve: larger σ_{hn} gives a wider half bell curve.

Next, a number of designed annealing cycles are applied to condense the material system and to connect graphene flakes into an integrated structure. The total number of annealing cycles is denoted by N_{cycles} and the current number of annealing cycles is denoted by N_{cycle}. Each annealing cycle consists of four stages and each has time duration $t_{\text{p}} = 50$ ps: (a) in the NPT ensemble, the pressure increases linearly from 1 atm to 1000 atm and the temperature is maintained at 300 K; (b) in the NVT ensemble, the temperature increases linearly from 300 K to the annealing temperature T_{A}; (c) in the NVT ensemble, the temperature is held at T_{A}; (d) in the NVT ensemble, the temperature decreases linearly from T_{A} to 300 K. The annealing cycle design is similar to the previous section. However, here the annealing temperature T_{A} is considered a variable. Because the temperature affects the level of movements of graphene flakes, it dictates the probability of graphene flakes, encountering each other and forming bonds, thus affecting the final GA structure. The annealing cycle design described above is illustrated in Fig. 4.9(c).

During the annealing process, the system volume decreases sharply in the first cycle and it gradually decreases in subsequent cycles, as shown in Fig. 4.9(d). After many annealing cycles, a compact system with interconnected graphene flakes and inclusions can be obtained, as shown in Fig. 4.9(e). Inclusions resemble water clusters in experiments which will be removed from the system during a drying process. Deleting the inclusions and followed by another NVT process for 50 ps, the final stable GA structure in the simulation is obtained, as shown in Fig. 4.9(f). The final relaxation is intended to eliminate the initial stress after

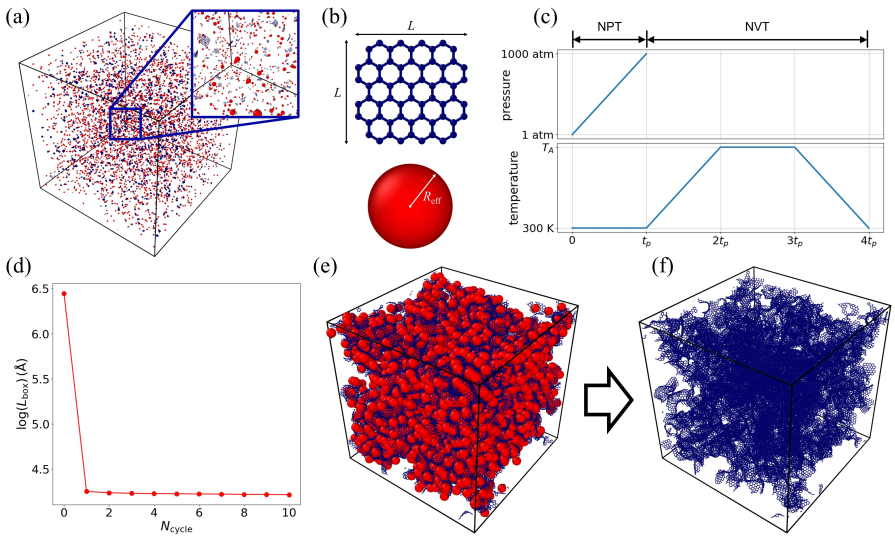

Figure 4.9: Construction of GA structures in the MD simulation. (a) Initial material system where $N_{\text{flake}} = 500$ and $N_{\text{inc}} = 1000$. (b) Dimensions of the graphene flake and the spherical inclusion. (c) Pressure and temperature profiles during one annealing cycle. (d) $\log(L_{\text{box}})$ as a function of N_{cycle}, where L_{box} denotes the side length of the cubic simulation box. (e) Condensed material system after 10 annealing cycles. (f) Final GA structure after the removal of inclusions.

annealing cycles. Stress–strain curves with and without the relaxation process are shown in Figs. 4.10 and 4.11, where the latter introduces an initial stress. MD simulations are conducted in a similar fashion as the previous section.

Mechanical properties of graphene aerogels

After the in silico fabrication of the GA structure described in the previous section, uniaxial tensile and compressive loads are applied to calculate the mechanical properties of the GA. Loads are applied in a quasi-static, incremental manner. At each step, the simulation box is deformed for a 1% uniaxial strain in the x direction in the NPT ensemble with a temperature of 300 K and a pressure of 1 atm maintained in the two unloaded y and z directions. Each strain increment is followed by an energy minimization and equilibration process in the NVT ensemble at 300 K. Under these loading conditions, a range of mechanical properties of GAs including density ρ, tensile strength σ_{u}, tensile failure strain ε_{u} (defined as the strain at the maximum tensile stress), tensile and compressive moduli E_{t} and E_{c} can be computed. This section is dedicated to systematically investigating how these mechanical properties change in response to changes of an extensive set of simulation variables, and more variables will be covered. In the following, the effects of various simulation variables are studied, including

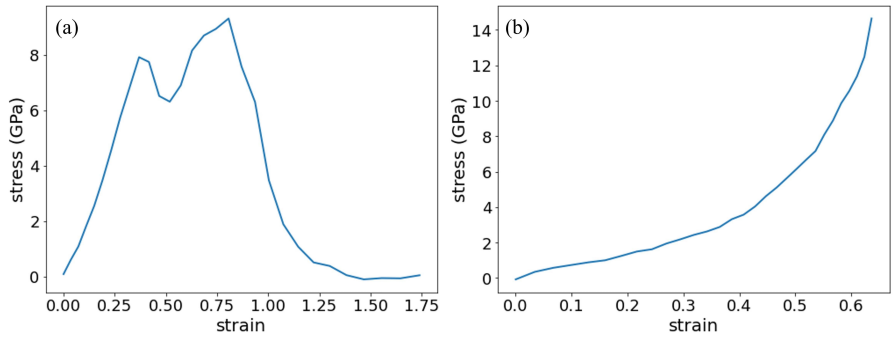

Figure 4.10: Stress-strain curves where $N_{\text{flake}} = 200$, $N_{\text{inc}} = 500$, $\sigma = 5.0$ Å, $N_{\text{cycles}} = 10$, and $T_{\text{A}} = 2000$ K. Stress-strain curves under (a) tension and (b) compression.

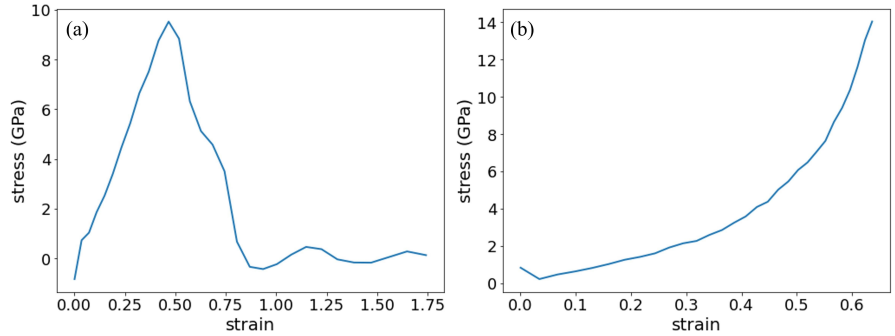

Figure 4.11: Stress-strain curves without the relaxation process after annealing cycles where $N_{\text{flake}} = 200$, $N_{\text{inc}} = 500$, $\sigma = 5.0$ Å, $N_{\text{cycles}} = 10$, and $T_{\text{A}} = 2000$ K. Stress-strain curves under (a) tension and (b) compression.

the effective radius of inclusions R_{eff} (or σ), inclusion-to-flake ratio $R = N_{\text{inc}}/N_{\text{flake}}$, the total number of particles $N_{\text{total}} = N_{\text{inc}} + N_{\text{flake}}$, the annealing temperature T_{A}, and the distribution of the side length of graphene flake L. When a parameter is not studied as a variable, the following values will be used as default: $N_{\text{flake}} = 200$, $R = 1.0$, $\sigma = 5.0$ Å, $N_{\text{cycles}} = 10$, and $T_{\text{A}} = 2000$ K, and L follow the log-normal distribution described in Eq. 4.1, unless otherwise specified.

To start with, the effect of effective radius of inclusions R_{eff} (or equivalently, σ) on the mechanical properties of GAs is studied. Intuitively, larger inclusions result in a higher porosity because these inclusions tend to push the graphene flakes away from each other, as illustrated in Fig. 4.12(a). Here, various mechanical properties of GA as a function of σ are calculated. Each data point on these graphs is based on 5 different random seeds and

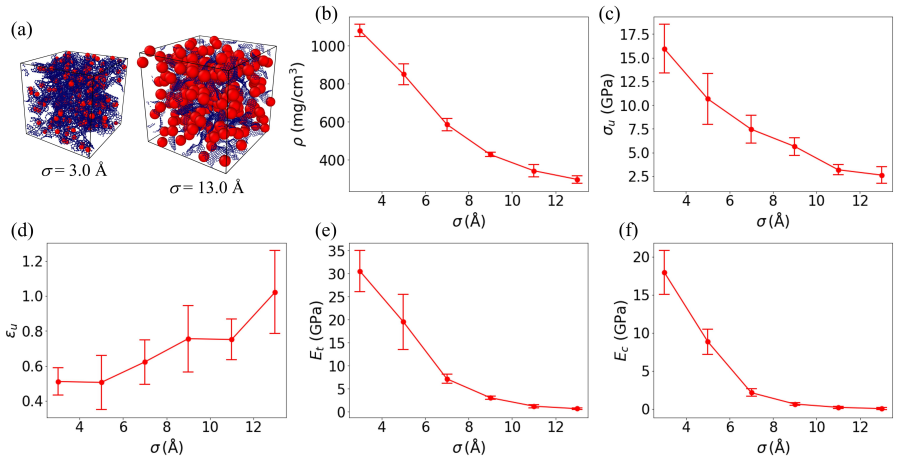

Figure 4.12: Mechanical properties of GA as a function of σ, proportional to the effective radius of inclusions. (a) Illustration of the effect of σ. (b) Density ρ, (c) tensile strength σ_{u}, (d) tensile failure strain ε_{u}, (e) tensile and (f) compressive moduli E_{t} and E_{c} of GA as a function of σ.

the error bar represents one standard deviation. Fig. 4.12(b) shows that as σ increases, the density ρ decreases. This is consistent with the previous section. Fig. 4.12(c) shows that as σ increases, the tensile strength σ_{u} decreases. However, this result presents larger error bars compared to the density results. This is because the failure of the GA structure has a stronger dependency on local structural details, and different random seeds give rise to diverse GA structures despite similar densities. The similar applies to the tensile failure strain ε_{u}, which also depends strongly on the local structure. However, the trend is opposite to the tensile strength, as shown in Fig. 4.12(d) – as σ increases, the failure strain ε_{u} increases. This suggests that GAs with a more loosely interconnected microstructure exhibit higher ductility compared with those with a tightly packed microstructure. The moduli under tension and compression are also calculated. Both tensile and compressive moduli E_{t} and E_{c} decrease as σ increases, and GAs are stiffer under tension than under compression, as shown in Figs. 4.12(e) and (f). The effect of another LJ parameter ϵ, which represents the depth of the potential well is also studied. It is shown in Fig. 4.13 that the mechanical properties of GAs are not strongly dependent on ϵ.

Next, the effect of the inclusion-to-flake ratio R is studied, which has not been researched in previous studies. Intuitively, the higher the inclusion-to-graphene ratio, the lower the GA density, since inclusions (which will eventually be removed from the system) occupy larger and larger volume, as illustrated in Fig. 4.14(a). This effect should be similar to the effect radius of inclusion, but via a different mechanism. The results are summarized in Figs. 4.14(b)–(f), where each data point is based on 5 random seeds. The trends resemble those with σ as the variable, where ρ, σ_{u}, E_{t}, and E_{c} decrease and ε_{u} increases as R increases.

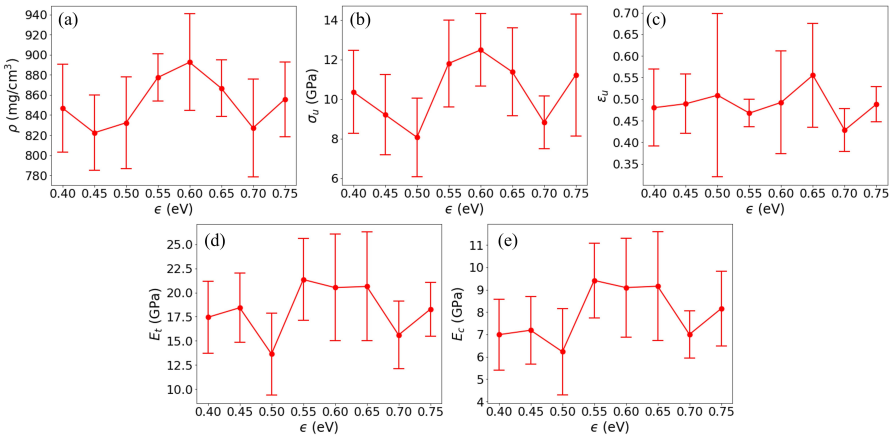

Figure 4.13: Mechanical properties of GA as a function of the LJ parameter ϵ. (a) Density ρ, (b) tensile strength σ_{u}, (c) tensile failure strain ε_{u}, (d) tensile and (e) compressive moduli E_{t} and E_{c} of GA as a function of ϵ.

However, the error bars are larger, indicating that adding more inclusions introduces more uncertainty compared with increasing σ. The result also hints that to achieve a low-density GA, one can use a large σ together with a high R. The caveat is that too many inclusions together with a large σ can result in disconnected graphene flakes after the annealing cycles, as shown in Fig. 4.15. Additionally, it is shown that increasing the number of annealing cycles does not resolve the issue, as shown in Fig. 4.16. A remedy for this issue is to increase the annealing temperature, hoping to increase the possibility of graphene flakes bumping into each other and forming bonds. The temperature effect on the GA structure will be presented in a later section. It is worth noting that fracture-related properties such as σ_{u} and ε_{u} are sensitive to local GA structures, which varies across different random seeds. Consequently, these results bear larger error bars as shown in Figs. 4.12 and 4.14. In contrast, fracture-independent properties such as ρ, E_{t}, and E_{c} bear smaller error bars.

Next, the effect of the total number of particles is studied, and the results are summarized in Fig. 4.17. The inclusion-to-flake ratio is fixed at $R = 2.0$ and various N_{flake} values are used to achieve material systems of different sizes, as illustrated in Fig. 4.17(a). In the present simulations, the periodic boundary conditions are applied in all three spatial dimensions, which approximate an infinitely large system by repeating the unit cell. However, it is more realistic and ideal to use a relatively large repeating unit cell to add to the structural diversity and to reduce randomness. The mechanical properties as a function of the total number of particles is less intuitive compared with the previous two variable choices. Again, ρ, σ_{u}, ε_{u}, E_{t}, and E_{c} are evaluated as a function of N_{flake}. The results are shown in Figs. 4.17(b–f), where all the mechanical properties of interest decrease as N_{flake} increases. In addition, for all properties, the error bars become smaller as the number of particles increases. This

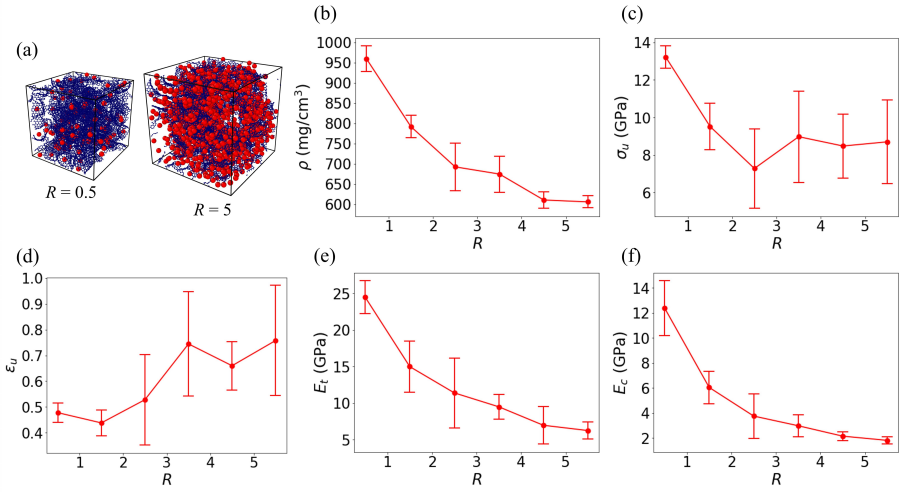

Figure 4.14: Mechanical properties of GA as a function of the inclusion-to-flake ratio R. (a) Illustration of the effect of R. (b) Density ρ, (c) tensile strength σ_{u}, (d) tensile failure strain ε_{u}, (e) tensile and (f) compressive moduli E_{t} and E_{c} of GA as a function of R.

suggests that using more particles approaches a homogenized material system which is less sensitive to local randomness. This effect is observed, especially for the tensile failure strain ε_{u}, which mostly depends on local structures. Nevertheless, the computational cost grows exponentially with the increase of number of particles in the simulation.

Of high interest is how the various mechanical properties change as a function of density ρ, which are properties without variables of simulation artifacts and can relate better to the real material. tensile strength σ_{u}, tensile failure strain ε_{u}, tensile and compressive moduli E_{t} and E_{c} are plotted as functions of density ρ with all simulation results to observe the general trends, as shown in Fig. 4.18. The tensile strength and moduli increase as the density increases, which agrees with the intuition, as shown in Figs. 4.18(a), (c) and (d). In contrast, as shown in Fig. 4.18(b), the tensile failure strain decreases as the density increases, which agrees with the previous results.

Structural integrity of graphene aerogels

The application of annealing cycles does not guarantee that a well-connected GA structure can be formed. In this section, many failed GA structures are observed where graphene flakes are not properly interconnected even after more than 10 annealing cycles, as shown in Figs. 4.15 and 4.16. This aspect of MD simulations of GAs has not been discussed in the literature, and this may explain why the ultra-low density of real GAs has been difficult to be achieved in MD simulations. This section aims to shed light on this aspect.

Previous work used the number of bonds per atom $N_{\mathrm{bond/atom}}$ to quantify the connec-

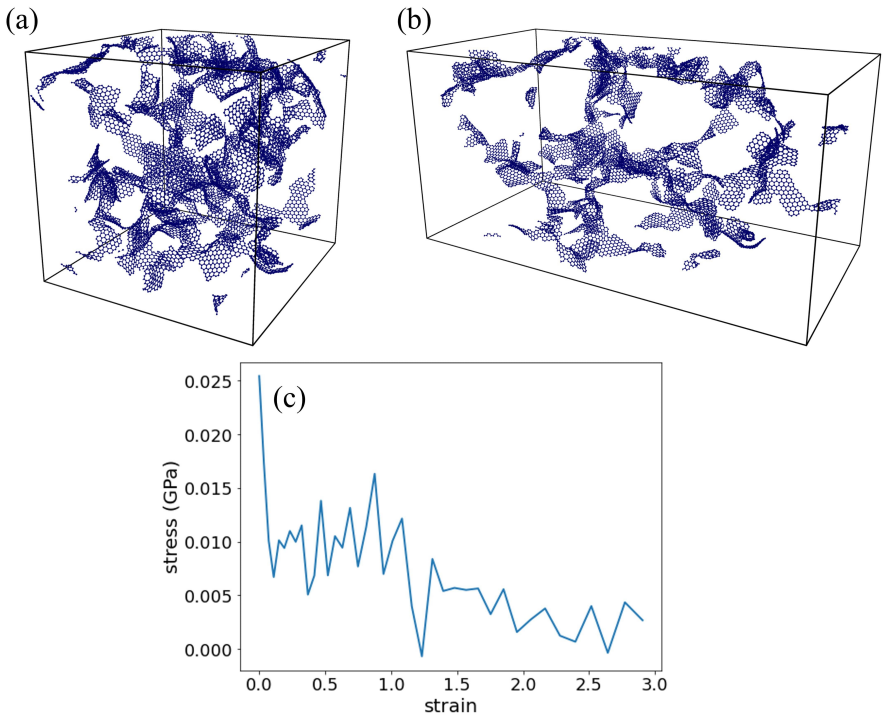

Figure 4.15: Disconnected GA structure. The structure when (a) unloaded and (b) under tension. (c) Stress-strain relation of the GA under tension.

tivity of graphene flakes. For an infinitely large planar graphene sheet, $N_{\text{bond/atom}}$ equals 1.5. Therefore, a value close to 1.5 should indicate a good interconnection between graphene flakes, thus resulting in a well-formed GA structure. However, previous studies only calculated $N_{\text{bond/atom}}$ to illustrate that graphene flakes have been sufficiently interconnected by showing the plateau of $N_{\text{bond/atom}}$ with increasing N_{cycle}. In this work, $N_{\text{bond/atom}}$ is further evaluated as a function of simulation parameters, as it can serve as an important indicator of the structural properties of GAs and whether a GA can be formed through annealing cycles. $N_{\text{bond/atom}}$ is calculated and plotted as a function of N_{cycle} under different simulation conditions (bonds are considered to form if the distance between two carbon atoms is less than 1.7 Å), as shown in Fig. 4.19. Fig. 4.19(a) shows the effect of σ (or equivalently, R_{eff}). Error bars are calculated based on 5 different random seeds. The results show that as σ increases from 3.0 Å to 13.0 Å, $N_{\text{bond/atom}}$ after 10 cycles decreases from over 1.46 to around 1.40, suggesting that a high σ leads to low connectivity. Nevertheless, for simulations, where $\sigma = 13.0$ Å, all 5 random seeds can still generate valid GA structures, an example provided in Fig. 4.20. Fig. 4.19(b) shows the effect of the inclusion-to-flake ratio R on $N_{\text{bond/atom}}$. R varies from 0.5 to 5.5, while other parameters are fixed. Error bars are calculated based on 5 different random seeds. The results show that as R increases from 0.5 to 5.5, $N_{\text{bond/atom}}$

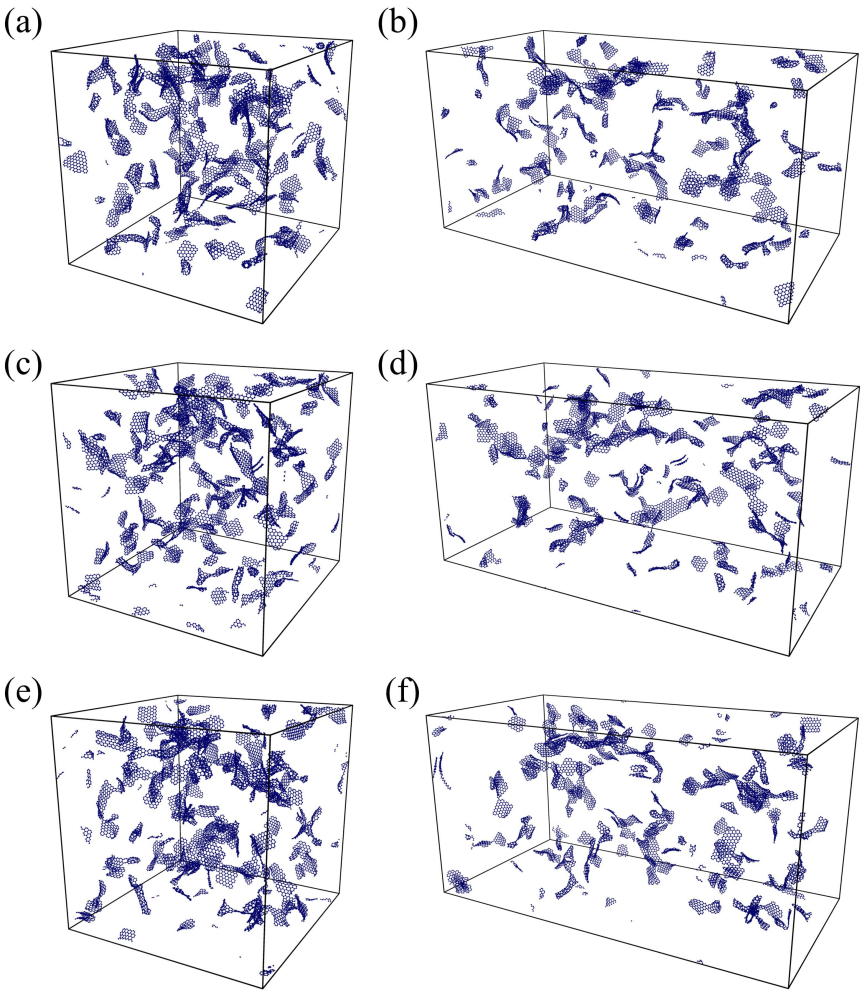

Figure 4.16: GA structure where $N_{\text{flake}} = 200$, $R = 5.0$, $\sigma = 15.0$ Å, and $T_{\text{A}} = 2000$ K under various numbers of annealing cycles. Initial structure and the structure under tension of GAs prepared with (a) 10, (b) 20, and (c) 50 annealing cycles. $N_{\text{bond/atom}}$ for (a-c) are 1.384, 1.386, 1.389, respectively.

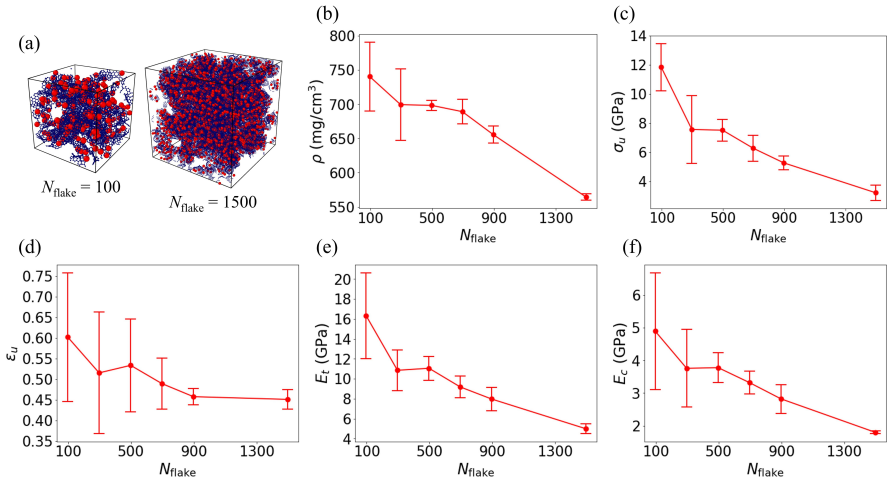

Figure 4.17: Mechanical properties of GA as a function of N_{flake}. (a) Illustration of the effect of N_{flake}. (b) Density ρ, (c) tensile strength σ_{u}, (d) tensile failure strain ε_{u}, (e) tensile and (f) compressive moduli E_{t} and E_{c} of GA as a function of N_{flake}.

decreases from over 1.46 to around 1.42, suggesting that a high R leads to low connectivity. For simulations, where R, all 5 random seeds can still generate valid GA structures, an example provided in Fig. 4.21.

However, combining a high σ and a high R can cause very low $N_{\text{bond/atom}}$ values, as shown in Fig. 4.19(c), where $\sigma = 13.0$ Å and R increases from 1.0 to 7.0. $N_{\text{bond/atom}}$ decreases from slightly below 1.42 to around 1.37. At $R = 2.0$ (where $N_{\text{bond/atom}}$ after 10 cycles is about 1.40), the GA structure fails to form properly where graphene flakes cannot sufficiently interconnect, as shown in Fig. 4.15. This structure has a density of 146 mg·cm^{-3}, which is slightly higher than the lowest density mentioned in previous simulation studies but it is still about more than 10 times denser than the lightest GAs fabricated in experiments. Even though simulation techniques can be fine-tuned to achieve a lower density, this result sheds light on one of the biggest limitations of MD simulation in modeling GAs. This is because the pore size in experiments is an order of magnitude larger than the pore size in the unit cell of the MD simulations. But increasing the MD simulation scale to match the pore size in experiments is infeasible due to high computational cost.

One possible solution is increasing the number of annealing cycles N_{cycles}. In theory, the more annealing cycles the material system experiences, the higher the possibility of graphene flakes encountering each other and forming bonds. Nevertheless, it is found that only increasing N_{cycles} shows a minimal effect on $N_{\text{bond/atom}}$. As an example, GA structures with $N_{\text{flake}} = 200$, $R = 5.0$, $\sigma = 15.0$ Å and $N_{\text{cycles}} = 10, 20, 50$ are calculated. $N_{\text{bond/atom}}$ values after these annealing cycles are 1.384, 1.386, and 1.389, respectively. The GA structure after 50 annealing cycles is not properly formed, and GA structures under the three cases are pro-

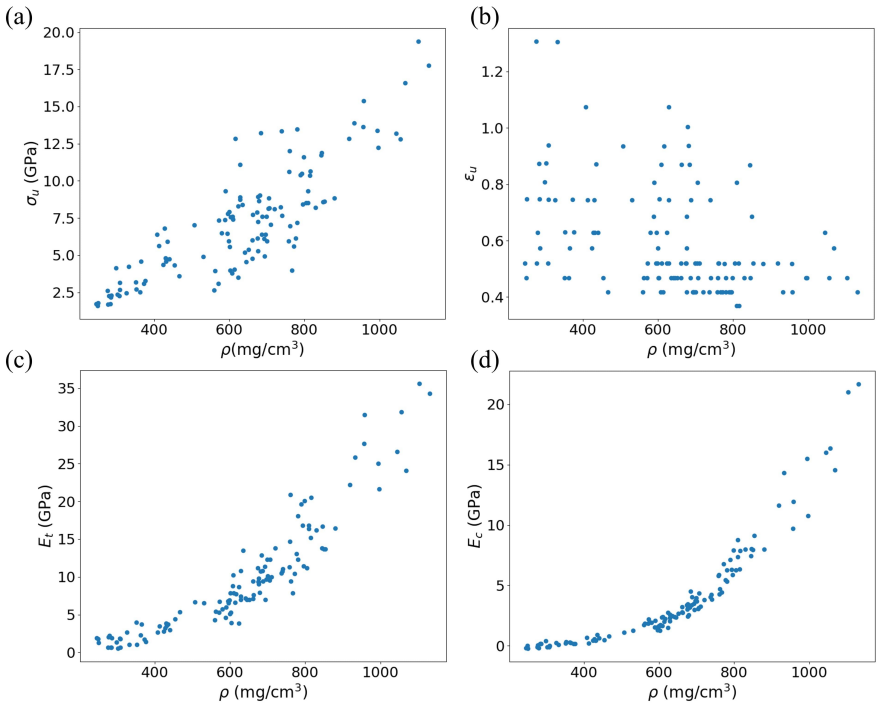

Figure 4.18: Mechanical properties of GA as a function of density ρ for all well-formed GAs. (a) Tensile strength σ_{u}, (b) tensile failure strain ε_{u}, (c) tensile and (d) compressive moduli E_{t} and E_{c} of GA as a function of ρ.

vided in Fig. 4.16. Another solution is to increase the annealing temperature T_{A}. In theory, a higher temperature will lead to intensified atom movements, which will further increase the possibility of graphene flake encounters and therefore result in new bond formation. The dependency of $N_{\mathrm{bond/atom}}$ on T_{A} is shown in Fig. 4.19(d), where GAs are constructed by the following set of parameters: $N_{\mathrm{flake}} = 400$, $R = 3.0$, $\sigma = 15.0$ Å, $N_{\mathrm{cycles}} = 10$, and $T_{\mathrm{A}} = 1000$, 2000, 3000, and 4000 K. As T_{A} increases from 1000 K to 3000 K, $N_{\mathrm{bond/atom}}$ after 10 annealing cycles increases from ~ 1.38 to ~ 1.40, a more significant improvement compared to increasing N_{cycles}. However, $N_{\mathrm{bond/atom}}$ at 4000 K is smaller than at 3000 K. This is because the high temperature has caused some of the bonds to break and GA to begin to become thermally unstable (i.e., the inability to maintain structural integrity and functionality at an elevated temperature), thus resulting in a smaller $N_{\mathrm{bond/atom}}$. An illustration of such effect is provided in Fig. 4.22. This temperature agrees with the melting point of graphite which ranges from 4000 to 5000 K [149] and that of freestanding graphene monolayers which ranges from 4000 K to 6000 K [56]. Therefore, the annealing temperature can be moderately increased to improve the structural integrity of GA structures.

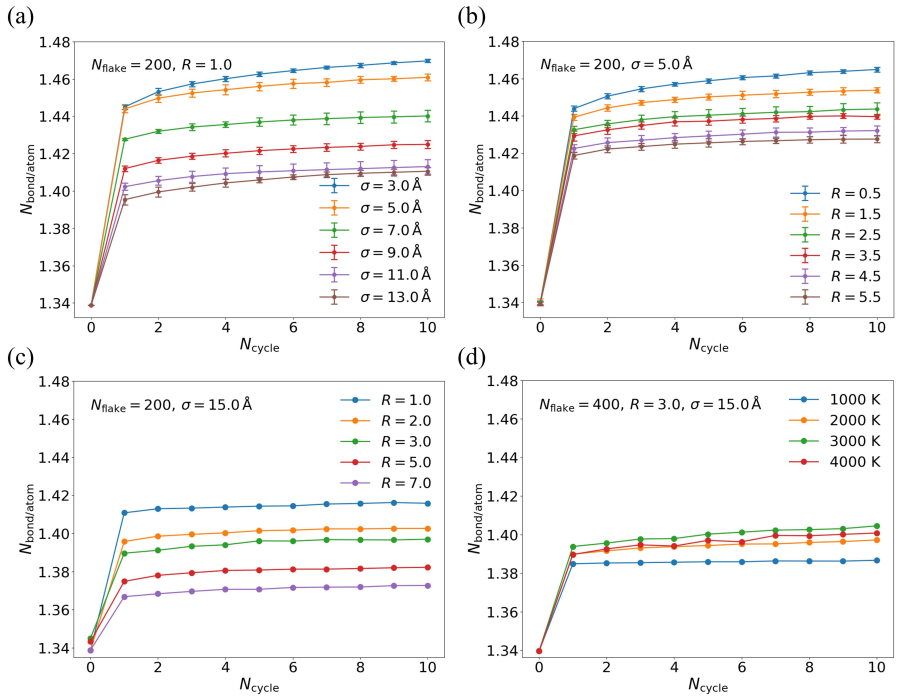

Figure 4.19: GA connectivity property in response to changes in various simulation parameters. $N_{\text{bond/atom}}$ versus N_{cycle} plots (a) under various σ with $N_{\text{flake}} = 200$ and $R = 1.0$, (b) under various inclusion-to-flake ratios R with $N_{\text{flake}} = 200$ and $\sigma = 5.0$ Å, (c) under various R with $N_{\text{flake}} = 200$ and $\sigma = 15.0$ Å, and (d) under various annealing temperature T_{A} with $N_{\text{flake}} = 200$, $R = 1.0$, and $\sigma = 5.0$ Å.

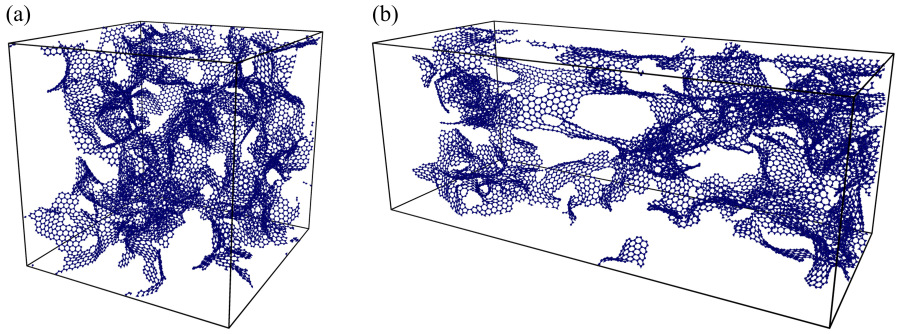

Figure 4.20: GA structure where $N_{\text{flake}} = 200$, $R = 1.0$, $\sigma = 13.0$ Å, and $T_{\text{A}} = 2000$ K. The structure when (a) unloaded and (b) subject to tension.

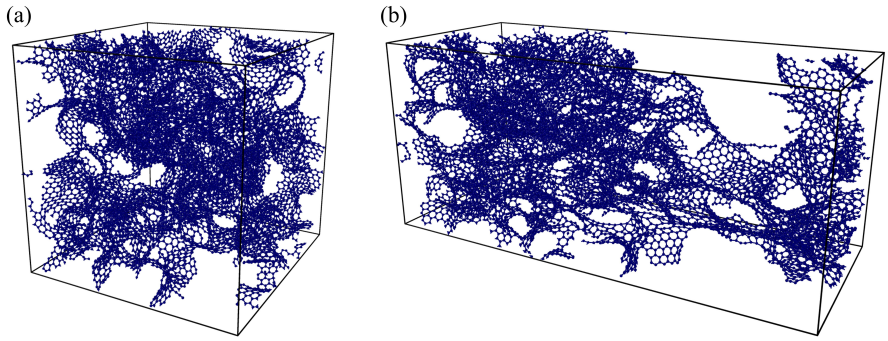

Figure 4.21: GA structure where $N_{\text{flake}} = 200$, $R = 5.5$, $\sigma = 5.0$ Å, and $T_{\text{A}} = 2000$ K. The structure when (a) unloaded and (b) subject to tension.

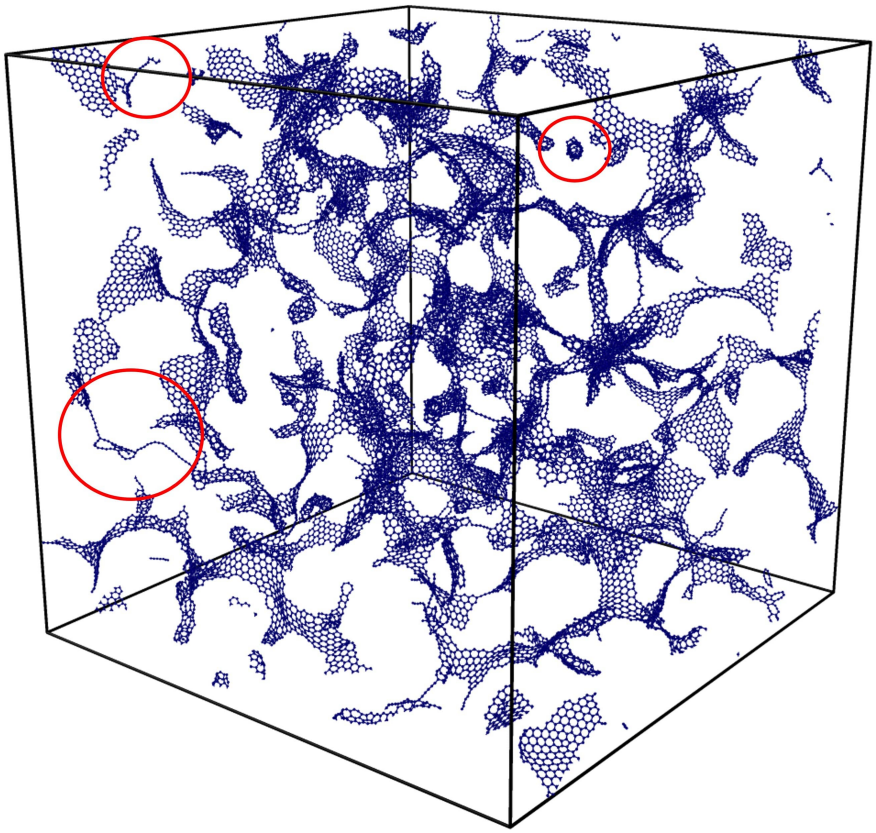

Figure 4.22: GA structure formed with annealing temperature $T_{\text{A}} = 4000$ K where bond breakings and thermally unstable behavior are observed. Problematic geometries are circled.

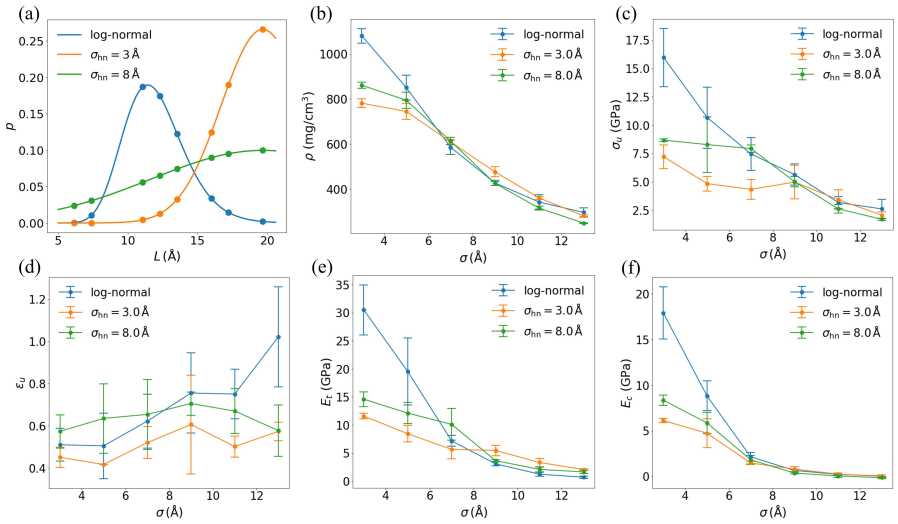

Figure 4.23: Mechanical properties of GA under different probability distributions of the graphene flake side length L. (a) Probability densities of the log-normal distribution, and half-normal distributions with $\sigma_{\text{hn}} = 3.0$ Å and 8.0 Å. (b) Density ρ, (c) tensile strength σ_{u}, (d) tensile failure strain ε_{u}, (e) tensile and (f) compressive moduli E_{t} and E_{c} of GA as a function of σ under three L distributions.

Effect of flake size distribution

Another opportunity to improve the connectivity of GAs is to use a different flake size distribution compared to the log-normal distribution, which has not been covered in the previous research. To examine whether larger graphene flakes will help improve the interconnection of graphene flakes, half-normal distributions (expressed in Eq. 4.18) are considered with the center set as the largest L value sampled by the log-normal distribution to bias towards larger graphene flakes. The σ_{hn} of the half normal distribution is a variable and $\sigma_{\text{hn}} = 3.0$ Å and 8.0 Å are used. $\sigma_{\text{hn}} = 3.0$ Å favors larger flakes more than $\sigma_{\text{hn}} = 8.0$ Å. The probability densities of all distributions for the graphene flake size in this work are compared in Fig. 4.23(a).

Next, ρ, σ_{u}, ε_{u}, E_{t}, and E_{c} of GAs originating from the three distributions are evaluated, as shown in Figs. 4.23(b)–(f). The results for log-normal distributions plotted here are the same as those shown in Fig. 4.12. To compare fairly, $N_{\text{flake}} = 200$, $R = 1.0$ are also used for the two half-normal distribution cases. Fig. 4.23(b) shows that for $\sigma <\sim 6.0$ Å, half-normal distributions produce higher ρ; for $\sigma >\sim 6.0$ Å, three distributions do not show significant distinctions. Similar trends can be observed for tensile strength σ_{u} and moduli E_{t} and E_{c}, as shown in Figs. 4.23(c), (e) and (f). However, for tensile failure strain ε_{u}, half-normal distributions are less sensitive to σ compared with the log-normal distribution, as

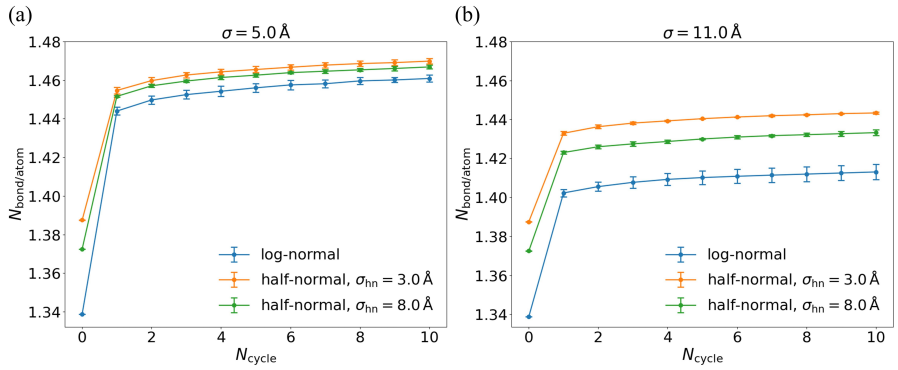

Figure 4.24: GA connectivity property under different distributions of graphene flake side length L. $N_{\text{bond/atom}}$ versus N_{cycle} plots with (a) $\sigma = 5.0$ Å and (b) $\sigma = 11.0$ Å.

shown in Fig. 4.23(d), suggesting that using larger graphene flakes may help reduce property randomness.

Next, the connectivity properties of GAs are studied under different flake size distributions. $N_{\text{bond/atom}}$ as a function of N_{cycle} under $\sigma = 5.0$ Å and 11.0 Å is shown in Fig. 4.24. The results show that as graphene flakes get more dominated by larger ones, $N_{\text{bond/atom}}$ increases. This suggests that using larger graphene flakes may help improve the structural integrity of GAs. The results of $\sigma = 3.0, 7.0, 9.0, 13.0$ Å are provided in Fig. 4.25.

Comparison between simulations and experiments

The simulation findings are compared with experimental results. The GAs were experimentally synthesized and characterized in previous work [96]. The density of GA was tuned by loading with MOF nanoparticles using the chemical reduction method and supercritical drying. By adjusting the MOF/GO mass ratio of the precursors, MOF/GA composites of different densities were obtained. Fig. 4.26 shows experimental data for mechanical properties of GA including tensile strength σ_{u}, tensile failure strain ε_{u}, tensile and compressive moduli E_{t} and E_{c} as a function of density ρ. In comparison to the simulation results shown in Fig. 4.18, the general trends for strength and moduli are similar and matching. Specifically, σ_{u}, E_{t} and E_{c} increase as ρ increases, as shown in Figs. 4.26(a), (c) and (d). However, the experimental results for strain ε_{u} show the opposite trends to the simulations, and the values are more than 10 times lower. This suggests that MD simulations cannot effectively capture the failure behavior of the GA, possibly due to the difference in microstructures and the defect properties. The images of GAs undergoing a catastrophic failure during the tensile test are provided in Fig. 4.27. The comparison above between simulations and experiments indicates that MD simulations can overall capture the main trends of the mechanical properties of GA. The main limitation is that the density of the simulated GAs is much higher

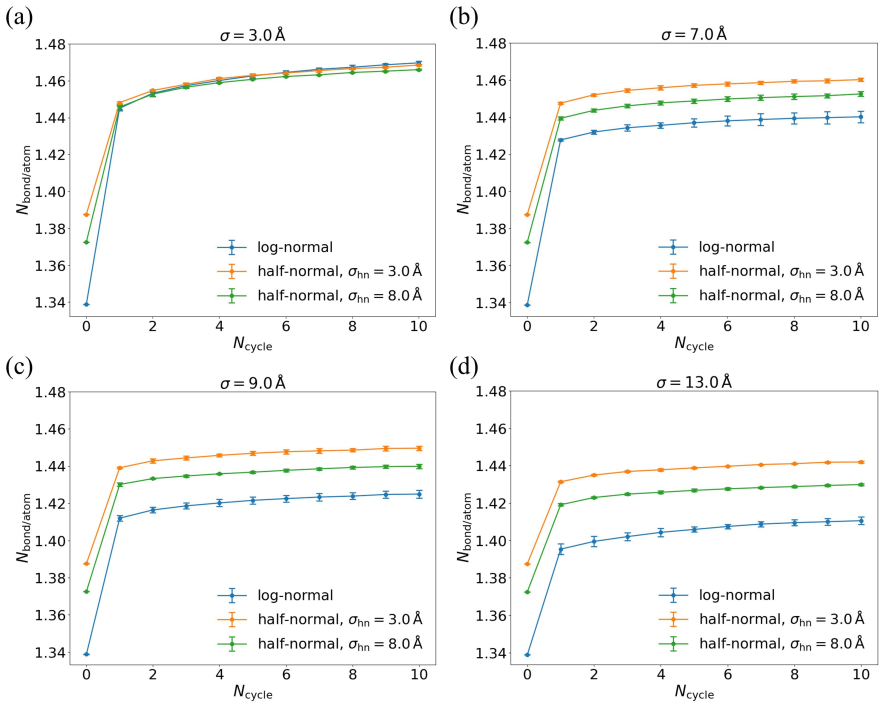

Figure 4.25: GA connectivity property under different distributions of graphene flake side length L. $N_{\text{bond/atom}}$ versus N_{cycle} plots with (a) $\sigma = 3.0$ Å, (b) $\sigma = 7.0$ Å, (c) $\sigma = 9.0$ Å, and (d) $\sigma = 13.0$ Å

than the experimental GA samples, meaning that the values cannot be directly compared but only the trends. Additionally, it is worth noting that based on various synthesis recipes, the mechanical properties of the synthesized GA samples vary substantially, making it very difficult to prepare ideal GA samples to compare with simulated GA structures.

Concluding remarks

In this section, various mechanical properties and the structural integrity of GA as a function of a wide range of simulation parameters are studied. Its contributions to the GA simulation research field are as follows. First, more parameters are covered compared to previous studies. For example, the effects of both LJ parameters ϵ and σ are discussed, while previous studies only considered σ. Second, the graphene size is additionally modeled with parametrized half normal distributions on top of the previous log-normal distribution. Third, thanks to the supercomputer resources, larger material systems up to 1500 graphene flakes are simulated in comparison with the literature [139, 129, 128] and illustrate the size effect on the GA properties. Lastly, the structural integrity and connectivity quality of GA structures are

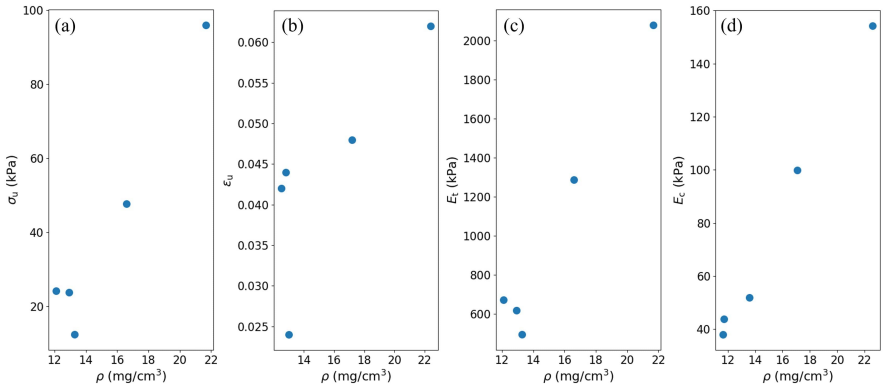

Figure 4.26: Experimental data of mechanical properties of GA as a function of density ρ. (a) Tensile strength σ_u, (b) tensile failure strain ε_u, (c) tensile and (d) compressive moduli E_t and E_c of GA as a function of ρ.

quantified, which has not been previously discussed in the literature. The results show that smaller and less inclusions during the in silico GA preparation are conducive to strength and stiffness but may lead to brittleness. It is also observed that simulating larger material systems reduces the randomness in property calculations. For the structural integrity aspect, it is shown that overly large or overly many inclusions may lead to disconnected GA structures, and that moderately increasing the annealing temperature helps alleviate this issue. Different distributions of graphene flake size are also studied, and larger flakes may improve the structural integrity and reduce the property randomness. In the present simulations, the lowest density achieved is still about 10 times higher than the experimental value. This can be explained by the difference in the pore size between the simulation and the experiment, and bridging or narrowing the gap requires building larger-scale simulation models. Finally, the findings are compared with the experimental results to showcase both the power and the limitation of the simulation technique. It is shown that the general trends for strength and moduli are similar, while the trend for failure strain is different, possibly due to difference in microstructures and the defect properties. This work may deepen the understanding of GA simulations, accelerate materials' design cycles, offer value to experimentalists in materials synthesis, and shed light on the improvement of computational approaches for GA as well as other novel nanomaterials [224].

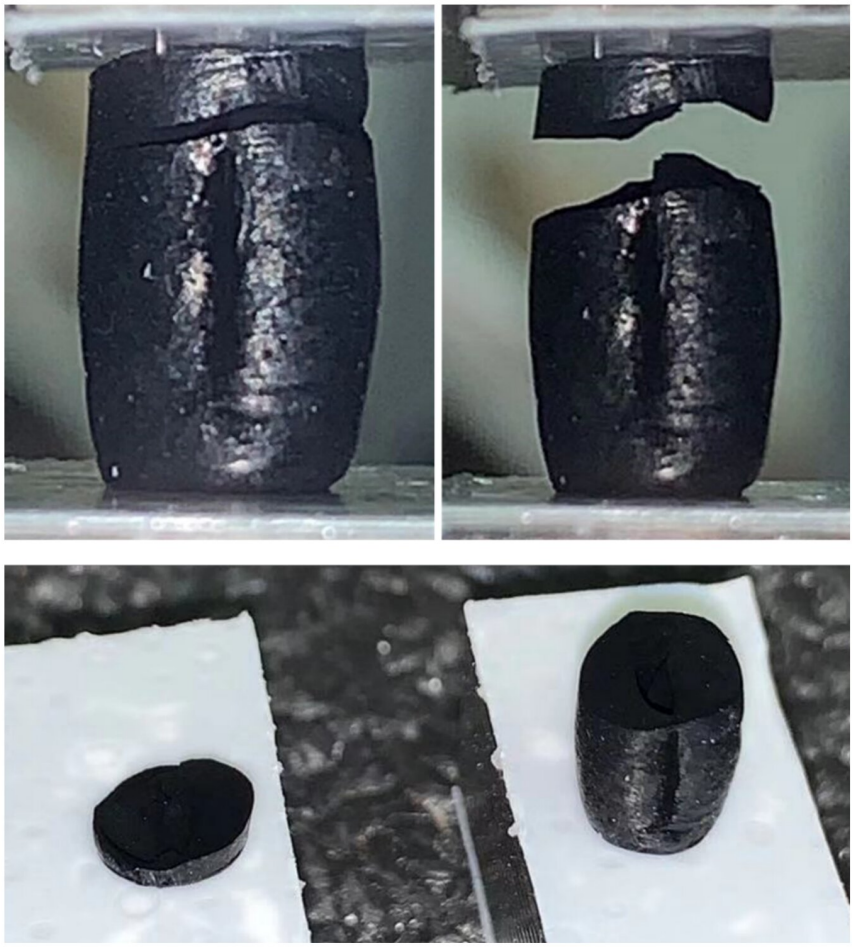

Figure 4.27: Images of GA showing catastrophic failure during tensile test. Compression tests were performed on dynamic mechanical analysis (DMA, TA Instrument Q800). A preload of 10 mN was applied on the GA samples to assure full contact. The samples were compressed to 80% strain with a loading rate of 10% strain/min. Tension tests were performed on universal testing machines (Instron) with a loading rate of 10% strain/min.

Chapter 5

Simulation acceleration via machine learning force fields

For curbing the global temperature increase [108], effective approaches for carbon capture are needed. By utilizing amine-based liquid sorbents, current methods suffer from a high-energy cost for the thermal desorption step that is responsible for of the total operating costs [151]. The use of solid sorbent materials for carbon capture has been proposed as an alternative to amine-based liquid sorbents due to their lower desorption energy requirement, which can potentially boost the commercial viability of point-source carbon capture. Including zeolites, MOFs, covalent-organic frameworks, zeolitic imidazolate frameworks, and porous polymer networks, solid sorbents are nanoporous materials that contain cages, channels, andor slits capable of capturing gas molecules. The MOF class has received particular attention due to their chemical diversity and potentially unlimited structural variations [228, 116, 159]. Generally, MOFs are built by combining two types of building blocks, namely, metal ions with organic linkers, to generate structures with pores ranging from a few to tens of angstroms. The absolute (adsorption capacity) and relative (adsorption selectivity) metrics can be tuned by leveraging the chemical and geometric structural aspects independently [167].

Thanks to the ever-improving computing power [125], high-throughput screening for superior MOFs for carbon capture has been made possible by the availability of open databases of Crystallographic Information Files (CIF) [116, 106, 51], ranging from 10^5 to 10^6 material candidates in total. Most existing in silico studies have focused on atomistic simulations that approximate the interatomic interactions using the LJ and Coulomb potentials. Although this particular choice of molecular model is adequate for CO2's physisorption in MOFs, it neglects the effect of chemisorption (i.e., bond formation with the adsorbate molecule as shown in Fig. 5.1(a)) which is of particular interest for MOFs containing coordinatively unsaturated metal sites, also known as open metal sites [66, 87]. The effect of chemisorption on an open metal site manifests itself more prominently at lower pressures, precisely where the desorption step happens and, therefore, is of utmost importance for the cost of regeneration energy.

The chemical specificity of chemisorption at open metal sites has been a constant chal-

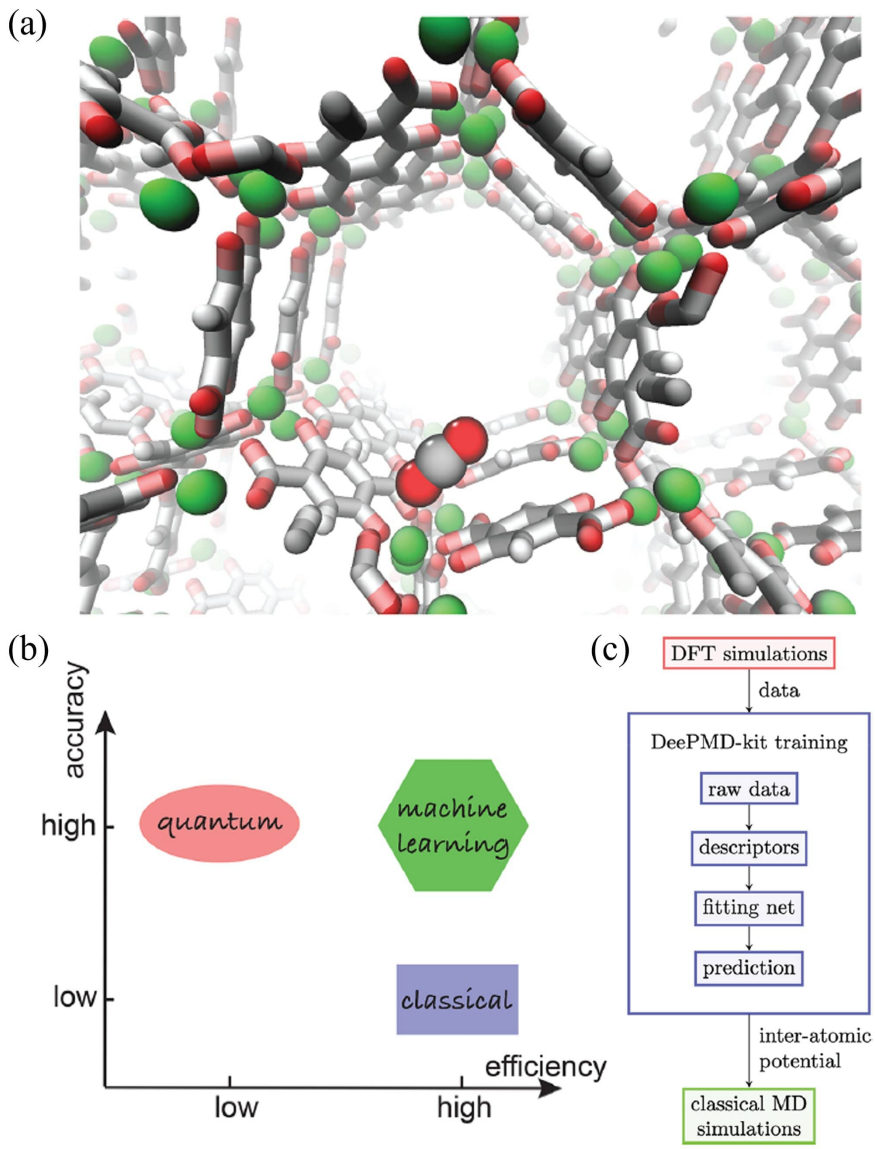

Figure 5.1: Atomistic simulations of CO_2 in Mg-MOF-74. (a) Illustration of one CO_2 molecule chemically adsorbed at an open metal site in Mg-MOF-74. (b) Comparisons of existing QC and classical atomistic simulations. (c) Scheme of the QMLFF-based simulation approach.

lenge for atomistic simulations based on nonspecific classical force fields, such as UFF and DREIDING [45]. Recent attempts to overcome this challenge have mainly resorted to electronic structure methods, such as DFT, Hartree-Fock, and second order Møller-Plesset (MP2) perturbation theory, which allowed the study of CO2's chemisorption on specific materials [127, 135, 6] through the sophisticated decomposition of the electronic interaction energy from quantum chemistry (QC) calculations into classical potentials such as Morse [89] and Buckingham [46, 27, 113], the creation of reparametrized polarizable potentials, and the realization of first-principles Monte Carlo simulations [53]. Nevertheless, despite presenting improved accuracy when compared with classical force fields, these approaches are still computationally too expensive and/or heavily dependent on human intervention (due to the lack of transferability), which makes them less attractive. Therefore, these two existing categories of QC and classical simulations, pose a trade-off between accuracy and efficiency. Particularly, to obtain the entropy contribution in a simulated system precisely, it requires both the accuracy of QC and the extensive sampling of classical simulations, which is challenging.

5.1 Machine learning force fields for metal-organic frameworks

The emerging ML force fields or potentials strive to obtain the best of both worlds, as illustrated in Fig. 5.1(b). Provided with accurate QC simulation data, ML potentials can have optimized parameters of their flexible non-analytical function forms such as a deep neural network, i.e., the constraint of a physics-based functional form is relieved. In practice, one can fine-tune the neural network architecture freely according to the materials system complexity to achieve an optimal performance. After proper training, an ML potential can inherit the accurate nature of the quantum-based method and can be used in efficient classical simulations. Previous efforts in classical MD simulations with ML force fields have been encouraging, including the prediction of thermal and phonon properties of graphene [146], extensive modeling of the bond breaking process of silicon [11], accurate simulations of nanoscale amorphous carbon structures [43], among others.

In this section, ML force fields are developed using the QC simulation data to solve the challenging chemisorption of CO_2 in Mg-MOF-74 (Fig. 5.1(a)). The pipeline of the ML potential development and implementation used in this study is presented in Fig. 5.1(c). Quantum-informed ML force fields (QMLFF) are developed using the DeePMD-kit package [173] as a template, which enables flexibly adjusting the neural network architecture according to the problem complexity and to conveniently interface with the training data obtained from QC simulations. After the training, QMLFF-based all-atom MD simulation is performed to investigate physico-chemical phenomena (namely, chemisorption and diffusion) of CO_2 in Mg-MOF-74.

Results

Machine learning force field

First, DFT-based calculations are conducted to optimize the Mg-MOF-74 structure, using the CP2K software package [75]. Starting from the DFT-optimized structure, QC-based molecular dynamics (QC-MD) simulations in the NVT ensemble are conducted and the trajectory for the ML training are generated. DFT calculations follow the protocol in previous similar studies [153]: Perdew, Burke, and Ernzerhof (PBE) exchange functional [132], DFT-D3 corrections for the van der Waals interaction [85], Gaussian plane-wave pseudopotentials [69], and DZVP basis sets for carbon, oxygen, hydrogen, and magnesium atoms [169]. Consistent with previous DFT studies [124] for a unit cell (containing 162 atoms) of Mg-MOF-74 in the hexagonal coordinate system, cell lengths along the a, b, and c axes are $l_a = l_b = 26.152$ Å and $l_c = 6.996$ Å, correspondingly. These values are slightly larger than experimental ones: $l_a = l_b = 25.921$ Å and $l_c = 6.863$ Å [141]. For one CO_2 molecule bound on a Mg site, the DFT calculation yields the bond length $l = 2.38$ Å for the $\mathrm{Mg}\cdots\mathrm{O_{CO2}}$ bond. This value is consistent with ones obtained from previous DFT studies [199]. It is further verified that the low-cost PM6 method [156] with Grimme's D3 correction for correlation [64] can yield consistent results with the ones from the PBE-based DFT calculations. For example, the bond length for CO_2 adsorbed at a Mg site is 2.23 ± 0.11 Å from this low-cost QC (PM6+D3) calculation, similar to the above result from the PBE+D3 level DFT calculation. Therefore, for the computationally challenging QC-MD (ground-state DFT-MD) simulations, the PM6+D3 method is applied to simulate the Mg-MOF-74 with various numbers of CO_2 molecules in the NVT ensemble. Notably, the choice of the computationally efficient PM6+D3 method is for the purpose of proof-of-concept and the application of other high-accuracy DFT functionals can achieve even better outcomes albeit computationally challenging. From the MD trajectory ($T_\mathrm{A} = 300$ K), the chemisorption of CO_2 on a Mg site in Mg-MOF-74 is observed with a mean $\mathrm{Mg}\cdots\mathrm{O_{CO2}}$ bond distance of 2.23 ± 0.11 Å and a mean tilting angle ($\angle\mathrm{Mg}\cdots\mathrm{O_{CO2}} - \mathrm{C_{CO2}}$) of $118.62 \pm 10.62°$. These simulation trajectories along with force and energy information are used for the training of a deep-learning potential for MD simulations. The temperature in QC-MD simulations is kept constant (at both 300 and 600 K) using a velocity-rescaling thermostat, and the time step is 1 fs. The trajectories of simulations at 600 K (yielding a good sampling of CO_2 everywhere inside the MOF channels) along with the force on each atom and the energy information are used for the training of ML potentials.

Then the Deep Potential-Smooth Edition (DeepPot-SE) model is applied to generate the interatomic ML potential. DeepPot-SE is a good candidate for the present system mainly thanks to the following advantages: 1) The only inputs are chemical species and atom coordinates. 2) The model is size extensive, i.e., the ML potential can be used for systems of different sizes. 3) The designed descriptor preserves translational, rotational, and permutational symmetries. 4) The model is continuously differentiable at the cutoff radius. 5) The model is interfaced with TensorFlow and LAMMPS via the DeePMD-kit package,

which makes the model training and deployment convenient. The DeepPot-SE model maps the atom configuration to the total energy via the following steps: Trajectory coordinates $\mathbf{R}$, local environment coordinates $\mathbf{R}^i$ (which preserves the translational symmetry and is predefined by the cutoff distance), local energies E^i, and the total system energy E. This is based on the general assumption of the neural-network type ML potential that the total energy equals the sum of atomic contributions, i.e., $E = \sum_i E_i$. What makes DeepPot-SE different from other models is the designed mapping from the local environment coordinates $\mathbf{R}^i$ to the local energy E^i, which consists of the following procedures in sequence. First, $\mathbf{R}^i$ is mapped to the generalized coordinate matrix $\tilde{\mathbf{R}}^i$, which is continuously differentiable at the cutoff radius. Second, $\tilde{\mathbf{R}}^i$ is fed into an embedding network to output a local embedding matrix $\mathbf{G}^i$. Third, $\mathbf{G}^i$ is transformed into a feature matrix (descriptor) that preserves the rotation and permutation symmetries. lastly, $\mathbf{G}^i$ is mapped to E^i by a fitting network. Fig. 5.1(c) illustrates the above training procedure, and the theoretical details of DeepPot-SE can be found in Ref. [206].

Both the embedding and the fitting networks are fully-connected, and the sizes are dictated by vectors n_{embed} and n_{fit}. The dimension of these vectors equals the number of hidden layers and the integer value of each entry denotes the size of each hidden layer. Network parameters w are updated by the Adam stochastic gradient descent method, which optimises the following loss function:

$$L(p_\epsilon, p_f, p_\xi) = \frac{1}{|\mathcal{B}|} \sum_{l \in \mathcal{B}} p_\epsilon |E_l - E_l^w|^2 + p_f |\mathcal{F}_l - \mathcal{F}_l^w|^2 + p_\xi |\Xi_l - \Xi_l^w|^2 \tag{5.1}$$

where $\mathcal{B}$ denotes the minibatch; $|\mathcal{B}|$ is the batch size; l denotes the index of the training data; E, $\mathcal{F}$, Ξ denote the energy, the force, and the virial, respectively; p_ϵ, p_f, p_ξ are tunable prefactors. The training data in this study do not contain the virial component. Therefore p_ξ is set as 0. The decaying learning rate $\alpha(t)$ is expressed as

$$\alpha(t) = \alpha_0 d^{\frac{t}{t_d}} \tag{5.2}$$

where d is the decay rate; t_d is the decay steps. The prefactor is structured as

$$p_* = p_*^{\text{start}} \frac{\alpha(t)}{\alpha_0} + p_*^{\text{limit}} (1 - \frac{\alpha(t)}{\alpha_0}) \tag{5.3}$$

where the subscript * takes on ϵ, f and ξ. A range of learning rates and various learning rate decaying mechanisms are explored to improve training. All ML hyperparameters used in this study are summarized in Table 5.1. At each frame, atom types, atom coordinates, atomic forces, system potential energy, and simulation box size are used in training. In the present training, the units of time, length, energy, force, pressure are ps, Å, eV, eV / Å, bar, respectively. The rooted mean squared error (RMSE), expressed as RMSE $= \sqrt{\sum_{i=1}^{N} (\hat{y}_i - y_i)^2 / N}$, is minimized during training, where $\hat{y}_i$ and y_i are the predicted property and the ground truth of ith sample; N is the total number of the samples.

Table 5.1: Hyperparameters for ML potential training.

r_{cut}	n_{embed}	n_{fit}	α_0	d	t_{d}	$\lvert\mathcal{B}\rvert$
6.0 Å	[25, 50, 100]	[240, 240, 240]	0.001	0.95	5000	100
$p_\epsilon^{\text{start}}$	$p_\epsilon^{\text{limit}}$	p_f^{start}	p_f^{limit}	p_ξ^{start}	p_ξ^{limit}	
0.0005	0.0005	1000	1	0	0	

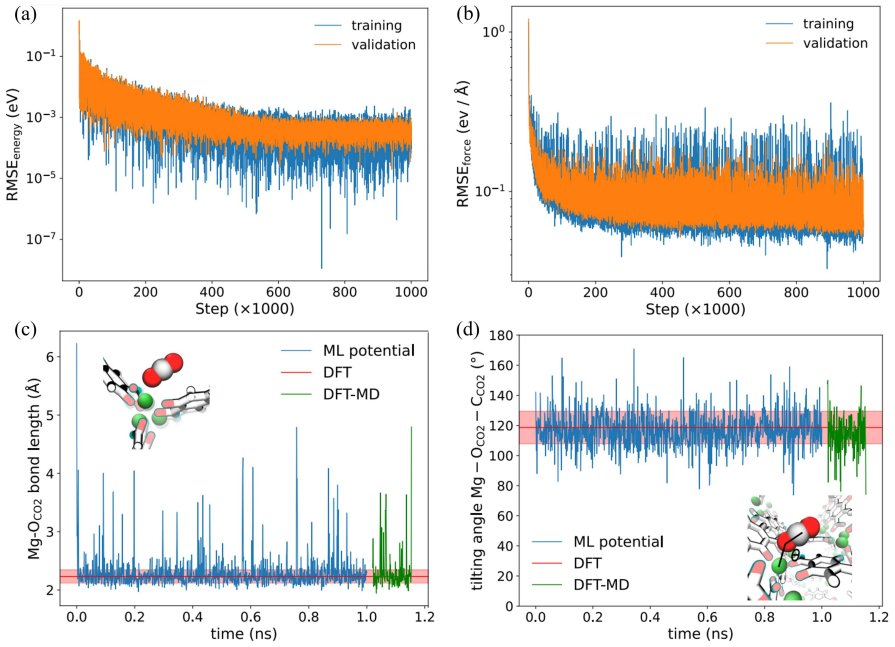

Figure 5.2: Training and verification of QMLFF with the trajectory from the QC MD simulation of Mg-MOF-74 with one CO_2 at 600 K that guarantees proper sampling for CO_2 both on and off the Mg sites. (a) Energy and (b) forces as a function of the training step. Time series of (c) Mg–OCO_2 bond length and (d) tilting angle Mg–OCO_2–CCO_2 from the QMLFF-based MD simulation (blue) and from the DFT-based MD simulation (green) at 300 K. The starting time for results from the DFT based MD simulation is shifted from 0 ns to 1.02 ns for clarity. The red horizontal lines represent the mean values from DFT calculations (at 0 K), and the shaded areas indicated one standard deviation from the mean.

The learning curves for the rooted mean squared error (RMSE) of energy and force as a function of the training step are shown in Figs. 5.2(a) and (b), respectively, up to 1 million training steps. The RMSEs of both the energy and the forces have reached a plateau toward the end of the training (for both the training and the validation data), indicating that the ML potential has been sufficiently trained.

To validate the obtained QMLFF, MD simulations are run in the NVT ensemble at 300

K for 1 ns to verify the structural stability of Mg-MOF-74 and calculated the $Mg \cdots O_{CO2}$ bond length (Fig. 5.2(c)) and the tilting angle $\angle Mg \cdots O_{CO2} - C_{CO2}$ (Fig. 5.2(d)). where the subscript "CO_2" denotes atoms belonging to the CO_2 molecule. The time series of the bond length and the tilting angle are shown in Figs. 5.2(c) and (d). Most time-dependent bonds and angles fall within one standard deviation of the ones obtained in QC calculations, suggesting that the ML potential can produce reasonable MOF-CO_2 structures. Fig. 5.2(c) appears to have many "spikes" that are larger than 3 Å. These events occur under the following two circumstances: (1) when the CO_2 is in the process of hopping from one Mg site to another (consistent with the CO_2 hoping dynamics found in experiment34); (2) when the CO_2 switches its oxygen atoms bound to the Mg site, both of which yielded a longer-than usual $Mg \cdots O$ distance. From the frequency of those events (Fig. 5.2(c)), the average residence time for the CO_2 on a Mg site is about 30 ps. To verify these results, a 135 ps DFT-based MD simulation is performed and the similar time dependencies is obtained (green lines in Figs. 5.2(c) and (d)). When comparing the efficiency of these two MD simulation methods, the QMLFF-based method is about 1000 times faster than the DFT-based method.

Additionally, DFT calculation using the nudged-elastic-band (NEB) method for adsorption energies of CO_2 in various locations inside Mg-MOF-74 is conducted. For each DFT-optimized CO_2-MOF complex, the QMLFF potential is used to predict the CO_2 adsorption energy. Overall, results from these two methods are comparable, as shown in Fig. 5.3.

DFT-MD data at 600 K are used for the main training because a higher temperature provides better sampling for CO_2 both on and off the Mg sites, so that the ML potential can be trained with more different configurations. An ML potential with DFT-MD data at 300 K are also trained. In the comparison of structural feature prediction for CO_2 on the Mg sites (Figs. 5.2 and 5.4), ML potentials trained with 600 K and 300 K data seem to present a minimal difference, which is expected. But it is anticipated that ML potential trained with 600 K data will result in more accurate calculations of free energy landscape and diffusion coefficients to be studied in the following.

Free energy landscape of CO_2 in Mg-MOF-74

Generally, the QC simulation is more accurate for calculating enthalpy than the classical one, while the classical simulation (benefiting from a long simulation trajectory) is more efficient for calculating entropy than the QC one. It is still challenging to obtain accurate binding free energy (with contributions from both enthalpy and entropy) from either QC or classical simulation. With the above QMLFF, unbiased MD simulations of Mg-MOF-74 with one CO_2 in the NVT ensemble are performed. A high temperature of 600 K is used to speed up the statistical sampling.

For the free energy landscape calculation, 25 trajectories at 600 K starting from different random seeds are generated and put together. Each trajectory has a length of 1 ns and a total of 100,000 frames. It is noteworthy that the QMLFF-based simulations are highly efficient (see Table 5.2). Trajectories of a total length of 25 ns are gathered to compute the density distribution n of CO_2 (namely positions of the C atom in CO_2) in Mg-MOF-74 that is further

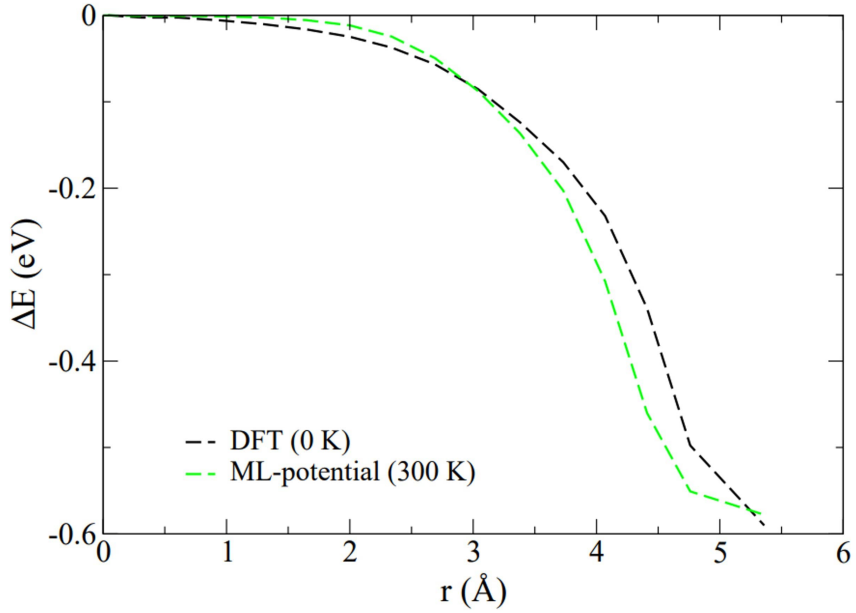

Figure 5.3: Adsorption energies of CO_2 when it moves from the channel center ($r = 0$ Å) to a Mg-site ($r \sim 5.4$ Å). The reference energy is chosen when CO_2 is at the center of a MOF channel.

Table 5.2: Cost of computation in this study

task	cores used (no GPU)	run-time for each simulation	number of simulations needed	simulation time
DFT (PM6+D3)	16	<1 day	2	$\sim$ ps
ML training	32	$\sim$1.5 days	2	NA
MD	16	$\sim$1 day	31	$\sim$ tens of ns

used to obtain the free energy landscape E using the equation $E = E_{\text{ref}} – k_{\text{B}}T\ln(n/n_{\text{ref}})$, where E is the free energy; k_{B} is the Boltzmann constant; T is the temperature; and the subscript "ref" denotes the reference at the channel center. The plots for density distributions on the x–y plane and the θ–z plane are shown in Fig. 5.5.

The free energy landscape on the x–y plane plotted against the Mg-MOF-74 framework is shown in Fig. 5.6(a). The lowest free energy areas are located near the Mg sites, while the center of the MOF channel has the highest free energy. The free energy landscape indicates that energetically it is very difficult for a bound CO_2 to escape the Mg site along the radial direction. The free energy landscape is also ploted on the θ-z plane, as shown in Fig. 5.6(b).

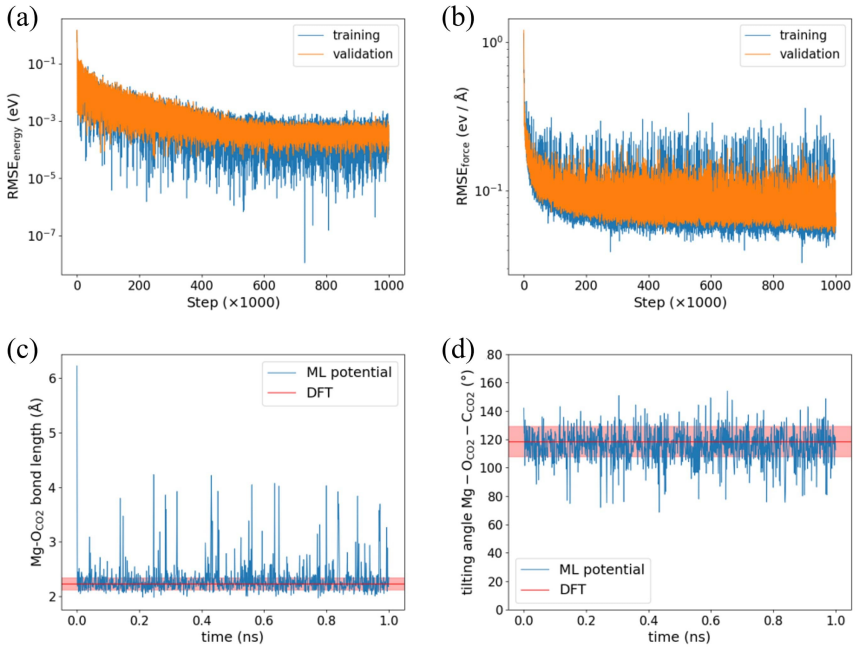

Figure 5.4: ML potential training and verification with DFT trajectories of Mg-MOF-74 and one CO_2 at 300 K as the training data. RMSEs of (a) energy and (b) forces as a function of the training step. Time series of (c) Mg-O_{CO_2} bond length and (d) the tilting angle Mg-O_{CO_2}-C_{CO_2}.

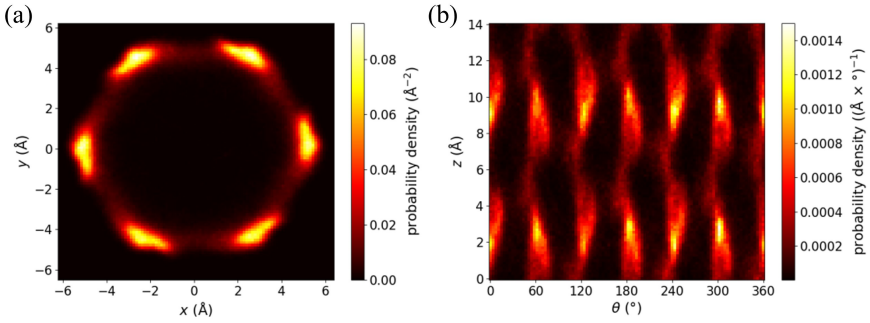

Figure 5.5: Probability-of-density distributions of CO_2 inside one Mg-MOF-74 channel. Probability density distributions in (a) the x-y plane and (b) the θ-z plane.

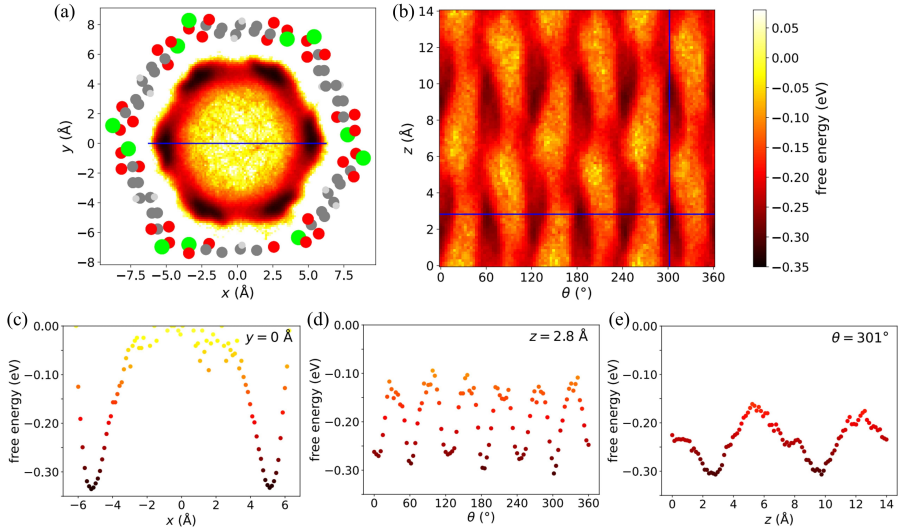

Figure 5.6: Free energy landscape of CO_2 inside one Mg-MOF-74 channel. (a) Free energy landscape on the x–y plane. The position of the Mg-MOF-74 framework is also plotted for reference. (b) Free energy landscape on the θ-z plane. (c) 1D free energy sliced along $y = 0$ Å from (a). 1D free energy sliced along (d) $z = 2.8$ Å and (e) $\theta = 301°$ from (b). All plots use the same color bar scale.

Each low free energy area corresponds to one Mg site. Compared with Fig. 5.6(a), it can be discerned that it is easier for a bound CO_2 to break free from one Mg site tangentially than radially.

More quantitatively, three 1D free energy changes are shown in Figs. 5.6(c-e), by slicing along $y = 0$ Å of Fig. 5.6(a) and along $z = 2.8$ Å and $\theta = 301°$ of Fig. 5.6(b), respectively. These slices pass a few local minima originating from Mg sites in both free energy landscapes (Figs. 5.6(a) and (b)). Fig. 5.6(c) shows that the binding free energy for CO_2 from the center of a channel to a Mg site is about -0.33 eV (or -31.8 kJ/mol). However, when hopping in the θ direction between two neighboring Mg sites, the free energy barrier (measured from the valley-to-peak in Fig. 5.6(d)) is only about 0.20 eV (or 19.3 kJ/mol). Additionally, if the CO_2 moves along the z direction from one Mg site to another neighboring one, the free energy barrier (Fig. 5.6(e)) is further reduced to 0.15 eV (or 14.5 kJ/mol). These results suggest that it is much easier for a bound CO_2 (on a Mg site) to diffuse along the channel surface (in either z or θ direction) than to reach the channel center radially. For comparison, A 30 ns classical-force-field (UFF+DDEC) based MD simulation is performed at 600 K. For the classical force field the interaction energies between non-bonded atoms are computed

through a combination of LJ and Coulomb potentials.

$$U_{ij}(r_{ij}) = 4\varepsilon_{ij}\left[\left(\frac{\sigma_{ij}}{r_{ij}}\right)^{12} - \left(\frac{\sigma_{ij}}{r_{ij}}\right)^{6}\right] + \frac{1}{4\pi\epsilon}\frac{q_i q_j}{r_{ij}} \tag{5.4}$$

where i and j are interacting atoms, r_{ij} is the distance between atoms i and j. ε_{ij} is the well depth and σ_{ij} the distance at which the intermolecular potential between the two particles is zero.q_i and q_j are the partial charges form atoms i and j calculated using the DDEC method [97]. LJ parameters for the MOF atoms are taken from UFF [143], and the parameters for CO_2 are taken from the TraPPE [136] force field. The LJ parameters between atoms of different types are calculated using the Lorentz–Berthelot mixing rules. Atomic charges are calculated using the DDEC method. The cutoff for LJ and charge–charge short-range interactions used is 12.8 Å with the LJ potential shifted to zero at the cutoff, the Ewald sum technique is applied to compute the long-range electrostatic interactions with a relative precision of 10^{-6}, and a supercell of $2 \times 2 \times 4$ is used to ensure that the box size is twice the cutoff radius. The free energy landscape (Fig. 5.7) shows a much weaker adsorption of CO_2 inside Mg-MOF-74 than the one shown in Fig. 5.6, i.e., no chemisorption. Therefore, the classical force field cannot properly describe the interaction between CO_2 and Mg-MOF-74.

In addition, the free energy landscapes is sliced along $x = 0$ Å and along $\theta = 270°$, passing benzene rings in the MOF (see Figs. 5.8(a) and (b)). Results show that benzene rings (considered as secondary binding sites for CO_2 in Mg-MOF-74) also yield a binding free energy of -0.22 eV (or -21.2 kJ/mol) (Fig. 5.8(a)), not as strong as that for the Mg sites. Note that the free energy barrier for CO_2 to hop between neighboring benzene rings is very small ($\sim$ 0.11 eV or 10.6 kJ/mol, Fig. 5.8(b)).

Diffusion of CO_2 in Mg-MOF-74

Next, the CO_2 diffusion phenomenon inside the Mg-MOF-74 channel is investigated. Specifically, the diffusion in z and θ directions are studied, corresponding to the axial and the angular movement, respectively. MD simulations are carried out in the NVT ensemble at different temperatures (300 K and 600 K) using the same ML potential to examine the difference in the CO_2 diffusion phenomenon, because the escaping of CO_2 from a Mg site is a thermally activated process.

The time dependency of z and θ are shown in Figs. 5.9(a-d). At 300 K, the CO_2 molecule underwent the stick-slip type of diffusion in both z and θ directions (Figs. 5.9(a) and (b)). The stick state corresponds to the bond forming between CO_2 and a Mg site, while each slip state signifies a bond breaking. In each slip event, CO_2 diffuses along the z direction by a fixed distance of $d = 6.996$ Å (the size of one unit cell in the z direction) or diffuses along the θ direction by a fixed angle of 60°. The CO_2 diffusion is much faster at 600 K than at 300 K (Figs. 5.9(c) and (d)). This suggests that thermal fluctuation at a high temperature will facilitate CO_2's hopping from one free energy minimum to another. The residence time for CO_2 on a Mg site (in a stick state) can last up to 1-2 ns before slipping quickly to a

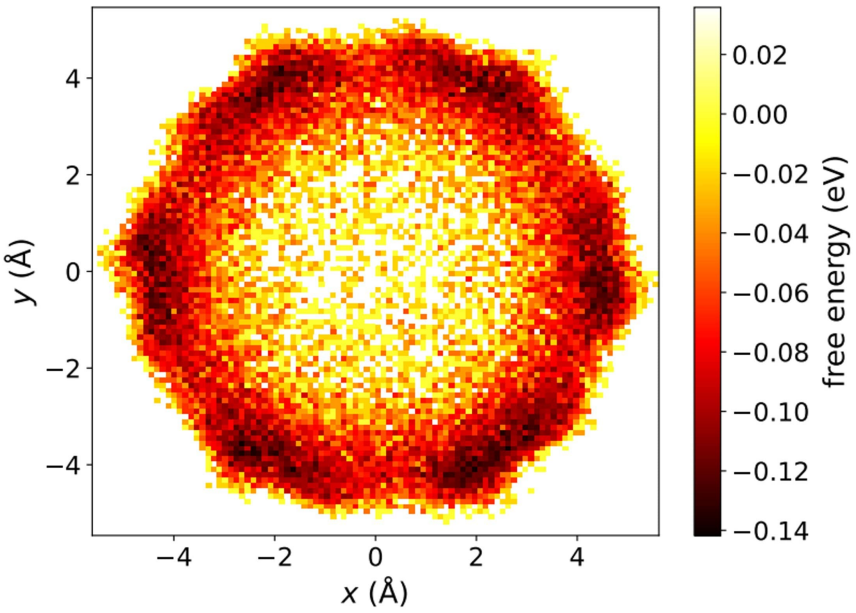

Figure 5.7: Free energy landscape generated from the 30-ns MD simulation at 600 K using the classical force fields (UFF+DDEC). The NVT ensemble is used and Mg-MOF-74 is kept rigid during the simulation. The binding free energy of CO_2 from the channel center to a Mg-site is -0.14 eV, which is about two times smaller (i.e. weaker binding) than the one obtained from the QMLFF-based MD simulation. No chemisorption is observed in the classical-force-field-based MD simulation.

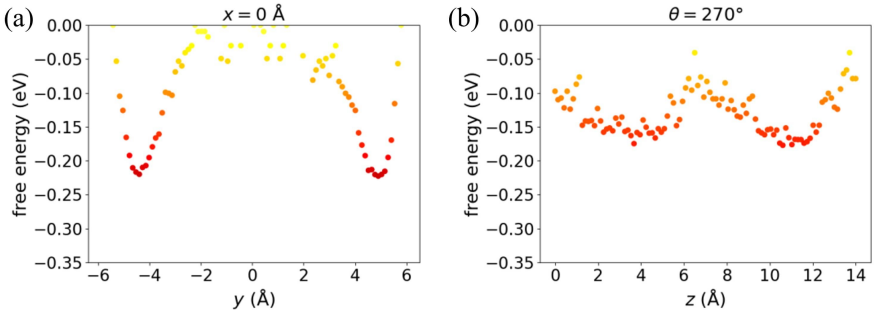

Figure 5.8: 1D free energy plot passing benzene rings obtained from the QMLFF-based MD simulation. 1D free energy plots sliced (a) along $x = 0$ Å on the x-y plane free energy landscape (Fig. 5.6(a)), and (b) along $\theta = 270°$ on the θ-z plane free energy landscape (Fig. 5.6(b)).

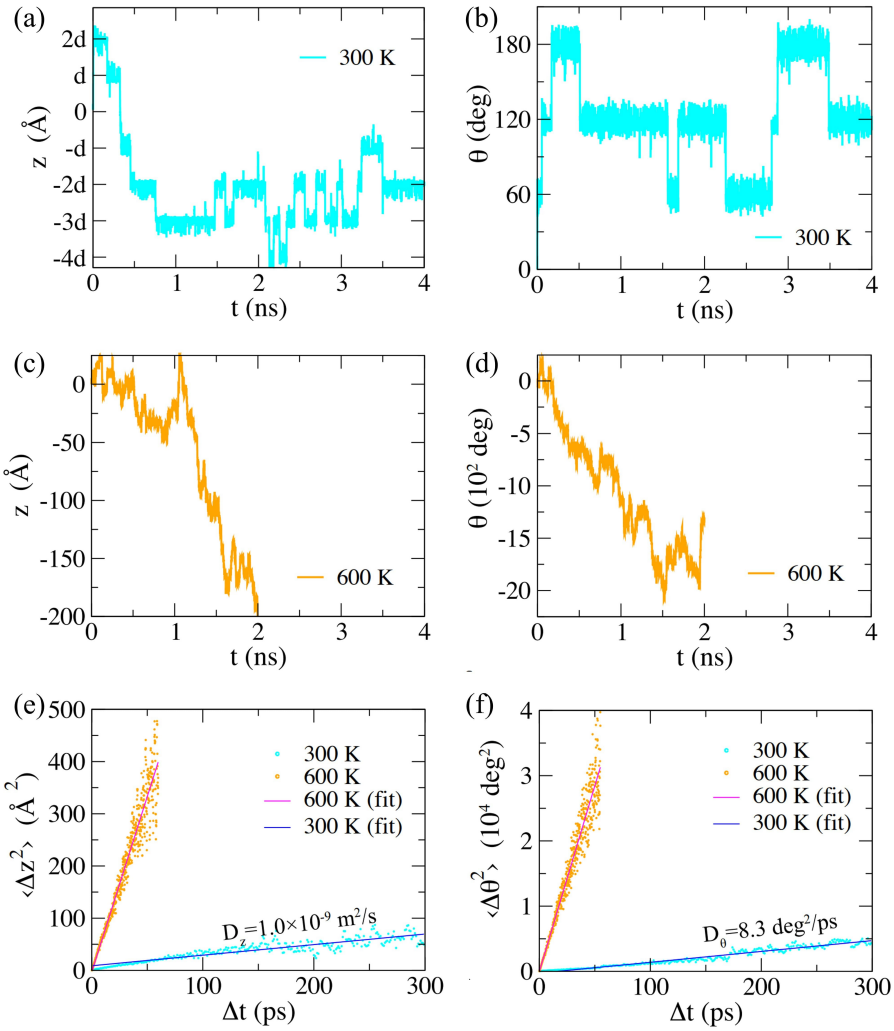

Figure 5.9: Diffusion phenomenon of one CO_2 molecule inside the Mg-MOF-74 channel. (a) z coordinate and (b) θ coordinate of the CO_2 molecule as functions of time. (c) $\langle \Delta z^2 \rangle$ and $\langle \Delta \theta^2 \rangle$ as functions of Δt.

neighboring Mg site. In contrast, at 600 K the stick state only occurred occasionally, yielding a much faster diffusion.

With the time series shown in Figs. 5.9(a-d), the diffusion coefficients of CO_2 in Mg-MOF-74, D_z and D_θ in z and θ directions respectively, can be calculated by taking the slope of the mean-squared displacement of CO_2 at large time intervals Δt, concretely

$$D_z = \lim_{\Delta t \to \infty} \frac{\langle \Delta z^2 \rangle}{2\Delta t} = \lim_{\Delta t \to \infty} \frac{\langle (z_t - z_{t-\Delta t})^2 \rangle}{2\Delta t} \tag{5.5}$$

$$D_\theta = \lim_{\Delta t \to \infty} \frac{\langle \Delta\theta^2 \rangle}{2\Delta t} = \lim_{\Delta t \to \infty} \frac{\langle (\theta_t - \theta_{t-\Delta t})^2 \rangle}{2\Delta t} \tag{5.6}$$

where $\langle \cdot \rangle$ denotes the time average. $\langle \Delta z^2 \rangle$ and $\langle \Delta\theta^2 \rangle$ are plotted as functions of Δt in Figs. 5.9(c) and (d), which show a strong linear relation. By linear-fitting the data points $D_z = 1.0 \times 10^{-9}$ m^2/s and $D_\theta = 8.3$ deg^2/s for 300 K, $D_z = 3.4 \times 10^{-8}$ m^2/s and $D_\theta = 285$ deg^2/s for 600 K are obtained. Notably, D_z at 300 K is very close to but smaller than the available experimental result 5.8 $\times 10^{-9}$m^2/s for CO_2 in Zn-MOF-74 [54], which is reasonable given the fact that the adsorption of CO_2 on a Zn site is weaker than on a Mg site.

The observed stick-slip events of CO_2 diffusion in Mg-MOF-74 are thermally activated after overcoming free-energy barriers, which can be described by the Arrhenius-type equation,

$$D = D_0 e^{-\Delta E / k_\mathrm{B} T} \tag{5.7}$$

where D and D_0 are the diffusion coefficient and the prefactor respectively, and ΔE is the activation free-energy (barrier). Thus, with simulation results for two temperatures (300 K and 600 K) above, the activation free-energy ΔE can be estimated using the following equation,

$$\Delta E = \left(\frac{1}{k_\mathrm{B} T_1} - \frac{1}{k_\mathrm{B} T_2}\right) \cdot \ln(D_2/D_1) \tag{5.8}$$

where T_1 and T_2 are 300 K and 600 K, respectively; D_1 and D_2 are the diffusion coefficients at 300 K and 600 K, respectively. For both the longitudinal and the angular diffusion, $D_2/D_1 \sim 34$. Therefore, the calculated free-energy barrier ΔE for the longitudinal or the angular motion is 0.18 eV, which is in excellent agreement with the result of the free-energy landscape shown in Fig. 5.6. For comparison, Fig. 5.6(d) and (e) show that the free-energy barriers are 0.17 and 0.16 eV for the angular and longitudinal motions, respectively.

It is worth mentioning that MD simulations ($T = 300$ K) with classical force fields (Figs. 5.10(a) and (b)) predicted much faster diffusion for CO_2 in Mg-MOF-74 due to the lack of CO_2 chemisorption on the Mg sites. As shown in Fig. 5.10(c), $D_z = 9.5 \times 10^{-9}$ m^2/s for CO_2's diffusion along the z direction in Mg-MOF-74, which is about an order of magnitude higher than the QMLFF-based result (Fig. 5.9(e)). Furthermore, $D_\theta = 208$ deg^2/s (Fig. 5.10(d)), which is about 50 times larger than the QMLFF-based result (Fig. 5.9(f)). These results highlight the necessity of applying the QMLFF method to model the CO_2 diffusion in MOFs with open metal sites.

Discussion

Generally, many physical quantities such as the free energy and the diffusion coefficient require extensive and accurate statistical samplings in atomistic simulations, which is prohibitive for the *ab initio* simulation due to the long waiting time and enormous computing resources. Although many statistical sampling methods (such as the umbrella sampling and

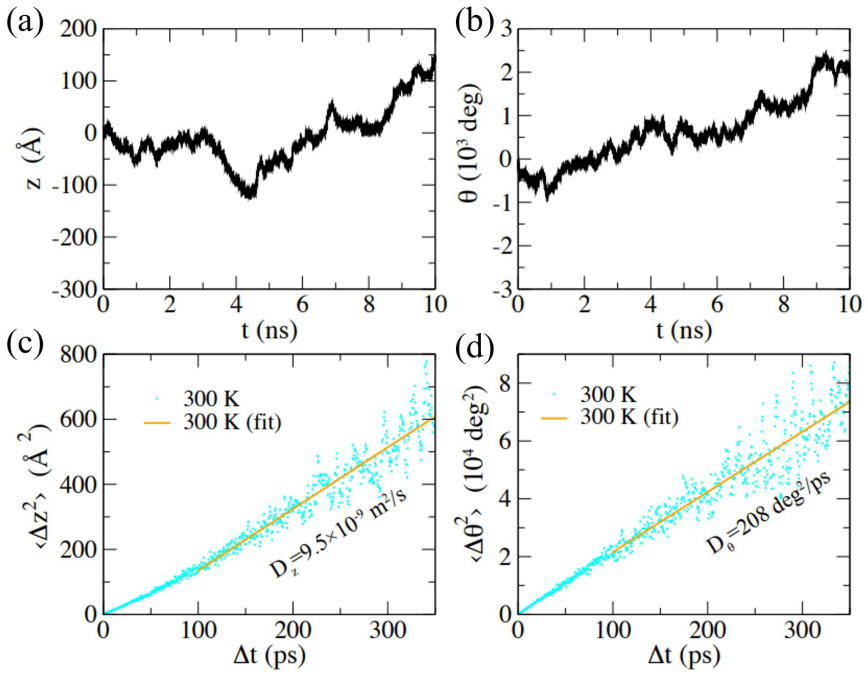

Figure 5.10: Diffusion of CO_2 inside Mg-MOF-74 channel from the 10-ns MD simulation with classical force fields (UFF+DDEC). (a) Diffusion along the z direction; (b) Diffusion along the θ direction; (c) $\langle \Delta z^2 \rangle$ and (d) $\langle \Delta \theta^2 \rangle$ as functions of Δt.

free energy perturbation) have been developed for classical atomistic simulations, the available classical force fields are generally not accurate. Typically, the classical simulation is fair for the physisorption of CO_2 in a solid sorbent but fails to describe the chemisorption. To overcome this difficulty, an approach that permits a highly efficient classical simulation using ML potentials (or QMLFF) trained according to data from QC simulations is developed. To my best knowledge, the free energy landscape for CO_2 inside the Mg-MOF-74 as well as CO_2's diffusion coefficients have not be obtained in previous simulations with a quantum-level accuracy. Particularly, the predicted diffusion coefficient for CO_2 in Mg-MOF-74 is reasonable when compared with limited experimental results.

One interesting application of the present method is to use ML potentials in Monte Carlo simulations to obtain CO_2 adsorption in MOFs at each temperature and pressure. It is believed that ML potentials capable of accurate energy prediction can be used in grand canonical Monte Carlo simulations to yield accurate isotherms for gas adsorption. Additionally, the present approach can be extended to study the CO_2 hydrolysis in MOFs with open metal sites [187], where simulations can be conducted in a similar fashion given high-fidelity trajectories as the training data for the ML potential.

The present simulation results can be further improved with following customized procedures. Within the present ML framework, the same set of hyperparameters is used for the training of various ML potentials. It is possible to fine-tune the step-dependent weights associated with the energy and the forces, depending on their respective importance in a simulation. Additionally, one can tweak the architectures of the embedding net and the fitting net, which potentially can improve the expressiveness of the ML model. Last but not least, one can feed a large amount of DFT training data (thus an enhanced sampling of CO_2 at all possible locations in Mg-MOF-74) to the ML model to improve the accuracy.

Concluding remarks

In this section, it is demonstrated that atomistic MD simulations with the quantum-informed ML potentials can yield results not only comparable to those directly from QC simulations but also close to experimentally measured ones. The present approach can be applied for any chemisorption of small gas molecules (such as CO_2, N_2 and H_2O) in a MOF with open-metal sites. More importantly, this QMLFF-based approach (free from human intervention) can be automated on high-performance clusters or supercomputers for *in silico* screening of $\sim$1 million MOFs. Broadly, it is expected that this low-cost and high-accuracy approach can greatly facilitate the in silico modeling for the chemisorption and diffusion of a small molecule in any solid sorbents [226].

Chapter 6

Summary and future directions

In the present thesis, ML-assisted simulation and design approaches for functional nanomaterials are demonstrated, with a focus on the graphene family. MD simulations are conducted to numerically investigate the mechanical behavior of graphene-based materials such as defect-containing graphene, GOs and GAs, and various ML techniques including KRR, Gaussian process metamodels, and deep RL are used in the predictive and generative modeling of these materials. Finally, the concept and the promise of ML interatomic potentials in achieving efficient and accurate simulations for MOF materials are presented. The research constituting the present thesis may shed light on some new possibilities of simulating and designing functional nanomaterials, which may further improve the performances of applications such as stretchable electronics, supercapacitor devices, carbon sequestration technologies, among others.

In the following a few future directions are proposed based on the present research. To begin with, the interpretability and explainability of ML model for materials research are still in question. Although ML has demonstrate great power in predicting material properties and designing new nanomaterials, it is no longer satisfactory for ML to be only a black box solution, which is unfortunately often the case for complex ML models such as deep neural networks (in comparison, a decision tree model is more explainable). Instead, it is hoped that ML can provide human experts with more insights that can lead to scientific discoveries. One future direction is to not only develop effective ML models to predict and design nanomaterials but also try to understand why the models can work so well.

Another direction is to further improve the databases for nanomaterials. Despite the rapid growth in recent years, databases for many useful information are still in their infancy or non-existent. One example is trained ML interatomic potentials, which are very valuable for materials simulations but are scattered throughout the Internet. To address this issue, one research direction can be using natural language processing (NLP)-based information extraction for properties of interest, through which we can explore large, unstructured text-based data to create and populate databases for nanomaterials.

Bibliography

[1] Shamima Ahmed et al. "Artificial intelligence and machine learning in finance: A bibliometric review". In: *Research in International Business and Finance* 61 (2022), p. 101646.

[2] Mohammad Amin Amani et al. "A machine learning-based model for the estimation of the temperature-dependent moduli of graphene oxide reinforced nanocomposites and its application in a thermally affected buckling analysis". In: *Engineering with Computers* 37 (2021), pp. 2245–2255.

[3] Bruce Ankenman, Barry L Nelson, and Jeremy Staum. "Stochastic kriging for simulation metamodeling". In: *2008 Winter Simulation Conference*. IEEE. 2008, pp. 362–370.

[4] R Ansari, S Ajori, and B Motevalli. "Mechanical properties of defective single-layered graphene sheets via molecular dynamics simulation". In: *Superlattices and Microstructures* 51.2 (2012), pp. 274–289.

[5] Paulo T Araujo, Mauricio Terrones, and Mildred S Dresselhaus. "Defects and impurities in graphene-like materials". In: *Materials Today* 15.3 (2012), pp. 98–109.

[6] Mehrdad Asgari et al. "An experimental and computational study of CO 2 adsorption in the sodalite-type M-BTT (M= Cr, Mn, Fe, Cu) metal–organic frameworks featuring open metal sites". In: *Chemical Science* 9.20 (2018), pp. 4579–4588.

[7] Jingwei Bai et al. "Graphene nanomesh". In: *Nature Nanotechnology* 5.3 (2010), pp. 190–194.

[8] Alexander A Balandin. "Thermal properties of graphene and nanostructured carbon materials". In: *Nature materials* 10.8 (2011), pp. 569–581.

[9] Alexander A Balandin et al. "Superior thermal conductivity of single-layer graphene". In: *Nano Letters* 8.3 (2008), pp. 902–907.

[10] Emmanuel Anuoluwa Bamidele et al. "Discovery and prediction capabilities in metal-based nanomaterials: An overview of the application of machine learning techniques and some recent advances". In: *Advanced Engineering Informatics* 52 (2022), p. 101593.

[11] Albert P Bartók et al. "Machine learning a general-purpose interatomic potential for silicon". In: *Physical Review X* 8.4 (2018), p. 041048.

[12] Claire Berger et al. "Ultrathin epitaxial graphite: 2D electron gas properties and a route toward graphene-based nanoelectronics". In: *The Journal of Physical Chemistry B* 108.52 (2004), pp. 19912–19916.

[13] Diana Berman et al. "Macroscale superlubricity enabled by graphene nanoscroll formation". In: *Science* 348.6239 (2015), pp. 1118–1122.

[14] Melina K Blees et al. "Graphene kirigami". In: *Nature* 524.7564 (2015), pp. 204–207.

[15] Olivier Bousquet, Ulrike von Luxburg, and Gunnar Rätsch. *Advanced Lectures on Machine Learning: ML Summer Schools 2003, Canberra, Australia, February 2-14, 2003, Tübingen, Germany, August 4-16, 2003, Revised Lectures*. Vol. 3176. Springer, 2011.

[16] J Scott Bunch et al. "Electromechanical resonators from graphene sheets". In: *Science* 315.5811 (2007), pp. 490–493.

[17] Jacob W Burress et al. "Graphene oxide framework materials: theoretical predictions and experimental results". In: *Angewandte Chemie International Edition* 49.47 (2010), pp. 8902–8904.

[18] Keith T Butler et al. "Machine learning for molecular and materials science". In: *Nature* 559.7715 (2018), pp. 547–555.

[19] Jiazhen Cai et al. "Machine learning-driven new material discovery". In: *Nanoscale Advances* 2.8 (2020), pp. 3115–3130.

[20] Leonardo C Campos et al. "Anisotropic etching and nanoribbon formation in single-layer graphene". In: *Nano Letters* 9.7 (2009), pp. 2600–2604.

[21] Cheuk Hei Chan, Mingzi Sun, and Bolong Huang. "Application of machine learning for advanced material prediction and design". In: *EcoMat* 4.4 (2022), e12194.

[22] Chun-Teh Chen and Grace X Gu. "Effect of constituent materials on composite performance: Exploring design strategies via machine learning". In: *Advanced Theory and Simulations* 2.6 (2019), p. 1900056.

[23] Chun-Teh Chen and Grace X Gu. "Generative deep neural networks for inverse materials design using backpropagation and active learning". In: *Advanced Science* 7.5 (2020), p. 1902607.

[24] Chun-Teh Chen and Grace X Gu. "Machine learning for composite materials". In: *MRS Communications* 9.2 (2019), pp. 556–566.

[25] Chun-Teh Chen et al. "Nacre-inspired design of graphene oxide–polydopamine nanocomposites for enhanced mechanical properties and multi-functionalities". In: *Nano Futures* 1.1 (2017), p. 011003.

[26] Da Chen, Hongbin Feng, and Jinghong Li. "Graphene oxide: preparation, functionalization, and electrochemical applications". In: *Chemical Reviews* 112.11 (2012), pp. 6027–6053.

[27] Linjiang Chen, Carole A Morrison, and Tina Düren. "Improving predictions of gas adsorption in metal–organic frameworks with coordinatively unsaturated metal sites: model potentials, ab initio parameterization, and GCMC simulations". In: *The Journal of Physical Chemistry C* 116.35 (2012), pp. 18899–18909.

[28] Zhe Chen et al. "Identifying physical and chemical contributions to friction: a comparative study of chemically inert and active graphene step edges". In: *ACS Applied Materials & Interfaces* 12.26 (2020), pp. 30007–30015.

[29] Zongping Chen et al. "Three-dimensional flexible and conductive interconnected graphene networks grown by chemical vapour deposition". In: *Nature Materials* 10.6 (2011), pp. 424–428.

[30] Yehong Cheng et al. "Enhanced mechanical, thermal, and electric properties of graphene aerogels via supercritical ethanol drying and high-temperature thermal reduction". In: *Scientific Reports* 7.1 (2017), p. 1439.

[31] Kimberly Chenoweth, Adri CT Van Duin, and William A Goddard. "ReaxFF reactive force field for molecular dynamics simulations of hydrocarbon oxidation". In: *The Journal of Physical Chemistry A* 112.5 (2008), pp. 1040–1053.

[32] Siwar Chibani and François-Xavier Coudert. "Machine learning approaches for the prediction of materials properties". In: *APL Materials* 8.8 (2020).

[33] Shih-Kai Chien, Yue-Tzu Yang, et al. "Influence of chemisorption on the thermal conductivity of graphene nanoribbons". In: *Carbon* 50.2 (2012), pp. 421–428.

[34] Liu Chu, Jiajia Shi, and Eduardo Souza de Cursi. "Vibration analysis of vacancy defected graphene sheets by Monte Carlo based finite element method". In: *Nanomaterials* 8.7 (2018), p. 489.

[35] Yanbiao Chu, Tarek Ragab, and Cemal Basaran. "The size effect in mechanical properties of finite-sized graphene nanoribbon". In: *Computational Materials Science* 81 (2014), pp. 269–274.

[36] Chul Chung et al. "Biomedical applications of graphene and graphene oxide". In: *Accounts of Chemical research* 46.10 (2013), pp. 2211–2224.

[37] David Cohen-Tanugi and Jeffrey C Grossman. "Mechanical strength of nanoporous graphene as a desalination membrane". In: *Nano Letters* 14.11 (2014), pp. 6171–6178.

[38] Stacy M Copp et al. "Fluorescence color by data-driven design of genomic silver clusters". In: *ACS Nano* 12.8 (2018), pp. 8240–8247.

[39] Kevin Crampon et al. "Machine-learning methods for ligand–protein molecular docking". In: *Drug Discovery Today* 27.1 (2022), pp. 151–164.

[40] Yaping Dan et al. "Intrinsic response of graphene vapor sensors". In: *Nano Letters* 9.4 (2009), pp. 1472–1475.

[41] Sujit S Datta et al. "Crystallographic etching of few-layer graphene". In: *Nano Letters* 8.7 (2008), pp. 1912–1915.

[42] Maryam Zarghami Dehaghani et al. "Fracture toughness and crack propagation behavior of nanoscale beryllium oxide graphene-like structures: a molecular dynamics simulation analysis". In: *Engineering Fracture Mechanics* 235 (2020), p. 107194.

[43] Volker L Deringer and Gábor Csányi. "Machine learning based interatomic potential for amorphous carbon". In: *Physical Review B* 95.9 (2017), p. 094203.

[44] Volker L Deringer et al. "Gaussian process regression for materials and molecules". In: *Chemical Reviews* 121.16 (2021), pp. 10073–10141.

[45] David Dubbeldam et al. "Design, parameterization, and implementation of atomic force fields for adsorption in nanoporous materials". In: *Advanced Theory and Simulations* 2.11 (2019), p. 1900135.

[46] Allison L Dzubak et al. "Ab initio carbon capture in open-site metal–organic frameworks". In: *Nature Chemistry* 4.10 (2012), pp. 810–816.

[47] Goki Eda et al. "Insulator to semimetal transition in graphene oxide". In: *The Journal of Physical Chemistry C* 113.35 (2009), pp. 15768–15771.

[48] Kasra Einalipour Eshkalak, Sadegh Sadeghzadeh, and Maisam Jalaly. "Mechanical properties of defective hybrid graphene-boron nitride nanosheets: A molecular dynamics study". In: *Computational Materials Science* 149 (2018), pp. 170–181.

[49] BB Fan, XB Yang, and R Zhang. "Anisotropic mechanical properties and Stone–Wales defects in graphene monolayer: A theoretical study". In: *Physics Letters A* 374.27 (2010), pp. 2781–2784.

[50] Qile Fang, Yi Shen, and Baoliang Chen. "Synthesis, decoration and properties of three-dimensional graphene-based macrostructures: a review". In: *Chemical Engineering Journal* 264 (2015), pp. 753–771.

[51] Amir H Farmahini et al. "Performance-based screening of porous materials for carbon capture". In: *Chemical Reviews* 121.17 (2021), pp. 10666–10741.

[52] Michael Fernandez, Ante Bilić, and Amanda S Barnard. "Machine learning and genetic algorithm prediction of energy differences between electronic calculations of graphene nanoflakes". In: *Nanotechnology* 28.38 (2017), 38LT03.

[53] Evgenii O Fetisov et al. "First principles Monte Carlo simulations of unary and binary adsorption: CO 2, N 2, and H 2 O in Mg-MOF-74". In: *Chemical Communications* 54.77 (2018), pp. 10816–10819.

[54] Alexander C Forse et al. "Unexpected diffusion anisotropy of carbon dioxide in the metal–organic framework Zn2 (dobpdc)". In: *Journal of the American Chemical Society* 140.5 (2018), pp. 1663–1673.

[55] Susumu Fujii et al. "Quantitative prediction of grain boundary thermal conductivities from local atomic environments". In: *Nature Communications* 11.1 (2020), p. 1854.

[56] Eric Ganz et al. "The initial stages of melting of graphene between 4000 K and 6000 K". In: *Physical Chemistry Chemical Physics* 19.5 (2017), pp. 3756–3762.

[57] Wei Gao and Rui Huang. "Thermomechanics of monolayer graphene: Rippling, thermal expansion and elasticity". In: *Journal of the Mechanics and Physics of Solids* 66 (2014), pp. 42–58.

[58] Daniel Garcia-Sanchez et al. "Imaging mechanical vibrations in suspended graphene sheets". In: *Nano Letters* 8.5 (2008), pp. 1399–1403.

[59] Vasilios Georgakilas et al. "Noncovalent functionalization of graphene and graphene oxide for energy materials, biosensing, catalytic, and biomedical applications". In: *Chemical Reviews* 116.9 (2016), pp. 5464–5519.

[60] Cristina Gómez-Navarro et al. "Atomic structure of reduced graphene oxide". In: *Nano Letters* 10.4 (2010), pp. 1144–1148.

[61] George Gorgolis and Costas Galiotis. "Graphene aerogels: a review". In: *2D Materials* 4.3 (2017), p. 032001.

[62] Rassin Grantab, Vivek B Shenoy, and Rodney S Ruoff. "Anomalous strength characteristics of tilt grain boundaries in graphene". In: *Science* 330.6006 (2010), pp. 946–948.

[63] Alexander A Green and Mark C Hersam. "Solution phase production of graphene with controlled thickness via density differentiation". In: *Nano Letters* 9.12 (2009), pp. 4031–4036.

[64] Stefan Grimme et al. "A consistent and accurate ab initio parametrization of density functional dispersion correction (DFT-D) for the 94 elements H-Pu". In: *The Journal of Chemical Physics* 132.15 (2010).

[65] Bhavana Gupta et al. "Role of oxygen functional groups in reduced graphene oxide for lubrication". In: *Scientific Reports* 7.1 (2017), p. 45030.

[66] Jacklyn N Hall and Praveen Bollini. "Quantification of Open-Metal Sites in Metal–Organic Frameworks Using Irreversible Water Adsorption". In: *Langmuir* 36.5 (2020), pp. 1345–1356.

[67] Lin Han et al. "Direct quantification of the mechanical anisotropy and fracture of an individual exoskeleton layer via uniaxial compression of micropillars". In: *Nano Letters* 11.9 (2011), pp. 3868–3874.

[68] Feng Hao, Daining Fang, and Zhiping Xu. "Mechanical and thermal transport properties of graphene with defects". In: *Applied Physics Letters* 99.4 (2011).

[69] Christian Hartwigsen, Sephen Gœdecker, and Jürg Hutter. "Relativistic separable dual-space Gaussian pseudopotentials from H to Rn". In: *Physical Review B* 58.7 (1998), p. 3641.

[70] William G Hoover. "Canonical dynamics: Equilibrium phase-space distributions". In: *Physical Review A* 31.3 (1985), p. 1695.

[71] H Horii and S Nemat-Nasser. "Elastic fields of interacting inhomogeneities". In: *International Journal of Solids and Structures* 21.7 (1985), pp. 731–745.

[72] Han Hu et al. "Compressible carbon nanotube–graphene hybrid aerogels with superhydrophobicity and superoleophilicity for oil sorption". In: *Environmental Science & Technology Letters* 1.3 (2014), pp. 214–220.

[73] Shang-Hsiu Hu et al. "Quantum-dot-tagged reduced graphene oxide nanocomposites for bright fluorescence bioimaging and photothermal therapy monitored in situ". In: *Advanced Materials* 24.13 (2012), pp. 1748–1754.

[74] Pinshane Y Huang et al. "Grains and grain boundaries in single-layer graphene atomic patchwork quilts". In: *Nature* 469.7330 (2011), pp. 389–392.

[75] Jürg Hutter et al. "cp2k: atomistic simulations of condensed matter systems". In: *Wiley Interdisciplinary Reviews: Computational Molecular Science* 4.1 (2014), pp. 15–25.

[76] Houk Jang et al. "Graphene-based flexible and stretchable electronics". In: *Advanced Materials* 28.22 (2016), pp. 4184–4202.

[77] Christian Janiesch, Patrick Zschech, and Kai Heinrich. "Machine learning and deep learning". In: *Electronic Markets* 31.3 (2021), pp. 685–695.

[78] Hu Young Jeong et al. "Graphene oxide thin films for flexible nonvolatile memory applications". In: *Nano Letters* 10.11 (2010), pp. 4381–4386.

[79] Yuying Jia et al. "Machine learning boosts the design and discovery of nanomaterials". In: *ACS Sustainable Chemistry & Engineering* 9.18 (2021), pp. 6130–6147.

[80] Wei Jian, David Hui, and Denvid Lau. "Nanoengineering in biomedicine: current development and future perspectives". In: *Nanotechnology Reviews* 9.1 (2020), pp. 700–715.

[81] Lili Jiang and Zhuangjun Fan. "Design of advanced porous graphene materials: from graphene nanomesh to 3D architectures". In: *Nanoscale* 6.4 (2014), pp. 1922–1945.

[82] Yiru Jiang et al. "Machine learning advances in microbiology: A review of methods and applications". In: *Frontiers in Microbiology* 13 (2022), p. 925454.

[83] Priya Johari and Vivek B Shenoy. "Modulating optical properties of graphene oxide: role of prominent functional groups". In: *ACS Nano* 5.9 (2011), pp. 7640–7647.

[84] Keun Soo Kim et al. "Large-scale pattern growth of graphene films for stretchable transparent electrodes". In: *Nature* 457.7230 (2009), pp. 706–710.

[85] Jiřı Klimeš and Angelos Michaelides. "Perspective: Advances and challenges in treating van der Waals dispersion forces in density functional theory". In: *The Journal of Chemical Physics* 137.12 (2012).

[86] Steven P Koenig et al. "Ultrastrong adhesion of graphene membranes". In: *Nature Nanotechnology* 6.9 (2011), pp. 543–546.

[87] Ülkü Kökçam-Demir et al. "Coordinatively unsaturated metal sites (open metal sites) in metal–organic frameworks: design and applications". In: *Chemical Society Reviews* 49.9 (2020), pp. 2751–2798.

[88] Mohamad Koohi-Moghadam et al. "Predicting disease-associated mutation of metal-binding sites in proteins using a deep learning approach". In: *Nature Machine Intelligence* 1.12 (2019), pp. 561–567.

[89] Ambarish R Kulkarni and David S Sholl. "Screening of copper open metal site MOFs for olefin/paraffin separations using DFT-derived force fields". In: *The Journal of Physical Chemistry C* 120.40 (2016), pp. 23044–23054.

[90] Changgu Lee et al. "Measurement of the elastic properties and intrinsic strength of monolayer graphene". In: *Science* 321.5887 (2008), pp. 385–388.

[91] Ossi Lehtinen et al. "Non-invasive transmission electron microscopy of vacancy defects in graphene produced by ion irradiation". In: *Nanoscale* 6.12 (2014), pp. 6569–6576.

[92] Charles Lewis et al. "Use of machine learning with temporal photoluminescence signals from cdte quantum dots for temperature measurement in microfluidic devices". In: *ACS Applied Nano Materials* 3.5 (2020), pp. 4045–4053.

[93] Sichao Li and Amanda S Barnard. "Inverse Design of Nanoparticles Using Multi-Target Machine Learning". In: *Advanced Theory and Simulations* 5.2 (2022), p. 2100414.

[94] Xing Li et al. "Self-supporting activated carbon/carbon nanotube/reduced graphene oxide flexible electrode for high performance supercapacitor". In: *Carbon* 129 (2018), pp. 236–244.

[95] Zheng Li et al. "Superstructured assembly of nanocarbons: fullerenes, nanotubes, and graphene". In: *Chemical Reviews* 115.15 (2015), pp. 7046–7117.

[96] Zhou Li et al. "Synthesis and characterization of UiO-66-NH2 incorporated graphene aerogel composites and their utilization for absorption of organic liquids". In: *Carbon* 201 (2023), pp. 561–567.

[97] Nidia Gabaldon Limas and Thomas A Manz. "Introducing DDEC6 atomic population analysis: part 4. Efficient parallel computation of net atomic charges, atomic spin moments, bond orders, and more". In: *RSC Advances* 8.5 (2018), pp. 2678–2707.

[98] Bo Liu and Kun Zhou. "Recent progress on graphene-analogous 2D nanomaterials: Properties, modeling and applications". In: *Progress in Materials Science* 100 (2019), pp. 99–169.

[99] Ruili Liu et al. "An interface-induced Co-assembly approach towards ordered mesoporous carbon/graphene aerogel for high-performance supercapacitors". In: *Advanced Functional Materials* 25.4 (2015), pp. 526–533.

[100] Xin Liu et al. "3D graphene aerogel-supported SnO 2 nanoparticles for efficient detection of NO 2". In: *Rsc Advances* 4.43 (2014), pp. 22601–22605.

[101] Kian Ping Loh et al. "Graphene oxide as a chemically tunable platform for optical applications". In: *Nature Chemistry* 2.12 (2010), pp. 1015–1024.

[102] Hu Long et al. "High surface area MoS2/graphene hybrid aerogel for ultrasensitive NO2 detection". In: *Advanced Functional Materials* 26.28 (2016), pp. 5158–5165.

[103] Shuaihua Lu et al. "Accelerated discovery of stable lead-free hybrid organic-inorganic perovskites via machine learning". In: *Nature Communications* 9.1 (2018), p. 3405.

[104] Shuaihua Lu et al. "Rapid discovery of ferroelectric photovoltaic perovskites and material descriptors via machine learning". In: *Small Methods* 3.11 (2019), p. 1900360.

[105] Wei Ma, Feng Cheng, and Yongmin Liu. "Deep-learning-enabled on-demand design of chiral metamaterials". In: *ACS Nano* 12.6 (2018), pp. 6326–6334.

[106] Sauradeep Majumdar et al. "Diversifying databases of metal organic frameworks for high-throughput computational screening". In: *ACS Applied Materials & Interfaces* 13.51 (2021), pp. 61004–61014.

[107] Artem Maksov et al. "Deep learning analysis of defect and phase evolution during electron beam-induced transformations in WS2". In: *npj Computational Materials* 5.1 (2019), p. 12.

[108] Michael E Mann, Raymond S Bradley, and Malcolm K Hughes. "Global-scale temperature patterns and climate forcing over the past six centuries". In: *Nature* 392.6678 (1998), pp. 779–787.

[109] Cristina Martin-Olmos et al. "Graphene MEMS: AFM probe performance improvement". In: *ACS Nano* 7.5 (2013), pp. 4164–4170.

[110] A Hamed Mashhadzadeh et al. "Theoretical studies on the mechanical and electronic properties of 2D and 3D structures of beryllium-oxide graphene and graphene nanobud". In: *Applied Surface Science* 476 (2019), pp. 36–48.

[111] Satoru Masubuchi et al. "Fabrication of graphene nanoribbon by local anodic oxidation lithography using atomic force microscope". In: *Applied Physics Letters* 94.8 (2009).

[112] Cecilia Mattevi, Hokwon Kim, and Manish Chhowalla. "A review of chemical vapour deposition of graphene on copper". In: *Journal of Materials Chemistry* 21.10 (2011), pp. 3324–3334.

[113] Rocio Mercado et al. "Force field development from periodic density functional theory calculations for gas separation applications using metal–organic frameworks". In: *The Journal of Physical Chemistry C* 120.23 (2016), pp. 12590–12604.

[114] M Mirakhory, MM Khatibi, and S Sadeghzadeh. "Vibration analysis of defected and pristine triangular single-layer graphene nanosheets". In: *Current Applied Physics* 18.11 (2018), pp. 1327–1337.

[115] Yousef Mohammadi et al. "Intelligent machine learning: tailor-making macromolecules". In: *Polymers* 11.4 (2019), p. 579.

[116] Seyed Mohamad Moosavi et al. "Understanding the diversity of the metal-organic framework ecosystem". In: *Nature Communications* 11.1 (2020), pp. 1–10.

[117] Benyamin Motevalli, Baichuan Sun, and Amanda S Barnard. "Understanding and predicting the cause of defects in graphene oxide nanostructures using machine learning". In: *The Journal of Physical Chemistry C* 124.13 (2020), pp. 7404–7413.

[118] Benyamin Motevalli et al. "The representative structure of graphene oxide nanoflakes from machine learning". In: *Nano Futures* 3.4 (2019), p. 045001.

[119] Brianna Mueller et al. "Artificial intelligence and machine learning in emergency medicine: a narrative review". In: *Acute Medicine & Surgery* 9.1 (2022), e740.

[120] SF Asbaghian Namin and R Pilafkan. "Vibration analysis of defective graphene sheets using nonlocal elasticity theory". In: *Physica E: Low-Dimensional Systems and Nanostructures* 93 (2017), pp. 257–264.

[121] Zhonghua Ni et al. "Anisotropic mechanical properties of graphene sheets from molecular dynamics". In: *Physica B: Condensed Matter* 405.5 (2010), pp. 1301–1306.

[122] Marcus M Noack et al. "Autonomous materials discovery driven by Gaussian process regression with inhomogeneous measurement noise and anisotropic kernels". In: *Scientific Reports* 10.1 (2020), p. 17663.

[123] Kostya S Novoselov et al. "Electric field effect in atomically thin carbon films". In: *Science* 306.5696 (2004), pp. 666–669.

[124] Aline de Oliveira, Guilherme Ferreira de Lima, and Heitor Avelino De Abreu. "Structural and electronic properties of M-MOF-74 (M= Mg, Co or Mn)". In: *Chemical Physics Letters* 691 (2018), pp. 283–290.

[125] Daniele Ongari, Leopold Talirz, and Berend Smit. "Too many materials and too many applications: An experimental problem waiting for a computational solution". In: *ACS Central Science* 6.11 (2020), pp. 1890–1900.

[126] Dimitrios G Papageorgiou, Ian A Kinloch, and Robert J Young. "Mechanical properties of graphene and graphene-based nanocomposites". In: *Progress in Materials Science* 90 (2017), pp. 75–127.

[127] Joonho Park et al. "Tuning metal–organic frameworks with open-metal sites and its origin for enhancing CO2 affinity by metal substitution". In: *The Journal of Physical Chemistry Letters* 3.7 (2012), pp. 826–829.

[128] Sandeep P Patil, Ambarish Kulkarni, and Bernd Markert. "Shockwave response of graphene aerogels: An all-atom simulation study". In: *Computational Materials Science* 189 (2021), p. 110252.

[129] Sandeep P Patil, Parag Shendye, and Bernd Markert. "Molecular investigation of mechanical properties and fracture behavior of graphene aerogel". In: *The Journal of Physical Chemistry B* 124.28 (2020), pp. 6132–6139.

[130] Fabian Pedregosa et al. "Scikit-learn: Machine learning in Python". In: *the Journal of Machine Learning Research* 12 (2011), pp. 2825–2830.

[131] Qing-Xiang Pei, Yong-Wei Zhang, and Vivek B Shenoy. "Mechanical properties of methyl functionalized graphene: a molecular dynamics study". In: *Nanotechnology* 21.11 (2010), p. 115709.

[132] John P Perdew, Kieron Burke, and Matthias Ernzerhof. "Generalized gradient approximation made simple". In: *Physical Review Letters* 77.18 (1996), p. 3865.

[133] Luiz Felipe C Pereira et al. "Anisotropic thermal conductivity and mechanical properties of phagraphene: a molecular dynamics study". In: *RSC Advances* 6.63 (2016), pp. 57773–57779.

[134] Jinglei Ping and Michael S Fuhrer. "Layer number and stacking sequence imaging of few-layer graphene by transmission electron microscopy". In: *Nano Letters* 12.9 (2012), pp. 4635–4641.

[135] Roberta Poloni et al. "Understanding trends in CO2 adsorption in metal–organic frameworks with open-metal sites". In: *The Journal of Physical Chemistry Letters* 5.5 (2014), pp. 861–865.

[136] Jeffrey J Potoff and J Ilja Siepmann. "Vapor–liquid equilibria of mixtures containing alkanes, carbon dioxide, and nitrogen". In: *AIChE Journal* 47.7 (2001), pp. 1676–1682.

[137] Zenan Qi, David K Campbell, and Harold S Park. "Atomistic simulations of tension-induced large deformation and stretchability in graphene kirigami". In: *Physical Review B* 90.24 (2014), p. 245437.

[138] Zenan Qi et al. "A molecular simulation analysis of producing monatomic carbon chains by stretching ultranarrow graphene nanoribbons". In: *Nanotechnology* 21.26 (2010), p. 265702.

[139] Zhao Qin et al. "The mechanics and design of a lightweight three-dimensional graphene assembly". In: *Science Advances* 3.1 (2017), e1601536.

[140] Ling Qiu, Dan Li, and Hui-Ming Cheng. "Structural control of graphene-based materials for unprecedented performance". In: *ACS Nano* 12.6 (2018), pp. 5085–5092.

[141] Wendy L Queen et al. "Site-specific CO2 adsorption and zero thermal expansion in an anisotropic pore network". In: *The Journal of Physical Chemistry C* 115.50 (2011), pp. 24915–24919.

[142] Paul Raccuglia et al. "Machine-learning-assisted materials discovery using failed experiments". In: *Nature* 533.7601 (2016), pp. 73–76.

[143] Anthony K Rappé et al. "UFF, a full periodic table force field for molecular mechanics and molecular dynamics simulations". In: *Journal of the American Chemical Society* 114.25 (1992), pp. 10024–10035.

[144] Antoine Reserbat-Plantey et al. "Electromechanical control of nitrogen-vacancy defect emission using graphene NEMS". In: *Nature Communications* 7.1 (2016), p. 10218.

[145] Alex W Robertson et al. "Structural reconstruction of the graphene monovacancy". In: *ACS Nano* 7.5 (2013), pp. 4495–4502.

[146] Patrick Rowe et al. "Development of a machine learning potential for graphene". In: *Physical Review B* 97.5 (2018), p. 054303.

[147] Farida Sabry et al. "Machine learning for healthcare wearable devices: the big picture". In: *Journal of Healthcare Engineering* 2022 (2022).

[148] Benjamin Sanchez-Lengeling and Alán Aspuru-Guzik. "Inverse molecular design using machine learning: Generative models for matter engineering". In: *Science* 361.6400 (2018), pp. 360–365.

[149] AI Savvatimskiy. "Measurements of the melting point of graphite and the properties of liquid carbon (a review for 1963–2003)". In: *Carbon* 43.6 (2005), pp. 1115–1142.

[150] Terry C Shyu et al. "A kirigami approach to engineering elasticity in nanocomposites through patterned defects". In: *Nature Materials* 14.8 (2015), pp. 785–789.

[151] Rebecca L Siegelman, Eugene J Kim, and Jeffrey R Long. "Porous materials for carbon dioxide separations". In: *Nature Materials* 20.8 (2021), pp. 1060–1072.

[152] David Silver et al. "Mastering the game of Go with deep neural networks and tree search". In: *Nature* 529.7587 (2016), pp. 484–489.

[153] Alex Smolyanitsky and Binquan Luan. "Nanopores in atomically thin 2D nanosheets limit aqueous single-stranded DNA transport". In: *Physical Review Letters* 127.13 (2021), p. 138103.

[154] Rafael A Soler-Crespo et al. "Engineering the mechanical properties of monolayer graphene oxide at the atomic level". In: *The Journal of Physical Chemistry Letters* 7.14 (2016), pp. 2702–2707.

[155] David Soriano et al. "Spin transport in hydrogenated graphene". In: *2D Materials* 2.2 (2015), p. 022002.

[156] James JP Stewart. "Optimization of parameters for semiempirical methods V: Modification of NDDO approximations and application to 70 elements". In: *Journal of Molecular modeling* 13 (2007), pp. 1173–1213.

[157] Steven J Stuart, Alan B Tutein, and Judith A Harrison. "A reactive potential for hydrocarbons with intermolecular interactions". In: *The Journal of Chemical Physics* 112.14 (2000), pp. 6472–6486.

[158] Zhu-Yin Sui et al. "High surface area porous carbons produced by steam activation of graphene aerogels". In: *Journal of Materials Chemistry A* 2.25 (2014), pp. 9891–9898.

[159] Kenji Sumida et al. "Carbon dioxide capture in metal–organic frameworks". In: *Chemical Reviews* 112.2 (2012), pp. 724–781.

[160] Haiyan Sun, Zhen Xu, and Chao Gao. "Multifunctional, ultra-flyweight, synergistically assembled carbon aerogels". In: *Advanced Materials* 25.18 (2013), pp. 2554–2560.

[161] Vahid Tahouneh, Mohammad Hasan Naei, and Mahmoud Mosavi Mashhadi. "Influence of vacancy defects on vibration analysis of graphene sheets applying isogeometric method: molecular and continuum approaches". In: *Steel and Composite Structures, An International Journal* 34.2 (2020), pp. 261–277.

[162] Vahid Tahouneh, Mohammad Hasan Naei, and Mahmoud Mosavi Mashhadi. "The effects of temperature and vacancy defect on the severity of the SLGS becoming anisotropic". In: *Steel and Composite Structures* 29.5 (2018), p. 647.

[163] Vahid Tahouneh, Mohammad Hasan Naei, and Mahmoud Mosavi Mashhadi. "Using IGA and trimming approaches for vibrational analysis of L-shape graphene sheets via nonlocal elasticity theory". In: *Steel and Composite Structures, An International Journal* 33.5 (2019), pp. 717–727.

[164] Levente Tapasztó et al. "Tailoring the atomic structure of graphene nanoribbons by scanning tunnelling microscope lithography". In: *Nature Nanotechnology* 3.7 (2008), pp. 397–401.

[165] Mahdi Tavakol et al. "Mechanical properties of graphene oxide: The impact of functional groups". In: *Applied Surface Science* 525 (2020), p. 146554.

[166] Aidan P Thompson et al. "LAMMPS-a flexible simulation tool for particle-based materials modeling at the atomic, meso, and continuum scales". In: *Computer Physics Communications* 271 (2022), p. 108171.

[167] Christopher A Trickett et al. "The chemistry of metal–organic frameworks for CO2 capture, regeneration and conversion". In: *Nature Reviews Materials* 2.8 (2017), pp. 1–16.

[168] Alex Vallone, Nooshin M Estakhri, and Nasim Mohammadi Estakhri. "Region-specified inverse design of absorption and scattering in nanoparticles by using machine learning". In: *Journal of Physics: Photonics* 5.2 (2023), p. 024002.

[169] Joost VandeVondele and Jürg Hutter. "Gaussian basis sets for accurate calculations on molecular systems in gas and condensed phases". In: *The Journal of Chemical Physics* 127.11 (2007).

[170] Aniruddh Vashisth et al. "ReaxFF simulations of laser-induced graphene (LIG) formation for multifunctional polymer nanocomposites". In: *ACS Applied Nano Materials* 3.2 (2020), pp. 1881–1890.

[171] Akarsh Verma and Avinash Parashar. "Molecular dynamics based simulations to study failure morphology of hydroxyl and epoxide functionalised graphene". In: *Computational Materials Science* 143 (2018), pp. 15–26.

[172] Changguo Wang et al. "Graphene wrinkling: formation, evolution and collapse". In: *Nanoscale* 5.10 (2013), pp. 4454–4461.

[173] Han Wang et al. "DeePMD-kit: A deep learning package for many-body potential energy representation and molecular dynamics". In: *Computer Physics Communications* 228 (2018), pp. 178–184.

[174] Jianlin Wang, Steven L Crouch, and Sofia G Mogilevskaya. "A complex boundary integral method for multiple circular holes in an infinite plane". In: *Engineering Analysis with Boundary Elements* 27.8 (2003), pp. 789–802.

[175] MC Wang et al. "Effect of defects on fracture strength of graphene sheets". In: *Computational Materials Science* 54 (2012), pp. 236–239.

[176] Yan Wang et al. "Supercapacitor devices based on graphene materials". In: *The Journal of Physical Chemistry C* 113.30 (2009), pp. 13103–13107.

[177] Thierry Warin and Aleksandar Stojkov. "Machine learning in finance: a metadata-based systematic review of the literature". In: *Journal of Risk and Financial Management* 14.7 (2021), p. 302.

[178] TO Wehling et al. "Molecular doping of graphene". In: *Nano Letters* 8.1 (2008), pp. 173–177.

[179] TO Wehling et al. "Resonant scattering by realistic impurities in graphene". In: *Physical Review Letters* 105.5 (2010), p. 056802.

[180] Ning Wei et al. "Thermal conductivity of graphene kirigami: Ultralow and strain robustness". In: *Carbon* 104 (2016), pp. 203–213.

[181] Xiaoding Wei et al. "Plasticity and ductility in graphene oxide through a mechanochemically induced damage tolerance mechanism". In: *Nature Communications* 6.1 (2015), p. 8029.

[182] Yujie Wei and Ronggui Yang. "Nanomechanics of graphene". In: *National Science Review* 6.2 (2019), pp. 324–348.

[183] Yujie Wei et al. "The nature of strength enhancement and weakening by pentagon–heptagon defects in graphene". In: *Nature Materials* 11.9 (2012), pp. 759–763.

[184] Zhongqing Wei et al. "Nanoscale tunable reduction of graphene oxide for graphene electronics". In: *Science* 328.5984 (2010), pp. 1373–1376.

[185] Freddie Withers, Marc Dubois, and Alexander K Savchenko. "Electron properties of fluorinated single-layer graphene transistors". In: *Physical Review B* 82.7 (2010), p. 073403.

[186] Marcus A Worsley et al. "Synthesis of graphene aerogel with high electrical conductivity". In: *Journal of the American Chemical Society* 132.40 (2010), pp. 14067–14069.

[187] Ashley M Wright et al. "A structural mimic of carbonic anhydrase in a metal-organic framework". In: *Chem* 4.12 (2018), pp. 2894–2901.

[188] Ying Wu, Haipeng Duan, and Hongxia Xi. "Machine learning-driven insights into defects of zirconium metal–organic frameworks for enhanced ethane–ethylene separation". In: *Chemistry of Materials* 32.7 (2020), pp. 2986–2997.

[189] Xiao Xie et al. "Large-range control of the microstructures and properties of three-dimensional porous graphene". In: *Scientific Reports* 3.1 (2013), p. 2117.

[190] Zhen Xu and Chao Gao. "Graphene fiber: a new trend in carbon fibers". In: *Materials Today* 18.9 (2015), pp. 480–492.

[191] Zhen Xu et al. "Ultrastrong fibers assembled from giant graphene oxide sheets". In: *Advanced Materials* 25.2 (2013), pp. 188–193.

[192] Charles Yang et al. "Prediction of composite microstructure stress-strain curves using convolutional neural networks". In: *Materials & Design* 189 (2020), p. 108509.

[193] Jing Yang et al. "Cellulose/graphene aerogel supported phase change composites with high thermal conductivity and good shape stability for thermal energy storage". In: *Carbon* 98 (2016), pp. 50–57.

[194] Xiaoming Yang et al. "Well-dispersed chitosan/graphene oxide nanocomposites". In: *ACS Applied Materials & Interfaces* 2.6 (2010), pp. 1707–1713.

[195] Yu Yang et al. "Flexible supercapacitors based on polyaniline arrays coated graphene aerogel electrodes". In: *Nanoscale Research Letters* 12 (2017), pp. 1–9.

[196] Oleg V Yazyev and Steven G Louie. "Topological defects in graphene: Dislocations and grain boundaries". In: *Physical Review B* 81.19 (2010), p. 195420.

[197] Min Yi and Zhigang Shen. "A review on mechanical exfoliation for the scalable production of graphene". In: *Journal of Materials Chemistry A* 3.22 (2015), pp. 11700–11715.

[198] Kichul Yoon, Alireza Ostadhossein, and Adri CT Van Duin. "Atomistic-scale simulations of the chemomechanical behavior of graphene under nanoprojectile impact". In: *Carbon* 99 (2016), pp. 58–64.

[199] Jiamei Yu and Perla B Balbuena. "Water effects on postcombustion CO2 capture in Mg-MOF-74". In: *The Journal of Physical Chemistry C* 117.7 (2013), pp. 3383–3388.

[200] Zenan Yu et al. "Functionalized graphene aerogel composites for high-performance asymmetric supercapacitors". In: *Nano Energy* 11 (2015), pp. 611–620.

[201] Ardavan Zandiatashbar et al. "Effect of defects on the intrinsic strength and stiffness of graphene". In: *Nature Communications* 5.1 (2014), p. 3186.

[202] Minxiang Zeng et al. "Accelerated design of catalytic water-cleaning nanomotors via machine learning". In: *ACS Applied Materials & Interfaces* 11.43 (2019), pp. 40099–40106.

[203] Erhui Zhang et al. "Polypyrrole nanospheres@ graphene aerogel with high specific surface area, compressibility, and proper water wettability prepared in dimethylformamide-dependent environment". In: *Polymer* 185 (2019), p. 121974.

[204] Hengji Zhang, Geunsik Lee, and Kyeongjae Cho. "Thermal transport in graphene and effects of vacancy defects". In: *Physical Review B* 84.11 (2011), p. 115460.

[205] Ji Zhang, Tarek Ragab, and Cemal Basaran. "Influence of vacancy defects on the damage mechanics of graphene nanoribbons". In: *International Journal of Damage Mechanics* 26.1 (2017), pp. 29–49.

[206] Linfeng Zhang et al. "End-to-end symmetry preserving inter-atomic potential energy model for finite and extended systems". In: *Advances in Neural Information Processing Systems* 31 (2018).

[207] Peng Zhang et al. "Fracture toughness of graphene". In: *Nature Communications* 5.1 (2014), p. 3782.

[208] Qiangqiang Zhang et al. "Mechanically robust honeycomb graphene aerogel multifunctional polymer composites". In: *Carbon* 93 (2015), pp. 659–670.

[209] Teng Zhang, Xiaoyan Li, and Huajian Gao. "Fracture of graphene: a review". In: *International Journal of Fracture* 196 (2015), pp. 1–31.

[210] Teng Zhang et al. "Flaw insensitive fracture in nanocrystalline graphene". In: *Nano Letters* 12.9 (2012), pp. 4605–4610.

[211] Xiangyu Zhang, Kexin Zhang, and Yongjin Lee. "Machine learning enabled tailor-made design of application-specific metal–organic frameworks". In: *ACS Applied Materials & Interfaces* 12.1 (2019), pp. 734–743.

[212] Xuetong Zhang et al. "Mechanically strong and highly conductive graphene aerogel and its use as electrodes for electrochemical power sources". In: *Journal of Materials Chemistry* 21.18 (2011), pp. 6494–6497.

[213] Zhizhou Zhang and Grace X Gu. "Finite-Element-Based Deep-Learning Model for Deformation Behavior of Digital Materials". In: *Advanced Theory and Simulations* 3.7 (2020), p. 2000031.

[214] Huijuan Zhao and Narayana R Aluru. "Temperature and strain-rate dependent fracture strength of graphene". In: *Journal of Applied Physics* 108.6 (2010).

[215] Huijuan Zhao, K Min, and Narayana R Aluru. "Size and chirality dependent elastic properties of graphene nanoribbons under uniaxial tension". In: *Nano Letters* 9.8 (2009), pp. 3012–3015.

[216] Bowen Zheng and Grace X Gu. "Machine learning-based detection of graphene defects with atomic precision". In: *Nano-Micro Letters* 12 (2020), pp. 1–13.

[217] Bowen Zheng and Grace X Gu. "Prediction of graphene oxide functionalization using gradient boosting: implications for material chemical composition identification". In: *ACS Applied Nano Materials* 4.3 (2021), pp. 3167–3174.

[218] Bowen Zheng and Grace X Gu. "Recovery from mechanical degradation of graphene by defect enlargement". In: *Nanotechnology* 31.8 (2019), p. 085707.

[219] Bowen Zheng and Grace X Gu. "Stress field characteristics and collective mechanical properties of defective graphene". In: *The Journal of Physical Chemistry C* 124.13 (2020), pp. 7421–7431.

[220] Bowen Zheng and Grace X Gu. "Tuning the graphene mechanical anisotropy via defect engineering". In: *Carbon* 155 (2019), pp. 697–705.

[221] Bowen Zheng, Zeyu Zheng, and Grace X Gu. "Designing mechanically tough graphene oxide materials using deep reinforcement learning". In: *npj Computational Materials* 8.1 (2022), p. 225.

[222] Bowen Zheng, Zeyu Zheng, and Grace X Gu. "Scalable graphene defect prediction using transferable learning". In: *Nanomaterials* 11.9 (2021), p. 2341.

[223] Bowen Zheng, Zeyu Zheng, and Grace X Gu. "Uncertainty quantification and prediction for mechanical properties of graphene aerogels via Gaussian process metamodels". In: *Nano Futures* 5.4 (2021), p. 045004.

[224] Bowen Zheng et al. "Investigation of mechanical properties and structural integrity of graphene aerogels via molecular dynamics simulations". In: *Physical Chemistry Chemical Physics* 25.33 (2023), pp. 21897–21907.

[225] Bowen Zheng et al. "Machine learning and experiments: A synergy for the development of functional materials". In: *MRS Bulletin* 48.2 (2023), pp. 142–152.

[226] Bowen Zheng et al. "Quantum Informed Machine-Learning Potentials for Molecular Dynamics Simulations of CO2's Chemisorption and Diffusion in Mg-MOF-74". In: *ACS Nano* 17.6 (2023), pp. 5579–5587.

[227] Jin-Hui Zhong et al. "Quantitative correlation between defect density and heterogeneous electron transfer rate of single layer graphene". In: *Journal of the American Chemical Society* 136.47 (2014), pp. 16609–16617.

[228] Hong-Cai Zhou, Jeffrey R Long, and Omar M Yaghi. "Introduction to metal–organic frameworks". In: *Chemical Reviews* 112.2 (2012), pp. 673–674.

[229] Cheng Zhu et al. "Highly compressible 3D periodic graphene aerogel microlattices". In: *Nature Communications* 6.1 (2015), p. 6962.

[230] Jingyi Zhu et al. "Defect-engineered graphene for high-energy-and high-power-density supercapacitor devices". In: *Advanced Materials* 28.33 (2016), pp. 7185–7192.

[231] Linggang Zhu, Jian Zhou, and Zhimei Sun. "Materials data toward machine learning: advances and challenges". In: *The Journal of Physical Chemistry Letters* 13.18 (2022), pp. 3965–3977.

[232] Shuze Zhu, Yinjun Huang, and Teng Li. "Extremely compliant and highly stretchable patterned graphene". In: *Applied Physics Letters* 104.17 (2014).

[233] Yanwu Zhu et al. "Carbon-based supercapacitors produced by activation of graphene". In: *Science* 332.6037 (2011), pp. 1537–1541.

[234] Yanwu Zhu et al. “Graphene and graphene oxide: synthesis, properties, and applications”. In: *Advanced Materials* 22.35 (2010), pp. 3906–3924.